From Quenches to Critical Dynamics and Non-Equilibrium Steady States: Universality in the Dynamics of Low-Dimensional Ultracold Bose Gases

Markus Karl

Dissertation
Fakultät für Physik und Astronomie
Universität Heidelberg
2016

Inaugural-Dissertation zur
Erlangung der Doktorwürde der
Naturwissenschaftlich-Mathematischen Gesamtfakultät der
Ruprecht-Karls-Universität Heidelberg

vorgelegt von
Markus Karl, M.Sc.
geboren in Wörth a. d. Donau

Tag der mündlichen Prüfung: 29.06.2016

From Quenches to
Critical Dynamics and Non-Equilibrium Steady States:
Universality in the Dynamics
of Low-Dimensional Ultracold Bose Gases

Gutachter: Prof. Dr. Thomas Gasenzer
Prof. Dr. Andreas Komnik

From Quenches to Critical Dynamics and Non-Equilibrium Steady States: Universality in the Dynamics of Low-Dimensional Ultracold Bose Gases

In this thesis, we study numerically critical dynamics in the ultracold Bose gas in one and two spatial dimensions. We concentrate on two specific setups, both amenable for experimental realisation: Hamiltonian parameter quenches in a two-component Bose gas in one spatial dimension and a driven-dissipative single-component gas in two spatial dimensions. The setups are chosen to excite critical dynamics, either via quenches close to a quantum critical point or via nucleation of vortex defects. The goal is to identify critical scaling and universal scaling forms in the time evolution of the respective systems. The analysis for the two-component Bose gas reveals that short-time quench dynamics can be described by a universal crossover function, where the quench-induced energy appears as the relevant energy scale. For the single-component gas, we find a new universal phase of time evolution, characterised by an anomalously slow phase ordering process of vortex defects. We discuss our results in the light of concepts of prethermalisation, generalised Gibbs ensembles and non-thermal fixed points, for universal critical phenomena far from thermal equilibrium.

Von Quenches zu Kritischer Dynamik und Stationären Nicht-Gleichgewichts-Zuständen: Universalität in der Dynamik niedrig-dimensionaler ultra-kalter Bose-Gas

In der vorliegenden Arbeit wird mit numerischen Mitteln kritische Dynamik in einem ultra-kalten Bose-Gas in einer und zwei Raumdimensionen untersucht. Dabei werden speziell zwei Varianten betrachtet, die beide besonders geeignet für eine Realisierung im Experiment sind: zum einen das plötzliches Verstellen eines hamiltonschen Parameters in einem zwei-komponentigen Bose-Gas in einer Raumdimension und zum anderen ein einkomponentiges Gas mit Dissipation und externem Treiben. Durch Ansteuern eines quantenkritischen Punktes im ersten Fall und das Erzeugen von Quantenwirbeln im zweiten Fall kann so kritische Dynamik explizit angeregt werden. Das Ziel der Untersuchung ist kritisches Skalieren und universelle Skalen-Formen in der Zeitentwicklung der jeweiligen Systeme zu identifizieren. Die Analyse des zweikomponentigen Gases zeigt, dass die Dynamik des Systems bereits für kurze Zeiten durch eine universelle Crossover-Funktion beschrieben werden kann. Die relevante Energie-Skala lässt sich dabei aus dem Parameter-Quench ableiten. Im Falle des einkomponentigen Gases wird eine neue universelle Phase der Zeitentwicklung identifiziert. Diese weist einen anomal langsamen Ordnungs-Prozess der Quantenwirbel auf. Die Ergebnisse werden in Bezug zu den Konzepten Präthermalisierung, verallgemeinerte Gibbssche Gesamtheiten und nicht-thermische Fixpunkte in ihrer Bedeutung für universelle kritische Phänomene fern des thermischen Gleichgewichts diskutiert.

Declaration by the author

This thesis is composed of my original work, and contains no material previously published or written by another person except where due reference has been made in the text. I have clearly stated the contribution by other authors to jointly- authored works that I have included in my thesis. The content of my thesis is the result of work I have carried out since the commencement of my graduate studies at the Heidelberg Graduate School of Fundamental Physics, Institut für Theoretische Physik, Universität Heidelberg and does not include material that has been submitted by myself to qualify for the award of any other degree or diploma in any university or other tertiary institution.

Contents

I Introduction

When thinking about the dynamics of quantum many-body systems, modern physics faces, apart from a variety of practical questions, a virtually philosophical question. Common sense dictates that a sufficiently macroscopic system eventually reaches some kind of equilibrium state. The most frequently encountered example for this in reality is thermodynamic equilibrium. But, given an isolated many-body system, how can it evolve into a steady state, as for example thermodynamic equilibrium, for almost all initial conditions? This, to date not entirely solved, paradox arises as 'isolated' is tantamount to demand that the system is subject to an energy-conserving Hamiltonian flow or unitary time evolution. In turn, time-reversibility is implied which contradicts the time-translation invariance of a stationary state.

Naturally, many efforts in the theory of dynamical complex systems nowadays evolve around the wish to develop a deep comprehension of this paradox and to eventually completely resolve it. However, at this point, understanding the situation should not be confused with the ability to compute or measure the time evolution of observables. [1] When it comes to many-body quantum systems, the complexity of the Hilbert space grows exponentially with the number of constituents. As an immediate consequence, not only the computational demand increases exponentially with system size but also the amount of information which has to be dealt with.

A promising way out of this misery, as it has always been for classical thermodynamics since the invention of Gibbs ensembles, is to concentrate on few universal properties instead of microscopic details. Doing so typically already requires to introduce effective degrees of freedom which emergently cover solely the important aspects of the physical behaviour but scale not as unfavourable with system size. The general understanding of the process of thermalisation in an isolated system then is that it appears thermal after a sufficiently long time when analysed in terms of those effective degrees of freedom. In practice, this is naturally realised when, for example, studying only the experimentally measurable observables or restricting computations to correlation functions of low order.

For specific observables of a quantum many-body system, the eigenstate thermalisation scenario constitutes a more quantitative understanding of thermalisation in an isolated quantum system [2–4]. If an observable O is considered subject to Hamiltonian time evolution and for an arbitrary initial state, the eigenstate thermalisation scenario argues that expectation values with respect to the initial state $\langle O \rangle_{\mathrm{i}}$ are described by a microcanonical classical statistical ensemble after sufficiently long time. For this to hold true, there are conditions on the energy spectrum of the Hamiltonian and the matrix elements of O in the energy eigenbasis, but the statement does not depend on the specific initial state.

[1] The computer scientist John P. Boyd states that "understanding only logarithmically grows with the number of floating point operations" [1]

Although it is widely believed that the great majority of isolated many body systems does thermalise, counter examples have been found. Kinoshita *et al.* demonstrated in [5] for the first time that, using trapped ultracold atoms, a situation can be engineered where no sign of thermalisation can be measured in a quantum system. It was shown that colliding atom clouds of a strongly interacting Bose gas in a one-dimensional geometry oscillate without a sign of degradation for essentially the system's lifetime. Here, the eigenstate thermalisation scenario apparently fails.

The (partial or complete) absence of thermalisation in an isolated many-body system is usually attributed to the property of integrability. Although the notion is not mathematically well defined in the context of quantum many-body systems [6], the general idea is that an infinite number of dynamically conserved quantities constrain the time evolution too strongly to allow thermalisation to a classical Gibbs ensemble. Practically, this often involves the possibility to solve a system exactly by the Bethe-Ansatz or similar techniques [7, 8]. The Kinoshita experiment, for example, is described by a Lieb-Liniger model, which falls into the class of quantum integrable models [9, 10].

Even if integrability hinders thermalisation in isolated many-body systems, this does not automatically imply that no statistically stationary state is reached. Rigol et al. have put forward that relaxation to a non-thermal equilibrium state nevertheless can happen in integrable quantum systems [11]. They succeeded to describe the late-time relaxed state of one-dimensional hard-core Bosons in terms of a classical statistical ensemble, using Jaynes' long standing concept of generalised Gibbs ensembles [12, 13]. By including all conserved quantities the integrable system provides in the statistical ensemble, instead of just energy, late-time stationary expectation values of observables can again be obtained from a canonical or microcanonical ensemble [11, 14]. Although it is not rigorously proven that all integrable models relax to stationary states for which generalised Gibbs ensembles can be constructed, it is widely believed to be the generic case [11, 15, 16].

The intriguing point in describing the non-equilibrium stationary state with a (generalised) statistical ensemble is that this restores the notion of universality. The concept of universality asserts that certain properties of a physical system are largely independent of its details [17]. The general applicability of this concept, and the reasons behind its emergence, have intrigued physicists for decades, and the research efforts culminated in the development of renormalisation group theory [18–20]. A prime example are critical phenomena in the vicinity of a continuous phase transition, where only the dimensionality of space and the order parameter, but not the microscopic details of interactions, are relevant. This permits a unified description, valid close to the critical point, of systems such diverse as superfluids and magnetic crystals. Scaling is closely related to universality, and the two can be seen as twin concepts [17]. For example, universality at a continuous phase transition manifests in the form of power laws in the vicinity of the critical point, where the values of the corresponding exponents are universal quantities. Measuring such scaling laws therefore provides a way for experimentally verifying universality, and for extracting the numerical values of critical exponents and critical amplitude ratios that characterise the different universality classes.

Universality classes have been extremely successful in classifying and characterising equilibrium states of matter. For example, there are different types of order in a magnetic material separated by a second-order phase transition at which the relevant physical prop-

erties become independent of the microscopic details of the system. This constitutes universality and allows to characterise an extensive range of different phenomena in terms of just a few classes governed by the same critical properties. Those manifest themselves typically in terms of scaling laws and symmetries and allow putting phenomena as different as opalescent water under high pressure, protein diffusion in cell membranes [21] and early-universe inflationary dynamics [22, 23] on the same structural footings. Typically, scaling is observed in thermal equilibrium or in relaxation dynamics close to equilibrium [24–29].

The ubiquitous presence of universal states in thermal equilibrium provokes the question if already the time evolution towards, but still far from, these universal states demonstrates likewise universal properties or critical scaling. And if so, a pressing follow-up question is if universal dynamic evolution can be grouped again in universality classes, either by systematically extending the existing Halperin–Hohenberg classes [30] or defining a completely new classification system. While recently the scaling hypothesis has been extended to far-from-equilibrium dynamics [27, 31–33], a comprehensive understanding of these questions is far from being achieved and currently subject to intense research.

A first step into the direction of classifying universality far from equilibrium is provided by the concept of prethermalisation [34, 35]. The idea thereby is that many-body systems generically, *i. e.* apart from the special class of exactly integrable ones, relax in three stages towards thermal equilibrium. In a first fast stage, coherences between modes with different eigenfrequencies simply dephase, without scattering. After dephasing, the system enters a stage in which details of the initial state are mainly lost. There, bulk quantities such as kinetic energy and pressure appear stationary at their final value in thermal equilibrium, describable by a thermal equation of state [35], or by some effective temperature. The prethermalised observables thereby depend on conserved quantities, such as energy or particle number, coming from the initial state but not on any details. In this sense, the prethermalisation plateau is universal. Eventually, the system will relax to a full thermal state, meaning that occupation numbers are described by a Bose–Einstein or Fermi–Dirac distribution but the time scale on which this happens can be arbitrarily long. In the context of weakly non-integrable systems, it is typically found that this type of three-staged relaxational dynamics happens [36–42], where the prethermalised plateau is typically describable in terms of the generalised Gibbs ensemble of the corresponding integrable model. In [43] prethermalisation was directly observed in the relative phase dynamics of a Bose gas, after splitting it in two halves.

In a context similar to prethermalisation, the concept of non-thermal fixed points has been proposed [44], which includes the time evolution itself in the picture of universality. The idea is, somewhat similar to prethermalisation, that the time evolution of correlation functions out of equilibrium in a many-body system is drawn to a universal attractor, in the sense of a renormalisation group fixed point [45]. In this scenario, the time evolution of an isolated system can be initialised with a large class of initial states but would nevertheless be drawn to a universal state, defined by the properties of the fixed point. In particular, universal scaling laws in momentum space distribution functions [45, 46] are expected together with universal scaling laws for the progress in time [47]. The latter implies that the universal state progresses algebraically slow in time. Thus, although an

isolated system does not become stationary in an universal out-of-equilibrium state and will eventually be attracted by the thermal fixed point, it can, depending on the critical exponents for the temporal scaling, spend an arbitrarily long time in the universal non-thermal state.

Due to this generic formulation, which is as well open to a more rigorous formulation in terms of non-perturbative renormalisation group methods [48, 49], it can encompass a variety of typical dynamical critical phenomena, (wave-)turbulence [50, 51], superfluid or quantum turbulence [52, 53], and relaxation dynamics such as coarsening and phase-ordering kinetics [54] following the creation of defects and nonlinear patterns. To date, non-thermal fixed point behaviour has been found numerically within the far-from-equilibrium evolution of many example systems, where they often are observed together with structure formation. Examples include ultracold Bose gases [55–60], early universe inflation [61], (non-)abelian gauge theories [62, 63], and classical turbulence [48]. See [64] for a review. Recently, non-thermal fixed points have been even demonstrated within the dynamics of holographically constructed superfluids [65], coming from the realm of gauge/gravity dualities for condensed matter [66–68]. The diverse applicability to very different systems implies that one may be able to use non-thermal fixed points to define universality classes for out-of-equilibrium time evolution [69]. In recent years, experimental techniques in the field of ultracold atomic gases tremendously advanced. It is nowadays possible to put many theoretical concepts for the way to thermalisation in isolated many-body systems to a practical test in clean and controlled quantum gas experiments [5, 27, 28, 43, 70–81]. It is therefore important to understand concepts like generalised Gibbs ensembles, pre-thermalisation, and non-thermal fixed points, which are typically proposed in the context of simple theoretical models, in more realistic setups, as realised in ultracold atom experiments. In this thesis, we study numerically critical dynamics, in a broad sense, in the ultracold Bose gas in the semi-classical regime [82–84]. We concentrate on two specific setups which are both within reach of current experimental capabilities.

The major part of this thesis will be concerned with a two-component (pseudo spin-$1/2$)[2] Bose gas in one spatial dimension, where experiments have already been able to observe critical scaling in far-from-equilibrium dynamics [73]. In the second part, we study dynamics in a single-component Bose gas in two spatial dimension. Here, we also relax the condition of isolation in favour of controlled external driving, to explore the connections between quasi-stationary states in isolated systems and true non-equilibrium stationary states.

The first part of this work thematises an isolated Bose gas with two linearly and non-linearly coupled components in one spatial dimension. This so-called spinor gas possesses a rich structure of phase transitions in its equilibrium phase diagram [85, 86]. This renders it ideal to study the relation between universal scaling in equilibrium and dynamical scaling in the time evolution ensuing a so-called parameter quench. Quenches provide a simple and efficient way to set off strong dynamics far from equilibrium, for theory and experiment alike. An equilibrium state is thereby prepared for a specific value of a Hamiltonian tuning parameter and thereafter the tuning parameter is suddenly switched

[2] We use the term ‘spinor gas’ for simplicity instead of ‘pseudo spin-$1/2$ gas’ throughout this work.

close to a critical value, possibly even changing to a different sector in the phase diagram.

In chapter II, we introduce the model for the two-component Bose gas in detail and give an overview over its properties concerning the equilibrium phase diagram. In particular, we discuss in what sense the two-component Bose gas resembles an effective model for spins, in terms of which we discuss the dynamic behaviour in the following.

As a first example for quench dynamics, we discuss in chapter II dynamic structure formation in the spinor gas. This constitutes also a brief detour to a two-dimensional system. In [60] we have demonstrated that structure formation is intimately connected to non-thermal fixed points in the two-component Bose gas. Here, we show, following [87], that the Hamiltonian tuning parameter controls the type of realised fixed point scaling, as it controls what types of spin structures form.

The subsequent chapters discussing the spinor gas are devoted to dynamics for quenches close to a critical point of a second order phase transition in one spatial dimension, without crossing it. With that, we study the effects of strong non-linear fluctuations, but without pattern formation, on dynamical critical scaling.

In chapter III, we derive in detail quench dynamics within Bogoliubov–de Gennes approximation for the spinor Bose gas. We introduce the concept of a parameter quench in terms of number states of Bogoliubov quasi-particles. With this we highlight the similarity to the formulation of quenches in the Ising spin chain [88]. Furthermore, we show how the equilibrium meanfield scaling behaviour can be identified within Bogoliubov quench dynamics and propose, based on this, a guide to analyse scaling in quench dynamics beyond Bogoliubov theory.

As the Bogoliubov quasi-particle picture for the spinor gas constitutes naturally an integrable system, we apply in chapter III the concept of generalised Gibbs ensembles to the spinor Bose gas. As a main result, we find that the ensemble is dominated by the conservation of quasi-particles with zero momentum. This means that it is possible to define for our dynamical setup a single effective temperature. We explain this effective temperature in terms of energy scales connected to the quench itself, not to the details of the initial state.

In chapter IV, we describe the experimental results from [73] which motivated our numerical studies of the one-dimensional spinor gas. The experiment observes static and dynamic meanfield scaling in pseudo-spin correlation functions for quenches in the spinor gas. By comparison to simulations we show that the experiment is not far away from measuring critical dynamics beyond the linear regime describable by Bogoliubov theory.

In chapter V, we present a thorough numerical study of quench dynamics in the one-dimensional spinor Bose gas. We employ a semi-classical simulation technique, the Truncated Wigner Method [83, 84], to go beyond the linear approximation. We determine numerically Ginzburg-like criteria, bounds in time and distance to the critical point, where interaction effects become important for the quench in the spinor gas. We find that, beyond the linear regime, meanfield scaling behaviour within quench dynamics is changed into crossover-like behaviour, reminiscent of thermal crossover behaviour in spin chains [89].

In chapter VI, we therefore review results on quenches in the Ising chain in a transverse field [90–92], which shares not only similarities in its behaviour but also structural symmetries in the Hamiltonian with the spinor Bose gas. The Ising model in a transverse field

is also an important example for the application of generalised Gibbs ensembles [90–95]. Spin correlations in the Ising model for quench dynamics behave effectively thermal very close to the critical point but are, in general, not describable by an effective temperature.

In light of these findings, we analyse in chapter VI quench dynamics of the spin correlation length in the spinor Bose gas, as a coarse grained (bulk) measure for correlations. The spinor gas does not reach a stationary or pre-thermalised state on numerically accessible time scales. We find as main result that, nevertheless, the correlation length in the spinor gas displays a crossover towards the critical point which follows the form of the thermal universal crossover function of the transverse-field Ising model [89]. We demonstrate that the Bogoliubov effective temperature of the spinor gas sets the temperature in the crossover function. This means that the relevant scale from the Bogoliubov generalised Gibbs ensemble remains a relevant scale beyond the linear regime. The effective temperature scale influences the correlation length before the dynamic evolution has reached a stationary state.

In the last part of chapter VI, concentrating on occupation number distribution of the single components, we demonstrate that the post-quench dynamics in the spinor gas shows signs of self-similar time evolution from this point of view. We identify a universal function, describing the time evolution, for the occupation number distribution which insensitive to the distance from the critical point.

In the second part of this thesis, we switch gears to a one-component Bose gas in two spatial dimensions, which has been used extensively as classical setting to study quantum turbulence [52, 53] and non-thermal fixed points [47, 55–57, 59]. In this case, we open the system to a thermal and a non-thermal environment, to study numerically how critical, self-similar time evolution reacts to driving and dissipation. In particular, the goal is to investigate if the structure of non-thermal fixed points in the Bose gas is in one-to-one correspondence with non-equilibrium steady states in presence of non-equilibrium driving and dissipation. This is especially interesting for experiments with exciton–polariton condensates [96–98], which are naturally strongly coupled to a non-thermal driving source.

In chapter VII, we start with investigating a new (as compared to [47, 55–57, 59]) class of initial states to set off dynamics in the Bose gas. Using regular lattices of vortices as initial state, we discover a new non-thermal fixed point in the Bose gas, which comes with an anomalously slow self-similar time evolution of occupation spectra. By coupling this kind of initial conditions to a thermal bath, we furthermore show that the previously discovered non-anomalous non-thermal fixed point [47, 59] is tightly connected to phase ordering kinetics from vortex diffusion [54, 99]. We clarify the connection between phase ordering kinetics and the fixed point structure in the Bose gas further. With this we map the anomalous critical exponent, defining our newly discovered fixed point, to an anomalously high dynamical critical exponent $z = 5$ of the ordering process. Based on our results and in light of findings for vortex glass phases in superconductors [100–104], we put forward that the anomalous fixed point in the Bose gas signals a glass-like phase of the vortex distribution.

In chapter VIII, we couple the Bose gas to non-thermal driving and dissipation, to probe the structure of true non-equilibrium steady states. We find that the Bose gas hosts two classes of stationary states, one which contains vortex ensembles and one which does not. We demonstrate that scaling properties of distribution functions in the vortex-less steady

state can be understood in terms of the Kardar–Parisi–Zhang universality class [105–108]. In particular, we find indications that the vortex-less steady state is connected to a fixed line in the Kardar–Parisi–Zhang equation, to which the vortex-less Bose gas effectively maps [48, 109, 110]. For the second, vortex-containing class of non-equilibrium steady states in the Bose gas, we demonstrate that scaling properties of distribution functions can fully be understood in terms of the vortex ensemble. Stationary occupation numbers for different realisations of the driving can be rescaled to a universal function, using moments of the vortex distribution as scale. With this scaling collapse and the form of the emerging universal function, we find strong numerical evidence that the vortex-containing steady state is in one-to-one correspondence with the anomalous non-thermal fixed point.

II Phenomenology of the Two-Component Bose Gas

The two-component Bose gas offers a rich phenomenology of phase transitions, rendering it the ideal model system to study dynamic critical phenomena. Apart from being subject to the standard Bose condensation, the phasespace structure of the ground state can contain first and second-order phase transitions where the degree of miscibility of the two components serves as order parameter. In addition, those transitions are connected to Hamiltonian tuning parameters which allows the transfer of theoretical studies of quench scenarios to experimental setups, due to the high amount of parameter control for typical Bose gas experiments. In recent years, the virtues of the two-component Bose gas as wildcard system for phase transitions have been exploited to study phenomena as different as turbulence in binary fluids, see for example [111, 112], the proliferation of topological defects, see for example [113–115] and phase transitions in spin systems, *cf.* [116]. In previous works, we have characterised the structure of non-thermal fixed points within the two-component Bose gas, *cf.* [60, 87, 117].

In this chapter, we introduce the general model for the two-component Bose gas and the language of pseudo-spins, which we make use of extensively in subsequent chapters. Thereafter, we discuss the structure of the equilibrium phase diagram and, in particular, how to obtain critical couplings and critical scaling exponents in meanfield approximation. Furthermore, we explain the method of semi-classical simulations we employ for the numerical treatment of the spinor gas, to simulate the dynamics evolution of the spinor Bose gas beyond meanfield theory.

As a first example for quench dynamics, we discuss in the second part of this chapter briefly dynamic structure formation in the spinor gas. We introduce the building blocks of structure formation, *i. e.* topological defects, in the spinor Bose gas and discuss their nucleation on basis of dynamical instabilities. Finally, we present a numerical study of the spinor gas in two-spatial dimensions [87], which highlights the way from structure formation to non-equilibrium critical scaling.

II.1 The Model

The microscopic Hamiltonian for two interacting Bose fields Φ_j, $j \in \{\uparrow,\downarrow\}$, in d spatial dimensions, with a linear coupling J and a zero-point detuning δ is $H = H_0 + H_{\text{cpl}} + H_{\text{int}}$,

with the quadratic and quartic parts given by

$$H_0 = \sum_{j=\uparrow,\downarrow} \int \mathrm{d}^d x\, \Phi_j^\dagger \Big[-\frac{\hbar^2}{2m}\nabla^2 + V(\boldsymbol{x}) \Big] \Phi_j \,, \tag{II.1a}$$

$$H_{\mathrm{cpl}} = -\hbar \int \mathrm{d}^d x \Big[J\Big(\Phi_\uparrow^\dagger \Phi_\downarrow + \mathrm{h.c.} \Big) + \delta \Big(\Phi_\uparrow^\dagger \Phi_\uparrow - \Phi_\downarrow^\dagger \Phi_\downarrow \Big) \Big] , \tag{II.1b}$$

$$H_{\mathrm{int}} = \frac{1}{2} \sum_{i,j=\uparrow,\downarrow} g_{ij} \int \mathrm{d}^d x\, \Phi_i^\dagger \Phi_i \Phi_j^\dagger \Phi_j \,. \tag{II.1c}$$

Here, m is the atomic mass which we assume equal for both species. For an actual experimental setup, this corresponds to realising the different species with different hyperfine levels of one atomic species. A trapping potential $V(\boldsymbol{x})$ is of relevance for the experimental realisation and will be discussed below. The internal symmetries of the Hamiltonian are dictated by the relations among the linear couplings, J and δ, and the non-linear couplings, $g_{\uparrow\uparrow}$, $g_{\downarrow\downarrow}$ and $g_{\uparrow\downarrow}$. The possible transitions from a miscible to an immiscible state are controlled by the inter-species couplings, J and g_{12}. Thus, in this work we mainly concentrate on the situation where $g_{\uparrow\uparrow} = g_{\downarrow\downarrow} = g$ and $\delta = 0$. We will discuss the relevance of our results for a realistic experimental situation, where $g_{\uparrow\uparrow} \neq g_{\downarrow\downarrow}$ and where the detuning δ is usually finite for various technical reasons. For $J = 0$, $\delta = 0$, and equal intra-species couplings $g_{\uparrow\uparrow} = g_{\downarrow\downarrow}$, a non-vanishing cross-coupling, $g_{\uparrow\downarrow} \neq g$, leads to a deviation from a fully $U(1)\times SU(2)$-symmetric theory. Adding the linear coupling, $J \neq 0$, leaves a residual Z_2 symmetry, which is broken if $\delta \neq 0$ or $g_{\uparrow\uparrow} \neq g_{\downarrow\downarrow}$.

Note that, in the context of cold atom experiments, the linear coupling term proportional to J in H_{cpl} in Eq. II.1b is usually interpreted as Rabi coupling and includes an additional factor $1/2$ in the definition, $J \to \Omega = 2J$. In particular, in experiments [73, 118] to which we compare our results, the linear coupling Ω relates to the notion used in this work by $\Omega = 2J$. Throughout this work we stick to the Josephson form of the linear coupling, as introduced in Eq. II.1b, if not stated otherwise, since this is a more commonly encountered definition in theory literature, for example [113, 116, 119].

In the case that mode occupation numbers are large as compared to 1, the Bose field operators can be replaced by classical complex fields, $\Phi_j \to \phi_j$, and then expressed in terms of phases and densities, $\phi_j = \sqrt{n_j}\mathrm{e}^{\mathrm{i}\,\theta_j}$. Using the language of the phase–density representation, it is particularly convenient to split the degrees of freedom in internal ones and hydrodynamic ones, for example with the definitions

$$\begin{aligned} n_+ &= \frac{n_\uparrow + n_\downarrow}{2} \,, \\ S_z &= \frac{n_\uparrow - n_\downarrow}{n_\uparrow + n_\downarrow} \,, \\ \theta_\pm &= \theta_\uparrow \pm \theta_\downarrow \,, \\ g_\pm &= g \pm g_{\uparrow\downarrow} = g(1 \pm \alpha) \,, \end{aligned} \tag{II.2}$$

where we have also introduced the dimensionless ratio α between the inter- and intra-

species coupling,

$$\alpha = \frac{g_{\uparrow\downarrow}}{g} \,. \tag{II.3}$$

The hydrodynamic degrees of freedom are indexed with '+' and are subject to the overall $U(1)$ symmetry. In later discussions they will be referred to as degrees of freedom from the symmetric sector of the model. The remaining symmetries connect to the internal degrees of freedom, indexed with '−', and can be cast into a language of classical spins, as discussed below. From the Hamiltonian given by Eq. (II.1) together with the definitions in Eq. (II.2) the microscopic action[1] in phase–density representation can be obtained,

$$\begin{aligned}\mathcal{S} = \int \mathrm{d}t\mathrm{d}^d x \Bigg\{ & - n_+ \left[\partial_t \theta_+ - S_z \partial_t \theta_-\right] \\ & - \frac{1}{2m}\left[\frac{\partial_{\boldsymbol{x}} n_+^2}{2n_+} + \frac{n_+ \partial_{\boldsymbol{x}} S_z^2}{2(1-S_z^2)}\right] \\ & - \frac{1}{2m}\frac{n_+}{2}\left[\partial_{\boldsymbol{x}}\theta_+^2 + \partial_{\boldsymbol{x}}\theta_-^2 + 2S_z \partial_{\boldsymbol{x}}\theta_+ \partial_{\boldsymbol{x}}\theta_-\right] \\ & - g_+ n_+^2 \left[1 + \frac{g_-}{g_+} S_z^2\right] + 2\delta n_+ S_z + 2J n_+ \sqrt{1-S_z^2}\cos\left(\theta_-\right) + 2\mu n_+ \Bigg\} \,,\end{aligned} \tag{II.4}$$

where the external potential, $V(\boldsymbol{x})$, has been replaced by a general chemical potential, μ, which can include V. Note that we set $\hbar = 1$ for the remainder of this work. In the form of Eq. (II.4) the hierarchy of symmetries and how they are controlled by the coupling constants is made explicit. The global $U(1)$ symmetry of θ_+ phase rotations is always present. A finite value of J lifts a symmetry connected to rotations of θ_- . A finite value of g_- lifts a symmetry connected to rotations of the spin axis, as can be seen from the term $\propto S_z^2$ in Eq. (II.4), but leaves a residual $Z_2 \times Z_2$ symmetry. One of this residual discrete symmetries is a spin-flip symmetry, $\theta_- \to -\theta_-$ and $S^z \to -S^z$, and can be lifted with a finite value for δ. The other discrete Z_2 symmetry is given by a discrete shift of the relative phase angle $\theta_- \to \theta_- \pm \pi$ together with $J \to -J$. If all internal coupling constants vanish, the symmetries are enhanced to form a full $SU(2)$ symmetry, connected to a full rotation symmetry of the spin on a Bloch sphere.

II.1.1 Spin-fluid representation of the two-component Bose gas

The model for two coupled Bose gases, defined in Eq. (II.1), with equal atomic masses can be interpreted to describe one gas of atoms in two spin states, as can be already inferred from the transformation to Eq. (II.4). This system can be viewed as a coherent spin fluid, as each volume element of it carries angular momentum proportional to the local density $2n_+$ of atoms, generalising the concept of classical relativistic spin fluids [120]. Such a fluid is not to be mixed up with the disordered state of a spin liquid, occurring, *e. g.*, in lattices giving rise to frustrated moments. The separation of the model into spin

[1] We use the standard Legendre transformation for the Lagrangian density of a non-relativistic scalar field, $\mathcal{L} = \int \mathrm{d}^d x \, \sum_j \frac{\mathrm{i}}{2}\left(\Phi_j^\dagger \partial_t \Phi_j - \Phi_j \partial_t \Phi_j^\dagger\right) - H$

degrees of freedom and hydrodynamic ones can be clarified even further by use of normalised Schwinger angular momenta $S_a = (2n_+)^{-1} \sum_{ij} \Phi_i^\dagger \sigma_{ij}^a \Phi_j$ with $a \in \{x,y,z\}$. The Pauli matrices σ_a form a representation of the $SU(2)$ spin algebra. In the phase-density representation, we obtain

$$S_x = n_+^{-1} \sqrt{n_\uparrow n_\downarrow} \cos\theta_- \,, \tag{II.5a}$$

$$S_y = n_+^{-1} \sqrt{n_\uparrow n_\downarrow} \sin\theta_- \,, \tag{II.5b}$$

$$S_z = (2n_+)^{-1} (n_\uparrow - n_\downarrow) \,, \tag{II.5c}$$

where the classical spin vector is normalised to $|\boldsymbol{S}| = 1$. The relations from Eq. (II.5) show that the remaining spin degrees of freedom which are not apparent in Eq. (II.4) are mainly determined by the relative phase angle, θ_-. In terms of the Bloch sphere picture, it determines the direction the coherent spin points to on the equator of the sphere at a point in space. When transformed completely to the spin language, the microscopic Hamiltonian reads, for $g_{\uparrow\uparrow} = g_{\downarrow\downarrow} = g$,

$$\begin{aligned} H = \int \mathrm{d}^d x \Bigg\{ & \frac{1}{4mn_+} \left(\partial_{\boldsymbol{x}} n_+\right)^2 + \frac{n_+}{4m} \left|\partial_{\boldsymbol{x}} \mathbf{S}\right|^2 + 2n_+ \left(m\boldsymbol{v}_{\mathrm{eff}}^2 - \mu\right) \\ & + g_+ n_+^2 + g_- n_+^2 S_z^2 - 2Jn_+ S_x - 2\delta n_+ S_z \Bigg\} \,. \end{aligned} \tag{II.6}$$

Details on the calculation can be found in [121] and have been discussed at length in [117]. From a hydrodynamic point of view it is useful to define an effective velocity field for the fluid [121], $\boldsymbol{v}_{\mathrm{eff}} = (n_\uparrow \boldsymbol{v}_\uparrow + n_\downarrow \boldsymbol{v}_\downarrow)/(2n_+)$, in terms of the velocities $\boldsymbol{v}_i = \partial_{\boldsymbol{x}} \theta_i / m$ of the spin components. It evaluates to

$$\boldsymbol{v}_{\mathrm{eff}} = \frac{1}{2m} \left[\partial_{\boldsymbol{x}} \theta_+ + \frac{S_z \left(S_y \partial_{\boldsymbol{x}} S_x - S_x \partial_{\boldsymbol{x}} S_y \right)}{1 - S_z^2} \right] . \tag{II.7}$$

The Hamiltonian Eq. (II.6) expresses the energy of the two-component Bose gas as that of a coherent spin field $\boldsymbol{S}(\boldsymbol{x})$ carried by a fluid with density $2n_+$ and current $\boldsymbol{j} = n_+ \boldsymbol{v}_{\mathrm{eff}}$. The current is a conserved quantity if $J = \delta = 0$. For a fluid at rest, *i. e.* $n_+ \approx$ const and $\partial_{\boldsymbol{x}} \theta_+ \approx 0$, the spin system assumes the form of a nonlinear sigma model [121] or XXX-type Heisenberg chain with single-ion anisotropy $\sim S_z^2$ in a transverse and/or longitudinal magnetic field [122], with an additional chiral-field term $\propto |\boldsymbol{v}_{\mathrm{eff}}|^2$.

The effective velocity field constitutes a rather complex coupling structure, for the spin sector itself and between the hydrodynamic degrees of freedom and the spin sector. First of all, the term $|\boldsymbol{v}_{\mathrm{eff}}|^2$ in the Hamiltonian Eq. (II.6) gives only a relevant contribution to the total energy, beyond simple hydrodynamic kinetic energy $\propto |\partial_{\boldsymbol{x}} \theta_+|^2$, if the spin field is sufficiently polarised. If $S_z \simeq 0$, one finds from Eq. (II.7) that $\boldsymbol{v}_{\mathrm{eff}} \simeq \partial_{\boldsymbol{x}} \theta_+$. For this reason, in first order perturbation theory around a z-spin unpolarised meanfield there is no coupling between spin sector and hydrodynamic sector. We discuss this point in more detail in the next chapter III.

Expanding the contribution to the energy from the effective velocity field one finds, in

particular, terms of the form

$$|\boldsymbol{v}_{\text{eff}}|^2 = \sum_{i=x,y} \left\{ A_i \partial_{\boldsymbol{x}} \theta_+ \cdot \partial_{\boldsymbol{x}} S_i + B_i \left| \partial_{\boldsymbol{x}} S_i \right|^2 \right\} + C \partial_{\boldsymbol{x}} S_x \cdot \partial_{\boldsymbol{x}} S_y + \dots , \tag{II.8}$$

where all pre-factors A_i, B_i, C are proportional to $S_z/(1 - S_z^2)$. The terms multiplied by A_i in Eq. (II.8) couple the fluid velocity field $\partial_{\boldsymbol{x}}$ to spin fluctuations on the equator of the Bloch sphere. Therewith, spin fluctuations in x- and y-spin direction are energetically suppressed if their spatial gradient is directed parallel to the fluid's flow. The terms multiplied by B_i and C in Eq. (II.8) constitute additional self-couplings of the spin field. They lead to a coupling between the direction of spatial changes in the spin field and the intrinsic spin direction. The B_i-terms weight the energy contribution from the spin gradients in x- and y-direction with the local spin polarisation. The C-term in Eq. (II.8) introduces an additional energy contribution from the local spatial overlap between gradients of spin fields in different directions, in contrast to the standard spin gradient term $\propto |\partial_{\boldsymbol{x}} \boldsymbol{S}|^2$ in the Hamiltonian (*cf.* Eq. (II.6)).

II.1.2 Structure of the Phase Diagram

The two-component Bose gas, as defined by the model given in Eq. (II.1), hosts two distinctly different groundstates at zero temperature depending on the Hamiltonian parameters g_- and J, together with phase transitions connecting them. The order parameter, with respect which the phase diagram (see Fig. II.1) can be formulated, is constituted by the magnetisation (polarisation) $m = \langle S_z \rangle$ of the spin field S_z. To deal with the Z_2 symmetry properly, the order parameter is formally defined as

$$m = \lim_{\delta \to 0} \lim_{V \to \infty} \frac{1}{V} \int_V \mathrm{d}^d x \, \langle S_z(\boldsymbol{x}) \rangle \, . \tag{II.9}$$

The groundstate phase diagram, spanned by the tuning parameters J and $\alpha = g_{\uparrow\downarrow}/g$, is then divided into regions where the magnetisation is zero (phase II and $\overline{\text{II}}$ in Fig. II.1) and regions where the magnetisation is finite (phase I and $\bar{\text{I}}$ in Fig. II.1). In the language of the two components, zero magnetisation corresponds to a state with the two components locally mixed, such that $n_\uparrow \simeq n_\downarrow$ everywhere, whereas a finite magnetisation is achieved if one component constitutes the majority in macroscopic patches. Therefore, the corresponding phase transitions are usually referred to as miscible–immiscible phase transitions. In this section, we discuss the equilibrium phase diagram, and the nature of the respective transitions, at zero temperature within meanfield theory.

First, we concentrate on the case without linear couplings (*i. e.* transition along the α-axis in Fig. II.1). The homogeneous[2] Bose gas of two linearly uncoupled components, defined by Eq. (II.1) with $J = \delta = 0$, possesses two distinct ground states depending on the choice α [85, 86, 123]. In the immiscible regime, $\alpha > 1$, the term $\propto g_- S_z^2$ in Eq. (II.6) gives a negative contribution to the total energy for all possible spin configurations. As the value of the z-projection of the coherent spin vector is bounded by $|S_z| < 1$, the

[2] We assume the absence of external sources and potentials, specifically $V_{\text{ext}}(\boldsymbol{x}) = 0$ throughout the remainder of this work

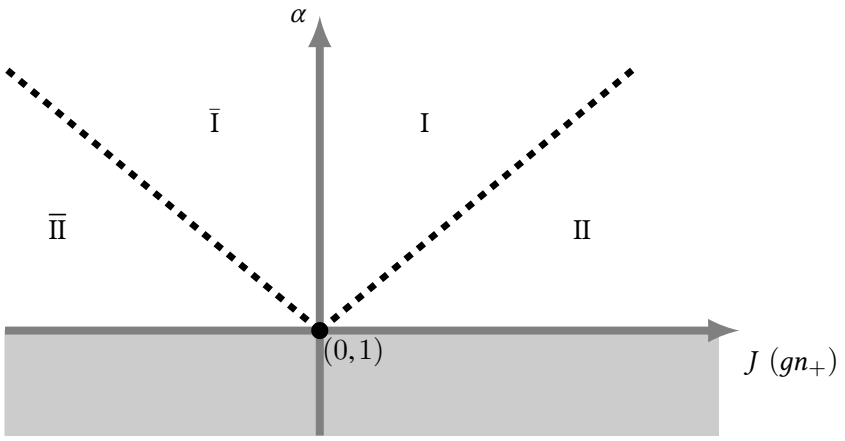

Figure II.1: Ground state phase diagram on the spin sector for the case $\delta = 0$ and $g_{\uparrow\uparrow} = g_{\downarrow\downarrow}$. *Phase I* is characterised by a finite magnetisation $m = \langle S_z \rangle \neq 0$, corresponding to demixed Bose gas components. *Phase II*, including the whole grey shaded area for $\alpha < 1$, is characterised by vanishing magnetisation $m = 0$. The phase transition is of second order across the dashed lines, which are defined by $|J(\alpha)| = n_+ g(\alpha - 1)$ and of first order along the line $J = 0$ across the point $(J, \alpha) = (0, 1)$. From right to left, *i. e.* I, II to $\bar{\text{I}}$, $\overline{\text{II}}$, the properties of the magnetisation stay as described before but the x projection of the spin vector changes direction from $\theta_- = 0$ to $\theta_- = \pi$. From the point of view of the ground state this can be absorbed in a reflection of the coordinate system and, thus, does not mark an additional phase transition. Note that the depicted critical lines refer to the meanfield values for the critical couplings.

energy in the spin sector is minimised by configurations with $S_z(\boldsymbol{x}) \simeq 1$ or $S_z(\boldsymbol{x}) \simeq -1$. Consequently, one has for the magnetisation $|m| = 1$. Spontaneous breaking of the discrete Z_2 symmetry under $S_z \to -S_z$ leads, in a non-equilibrium or thermal system, to the formation of domains in the z-projection of the spin. In a description based on classical fields they appear as oppositely signed patches of the spin density field S_z with $S_z \simeq \pm 1$, similar to the ferromagnetic phase of the classical Heisenberg model [124, 125].

On the contrary, in the miscible regime for $J = \delta = 0$, $\alpha < 1$, spin configurations with $S_z(\boldsymbol{x}) \equiv 0$ are preferred energetically, which leads to a groundstate on the spin sector with magnetisation $m = 0$, within meanfield calculations. As the ground state order parameter $\langle S_z \rangle$ jumps discontinuously form $m = 0$ to $|m| = 1$ as α crosses 1, the transition is of first order. In addition, in both phases, there is an unbroken residual $U(1)$ symmetry for the spin being free to move on the equator of the Bloch sphere. This symmetry is the major determining *factum* for the spectrum of topological defects. The connected massless excitations of the relative phase have important consequences on the possible phase-ordering kinetic processes in the system, see for example [115, 126]. For the phase transition in equilibrium, due to this remaining $U(1)$ symmetry, the Mermin–Wagner theorem implies that no equilibrium long-range order can build up in the thermodynamic

limit in $d \leq 2$ spatial dimensions.

A finite linear coupling J changes the picture, as it constitutes a second relevant tuning parameter. The linear coupling term (*i. e.* the term $\propto J$ in Eq. (II.6)) induces a local mixing of $|\downarrow\rangle$- and $|\uparrow\rangle$-species. If the energy scale for this process, provided by J exceeds, the energy scale $-g_- n_- +$ for the repulsive demixing (in the region $\alpha > 1$ in Fig. II.1), the the spinor Bose gas is rendered miscible again.

Analysing the free energy for the groundstate shows indeed that a second type of phase transition exists if $\alpha > 1$. On the meanfield level in the homogeneous system, one simply has to minimise the energy functional with respect to $\boldsymbol{S}$, assuming a spatially constant spin vector on the Bloch sphere. Analysing the energy functional Eq. (II.6), after dropping all terms containing spatial derivatives, shows that the equator-projection of spin vector needs to point along the x-direction, if J is taken positive. The remaining part of the energy functional can be minimised by the choice

$$\langle S_z \rangle = \begin{cases} 0 & \text{if } J > -g_- n_+ \,, \\ \pm \sqrt{1 - \left(\frac{J}{-g_- n_+}\right)^2} & \text{if } J < -g_- n_+ \,, \end{cases} \tag{II.10}$$

implying $\langle S_x \rangle = 1$ or $\langle S_x \rangle = J/(-g_- n_+)$ by virtue of the normalisation. A detailed analysis of the extrema of the energy functional shows that a bifurcation happens at the point $J = J_\mathrm{c} = -g_- n_+$. If $J > J_\mathrm{c}$, the magnetisation $m = 0$ constitutes the stable energy minimum, which turns into an energy maximum at $J = J_\mathrm{c}$. Simultaneously, the former minimum $m = 0$ forks into two new minima $m \neq 0$ for $J < J_\mathrm{c}$, which are connected by a global spin flip. For the groundstate, the system will spontaneously choose one sign and develops a magnetisation which is continuous in J, *cf.* Eq. (II.10). Consequently, one finds a second-order phase transition in the groundstate at meanfield level, controlled by the tuning parameter J, which is connected to a spontaneously broken Z_2 symmetry.

On the meanfield level, the magnetisation scales as

$$m \sim \varepsilon^{1/2} \,, \tag{II.11}$$

at the critical point, where the reduced tuning parameter is not contributed by the temperature but the linear coupling, $\epsilon = (J - J_\mathrm{c})/J_\mathrm{c}$. It can be shown that the phase structure for the ground state persists if thermal and quantum fluctuations are included in the analysis, see for example [85, 86].

A summary of the ground state phase diagram for $\delta = 0$ is depicted in Fig. II.1, using the meanfield values for the critical couplings to locate the lines of phase transitions. We point out that the linear coupling can be chosen negative or even to have a non-trivial phase. In this case the coordinate system for the spin degrees of freedom can be rotated such that the x direction of the spin projection matches the phase of the coupling. Nevertheless, if the initial state defines a direction in spin space dynamical instabilities can be triggered quenching from the left to the right side in the phase diagram Fig. II.1, as we discuss in Sect. II.4. Similarly, although the ground state is generically mixed for $\alpha < 1$, dynamical instabilities can be employed to achieve a transient demixed state.

II.2 Critical Scaling in Equilibrium

We continue to consider the case $\alpha > 1$ at finite $J > 0$, as a main part of this work will be concerned with universal dynamics taking place in this part of the phase diagram. Therefore, we discuss the equilibrium properties of the miscible–immiscible quantum phase transition controlled by J in more detail in this section.

II.2.1 Scaling Forms

In the vicinity of the phase transition at $J_c = n_+ g_-$ at zero temperature, correlations show scaling behaviour with respect to the relative distance $\varepsilon = (J - J_c)/J_c$ to the critical point. Equilibrium renormalisation-group theory predicts a universal scaling form for the correlation function of (dimensionless) spin degrees of freedom near a critical point, see for example [127],

$$G(\mathbf{r}) = C\xi^{-(d-2+\eta)}\mathcal{F}_{\pm}\left(\frac{|\mathbf{r}|}{\xi}\right) \tag{II.12}$$

where η is the so-called anomalous dimension, a scaling exponent which determines the non-trivial part of the scaling behaviour of the correlation function itself at the critical point. The function $\mathcal{F}_{\pm}(x)$ is universal, *i. e.* determined only by the universality class the considered transition lies in and only depending on dimensionless ratios of physical parameters. The index ± indicates that the function can be different in the symmetry-broken or unbroken phase. In any case, it fulfils the asymptotic behaviour

$$\mathcal{F}_{\pm}(x) = \begin{cases} D\, e^{-x} \text{for } x \to \infty\,, \\ \overline{D} x^{-1} \text{for } x \to 0\,, \end{cases} \tag{II.13}$$

with D, $\overline{D}$, and C in Eq. (II.12) being non-universal constants. The length ξ in Eq. (II.12) is the correlation length due to the long-range asymptotic behaviour of $\mathcal{F}$ and, typically, follows a scaling law near criticality of the form

$$\xi = |\varepsilon|^{-\nu}\,, \tag{II.14}$$

defining the critical exponent ν. The logic of the scaling hypothesis holds for a quantum phase transition at zero temperature and a classical phase transition alike, identifying the control parameter with the corresponding Hamiltonian parameter. The crucial difference, however, is the dimensionality d which has to be inserted in the expressions. For a quantum phase transition, d needs to be by one higher as compared to a classical thermal transition in the same universality class [128].

II.2.2 Meanfield Scaling in the Spinor Bose Gas

The mean-field prediction for ν for the spin sector of our model can be derived within semi-classical Landau theory as follows. Neglecting fluctuations of the total density n_+ and phase θ_+, the Hamiltonian (II.6) can be written in terms of Euler angle representation

of the spin, $S_x = \cos\Theta\cos\theta_-$, $S_y = \cos\Theta\sin\theta_-$, and $S_z = \sin\theta_-$, as

$$H = \int \mathrm{d}^d x \left\{ \frac{n_+}{4m}\left[(\partial_{\mathbf{x}}\theta_-)^2 + (\partial_{\mathbf{x}}\Theta)^2\right] - 2Jn_+\cos\Theta\,\cos\theta_- - n_+ J_c \sin^2\Theta \right\}, \tag{II.15}$$

with $-\pi/2 \le \Theta \le \pi/2$, $-\pi \le \theta_- \le \pi$, and θ_- and Θ being mutually dual variables. We have, for the time being, set $\delta = \mu = 0$. For $J_c = 0$, this model bears an O(2) symmetry around the S_x axis and undergoes a quantum phase transition in the Kosterlitz-Thouless class [129]. Choosing $J_c > 0$, the energy density exhibits the possibility of spontaneous Z_2 symmetry breaking at $\varepsilon = 0$ which becomes apparent by expanding around $\Theta = 0$, $\theta_- = 0$,

$$\mathcal{H}_{\mathrm{pot}} = n_+ J_c\left[-2(\varepsilon+1) + \varepsilon\,\Theta^2 + \frac{3-\varepsilon}{12}\,\Theta^4 + O(\Theta^6)\right]. \tag{II.16}$$

While for $\varepsilon > 0$ there is only one minimum at $\Theta = 0$, the ground state can assume, for $-2 < \varepsilon < 0$, different values $\Theta_0 = \arccos(1+\varepsilon)$. Hence, while the potential remains symmetric under $\Theta \to -\Theta$, the ground state is two-fold degenerate with respect to the spin orientations

$$\langle S_z\rangle = \pm\sqrt{|\varepsilon|(2-|\varepsilon|)} = \pm\sqrt{1-\left(\frac{J}{J_c}\right)^2}, \tag{II.17}$$

and the Z_2 symmetry is spontaneously broken. The expectation value $\langle\Theta\rangle$ or, equivalently, $m = \langle S_z\rangle$, is the order parameter of the transition.

The inverse coherence length squared is proportional to the 'mass' parameter in the potential Eq. (II.16), *i. e.* the second derivative of $\mathcal{H}_{\mathrm{pot}}$ with respect to Θ at the value of the order parameter. In mean-field approximation, it follows from the Eq. (II.16) that

$$\xi^{-2} \propto \begin{cases} \varepsilon & \text{for } \varepsilon \ge 0 \text{ (symmetric phase)}, \\ |\varepsilon|\,(2-|\varepsilon|) & \text{for } -2 < \varepsilon < 0 \text{ (symmetry-broken phase)}. \end{cases} \tag{II.18}$$

Together with Eq. (II.14), this shows that, in both phases, $\nu = 1/2$. Naturally, to meanfield order this result is independent of the dimensionality.

Within the same level of approximation the whole correlation function could be obtained from Eq. (II.15) together with Eq. (II.16). To do so, the inverse propagator for Θ can be read off when $\mathcal{H}_{\mathrm{pot}}$ is taken into account up to second order in Θ and the kinetic part of $\mathcal{H}$ is transformed to momentum space. Inverting the expression and evaluating it in position space yields essentially Eq. (II.13). At meanfield level, the expression for the correlation function can not be refined beyond the asymptotic form which is part of the scaling hypothesis. This implies also that the anomalous dimension is $\eta = 0$.

To obtain values for the static critical scaling exponents beyond the meanfield predictions lies not in the scope of this work. A good starting point would certainly be the fourth-order approximation of the potential of the Eq. (II.16). As it reassembles a standard real scalar field theory with ϕ^4 potential, it might be possible to apply results from

Wilson-Fisher renormalisation group theory (see *e. g.* [130]). However, one needs to be careful with this approach, since the full potential in Eq. (II.15) resums the field Θ in an infinite series, possibly introducing marginally relevant operators that are not considered through Eq. (II.16). Moreover, in Eq. (II.15) the effects of a coupling to the symmetric sector are not included beyond zero order. To address this problems, a thorough renormalisation group analysis needs to be carried out for the full model.

II.3 Topological Defects

On the level of solutions for the classical fields, the two-component Bose gas, as defined via the Hamiltonian Eq. (II.1), hosts a variety of energy minimising field configurations with a non-trivial spatial profile, such as domain walls in the spin, spin textures (*e. g.* skyrmions, see for example [125]), or vortices. These so-called topological defects share the feature of constituting a tremendously stable, highly localised, and non-dipersive inhomogeneity in the classical fields, which can be treated as a particle-like object. Therefore, the presence of topological defects has the potential to tremendously influence the dynamics of the two-component Bose gas in the semi-classical regime. In general, theories for dynamical critical phenomena, such as the theory of phase ordering kinetics [54, 99] and the Kibble–Zurek mechanism [131, 132] often solely focus on those objects.

In this section, after introducing the general idea of topological solutions, we derive the spatial profile for a domain wall in the z-spin in the linearly coupled immiscible regime of the spinor Bose gas. Thereafter, we discuss on phenomenological grounds point defects, in particular vortices and spin textures, which play an important role in structure formation processes in the spinor Bose gas in two spatial dimensions. The goal of this section is to provide an overview over the building blocks of structure formation, which exist in our system and typically come together with dynamical instabilities (see Sect. II.4). We discuss dynamical structure formation in the spinor gas in Sect. II.6.

II.3.1 Relevance of Topological Solutions

The groundstate of a system which is modelled by a Galilei-invariant action is in general expected to share the full Galilei symmetry, in particular translation and rotation invariance. However, if the groundstate exhibits a degeneracy, meaning that the energy functional allows for a manifold of possible groundstates, it turns out that energetically low lying states can exist which break Galilei symmetry. At meanfield level the groundstate manifold is given by all field configurations which lie in a minimum of the potential energy. Depending on the properties of this manifold, stationary solutions to the classical field equations, *i. e.* local minima of the action, may be present which interpolate between different groundstates, the latter being realised on the boundaries of the system. These field configurations then necessarily form localised features, so-called defects, breaking translation or rotation invariance. If such boundary conditions are imposed the corresponding field configuration can not be continuously deformed into a pure groundstate solution. Thus, although defect solutions correspond only to local minima of the energy or action respectively, their decay to a global minimum can be prevented by boundary

conditions. With respect to this they are termed topological defects. As a direct consequence, topological defects are extraordinarily insensitive to perturbations and decay only on very large time scales [133], even under realistic experimental conditions.

Beyond meanfield level topological defects are known to serve as energetically favourable excitations for thermal or non-equilibrium quantum systems. Even for trivial boundary conditions fluctuations can locally form defect solutions which behave then as quasiparticles, due to their stability, and dominate the thermodynamic or dynamic properties of the system. For example, it has been demonstrated that the nucleation of vortices or solitons in an out-of-equilibrium one-component Bose gas can slow down the evolution towards thermal equilibrium tremendously, thereby increasing the long-range order in the system [58, 59]. The two-component system allows for an even larger class of topological defects, due to an enlarged groundstate manifold. In the following, we discuss two important types of defect solutions which can be found in different sectors, either hydrodynamic or spin, of the model Eq. (II.6).

II.3.2 Domain Walls

In the immiscible regime, $\alpha > 1$ and $J < J_c$, we have shown that there are two solutions for the z-projection of the spin which minimise the microscopic energy on the spin sector, $\langle S_z\rangle(y) \equiv \sqrt{1-(J/J_c)^2}$ or $\langle S_z\rangle(y) \equiv -\sqrt{1-(J/J_c)^2}$ (see Sect. II.1.2). While the full quantum groundstate will consist of a quantum superposition of the two states, a corresponding classical statistical ensemble of fields will always contain a classical mixture of both states. Nevertheless, signatures of the two-fold degeneracy of the groundstate can manifest themselves also through the classical equations of motion. The consequence is the existence of truly static solutions to the equations of motion which interpolate smoothly between the two energy minima. These so-called domain walls fall into the class of topological solitons and can be viewed as the classical analogue for quantum tunneling of states between the two degenerate groundstates.

In this section, we derive the functional form of a single domain wall in the classical spin field, in one spatial dimension. To do so, we utilise the so-called Bogomol'nyi trick [134] which is a quite common approach for finding energy-minimising solutions to classical equations of motion. We also comment on the generalisation of the domain wall solution to higher dimensions.

We start from the expression Eq. (II.6) for the classical energy, where we set $\theta_- = 0$ and add a constant,

$$H = n_+ \int \mathrm{d}y \left\{ \frac{\left(\partial_y S_z\right)^2}{4m\left(1-S_z^2\right)} + J_c\left(1-S_z^2\right) - 2J\sqrt{\left(1-S_z^2\right)} \right\}. \tag{II.19}$$

As we search for a solution which still minimises the energy in a certain way, $\theta_- = 0$ is enforced if $J \neq 0$. If $J = 0$, the the effective velocity term in Eq. (II.6) energetically prevents a non-constant θ_- in one spatial dimension. In higher dimension, however, the spin can have a chiral component, *i. e.* a spatially changing angle θ_-, as the z-projection changes along the wall. The strategy now is to identify a lower bound for the energy in the form of Eq. (II.19) which simultaneously is a purely topological term, a so-called

Bogomol'nyi–Prasad–Sommerfield bound [135–137].

First, write the integrand of Eq. (II.19) as a quadratic term plus a total derivative by completing the square with respect to $(\partial_y S_z)^2$ to obtain,

$$\begin{aligned} H =& n_+ \int \mathrm{d}y \, \frac{\left| \partial_y S_z + \xi_\mathrm{s}^{-1} \left(1 - S_z^2\right) \left[\frac{J}{J_\mathrm{c} \sqrt{1-S_z^2}} - 1 \right] \right|^2}{4m \left(1 - S_z^2\right)} \\ & - n_+ \int \mathrm{d}y \, 2 \xi_\mathrm{s}^{-1} \frac{\partial_y S_z}{4m} \left(\frac{J}{J_\mathrm{c} \sqrt{1 - S_z^2}} - 1 \right), \end{aligned} \tag{II.20}$$

where another constant is added to the energy and the spin healing length

$$\xi_\mathrm{s} = \left(\sqrt{-4m g_- n_+} \right)^{-1} = \left(\sqrt{4m J_\mathrm{c}} \right)^{-1}, \tag{II.21}$$

is introduced. Since the first term on the right hand side of the expression Eq. (II.20) is positive definite, the second term constitutes a lower bound. Furthermore, the second term in the expression Eq. (II.20) can be reformulated as integral over a total derivative,

$$H \geq -2 \frac{n_+}{4m} \xi_\mathrm{s}^{-1} \int \mathrm{d}y \, \partial_y \left[\frac{J}{J_\mathrm{c}} \arcsin S_z - S_z \right] = Q_\mathrm{w} \,. \tag{II.22}$$

Therefore, being the integral over a total derivative, the value of Q_w in Eq. (II.22) is solely determined by boundary conditions.

If the spin field S_z is forced to lie in different minima of the energy functional at the boundaries, for example

$$S_z|_{y \to \mp \infty} = \pm \sqrt{1 - (J/J_\mathrm{c})^2} \,, \tag{II.23}$$

the value of the topological charge Q_w can not be changed by continuous deformations of the profile. Therefore, the value of Q_w also can not be changed by Hamiltonian time evolution. As an immediate consequence, any solution for the spin field which saturates the bound in Eq. (II.22), meaning that it minimises the energy on the topological sector with charge Q_w, is static.

A solution to the first-order differential equation

$$\partial_y S_z + \xi_\mathrm{s}^{-1} \left(1 - S_z^2\right) \left[\frac{J}{J_\mathrm{c} \sqrt{1 - S_z^2}} - 1 \right] = 0 \,, \tag{II.24}$$

together with boundary conditions given in Eq. (II.23), defines the z-spin profile of the domain wall. It minimises the energy at a non-zero value of the topological charge Q_w, due to Eq. (II.20) and Eq. (II.22), while continuously interpolating between the two minima

of the energy. Separation of variables yields the inverse of the domain wall solution,

$$y - y_0 = \pm \int_0^{S_z^{\mathrm{w}}} \mathrm{d}S_z \left\{ \xi_{\mathrm{s}}^{-1} \left(1 - S_z^2\right) \left[\frac{J}{J_{\mathrm{c}} \sqrt{1 - S_z^2}} - 1 \right] \right\}^{-1}$$
$$= \pm \xi_{\mathrm{s}} \gamma \left[\operatorname{artanh}\left(S_z^{\mathrm{w}} \gamma\right) + \operatorname{artanh}\left(\frac{J \gamma S_z^{\mathrm{w}}}{J_{\mathrm{c}} \sqrt{1 - S_z^{\mathrm{w}2}}} \right) \right], \tag{II.25}$$

where we have introduced the definition $\gamma = 1/\sqrt{1 - (J/J_{\mathrm{c}})^2}$ in the second line. In general, the expression Eq. (II.25) needs to be inverted numerically to obtain the domain wall profile S_z^{w}.

For small linear couplings, $J/J_{\mathrm{c}} \ll 1$, the second term on the right-hand side in Eq. (II.25) can be dropped and the wall profile can be obtained,

$$S_z^{\mathrm{w}} = \frac{1}{\gamma} \tanh\left(\pm \frac{y - y_0}{\xi_{\mathrm{s}} \gamma} \right), \tag{II.26}$$

$$\left(S_x^{\mathrm{w}}, S_y^{\mathrm{w}}\right)^T = \sqrt{1 - \gamma^{-2} \tanh^2\left(\pm \frac{y - y_0}{\xi_{\mathrm{s}} \gamma} \right)} \left(\cos\theta_-, \sin\theta_-\right)^T \tag{II.27}$$

Note that the solution is exact if $J = 0$. The arbitrary sign in Eq. (II.26) originates in the possibility for the wall to be charged negatively or positively. From the approximate solution given in Eq. (II.26) one finds that the domain wall profile is sharpest for $J = 0$ and is 'melted' by the presences of the linear coupling.

The arguments from above can also be generalised to higher spatial dimensions. Then the wall solution, Eq. (II.25), is also valid but the kink in S_z can occur along any direction and the defect extends to the whole transverse $d - 1$ dimensional hyperplane. The higher dimensional configurations allow in addition for a local movement of the defect brane [115, 137], in directions perpendicular to the brane. Since defect configurations posses high stability, due to energetic and topological reasons, perturbations typically result in transverse vibrations of the defect brane which travel as low-momentum waves along the domain boundaries. This is equivalent to Kelvin waves on vortex lines in liquid helium [138, 139].

The simple domain wall we derived here is only one out of many possibilities for topological solitons. In the immiscible regime there exist multi-domain solutions. In the dilute limit, when the domain-wall separation is much larger than their extent, multi-domain solutions can be obtained simply by subsequent multiplication of the single-domain solution. For vanishing linear coupling also exact multi-domain solutions are known, being described by Jacobi elliptic functions [140, 141].

In the miscible regime in one spatial dimension, the Gross-Pitaevskii soliton solution is possible, as well as it is always possible to put Gross-Pitaevskii solitons in the total phase, θ_+. At finite linear coupling in the miscible regime, the effective potential of the spin sector resembles in structure the sine-Gordon model, as can be seen from Eq. (II.15). Thus, sine-Gordon soliton solutions in the relative phase are of relevance in this case

which has been even demonstrated experimentally [142].

II.3.3 Vortices and Spin Textures

If the Bose gas is considered in two spatial dimensions, domains walls, as discussed in Sect. II.3.2, naturally extend to one-dimensional objects, *i. e.* defect lines. There exists another important class of topological defects in the Bose gas in two dimensions, the vortex-like defects, where the defect core is zero dimensional again. The simplest example for these objects is given by the Gross-Pitaevskii vortex solution (see for example [143]). Despite of being a stationary solution to the one-component Gross–Pitaevskii equation, its topological nature is connected to the $U(1)$ degeneracy of the groundstate. Thus, also for the two-component gas stable vortices can form in each component, as long as every component is individually subject to a global $U(1)$ symmetry. This means that the Gross-Pitaevskii vortex is of importance at zero linear coupling. In addition, for energetic reasons, the spinor gas needs to be placed in the miscible phase for vortices to be favourable in individual components. Apart from that, they can always form in the symmetric sector, in the overall condensate density and phase n_+ and θ_+.

In this section, we first discuss properties of the Gross–Pitaevskii vortex, as it can be found in the single-component Bose gas. The influence of vortex ensembles on the dynamics of the single-component Bose gas in two spatial dimensions will be an integral part of the considerations in chapter VII and in chapter VIII. Thereafter, we discuss vortex-like defects in the spinor gas and how they generalise, in particular, to the immiscible regime where they appear as spin textures.

The Gross–Pitaevskii Vortex

For the discussion of the vortex solution we assume $\alpha = 0$ and $d = 2$ in the model given in Eq. (II.1) and the vortex to exist in one of the components. The density, $n_1(\mathbf{x})$, needs to assume a constant value as $r = |\mathbf{x}| \to \infty$ in order to keep the potential energy finite but the phase is not affected by this argument. Therefore, it can be chosen to wind around the boundary at spatial infinity with an integer number of windings, $\theta_\uparrow(r = \infty, \varphi) = w\varphi$, where φ is the polar angle. This solution for the phase, extended to the whole space, leads to a divergence of the velocity field,

$$\mathbf{v}_\uparrow(r, \varphi) = \nabla\theta_\uparrow = \frac{w}{2\pi r}\mathbf{e}_\varphi \,, \tag{II.28}$$

and consequently to a divergence of the kinetic energy density for $r \to 0$. Therefore, the vortex solution requires a defect in the density, $n_\uparrow(r) \to 0$ as $r \to 0$, leading to a non-trivial vortex core where the density drops. An approximate solution for the vortex density profile, satisfying the stationary Gross–Pitaevskii equation for $w = \pm 1$ asymptotically, *i. e.* in the limits $r \to \infty$ and $r \to 0$ is given by

$$\sqrt{n_\uparrow(r)} = \frac{n_0 r}{2\xi_\mathrm{h}\sqrt{2 + \frac{r^2}{\xi_\mathrm{h}^2}}} \,, \tag{II.29}$$

see for example [124, 143].

A conserved topological charge for the vortex solution can be defined in terms of the winding number,

$$Q_v = \frac{1}{2\pi} \oint_C \nabla\theta_\uparrow = \frac{1}{2\pi} \int \mathrm{d}^2x \, \nabla \times \mathbf{v}_\uparrow = w \,, \tag{II.30}$$

where the integration contour C has to enclose the vortex core. As for the domain walls and solitons before, an arbitrary number of elementary vortex solutions can be multiplied to yield a multi-vortex solution. The result is approximately stationary, apart from movement of the defects themselves, if the defect separation is much larger than the extent of the defect core. An especially important role play neutral ensembles of elementary vortices in $d = 2$, as they can be treated as a dilute gas of charged particles. These turn out to interact via a Coulomb-type (in $2d$) force [144],

$$\boldsymbol{F}_{12} \sim w_1 w_2 \frac{1}{r} \boldsymbol{e}_r \,, \tag{II.31}$$

where r is the distance between a pair of vortices with winding numbers w_1 and w_2. Based on this treatment of defects as particles, the theory of the Berezinskii–Kosterlitz–Thouless transition in the two-dimensional Bose gas can be formulated solely in terms of the defect picture, see for example [145, 146].

Since w can be positive or negative, depending on the vortex circulation, a dynamical creation of vortices in a system with trivial boundary conditions is possible, as they can always be nucleated as vortex–anti-vortex pairs. The result of a dynamic generation mechanism for vortices is therefore typically a dilute neutral vortex gas. As the energy of a vortex defect increases with the winding number, vortex gases which are dynamically generated from instabilities consist usually of elementary vortices, with winding number $w = \pm 1$.

Vortices in the Spinor Bose Gas

For $0 < \alpha < 1$, in the miscible regime of the spinor Bose gas, a vortex in one component can exist in the bulk of the second component. Then one has $n_\uparrow$ following the defect profile given in Eq. (II.29), together with $n_\downarrow = \frac{n_0}{2}$ in the core region of $n_\uparrow$ (or *vice versa*). Although the potential energy in the core is enlarged by the presence of the second component, the configuration is still energetically favourable for $\alpha < 1$ and topologically protected, with $\theta_\uparrow$ having a non-zero winding number w.

In the immiscible regime of the spinor Bose gas, $\alpha > 1$, the core of a vortex in one component fills with the other component, leading to an energetically beneficial S_z polarisation in the core. For the defect structure to have a finite energy, the asymptotic form of the density profile of the filling component needs to behave as $n_{\mathrm{fill}} = n_0$ for $r \to 0$ and $n_{\mathrm{fill}} = 0$ for $r \to \infty$, where r is the distance form the defect core. Therefore, the defects live in domains where the filling component is the minority and can dissolve upon entering the neighbouring domains. The energy of the defect is thereby released into vibrational modes of the domain borders.

As the density of the filling component is finite in the core, its phase can not carry any angular momentum. Thus, together with the non-trivial phase winding in the other

component's phase $\theta_\uparrow$, the defect has the quantised phase winding of a regular vortex, without the defect in the total density. The structure of this defect from the perspective of spin degrees of freedom resembles in some aspects[3] the skyrmion spin texture in the non-linear sigma model [121, 147].

Skyrmions are known exact topological solutions of the $O(3)$-symmetric non-linear sigma model with a spin profile given by [147]

$$S_z = \frac{r^2 - 4\xi_s^2}{r^2 + 4\xi_s^2}\,, \tag{II.32}$$

$$\left(S_x, S_y\right)^T = \frac{4\xi_s r}{r^2 + 4\xi_s^2}\left(\cos\left(\pm\frac{\theta_-}{2\pi}\right), \sin\left(\pm\frac{\theta_-}{2\pi}\right)\right)^T . \tag{II.33}$$

The spin profile of the filled vortex in the immiscible regime (*i. e.* at a finite $\alpha > 1$) shows slight deviations from the exact analytic form of the skyrmion solution but demonstrates the same qualitative behaviour. Note that the filled vortex has a non-trivial phase winding of the total phase, $\theta_+ = \pm w/(2\pi)\theta$. Therefore, the effective velocity field, Eq. (II.7), evaluates to

$$\boldsymbol{v}_{\text{eff}} = \pm\frac{1}{4\pi r}[1 + S_z]\boldsymbol{e}_\theta\,, \tag{II.34}$$

, which is regular for $r \to 0$. This allows for a defect-less structure from the perspective of the total density. The conserved topological charge of the skyrmion in the non-linear sigma model in two spatial dimensions can be reformulated in terms of the effective velocity [121],

$$Q_s = \frac{1}{2\pi}\int d^2x\, \nabla \times \boldsymbol{v}_{\text{eff}}\,, \tag{II.35}$$

similar to Q_v, given in Eq. (II.30). However, in the immiscible regime, at a finite $\alpha > 1$, not Q_s acts as the conserved topological charge but Q_v in each component individually.

As before, multiple skyrmion solutions can be combined, with each other and with domain walls, to yield more complex structures of topological defects in the immiscible regime. In particular, the dynamic evolution of the defect structures allows for interaction between domain walls and skyrmions. A strongly curved wall can 'close' to form a point defect while a point defect can be absorbed by a wall (see for example [117]).

II.3.4 Stability of Topological Defects

We close this section with a remark on the stability of the discussed topological solutions under the dynamical evolution of the two-component Bose gas. None of the topological defects, we discussed for the spinor Bose gas in Sect. II.3.2 and Sect. II.3.3, is an exact topological solution of the full model for the two-component gas. Rather, the structures are truly topologically protected only on certain sectors of the model, under the assumption that the sector decouples from the other sectors. However, in practice it turns out that the defect solutions are locally stable and do only dissolve via interactions with other defects.

[3] The filled vortex in the immiscible regime has a non-trivial phase winding of θ_+ while the total phase is no degree of freedom of the non-linear sigma model. In addition, as elaborated in [121], the analytic form of the spin density profiles may differ. However, one usually refers to the filled vortex as 'skyrmion'.

Furthermore, they constitute local spatial variations in a field configuration which keep the energy minimal. Therefore, they are prone to be generated by dynamical instabilities (see Sect. II.4).

We focus on computational domains with spatially periodic boundary conditions. Thus, apart from periodicity of the field configurations, we do not impose any non-trivial topological boundary conditions and, hence, the total topological charge Q_w (Eq. (II.22)), Q_v (Eq. (II.30)), or Q_s (Eq. (II.35)) is zero. Using dynamical instabilities, as described in Sect. II.4, initially homogeneous field configurations are strongly perturbed locally and typically undergo a subsequent local nucleation of topological defects. This is possible, despite conservation of topological charge, since all discussed defects can have a negative or positive local charge. Consequently, our boundary conditions only enforce that defects are always generated in defect–anti-defect pairs (for point defects) or that higher-dimensional defect boundaries are closed. The dynamics following the nucleation of defects is then constrained by the total charge being zero. Defects can move but can not dissolve under local perturbations. To do so, interactions between defects of opposite local topological charge are required, such as the mutual annihilation of a vortex–anti-vortex pair.

II.4 Dynamical Instabilities

Studying the dynamics of phase transitions in isolated systems, as we do for the remainder of this work, requires mechanisms which act effectively as a driving source within unitary time evolution. It turns out that classical instabilities, as typically found in pattern formation processes of hydrodynamic systems, are efficient in achieving that goal.

In this section, we first line out how instabilities in the classical equations of motion can, in general, be employed to set off far-from-equilibrium dynamics. Thereafter, we discuss in detail two types of instabilities in the spinor Bose gas which generate spin patterns, *i. e.* spin domains. One type is triggered by parametrically crossing the miscible–immiscible transition and nucleates stable domain walls (see Sect. II.3.2). The second type is triggered by special choices of initial states within the miscible phase and leads to transient patterns in the spin. Both types of instability are put to practical use in Sect. II.6.

II.4.1 Instabilities as Driving Mechanism

In the context of many-body quantum systems, instabilities of the underlying classical fields are ubiquitously known for sourcing universal dynamics, in situations as different as preheating in the early universe [61, 148, 149], turbulence in gauge fields [62, 63], or the expanding quark-gluon plasma [69, 150]. For spinor Bose–Einstein condensates, there is a zoo of so-called modulational instabilities known and frequently exploited in theory and experiment, as they produce modulations in the spin densities which then usually develop into domains, see for example [123, 151–154].

In addition, there are also hydrodynamic instabilities known which lead to the formation of hydrodynamic turbulence in the long run. Prominent examples are the thermal counter-flow instabilities [155] in superfluid helium and its analogue in multi-component superfluids, the so-called counter-superflow instabilities [111, 156–158].

Viewed as a driving mechanism, classical dynamical instabilities typically function all in a similar way. Linearised about a state from the class of dynamically unstable states, the equations of motion reveal unstable modes. These modes, typically localised in a narrow region of momentum space, grow exponentially fast under the action of the liearised equations of motion.

The exponential growth stops when higher order mechanisms, *i. e.* scattering mechanisms, become relevant and start to deplete the highly occupied unstable modes, filling neighbouring modes. The non-linear evolution thereafter depends on the system and is usually strongly influenced by conserved quantities. Nevertheless, the unstable modes act as sources for quasi-particles, localised in momentum space, after an initial phase of fast growth.

The subsequent non-linear evolution potentially reflects the universal dynamic properties of the system irrespective of the instability which has set it off. Furthermore, the picture is applicable even in an isolated system. There, the initial growth of unstable modes may come with a massive redistribution of conserved quantities but is subject to the conservation laws of the equations of motion.

II.4.2 The Immiscible Regime

On the spin sector of the two-component Bose gas, there are two types of dynamical instabilities, one connected to an unstable preparation of the z-spin and the other connected to an unstable preparation of the relative phase θ_-. Let the initial state of the spin density field be prepared as a groundstate in one sector (*i. e.* region I or II in Fig. II.1) of the phase diagram and let the Hamiltonian lie in the other, by choice of J or α. As a consequence, the spin configuration will change exponentially fast towards, even on meanfield level, as the initial state is energetically maximally unfavourable. This statement can be made more qualitative by analysing the excitation spectrum within the linearised classical equations of motion. We do so in the following, for the case that the initial state is miscible and the Hamiltonian is parametrcially in the immiscible phase.

A Bogoliubov analysis of the homogeneously mixed system ($\langle S_z\rangle \equiv 0$) gives, for $a_{\uparrow\uparrow} = a_{\downarrow\downarrow} = 0$, two decoupled excitation branches [151]

$$\begin{aligned}\omega_+(\kappa,\alpha) &= 2J_c\,\sqrt{(\alpha+1)(\alpha-1)^{-1}\kappa^2+\kappa^4},\\ \omega_-(\kappa,\varepsilon) &= 2J_c\,\sqrt{\varepsilon(\varepsilon+1)+(2\varepsilon+1)\kappa^2+\kappa^4}\end{aligned} \tag{II.36}$$

of density and spin waves, respectively, where $\kappa^2 \equiv k^2/[4mJ_c]$, and $\varepsilon = (J-J_c)/J_c$ is the relative proximity to the critical coupling J_c. For $\alpha > 1$ and $-1 < \varepsilon < 0$, which places the Hamiltonian in the immiscible regime (region I in Fig. II.1), the spin-wave frequency ω_- is imaginary for modes with momenta $\kappa < \kappa_c = \sqrt{-\varepsilon}$. These modes therefore become unstable, meaning that they grow exponentially instead of oscillating with their eigenfrequency. This results in spin excitations with growing amplitude [123] and leads to a macroscopic spatial modulation of the z spin field, indicating a demixing of the two

components. Thereby, the fastest growing, *i. e.* most unstable, mode

$$\kappa^2 = \kappa_f^2 = \max\{-\varepsilon - 1/2, 0\}\,, \tag{II.37}$$

sets the spatial scale of the modulation. Due to the full non-linearity of the two-component Gross-Pitaevskii model, eventually domains form in the z-spin out of the modulations, separated by domain walls of the form discussed in Sect. II.3.2.

In contrast, if the Hamiltonian lies in the miscible region, *e. g.* $\varepsilon > 0$ in Eq. (II.36), the spin-wave modes acquire a gap $\omega_-(k=0) = 2\sqrt{J(J-J_c)} \equiv \Delta(\varepsilon) = 2J_c\sqrt{\varepsilon(\varepsilon+1)}$ in their excitation spectrum together with $\omega_-(k)^2 > 0$, such that the mixed state remains stable [151, 159]. The disappearance of the gap at $\varepsilon = 0$ defines the critical line in Fig. II.1 and is a hallmark of a second-order (quantum) phase transition in the α-J plane. The time evolution of the linearised spin modes, when not crossing the transition, is discussed in detail in chapter III.

II.4.3 The miscible regime

The second type of dynamical instability in the spin sector is related to the spin projection onto the equator of the Bloch sphere, characterised by the relative phase θ_-. The logic, on the other hand, remains the same. If the relative phase[4] of the initial state is not the relative phase of the groundstate of the Hamiltonian, an instability can be triggered. An important difference here is that the primary instability generates phase excitations. Modulations of the z-spin are subsequently generated, partially by non-linear processes, without necessarily leading to stable domains.

An example, we will utilise for dynamical pattern formation in the miscible regime in Sect. II.6, is the counter-superflow instability. It exists in the miscible regime, $\alpha < 1$ and $J = 0$, destabilising the homogeneously mixed state $\langle S_z\rangle = 0$ for certain parameter choices. When the initial state is prepared such that the two components move with uniform but different velocity,

$$\psi_j = n_j \mathrm{e}^{\mathrm{i}\sqrt{mgn_0}\mathbf{v}_j\cdot\mathbf{x}}\,, \tag{II.38}$$

with $\mathbf{v}_j = \text{const}$, a Bogoliubov analysis of this field configuration reveals unstable modes in the linear excitation spectrum for a high enough relative velocity. The linear excitation spectrum is found to be [112]

$$\frac{\omega_{\text{csi}}^2(k)}{(gn_0)^2} = \frac{1}{4}k^4 + k^2 + \frac{1}{4}k_\parallel^2 v_r^2 \pm \sqrt{\left(\frac{1}{4}k^4 + k^2\right)k_\parallel^2 v_r^2 + k^4\alpha^2}\,, \tag{II.39}$$

where $v_r = |\boldsymbol{v}_\uparrow - \boldsymbol{v}_\downarrow|$ and $k_\parallel = |\boldsymbol{k}\cdot(\boldsymbol{v}_\uparrow - \boldsymbol{v}_\downarrow)|/v_r$. This excitation spectrum has a window of momenta in the $k_\parallel$-$k_\perp$ plane, defined by the inequality relation (see [112] and in particular

[4] Note that θ_- here assumes a physical meaning, despite being a phase angle, since it is a phase difference and as such in principle measurable via interference

Fig. 1 therein)

$$\sqrt{\frac{1}{4}k^4 + k^4(1-\alpha)} < \frac{1}{2}k_\parallel v_r < \sqrt{\frac{1}{4}k^4 + k^4(1-\alpha)}\,, \tag{II.40}$$

where the imaginary part of ω_{csi} is non-zero, All linear excitation modes are, therefore, stable if the relative velocity is smaller than a critical value

$$v_r < 2\sqrt{1-\alpha} = v_{\mathrm{c}}\,, \tag{II.41}$$

and unstable modes exist if $v_r > v_{\mathrm{c}}$.

Once triggered, the instability leads to a momentum exchange between the superfluid flows of the two components, causing the decay of the uniform counter-superflow [112]. Interpreted from a purely hydrodynamic point of view, the instability provides a friction-like mechanism for the relative motion. In [111, 112] it has been demonstrated numerically that initial state surpassing that threshold can develop into quantum turbulence in two-component Bose gases and, similarly, in [156, 157] for spin-1 gases, producing solitonic excitations and vortices.

II.5 Simulation Method and Numerical Procedures

A major part of this work will be concerned with solving the model Eq. (II.1) for the two-component Bose gas numerically, with respect to dynamics of correlation functions. We will employ semi-classical simulation techniques and, in particular for the two-component Bose gas, the Truncated Wigner method [83, 84] to reach beyond meanfield or linear approximations. In this section, we introduce the concept and explain how observables are computed within the Truncated Wigner approximation. Thereafter, we discuss properties of correlation functions of the pseudo-spin fields (Eq. (II.2)) out of equilibrium, which will be the observables we concentrate on throughout the first part of this work. In particular, we explain how dynamic correlation lengths from spin correlation functions will be retrieved.

II.5.1 Truncated Wigner Method

An integral part of this work is concerned with the dynamics of the two-component Bose gas far from equilibrium and beyond the meanfield or the linearised theory. Simultaneously, we are interested in critical phenomena and scaling behaviour which can be expected to be dominated by large occupation numbers of infrared momentum modes. Restricting the Bose gas to the semi-classical, highly degenerate regime, we employ the Truncated Wigner approach [83, 84] as simulation method to for studying the full non-linear dynamics of the two-component Bose gas. In this section, we outline the approach. Additional details on the employed algorithms and code can be found in Appendix B. We put the method to practical use in the next section Sect. II.6 (for the spinor gas in $2d$). The results presented in chapter V and chapter VI are obtained from Truncated Wigner simulations of the $1d$ Bose gas. For the results presented in chapters VII and chapters VIII we

employ additionally a generalisation, the method of the stochastically projected Gross–Pitaevskii equation [160–162], which is explained at the beginning of chapter VII.

Semi-Classical Simulations

In the low momentum region, where particle occupation numbers are typically high for a Bose gas in the semi-classical regime, the Wigner function $W(\phi_j^\dagger, \phi_j)$, which describes the statistical nature of the fields, is approximately positive. Thus, it can be treated as classical probability distribution. Its time evolution, if quantum fluctuations are small, is given by a classical Liouville equation [84]. As a result, the dynamics of these modes can be represented by an (classical statistical) ensemble of field trajectories which are propagated according to the classical equations of motion. The classical equations of motion, as derived from Eq. (II.1) for the fundamental Bose fields $\phi_j^\dagger, \phi_j$, read

$$\mathrm{i}\partial_t \phi_\uparrow = \left[\mathcal{H}_0 + g\left(|\phi_\uparrow|^2 + \alpha\,|\phi_\downarrow|^2\right)\right]\phi_\uparrow + 2J\phi_\downarrow\,, \tag{II.42a}$$

$$\mathrm{i}\partial_t \phi_\downarrow = \left[\mathcal{H}_0 + g\left(|\phi_\downarrow|^2 + \alpha\,|\phi_\uparrow|^2\right)\right]\phi_\downarrow + 2J\phi_\uparrow\,, \tag{II.42b}$$

where $\mathcal{H}_0 = -\nabla^2/(2m) + V(\mathbf{x})$.

The Truncated Wigner method then consists of the following steps. One chooses an initial state which can be described in terms of a positive-definite Wigner distribution $W(\phi_j^\dagger, \phi_j)|_{t=0}$. From this initial Wigner distribution, initial classical field configurations $\phi_j(t = 0, \boldsymbol{x})$ can be sampled with Monte Carlo methods (in our case, direct sampling suffices). The samples are then propagated according to Eq. (II.42) to a time t, $\phi_j(t = 0, \boldsymbol{x}) \to \phi_j(t, \boldsymbol{x})$. Observables are finally computed from averages over the classical ensemble of fields,

$$\langle O\rangle_t = \frac{1}{\mathcal{N}}\sum_l^{\mathcal{N}} O_{\mathrm{cl}}(\phi_j^l(t, \boldsymbol{x}))\,. \tag{II.43}$$

The applicability of the Truncated Wigner method depends vitally on the desired initial state, as the Wigner function for this state needs $W(\phi_j^\dagger, \phi_j)|_{t=0}$ to be known in advance. A simple choice, we will employ, is to start in a zero-temperature state of the non-interacting, uncoupled system. The Wigner function then factorises in Wigner functions for the individual momentum modes and each momentum mode is described by a Gaussian Wigner function. Initial field configurations in momentum space $\phi_j^l(\boldsymbol{k}, t_0)$ can then be sampled from the Gaussian distributions via direct sampling. The advantage here is that quantum fluctuations are included in the initial state, as they lead to a positive-definite Wigner distribution for a non-interacting zero-temperature state.

For the simulations presented in this work we choose $V = 0$. We solve the set of partial differential equations Eq. (II.42) numerically efficient and with high accuracy using spectral methods (see for example [1]). Details of the algorithms we use, their implementation, and the hardware we employ can be found in Appendix B.

Observables in the Spinor Bose gas

Typically, we sample an ensemble of initial states at zero spin temperature, showing ground-state Gaussian fluctuations around a fully S_x-polarised configuration. Other than in experiment we assume all couplings to vanish initially, such that the sampling process can be carried out using the Wigner function of the free Hamiltonian. In our simulations, the linear coupling J is suddenly quenched, at time $t = 0$, from a large positive value to positive values close to the critical value J_c, while simultaneously switching on the non-linear couplings from zero to finite positive values. The ensembles of initial field configurations we use are described in detail when needed in the subsequent chapters.

A typical observable will be the time-dependent equal-time spin-spin correlation function $\mathcal{G}_{zz}(y,t;\varepsilon) = \langle S_z(y)S_z(0)\rangle(t,\varepsilon)$, from which in particular the spin correlation length $\xi(t,\varepsilon)$ can be inferred (see Sect. II.5.2). In practice, the occupation spectrum $\langle S_z(-k)S_z(k)\rangle$ of the corresponding operator is computed first. Within the truncated Wigner approximation, this can be efficiently achieved by computing the spatial Fourier transforms of the realisations of field configurations $S_z(k,t)$ and then averaging the quantity $S_z(-k,t)S_z(k,t)$ over the ensemble of initial field configurations. Thus, when discussing numerical results in the following chapters, the average $\langle\ .\ \rangle$ is to be seen as a statistical average approximating the quantum expectation value within the truncated Wigner framework.

II.5.2 Correlation Length out of Equilibrium

It turns out that a practical definition of a correlation length out of thermal equilibrium bears ambiguities. In general, the correlation length should reflect the length scale of the spatial decay of the correlation function, the latter being a generally well defined observable. Away from critical points, it is expected that spatial correlations of an order parameter field between to points decay exponentially fast as the distance r between the points increases, *i. e.* $G(r) \sim \mathrm{e}^{-r/\xi}$ as $r \to \infty$. This is expected to be equally true at any instance in time out of equilibrium and would serve as unambiguous definition of the correlation length ξ. In thermal equilibrium close to critical points, typically one finds in addition that $G(r) \sim r^{-1}$ as $r \to 0$. Both conditions together enforce a monotonic decay of the correlation function as r increases. In this case, ξ can be determined from data by means of fitting an exponential function.

Out of equilibrium, on the other hand, one has to allow for an additional, possibly universal, function which multiplies the exponential decay, $G(r,t) \sim K(r,t)\, e^{-r/\xi}$. In general, the function K can oscillate heavily in time and space. Examples for that behaviour can be found in subsequent chapters and Fig. II.2. Depending on the exact functional form of K it is from a practical point of view problematic to directly determine the correlation length, *i. e.* the long range characteristics, by means of a fit. In the following, we discuss our operative solution to this problem.

In the case of a spin-spin correlation function one has to deal not only with spatial oscillations of the correlation function. Given the equal-time correlation function, $\mathcal{G}(r,t) = \langle S^a(0,t)S^b(r,t)\rangle$, as obtainable directly from simulation, we define a normalised correlation function[5] by $G(r,t) = \mathcal{G}(r,t)/\lim_{r\to 0}\tilde{G}(r,t)$.

[5]We reserve the symbol G for the normalised spin correlation functions (or structure factors) of the spinor

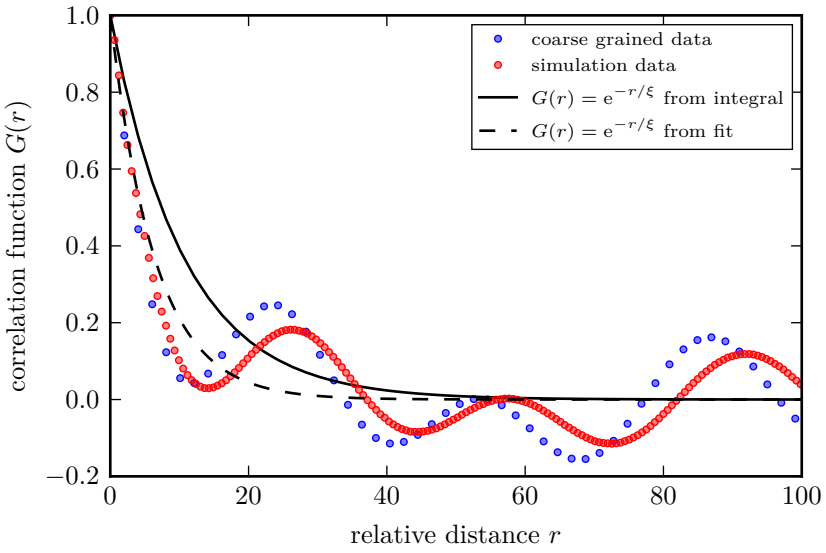

Figure II.2: Example for a z-Spin correlation function as determined from simulation (*cf.* chapter V). The function is normalised as described in the main text of section Sect. II.5.2, where red data points correspond to direct simulation data and blue data points to the correlation function after applying a filter to the structure factor $G(k)$, as described in the main text. Note that the filter introduces a coarse-graining of the correlation function. The dashed black line represents a fit of a decaying exponential function to the short-distance (0 to 10) decay of the numerical correlation function. The solid black line shows a decaying exponential function where the decay length has been obtained by applying Eq. (III.29) to the filtered numerical correlation function

For any attempts of fitting an exponential decay to it, one faces the problem that the functions oscillates in addition to a decaying envelope and can become negative, due to anti-correlations in the spin, cf Fig. II.2. *Ad hoc*, a possible solution is to restrict the range in distance to which an exponential decay is fitted to small distances. Then, the decay dominates possible oscillations and, in addition, the range can be adapted to positive values of the correlation function. An example for a z-Spin correlation function, as obtained from simulations in chapter V, is shown in Fig. II.2, together with an exponential function fitted to its short-range decay (dashed line). This method for determining the correlation length is unambiguously applicable but, on the other hand, sensitive to short-range characteristics. In particular, one needs to rely on the short-range decay being proportional to the true long-range decay, which might not be true close to critical points.

Instead of fitting, a correlation length can also be defined by integrating over the func-

gas, while the symbol $\mathcal{G}$ is used for the unnormalised ones. In chapter VI, we also discuss correlators of the Ising model, for which the symbol C will be reserved exclusively.

tion, if the correlation function is normalised beforehand,

$$\xi(t) = \int_0^\infty \mathrm{d}r\, G(t,r)\,. \tag{II.44}$$

The quantity carries naturally the dimension of a length in one spatial dimension, as G is by definition dimensionless, and is equal to what we defined before if $G(r)$ is a pure exponential function. In higher dimensions, the definition can be equally applied to the angular averaged correlation function. The definition of xi in Eq. (III.29) reproduces the expected correlation length for the thermal asymptotic behaviour but can be applied without any prior knowledge of the oscillatory part of the correlation function. Specifically, if the oscillations are not too large in amplitude they will average out.

The practical application of Eq. (III.29) to numerical data comes with a few caveats which we want to comment on. Firstly, on a finite computational grid, the limit $\lim_{r\to 0} G(r)$ is not necessarily reflected by just evaluating the lattice data at $r = 0$ since the lattice naturally regularises expressions near the cut-offs $\Lambda = a$ and L, where a is the lattice constant and $L = Na$ the system size. In addition, the stochastic simulation methods we work with introduce a certain level of noisy background through the initial conditions. In the thermodynamic limit this gives a Dirac delta function at $r = 0$ in the correlation function, *i. e.* an unphysical divergence which has to be properly renormalised. On the lattice, this will be reflected by a discontinuous jump of the correlation function at $r = 0$. Both problems, which arise from the regularisation at $r = 0$, can be circumvented by extrapolating the lattice data from $G(r = a)$ to obtain the limit $\lim_{r\to 0} G(r)$ and essentially ignoring the data point $G(r = 0)$. Whenever simulation data for correlation functions and lengths are shown in the remainder of this work, we chose the described approach for the evaluation of the numerical data.

A second caveat arises from the finite infrared cut-off of the lattice, *i. e.* the system size L. Although we make sure that the correlation function has enough room to decay to zero, given a certain parameter setting, by simply choosing L large enough it is the noise in the initial state which can cause a weak divergence of Eq. (III.29). For any finite ensemble of initial conditions a certain average level ϵ of noise will always present in the correlation function, even when the physical part is already way smaller than machine precision could resolve. When normalising the numerical data for $G(r)$, in order to apply Eq. (III.29), this unphysical background noise level gets amplified and spoils the integral. Thus, we apply a filter to the normalised numerical correlation function. The healing length or the critical linear coupling provides natural momentum scales, separating long-range physical behaviour from microscopic features. Such a scale k^* can be used to define a filter in momentum space, by cutting away all modes $k > k^*$ in the structure factor $G(k) = \mathcal{FT}\{G(r)\}$ of the correlation function, before calculating the integral in Eq. (III.29). Note that the filter is applied to the simulation data for $G(k)$ after the simulation. The ultra-violet cut-offs k_{UV} of our simulations are typically between $k_{\mathrm{UV}} = 2k^*$ and $k_{\mathrm{UV}} = 10k^*$. This is important, as momentum modes $k > k^*$ can serve as effective thermal bath for the infrared modes in the case of energy conserving simulations.

We show an example for the operational use of Eq. (III.29) as definition for the correlation length in Fig. II.2. Here, we show numerically computed, normalised correlation functions (unfiltered, red data points and correspondingly filtered, blue data points) and

the corresponding exponential functions $e^{-r/\xi}$, where xi is computed from Eq. (III.29) (see solid black line). We point out that there are isolated cases where the computed correlation length undershoots, *i. e.* where the determined exponential function decays faster than the envelope of the oscillations. This happens mainly where the oscillating prefactor is exceptionally dominant. However, for generic situations, the determined exponential function rather interpolates through the oscillations.

II.6 Dynamic Pattern Formation in the Spinor Bose Gas

A major part of this work is concerned with dynamics of the spinor Bose gas within the miscible (paramagnetic) regime of the two-component Bose gas. The type of far-from-equilibrium dynamics for the spinor gas we study in subsequent chapters will be dominated by strong spin fluctuations but will not lead to a dominant formation of spin patterns.

In this section, in contrast, we briefly discuss the situation when pattern formation dominates the dynamical evolution. In [60, 87], we have connected the formation of transient spin structures and spin defects with the appearance of non-thermal fixed points within the far-from-equilibrium dynamics in the spinor Bose gas. The idea is to probe the structure of the phase diagram far from equilibrium, with triggering dynamical instabilities in specific parts of the phase diagram (see Sect. II.4). The early stage of dynamics will be dominated by pattern formation and defect nucleation, connected to the specific instability triggered. The actual interest, however, is if thereafter stage of time evolution follows, in which the correlation function have universal properties.

In [60, 87], we find that the dynamic evolution after exciting strong pattern forming dynamics in the spinor gas typically turns universal. This is signalled by power laws in spin structure factors and occupation spectra together with a critically slowdown of the time evolution. In this section, we give an overview over our findings for universal dynamics in the spinor gas from pattern formation and the connection to the concept of non-thermal fixed points, following[6] [87]. The goal thereby is to complement the picture for dynamics far from equilibrium in the spinor gas, which we will discuss from the paramagnetic side in the rest of this work.

II.6.1 Pattern Formation from Instabilities

At $J = 0$, our model Eq. (II.6) has only one relevant Hamiltonian tuning parameter on the spin sector which is α (Eq. (II.3)). As discussed in Sect. II.1.2, with that tuning parameter a first-order phase transition from S_z-ordered to S_z-disordered is addressed. Consequently and in contrast to the situation for a finite linear coupling, the value of the order parameter $\langle S_z \rangle$ in equilibrium does not depend on the quench parameter α. Additionally, the spin projection of the equator on the Bloch sphere is $U(1)$ degenerate which implies that it does not order in equilibrium due to the Mermin–Wagner theorem. With these properties of

[6] For the publication of [87], I provided the numerical data, carried out the data analysis and contributed to the interpretation of the results and the text of the manuscript.

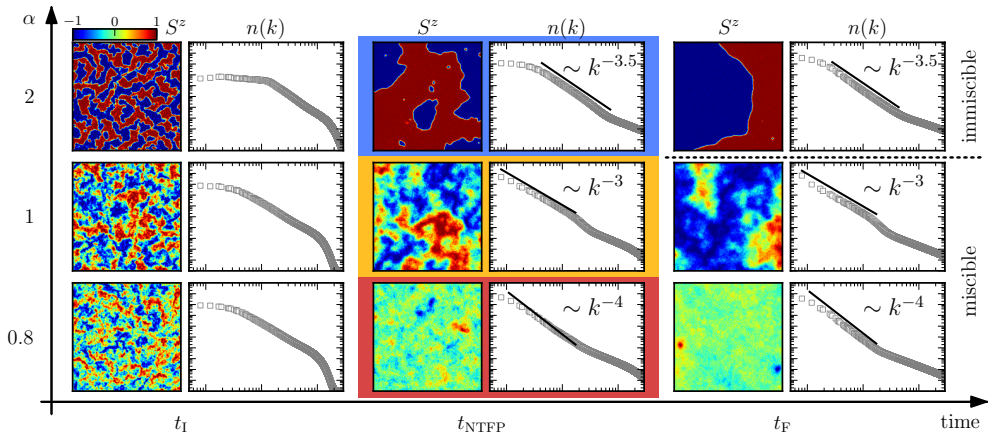

Figure II.3: Three snapshots (columns) of the evolving two-component Bose gas for three different values of the coupling ratio α (rows). In each case we show the spatial distribution of density imbalance S_z as well as the momentum distribution $n(k)$ as a function of the radial momentum k of particles in the gas. Tick labels for the spectra graphs are the same as in Fig. II.4. Until t_I the dynamics is characterised by the instability and isotropisation of density fluctuations. At $t_\mathrm{NTFP} = 10\, t_\mathrm{I}$, one observes the development of different power laws in the momentum distributions. They remain metastable for a long time beyond $t_\mathrm{f} = 100\, t_\mathrm{I}$ and reveal different non-thermal fixed points. The change of power laws at $\alpha = 1$ indicates a dynamical phase transition. Figure adapted from [87].

the transition it is considerably easier to disentangle universal properties originating in the out-of-equilibrium situation and those from the equilibrium phase transition.

The system hosts skyrmions and topological domain walls in the immiscible phase and Gross–Pitaevskii vortices in the miscible phase (see Sect. II.3). Large-scale correlations in the system are universal in the sense that they are fixed by the type of defect, but are completely insensitive to the specific positions and velocities of the defects. Distinguishable types of defects are hosted for different values of the tuning parameter α, for energetical reasons as outlined in (see Sect. II.3). Hence, the dynamics can be tuned to a transition between different metastable non-equilibrium ordered states.

The two-component Bose systems we consider are described by the Hamiltonian Eq. (II.1) at vanishing linear coupling ($\hbar = 1$)

$$\mathcal{H} = \frac{1}{2m}\nabla\phi_j^\dagger\nabla\phi_j + \frac{g}{2}(\phi_j^\dagger\phi_j)^2 - g(1-\alpha)\phi_\uparrow^\dagger\phi_1\phi_\downarrow^\dagger\phi_2\,. \tag{II.45}$$

The considered systems allow for good experimental control and have been studied intensely [113, 118, 163, 164]. In experiment, α can be varied by means of a Feshbach resonance. As discussed in the previous sections, two different ground states exist depending on the value of the parameter α. Here, we make use of α to change the properties of the system in the yet unexplored region of non-equilibrium quasi-stationary states. A focus is set on long-lived states with non- or quasi-topological defects including domain

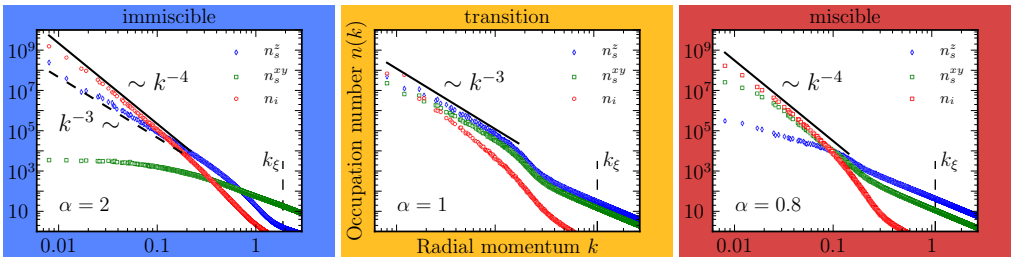

Figure II.4: Decomposition of correlation functions of the two-component Bose gas in the three different non-equilibrium ordered states parametrised by the coupling ratio α. Shown are the z-spin occupation spectrum n_s^z, the sum of x- and y-spin occupation spectrum n_s^{xy} and the incompressible component n_i at time t_{NTFP}. For details of the decomposition procedure see [60]. Figure adapted from [87].

walls [86, 163], single-species vortices, and skyrmions [121] in the coupled system (see Sect. II.3).

Since the dynamics we are interested in exclusively affects the low-momentum, strongly populated field modes, we employ the Truncated Wigner method for simulations which yields, within numerical accuracy, exact results for the time-evolving observables. Details can be found in the next section Sect. II.5.1. In order to discuss the contribution of the different (quasi-)topological configurations in detail, we make use of the spin representation of the two-species fluid, as explained in Sect. II.1.1. The effective spin field $S_z(\boldsymbol{x})$ (see Eq. (II.2)) is an essential observable for the detection of domain walls. Furthermore, we make use of a hydrodynamic decomposition of the superfluid flow which allows for the detection of vortex contributions to the occupation spectra [165, 166]. For details on numerical parameters and decomposition methods we refer the reader to the supplementary material of [87].

In Fig. II.3, we unravel the time evolution of the two-component Bose gas comprehensively in different phases (choices of α), form initial pattern formation to a universal late stage. The parameters of our simulation are chosen such that the final states are close to the ground state of the system. To clarify the type of non-equilibrium order during the intermediate stages of the evolution, we show the imbalance between the two components S_z as well as the angular-averaged momentum distribution

$$n(k,t) = \int \mathrm{d}\Omega \, \langle \phi_\uparrow^\dagger(\boldsymbol{k}) \phi_\uparrow(\boldsymbol{k}) \rangle + \langle \phi_\downarrow^\dagger(\boldsymbol{k}) \phi_\downarrow(\boldsymbol{k}) \rangle \tag{II.46}$$

for three characteristic times. The initial time, t_{I}, marks the stage of an isotropic momentum distribution which is overpopulated within an intermediate range of momenta, as compared to the ensuing equilibrium distribution. It is marked by a strong fall-off at large momenta. In our driving scheme this state is reached in the wake of an instability. For the immiscible case, $\alpha > 1$, we use the modulational instability in which small low-momentum fluctuations in the polarisation are amplified to macroscopic spin domains. In the miscible regime, $\alpha \leq 1$, we invoke a counter-superflow instability [111, 112] by

choosing oppositely directed flow vectors for the two field components. Above the critical relative velocity, momentum exchange between the two fluids causes the superflow to decay and spin domains to form. The mechanisms have been discussed in the previous section Sect. II.4. Subsequently, overpopulation at intermediate momenta is encountered for all values of the parameter α. Its microscopic origin is seen in the coloured distributions of the density imbalance S_z in Fig. II.3 which show strong fluctuations and the onset of domain formation. We estimate $t_\mathrm{I} \simeq 10/\omega_\mathrm{I}$, with ω_I being the energy of the fastest growing unstable mode. Note that the dynamics up to t_I is different for different α and involves for example isotropisation in case of $\alpha \leq 0$, see the supplement of [87]. The further dynamical evolution of overpopulated states involves particle transport towards small momenta and energy transport towards high momenta [55, 56]. In Fig. II.3 this is best observed by comparing the high momentum tails of the momentum distributions at t_I and t_NTFP. Particle transport towards low momenta eventually fills the zero-mode (not seen), a process most important in the miscible regime $\alpha = 0.8$. The key insight gained from the spectra concerns the development of infrared power laws in the momentum distribution $n(k) \sim k^{-\zeta}$ at $t_\mathrm{NTFP} \simeq 10^2/\omega_\mathrm{I}$. These power laws depend on the external parameter α: $\zeta \sim 3.5$ for $\alpha > 1$, $\zeta \sim 3$ for $\alpha = 1$ and $\zeta \sim 4$ for $\alpha < 1$. Also, the pattern of imbalance fluctuations in the system depends on the interaction strength.

We highlight the most striking observations at late times before we carry on developing a detailed understanding of the relation between the dominant fluctuations and the observed power laws. In the immiscible regime the system consists of few large domains with additional inclusions of small point-like domains. As compared to the initial time, domains have considerably grown. A special situation is encountered at the transition point, $\alpha = 1$, where domain-like structures persist to extremely long times. This is remarkable since in this regime domains are not energetically favourable as compared to overlapping particle densities. For $\alpha = 0.8$, imbalance fluctuations have decayed up to few small areas of strong imbalance. Let us finally look at the largest computed time $t_\mathrm{f} \simeq 10^3/\omega_\mathrm{I}$. For $\alpha > 1$, two domains of equal size remain, which reflects the immiscibility in the ground state. The small-scale domain-fluctuations have considerably reduced in number. At the transition point, we observe the persistence of domain-like structures which we attribute to a diverging time scale τ of domain decay as $\alpha \to 1$ from below, see the supplement of [87]. For $\alpha < 1$, small long-lived imbalance fluctuations remain, whereas the background tends to become very smooth, $S_z \approx 0$.

II.6.2 Universal Scaling Laws and Defects

Finally, we investigate the microscopic origin of the scaling found in the momentum distributions. The bimodal power laws in these distributions are signatures of the system having approached a non-thermal fixed point [44–46]. At long times they become more pronounced in all three cases (compare the occupation spectra in the three columns in Fig. II.3). In [60], the corresponding time evolution of the occupation spectra in the universal stage has been analysed in more detail (see Fig. 2, Fig. 6, and Fig. 10 in Ref. [60]). The occupation spectra demonstrate a typical shift towards the infrared momentum region together with a slowing down of the dynamic evolution.

In Fig. II.4, the result of a decomposition of the momentum distribution according to

spin and fluid degrees of freedom at $t = t_{\mathrm{NTFP}}$ is presented (see also the supplementary material of [87]). We show spin-spin correlation functions as well as correlations in the incompressible velocity as a function of momentum. In the following, we show that it is possible to explain and understand the scaling properties of the total momentum distribution (shown in Fig. II.3) based on the decomposition, depicted in Fig. II.4. With this, one can understand the scaling laws in the occupation spectrum in terms of mixtures of defect power laws (Porod tails [167, 168]).

In the immiscible regime, see Fig. II.4 (left), the main contribution to the spectrum in the infrared region is provided by the incompressible component n_{i}, corresponding to flow orientations transverse to the direction in which the flow velocity varies. Although we are dealing with a multi-component gas, this feature is similar to superfluid turbulent flow in a single-component Bose gas. Thereby the incompressible spectrum shows $n_{\mathrm{i}} \sim k^{-4}$ scaling over approximately one decade which is generated by coherent vortical flows $\mathbf{w}_i$ around topological defects [55, 56, 60, 87]. The cores of these vortex-like structures can be seen in the spin imbalance, see Fig. II.3, since they are filled with particles of the other species and thus are of the skyrmion type. They are created during the merging process of domains and, persisting due to their topological nature, give the main contribution to the incompressible component spectrum. However, spin excitations n_{s}^{z} overtake in an intermediate momentum region, showing a scaling of $n_{\mathrm{s}}^{z} \sim k^{-3}$. Looking more closely, one observes that the scaling behaviour terminates in the infrared at a scale π/L_{D} given by the mean domain size L_{D}, while the cut-off in the ultra-violet at π/ξ_{s} is set by the width of the domain walls, *i. e.*, the spin healing length $\xi_{\mathrm{s}} = 1/\sqrt{2mJ_{\mathrm{c}}}$. Since the two contributions n_{s}^{z} and n_{i} are of comparable magnitude within an intermediate momentum range, the sum of all contributions, giving the full spectrum $n(k)$, appears to follow the power law $n(k) \sim k^{-3.5}$ in the infrared, as discussed above.

The situation on the other side of the transition can also be clarified. When α falls below 1 domains are energetically suppressed. Thus, vortices dominate the non-thermal fixed point and induce the characteristic scaling $n \sim n_{\mathrm{i}} \sim k^{-4}$, see Fig. II.4 (right). Here, it is also visible in the scaling of relative phase fluctuations n_{s}^{xy}, which is related to constant particle densities on scales larger than ξ as compared to the skyrmionic case above.

The picture changes dramatically on the transition point, $\alpha = 1$. As shown in Fig. II.4 (middle), vortical flow is much less important in this regime. The momentum distribution is dominated by spin fluctuations scaling as $n \sim n_{\mathrm{s}}^{z} \sim n_{\mathrm{s}}^{xy} \sim k^{-3}$. We attribute this feature to the enhanced symmetry in the Hamiltonian and the resulting increased dimensionality of the groundstate manifold for $\alpha = 1$, which removes the topological protection of vortices. The stability of domain walls at the transition point takes over but is non-topological in nature. Instead, conservation laws restrict the decay of this particular type of defect [169]. This argument can be made even more transparent by studying the critical dynamics at the transition from $\alpha < 1$ towards $\alpha = 1$, where two non-equilibrium ordered states meet each other, vortices and domains [87].

II.6.3 Conclusion

We conclude that it is possible to establish the notion of a dynamical phase between different far-from-equilibrium ordered states in a two-component Bose gas. The whole situa-

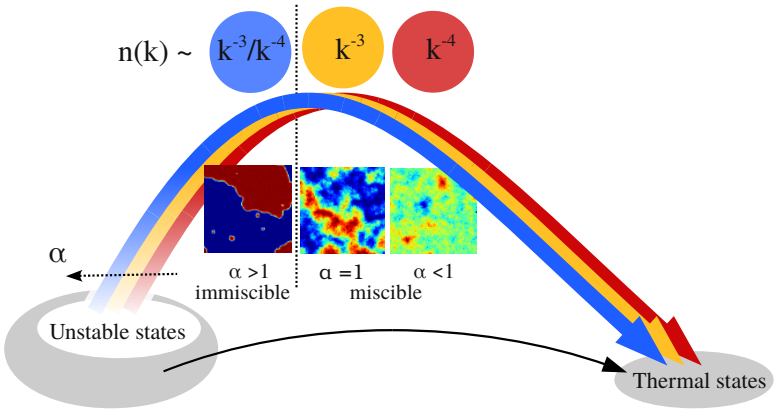

Figure II.5: Illustration of the dynamical evolution, with a focus on the possible transition between far-from-equilibrium transient states. The set in the bottom left corner represents an ensemble of out-of-equilibrium initial states. Amongst these, a subset subjected to a dynamical instability is marked in white. It is chosen such that for all values of the the ratio α of inter- to intra-species couplings the system belongs to the unstable subset. Subsequently, the time evolution of the closed system leads to non- and quasi-topological defect formation. The type of defects created determines the scaling in the low-momentum regime of the particle spectrum of the gas. Our results reveal three different types of scaling behaviour corresponding to three types of defect configurations, and a dynamical phase transition between the far-from-equilibrium universal states. Figure adapted from [87].

tion is summarised in Fig. II.5. Beyond that, the underlying concept of (non-)topological defects determining bulk features of correlation functions in far-from-equilibrium situations is very general. In the spinor Bose gas, a change of a Hamiltonian parameter addressing different equilibrium phases is required to tune between far-from-equilibrium ordered states. We point out the possibility of a universal duality between decaying defects and inverse particle cascades. This requires the generation of (quasi-)topological configurations far from thermal equilibrium and their slow decay, going together with an increase of coherence and defect separation [59]. Under these conditions, an inverse particle cascade is generated, and the associated power laws can be found from the scaling properties of the respective single defect. A variety of (quasi-)topological excitations are known to exist in multi-component fields [133, 169], examples are monopoles in gauge fields [170] and exotic magnets [171], as well as skyrmions in Bose-Einstein condensates [121, 172] and liquid crystals [173]. New interesting features that are readily accessible in experiment are expected for ultracold spinor gases [74, 157, 174–176]. The transition between different types of transient non-equilibrium order can be controlled by changing the symmetry properties of the Hamiltonian and thus topology and local conservation laws of the system. This offers interesting prospects for far-from-equilibrium dynamical phase transitions in very different areas of physics.

III Bogoliubov Theory as a Roadmap

For a Bose gas deep in the semi-classical regime, Bogoliubov theory is typically a good starting point to compute dynamic or thermodynamic properties. The basic idea thereby is to chose a state, which can be described by a classical field to a good degree, and introduce small fluctuations around this meanfield. The fluctuations can then be treated as quantum (quasi-)particles, as they are assumed to be non-interacting due to their smallness. In the basis of non-interacting quasi-particles, observables, such as correlation functions, can be computed easily, either in thermal equilibrium or fully time-dependent. For an introduction to Bogoliubov theory for the one-component Bose gas we refer the reader to [143, 177].

In this chapter, we discuss an implementation of Bogoliubov theory for the spinor Bose gas as defined by the model Eq. (II.1), with emphasis on the spin sector. First, we demonstrate how to linearise and, thereafter, diagonalise the model Eq. (II.1). As a next step, we introduce the concept of a parameter quench, using the diagonal basis of Bogoliubov quasi-particles. In this context, we discuss the class of initial states which we also use in the numerical implementation in subsequent chapters. Finally, we apply the quench concept to derive the post-quench time evolution of spin correlation functions, within the linearised theory, for quenches in the paramagnetic regime.

The intention of the first part of this chapter is two-fold. We derive several semi-analytic expressions, for example for the spin correlation function, which approximate the quench dynamics in the spinor Bose gas. These expressions will serve as gauge to compare the numerical results in the subsequent chapters to. They provide specifically expectations for the behaviour of the interacting system at early times and far away from the critical point.

The second intention is to identify scaling laws, the hallmark of critical behaviour, for post-quench observables within Bogoliubov theory. In particular, we pinpoint where the static meanfield critical exponents $\nu = 1/2$ and $\eta = 0$ (see Sect. II.2) appear in time-dependent Bogoliubov correlation functions. Additionally, we show that the post-quench time-evolution of the equal-time spin correlation function reveals the dynamical critical exponent z. The value of z depends on the closeness of the quench to the critical point and is found to be $z = 1$ for close and $z = 2$ far away from the critical point. As a main result of this analysis, we find that the post-quench equal-time correlation function (or rather the power spectrum) of the z-spin follows a scaling form, with scaling exponents as described above, within Bogoliubov dynamics. We find two realisations of the scaling form, one for quenches close to the critical point and one far from the critical.

The knowledge where to expect meanfield scaling behaviour within the post-quench time evolution of an observable, will allow us in the context of simulations, firstly, to decide when deviations due to interactions set in and, secondly, to analyse the deviations for anomalous contributions to the scaling exponent. In this sense, we propose to use

Bogoliubov theory as a roadmap for finding critical behaviour out of equilibrium.

In the second part of this chapter, we introduce the concept of generalised Gibbs ensemble and apply it to the Bogoliubov formulation for the spin sector of the Bose gas. With this, we are able to characterise and classify the introduced initial states in terms of mode-dependent temperatures. As a main result, we find that the relevant initial states can be characterised to a large extent by a single relevant energy scale, an effective temperature. The energy introduced by the quench provides this scale.

III.1 Bogoliubov Transformation for Spins

In this section, we present an implementation of the Bogoliubov diagonalisation for the spinor Bose gas. Since the goal is to obtain correlation functions for the pseudo-spin field, we away adopt the point of view of the semi-classical approximation, in which the Bose gas is described in terms of classical phase and density fields. This led to the language of pseudo-spins in the first place (see Sect. II.1.1 and Eq. (II.5)). Therefore, we start from the semi-classical Lagrangian given in Eq. (II.4). We proceed as follows: first the Lagrangian Eq. (II.4) is approximated to quadratic order in the classical phase and density fields. Thereafter, the linearised fields are re-quantised and a quasi-particle operator basis is introduce, which diagonalises the quadratic Lagrangian. Finally, we discuss the quasi-particle excitation spectrum, from which, in particular, the meanfield critical coupling J_c of the phase transition (see Sect. II.1.2) can be deduced.

III.1.1 Linearisation of the Spinor Bose Gas

For now, we choose to linearise around a groundstate in the paramagnetic phase and anticipate that there will be a finite constant density in the symmetric sector, as we place the system in the quasi-condensed regime. Therefore, based on Eq. (II.2), we define

$$\begin{aligned} n_+(y,t) &= n_0 + \delta n_+(y,t)\,, \\ S_z(y,t) &= \frac{\delta n_-(y,t)}{n_0}\,, \\ \theta_\pm(y,t) &= \delta\theta_\pm(y,t)\,. \end{aligned} \tag{III.1}$$

where the δ-preceded fields are taken to be 'small' for the linearisisation procedure. The constant part of the z-spin is zero, as this defines the groundstate in the paramagnetic phase. Any constant offsets of the phase in the symmetric sector can be gauged to zero. Finally, we choose the groundstate we linearise around to have a spin pointing into the direction of the transverse field. Thus, θ_- , which represents the spin orientation on the equator of the Bloch sphere, has no constant part either.

Inserting the definitions of Eq. (III.1) in Eq. (II.4) yields the following action, when only terms are retained which are at most quadratic in δ-variables,

$$\mathcal{S}_\epsilon = \int \mathrm{d}t\mathrm{d}y\ \{-n_0[\partial_t\delta\theta_+ + 2(g_+n_0 - 2J - \mu)\delta n_+]\} + S_+ + S_- \tag{III.2}$$

with

$$\mathcal{S}_+ = \int \mathrm{d}t\mathrm{d}y \left\{ -\delta n_+ \partial_t \delta\theta_+ - \left[\frac{\left(\partial_y \delta n_+\right)^2}{4mn_0} + \frac{n_0}{4m}\left(\partial_y \delta\theta_+\right)^2 \right] - g_+ \delta n_+^2 \right\}, \tag{III.3a}$$

$$\mathcal{S}_- = \int \mathrm{d}t\mathrm{d}y \left\{ -\delta n_- \partial_t \delta\theta_- - \left[\frac{\left(\partial_y \delta n_-\right)^2}{4mn_0} + \frac{n_0}{4m}\left(\partial_y \delta\theta_-\right)^2 \right] - \left(g_- + \frac{J}{n_0}\right) \delta n_-^2 - J n_0 \delta\theta_-^2 \right\}. \tag{III.3b}$$

Keeping the action up to quadratic order in δ-terms, implies linear classical equations of motion for the fluctuations. Up to the first term in Eq. (III.2), terms of first order in δ or constants vanish due to the ansatz for the fields in given Eq. (III.1). It is a consequence of the meanfields fulfilling the classical equation of motions. The first term in Eq. (III.2) constitutes a condition on the chemical potential μ for the groundstate. A choice of $\mu = n_0 g_+ - J$ renders the action purely quadratic in δ. The remaining linear term, $-n_0 \partial_t \delta\theta_+$ is a total time derivative and can be dropped.

Remarkably, the remaining two terms in Eq. (III.2), $\mathcal{S}_+$ and $\mathcal{S}_-$, can be seen as the sum of two independent quadratic actions, one for the symmetric sector (the fields $\delta\theta_+$ and δn_+) and one for the asymmetric sector (the fields $\delta\theta_-$ and δn_-). This means that the spin dynamics decouples on the Bogoliubov level from the dynamics of the symmetric sector. The action for the symmetric sector S_+ thereby resembles the Tomonaga–Luttinger liquid description of a one-component Bose gas. In the following, we make use of the fact that the spin sector can be treated independently within the linearised picture while everything which happens on the symmetric sector reflects the physics of an ordinary one-component Bose gas.

III.1.2 Bogoliubov Diagonalisation

The next step is to diagonalise the action $\mathcal{S}_-$, given in Eq. (III.3b), introducing a new basis $b_k^\dagger$, b_k as a linear combination of the old basis, $\delta\theta_-(y)$, $\delta\delta n_-(y)$. Since the spin part of the action, Eq. (III.3b), also resembles in structure a Luttinger liquid the necessary Bogoliubov transformation can be obtained by an educated guess,

$$\delta n_-(y) = \sqrt{\frac{n_0}{2L}} \sum_k \mathrm{i} e^{\mathrm{i}\, yk} f_k b_k - \mathrm{i} e^{\mathrm{i}\, yk} f_k b_{-k}^\dagger, \tag{III.4a}$$

$$\delta\theta_-(y) = \sqrt{\frac{1}{2n_0 L}} \sum_k \frac{e^{\mathrm{i}\, yk}}{f_k} b_k + \frac{e^{\mathrm{i}\, yk}}{f_k} b_{-k}^\dagger, \tag{III.4b}$$

which is shown to diagonalise the action S_- in the following. Note that the transformation given in Eq. (III.4) switches to a description in terms of plane waves with momenta k, as the spatial derivative in S_- is diagonal in momentum space.

Before going on, we re-quantise the phase and density fluctuation fields by interpreting $\delta\theta_-(y)$, $\delta\delta n_-(y)$ and likewise $b_k^\dagger$ and b_k as quantum operators for bosonic fields. The operators b_k and $b_k^\dagger$ should correspond to annihilation and creation operators for bosonic

quasi-particle excitations and, therefore, fulfil the commutator algebra,

$$[b_k(t), b_j^\dagger(t')] = \delta_{k,j}\,\delta(t-t')\,,$$
$$[b_k(t), b_j(t')] = [b_k^\dagger(t), b_j^\dagger(t')] = 0\,. \tag{III.5}$$

The classical phase and density fluctuation fields are conjugate degrees of freedom, as can be seen from the action S_-. Hence, the corresponding canonical commutation relations for the phase and density field operators are

$$[\delta\theta_-(y,t), \delta n_-(y',t')] = \mathrm{i}\delta(y-y')\,\delta(t-t')\,,$$
$$[\delta\theta_-(y,t), \delta\theta_-(y',t')] = [\delta n_-(y,t), \delta n_-(y',t')] = 0\,. \tag{III.6}$$

The Bogoliubov transformation given in Eq. (III.4) is tailored to preserve the commutator structures on both sides, *i. e.* Eq. (III.6) and Eq. (III.5), provided that the function f_k is real-valued and symmetric in k.

Finally, we determine the expression for f_k which renders the action S_- diagonal in the quasi-particle basis. The action for the spin sector, S_-, given in Eq. (III.3b), can be reformulated to

$$\mathcal{S}_- = \int \mathrm{d}t\mathrm{d}y \left\{ -\frac{1}{2}\left[\delta n_- \partial_t \delta\theta_- - \partial_t \delta n_- \delta\theta_-\right] - \frac{1}{2n_0}\delta n_- A^2\,\delta n_- - \frac{n_0}{2}\delta\theta_- B^2\,\delta\theta_- \right\}\,, \tag{III.7}$$

where we have symmetrised the first term by means of partial integration and defined the operators $A^2 = -\partial_y^2/2m + 2n_0 g_- + 2J$ and $B^2 = -\partial_y^2/2m + 2J$. Then, inserting the mode expansion given in Eq. (III.4) into S_-, in the form of Eq. (III.7), yields

$$\mathcal{S}_- = \int \mathrm{d}t \sum_k \left\{ \frac{\mathrm{i}}{2}\left[b_k^\dagger \dot{b}_k - h.c.\right] - \frac{A_k^2 f_k^2}{4}\left[b_k^\dagger b_k + b_k b_k^\dagger - b_k^2 - \left(b_k^\dagger\right)^2\right] \right.$$
$$\left. - \frac{B_k^2}{4f_k^2}\left[b_k^\dagger b_k + b_k b_k^\dagger + b_k^2 + \left(b_k^\dagger\right)^2\right] \right\}\,. \tag{III.8}$$

The operators A^2 and B^2 are expressed in momentum space simply by $-\partial_y^2 \to k^2$.

The diagonal form of S_-, in which each Bogoliubov momentum mode forms a harmonic oscillator, can now be achieved by setting $f_k^2 = B_k/A_k$. This yields automatically the Bogoliubov quasi-particle dispersion (the excitation spectrum), $\omega_-(k) = A_k B_k$.

Hence, as a result of the Bogoliubov transformation Eq. (III.4) with mode expansion coefficients

$$f_k^2 = \sqrt{\frac{\epsilon_k + 2J}{\epsilon_k + 2n_0 g_- + 2J}}\,, \tag{III.9}$$

the action S_- becomes diagonal,

$$\mathcal{S}_- = \int \mathrm{d}t \sum_k \left\{ \frac{\mathrm{i}}{2}\left[b_k^\dagger \dot{b}_k - h.c.\right] - \omega_-(k)\left[b_k^\dagger b_k \frac{1}{2}\right] \right\}\,, \tag{III.10}$$

The Bogoliubov eigenfrequencies read

$$\omega_-(k) = \sqrt{(\epsilon_k + 2n_0 g_- + 2J)(\epsilon_k + 2J)}\,, \tag{III.11}$$

with $\epsilon_k = k^2/2m$.

The same procedure works for the symmetric sector as well and the corresponding expressions can be obtained by simply setting $g_- \to g_+$ and $J \to 0$ (as this maps $S_- \to S_+$, *cf.* Eq. (III.3a) and Eq. (III.3b)). In particular, with $g_- \to g_+$ and $J \to 0$ in Eq. (III.11) one finds the quasi-particle excitation spectrum $\omega_+(k)$ for the linearised symmetric sector,

$$\omega_+(k) = \sqrt{\epsilon_k(\epsilon_k + 2n_0 g_+)}\,. \tag{III.12}$$

The form of $\omega_+(k)$ resembles the standard Bogoliubov excitation spectrum, obtained for the ordinary one-component Bose gas, see for example [143]

III.1.3 The Bogoliubov Quasi-Particles

Before we go on with discussing dynamics within the Bogoliubov picture, we discuss important aspects of the quasi particle basis. Specifically, we show that the meanfield critical point of the miscible–immiscible phase transition in the spin sector (see Sect. II.1.2) can also be determined via the Bogoliubov excitation spectrum. Thereafter, we derive the relation between the occupation spectrum of quasi-particles and the correlation functions of the spin fluctuation fields ($\delta\theta_-(y)$ and $\delta n_-(y)$).

The Excitation Spectrum

Comparing the the quasi-particle excitation spectrum on both sectors, ω_- (Eq. (III.11)) to ω_+ (Eq. (III.12)), one finds that for the form of ω_- (see Fig. III.1 for examples) the interplay between two couplings, J and g_-, is relevant. Note that we assume $J \geq 0$ in the following and for the remainder of this work.

In the fully miscible regime, $\alpha < 1$, one has $g_- = g(1-\alpha) > 0$, and as a consequence ω_- is real-valued for all momenta and values of $J \geq 0$. Importantly, the excitation spectrum $\omega_-(k)$ has a gap in this regime, meaning that $\lim_{k\to 0} \omega_-(k) > 0$, if $J > 0$. Explicitly, one finds

$$\lim_{k\to 0} \omega_-(k) = \Delta = 2\sqrt{J\,(n_0 g_- + J)}\,. \tag{III.13}$$

If, in contrast, the inter-species scattering strength exceeds the intra-species scattering strength ($\alpha > 1$) g_- is negative. Consequently, one finds that ω_- can acquire a complex value, depending on the strength of the linear coupling. The critical value of the linear coupling for this to happen is

$$J_c = -n_0 g_- = n_0 g(1-\alpha)\,, \tag{III.14}$$

as the first factor under the square root in Eq. (III.11) can become negative if $J < J_c$.

In the paramagnetic regime, where $J > J_c$, the spectrum $\omega_-(k)$ is real-valued for all modes but is, in contrast to the standard gap-less Bogoliubov dispersion, dominated by

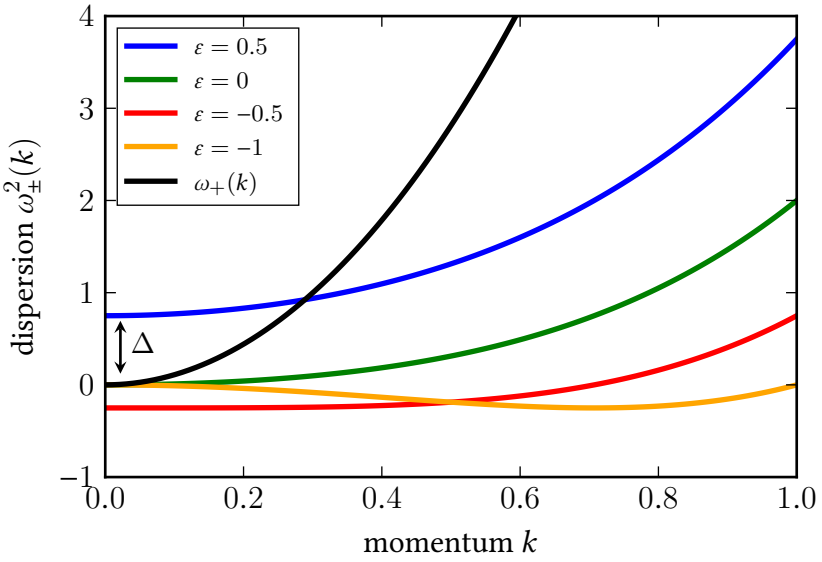

Figure III.1: The figure shows the Bogoliubov dispersion relation of the spin sector, ω_- (see Eq. (III.11)), (coloured curves) for four characteristic cases. As discussed in the main text, we show the dispersion deep in the paramagnetic phase, $J > J_c$ (blue), for the ferromagnetic phase, $J_c > J > J_c/2$, (red), for the domain-building ferromagnetic phase, $J < J_c/2$, and at the critical point (green), where the gap vanishes. In comparison, the black curve depicts the Bogoliubov dispersion relation for the symmetric sector, $\omega_+^2(k)$ (see Eq. (III.12)) for a ratio of scattering lengths $g_{\uparrow\downarrow}/g = 1.2$.

a flat part for very low momenta, *cf.* Fig. III.1. If a large distance to the critical point is chosen a linear regime, where $\omega_-(k) \sim k^1$, can be almost completely avoided. Consequently, one can expect that the phenomenology for the dynamics in the infrared here is dominated rather by the gap than a 'lightcone'.

In the ferromagnetic case $J < J_c$, the excitation spectrum acquires imaginary values (or $\omega_-^2 < 0$ equivalently) for infrared momenta $\epsilon_k < |2J - J_c|$ (see Fig. III.1). In particular, the gap in Eq. (III.13) turns imaginary but is finite $|\Delta| > 0$. The Bogoliubov modes with imaginary frequencies will have a exponentially fast changing amplitude in their time evolution, instead of an oscillating phase. This is a clear sign of an instability and, hence, the dynamic manifestation of a phase transition. Since the gap vanishes at $J = J_c = -g_- n_0$ but stays finite else, the spin excitation spectrum ω_- reveals the second-order phase transition (in meanfield approximation), we have discussed in Sect. II.1.2 and Sect. II.2. On this level of Bogoliubov approximation, we find the same value for the critical coupling $J_c = -g_- n_0$ as via the analysis of the meanfield free energy (see Sect. II.1.2)

In the case $J < J_c$, one can in addition distinguish two cases. Firstly, if $J_c > J > J_c/2$, the maximum of $|\omega_-|$ is precisely the gap, meaning that the zero mode of the quasi-particle operators will grow fastest in amplitude and so does the related zero mode of spin excitations. Thus, the system chooses a z-spin direction and and builds up a fully polarised

state. In the second case, $J < J_c/2$ the most unstable mode is located at a finite momentum, $k_{\max} = \sqrt{2m(J_c - 2J)}$, which leads the quasi-particle and z-spin amplitude to grow fastest at a characteristic momentum. The induced characteristic scale, $\xi_d \simeq 1/k_{\max}$, marks the size of z-spin domains which will be nucleated by the instability.

In Fig. III.1 we show in addition the dispersion relation for the symmetric sector, $\omega_+(k)$ (see Eq. (III.12)). One finds that the two dispersion relations only can have a crossing in the regime $J > J_c$. Since one can expect this crossing to morph into an avoided crossing beyond Bogoliubov approximation, a coupling of the symmetric sector to the spin sector is expected to occur first at the crossing point. The momentum mode for which both excitation spectra $\omega_-(k)$ and $\omega_+(k)$cross in Bogoliubov theory is[1]

$$k_{\text{cross}} = \sqrt{2m \frac{2J(J - J_c)}{g_+ n_0 - 2J + J_c}} \,. \tag{III.15}$$

The Quasi-Particle Basis

To analyse the physical meaning of the quasi-particle basis, the Bogoliubov transformation from Eq. (III.4) needs to be inverted. A suitable combination of Eq. (III.4a) and Eq. (III.4b), after inversion of the Fourier transformation, yields

$$b_k = \int \mathrm{d}y \left\{ -\mathrm{i} \frac{e^{-\mathrm{i}\, ky}}{\sqrt{2n_0 L}} \frac{\delta n_-(y)}{f_k} + e^{-\mathrm{i}\, ky} \sqrt{\frac{n_0}{2L}} f_k \delta\theta_-(y) \right\} , \tag{III.16}$$

where $b_k^\dagger$ is given by the Hermitian conjugate of Eq. (III.16). To obtain the expression, we have used that the mode function f_k is real-valued and symmetric in k. This shows that the quasi-particle operators b_k and $b_k^\dagger$ describe a coherent superposition of spin excitation modes in z spin direction, $S_z(k) = \delta n_-(k)/n_0$, and spin excitation modes in y spin direction, $S_y(k) = \delta\theta_-(k)$. The momentum mode expansion of the spin fluctuation fields (or operators) are defined as

$$\delta S_i(k) = \frac{1}{\sqrt{L}} \int \mathrm{d}y \mathrm{e}^{-\mathrm{i}\, yk} S_i(y) \,, \tag{III.17}$$

with $S_i(-k) = S_i^\dagger(k)$ due the spin fields being real-valued.

The inverse transformation Eq. (III.16) shows also, that the Bogoliubov mode function f_k controls the weight between both spin directions in the superposition[2]. If $f_k = 1$ for a mode k, a quasi-particle excitation creates spin excitations in both spin directions in equal superposition. This happens, in particular, for ultra-violet modes $\epsilon_k \gg J$ in Eq. (III.9), for which $\lim_{k\to\infty} f_k = 1$ holds. The same is true for the case of strong linear coupling $J \gg J_c$, as one has then $\lim_{J\to\infty} f_k \equiv 1$, for all momentum modes.

In contrast, in the infrared limit $k \to 0$ one finds $\lim_{k\to 0} f_k^2 = \sqrt{J/(J - J_c)}$. Therefore,

[1] A closer look reveals that, actually, the crossing disappears if $J/J_c > \alpha/(\alpha - 1)$, since then the condition $\left(\omega_-^2 = \omega_+^2\right)|_{k_{\text{cross}}}$ has no real-valued solution.

[2] We restrict the discussion to $g_- < 0$ and $J > -n_0 g_-$, the paramagnetic regime, such that f_k from Eq. (III.9) is real-valued

one has $f_k > 1$ for $J > J_c$ for in the infrared momentum region, with growing f_k as J moves closer to the critical value. This means that, close to the critical point and for infrared momenta $\epsilon_k \ll 2J_c$, excitations of the relative phase dominate in the superposition Eq. (III.16) for quasi-particle excitations.

Quasi-Particle Occupation Number

For the discussion of the Bogoliubov time evolution of spin observables in the subsequent sections, it is convenient to compute two expressions for the occupation number operator of Bogoliubov quasi-particles, $n_B(k) = b_k^\dagger b_k$, beforehand. In particular, it is helpful to compute $n_B(k)$ in terms of the spin fluctuation field operators $\delta\theta_-(y)$ and $\delta n_-(y)$ and to compute the relation between $n_B(k)$ at two different linear couplings. The latter will also provide a convenient language for introducing the notion of quenches in the Bogoliubov framework.

The relation between the quasi-particle occupation $n_B(k)$ and spin fluctuation operators can be right away found using the inverse Bogoliubov transformation Eq. (III.16), which yields

$$b_k^\dagger b_k + \frac{1}{2} = \frac{1}{2}\int \mathrm{d}y\,\mathrm{d}y' \left\{ \frac{e^{-\mathrm{i}\,k(y-y')}}{n_0 L}\frac{\delta n_-(y)\delta n_-(y')}{f_k^2} + e^{-\mathrm{i}\,k(y-y')}\frac{n_0}{L} f_k^2 \delta\theta(y)\delta\theta(y') \right\}, \tag{III.18}$$

The '$1/2$' on the left-hand side is an immediate consequence of treating spin fluctuations and quasi-particles in a quantised manner, as explained in the context of the commutation relations Eq. (III.5) and Eq. (III.6). In practice, the expression Eq. (III.18) will be useful in terms of quantum averages. Both sides can be averaged over with respect to any ensemble or density matrix and will yield a relation between the mean quasi-particle occupation and the spin-spin correlation functions.

To find an expression for $n_B(k)|_{J=J_f}$ in terms of the Bogoliubov basis at a different linear coupling $J = J_i$, we first show how the Bogoliubov basis itself transforms[3] under a change of the linear coupling. Let b_k^i be the quasi-particle annihilation operator at coupling $J = J_i$ and, likewise, b_k^f at $J = J_i$. Starting with Eq. (III.16) for b_k^i, one can exploit that the spin fluctuation operators $\delta\theta_-(y)$ and $\delta n_-(y)$ do not change their meaning when changing the value of J. Therefore, Eq. (III.4a) and Eq. (III.4b), written in terms of the new operator basis b_k^f, diagonalise the action S_- (see Eq. (III.3b)) at the linear coupling $J = J_f$. Combining Eq. (III.16) at $J = J_i$ with Eq. (III.4) at $J = J_f$ results in

$$b_k^i = u_k b_k^f + v_k b_{-k}^{\dagger\,f}, \tag{III.19}$$

[3] This transformation is equally helpful to introduce the notion of quenches. The index convention 'i' for 'initial' and 'f' for 'final' is chosen for that reason to match the naming convention in subsequent chapters

with u_k and v_k given by

$$v_k = \frac{\left(f_k^{\mathrm{i}}\right)^2 - \left(f_k^{\mathrm{f}}\right)^2}{2 f_k^{\mathrm{f}} f_k^{\mathrm{i}}}\,,$$
$$u_k = \frac{\left(f_k^{\mathrm{i}}\right)^2 + \left(f_k^{\mathrm{f}}\right)^2}{2 f_k^{\mathrm{f}} f_k^{\mathrm{i}}}\,, \tag{III.20}$$

and $|u_k|^2 - |v_k|^2 = 1$, with $f_k^{\mathrm{i,f}} = f_k|_{J=J_{\mathrm{i,f}}}$ (see Eq. (III.9)).

The transformation is conveniently expressed in terms of pseudo-rapidities η_k, which are defined via $\sinh(\eta_k) = v_k$ and $\cosh(\eta_k)$. From Eq. (III.20) one finds

$$\eta_k(J_{\mathrm{i}}, J_{\mathrm{f}}) = \log\left[f^{\mathrm{i}}(k)/2f^{\mathrm{f}}(k)\right]. \tag{III.21}$$

With that, the transformation can be expressed as

$$(b_k^{\mathrm{i}},\, b_{-k}^{\dagger\,\mathrm{i}})^{\mathrm{T}} = M_k\,(b_k^{\mathrm{f}},\, b_{-k}^{\dagger\,\mathrm{f}})^{\mathrm{T}}\,, \tag{III.22}$$

where the matrix M, with

$$M_k = \begin{pmatrix} \cosh\eta_k & \sinh\eta_k \\ \sinh\eta_k & \cosh\eta_k \end{pmatrix}\,, \tag{III.23}$$

and $\eta_k = \eta_k(J_{\mathrm{i}}, J_{\mathrm{f}})$, is an element of the symplectic group (see for example [178]). The inverse transformation M_k^{-1} is simply found by exchanging $\eta_k(J_{\mathrm{i}}, J_{\mathrm{f}}) \to -\eta_k(J_{\mathrm{i}}, J_{\mathrm{f}}) = \eta_k(J_{\mathrm{f}}, J_{\mathrm{i}})$ in Eq. (III.23).

With the relation in Eq. (III.22), the quasi-particle number operator $n_{\mathrm{B}}(k)$ at linear couplings J_{f} can be finally expressed in terms of b_k^{i} and $b_{-k}^{\dagger\,\mathrm{i}}$,

$$b_k^{\dagger\,\mathrm{f}} b_k^{\mathrm{f}} + \frac{1}{2} = \left(\sinh^2\eta_k + \frac{1}{2}\right)\left(b_k^{\dagger\,\mathrm{i}} b_k^{\mathrm{i}} + b_{-k}^{\dagger\,\mathrm{i}} b_{-k}^{\mathrm{i}} + 1\right) - \sinh\eta_k \cosh\eta_k \left(b_{-k}^{\mathrm{i}} b_k^{\mathrm{i}} + b_{-k}^{\dagger\,\mathrm{i}} b_k^{\dagger\,\mathrm{i}}\right)\,, \tag{III.24}$$

where the pseudo-rapidities $\eta_k = \eta_k(J_{\mathrm{i}}, J_{\mathrm{f}})$ are given in Eq. (III.21).

III.2 Quench Dynamics within the Gaussian Theory

Having obtained a description of the linearised spin sector in Sect. III.1 in terms of a standard quadratic field theory (*i. e.* the formulation of the action S_- Eq. (III.10) in terms of Bogoliubov operators), we are now in the position of discussing dynamics within that theory. Specifically, in the remainder of this chapter we study dynamics after a sudden change of the linear coupling J within the paramagnetic regime $J > J_{\mathrm{c}}$.

In this section, we first discuss the implementation of such a sudden parameter quench within the framework of Bogoliubov theory, we have introduced in Sect. III.1. Thereafter, the post-quench time evolution of the spin correlation structure factor $\langle S_z(k,t_1) S_z(k,t_2)\rangle$ is computed within Bogoliubov theory, building on the diagonalisation framework from

the last section. We do so, first, for a general pre-quench state and discuss afterwards possible choices for the pre-quench state, together with their physical interpretation. In the last part of this section, an expression for the equal-time spin structure factor $\langle S_z(k,t)S_z(k,t)\rangle$ is obtained, for the same quench scenario we study numerically beyond Bogoliubov theory in the subsequent chapters.

III.2.1 Sudden Quenches in the Linear Coupling

The notion of a sudden parameter quench of the linear coupling J we adopt in this work is the following. First, one prepares a state $|\Omega\rangle_\mathrm{i}$ which is well defined in terms of the Bogoliubov basis b_k^i at linear coupling $J_\mathrm{i} > J_\mathrm{c}$. A natural choice, which we mainly study in the subsequent chapters, is the vacuum of all quasi-particles operators b_k^i, $|\Omega\rangle_\mathrm{i} = \otimes_k |0\rangle_k$ with $b_k|0\rangle_k = 0$. Thereafter, one computes the time evolution of the Bogoliubov operators with respect to a different value of the linear coupling J_f in the action S_-. Expectation values for observables are then taken with respect to $|\Omega\rangle_\mathrm{i}$.

For the operators b_k^f and $b_k^{\dagger\,\mathrm{f}}$ at a fixed value $J_\mathrm{f} > J_\mathrm{c}$ for the linear coupling, the the time evolution can be given right away, as the operators form a simple harmonic oscillator at each mode in the action Eq. (III.10) at $J = J_\mathrm{f}$. The solution to the Heisenberg equations of motion is

$$\begin{aligned} b_k^\mathrm{f}(t) &= b_k^\mathrm{f}(t=0)\cdot e^{-\mathrm{i}\omega_-(k,J_\mathrm{f})\,t} \\ b_k^{\dagger\,\mathrm{f}}(t) &= b_k^{\dagger\,\mathrm{f}}(t=0)\cdot e^{\mathrm{i}\omega_-(k,J_\mathrm{f})\,t}\,, \end{aligned} \tag{III.25}$$

as they agree with the solutions to the classical equations of motion for a quadratic action of the form Eq. (III.10).

The quench is then implemented by a sequence of transformations. First, map $b_k^\mathrm{f}(t=0)$ and $b_k^{\dagger\,\mathrm{f}}(t=0)$ in Eq. (III.25) to b_k^i and $b_k^{\dagger\,\mathrm{f}}$. For this purpose use the transformation, defined in Eq. (III.22), via matrix M_k. Second, evolve the b_k^f in time by multiplying a simple phase, according to Eq. (III.25). And third, express the observable in question at time t in terms of Bogoliubov operators $b_k^\mathrm{f}(t)$ and $b_k^{\dagger\,\mathrm{f}}(t)$. To compute actual expectation values after the last step, and depending on the complexity of the observable, one might need to employ Wick's theorem. A simple application for the procedure is the post-quench occupation of Bogoliubov quasi-particles. The time evolution given in Eq. (III.25) implies that the occupation number operator at J_f, $n_\mathrm{B}(t,k)$ has no time dependence, $n_\mathrm{B}(k,t) = n_\mathrm{B}(k) = b_k^{\dagger\,\mathrm{f}} b_k^\mathrm{f}|_{t=0}$. The post-quench occupation is then determined via Eq. (III.24) applied to $|\Omega\rangle_\mathrm{i}$,

$$ {}_\mathrm{i}\langle\Omega|n_\mathrm{B}(k)|\Omega\rangle_\mathrm{i} = \sinh^2\eta_k(J_\mathrm{i},J_\mathrm{f})\,, \tag{III.26}$$

with $\eta_k(J_\mathrm{i},J_\mathrm{f})$ given in Eq. (III.21).

Due to its stationarity with respect to the time evolution after the quench, ${}_\mathrm{i}\langle\Omega|n_\mathrm{B}(k)|\Omega\rangle_\mathrm{i}$ constitutes a conserved number for every mode k, which is solely determined by the initial state. Based on this property, the concept of generalised Gibbs ensembles can be applied, as we discuss together with consequences thereof for the post-quench dynamics in Sect. III.4.

III.2.2 Time Evolution of the Spin Correlation Function

In this section, we focus on the correlation function of the z-spin fluctuations $S_z(t,pz) = \delta n_-(t,y)/n_0 + O(\delta^2)$ and derive its time dependence after the quench (along the lines of Sect. III.2.1). Specifically, we compute the two-time correlation function

$$\mathcal{G}_{zz}(t_1,t_2,y) = \langle S_z(t_1,0)S_z(t_2,y)\rangle = \frac{1}{n_0^2}\langle \delta n_-(t_1,0)n_-(t_2,y)\rangle\,, \tag{III.27}$$

for quenches in the paramagnetic regime (as discussed in Sect. III.2.1) within Bogoliubov theory. In this section, we derive a general expression for $\mathcal{G}_{zz}(t_1,t_2,y)$ in terms of initial spin fluctuations, *i. e.* without specifying the initial state completely. In the following section, Sect. III.2.3, we discuss possible initial states separately and finally combine both in Sect. III.3.

A sequence of transformations from the spin to the quasi-particle basis and back, as lined out in Sect. III.2.1, yields the time evolution of spin fluctuation operators, $\delta n_-(t,y)$ and $\delta\theta_-(t,y)$. Specifically, use Eq. (III.4) for operators at time t and the quasi-particle operators at $J = J_\mathrm{f}$, b_k^f. Then insert the time evolution of the quasi-particle operators at J_f (from Eq. (III.25)) and, finally, apply the inverse transformation Eq. (III.16) at time $t = 0$. The sequence yields for $\delta n_-(t,y)$

$$\delta n_-(t,y) = \frac{n_0}{\sqrt{L}}\sum_k \left(\cos(\omega_- t)S_z(k)|_{t=0} + n_0 f_k^2 \sin(\omega_- t)S_y(k)|_{t=0}\right)\mathrm{e}^{\mathrm{i}\,yk}\,, \tag{III.28}$$

and likewise for the operator $\delta\theta_-(t,y)$

$$\delta\theta_-(t,y) = \frac{1}{\sqrt{L}}\sum_k \left(-\sin(\omega_- t)\frac{S_z(k)|_{t=0}}{f_k^2} + \cos(\omega_- t)S_y|_{t=0}\right)\mathrm{e}^{\mathrm{i}\,yk}\,, \tag{III.29}$$

where we have used that $S_i^\dagger(k) = S_i(-k)$. Recall Eq. (III.25) for the mode expansion of fluctuation fields.

We point out that Eq. (III.28) and Eq. (III.29) do not contain any reference to an initial value for the linear coupling, or form of initial state in general, yet. Before we go on, we specify to a class of initial states. We assume an initial state where only the initial spin-spin correlations $\langle \S_z(k)\S_z(-k)\rangle|_{t=0} \neq 0$ and $\langle S_y(k)S_y(-k)\rangle|_{t=0} \neq 0$ are non-zero. All other spin-spin combinations are taken to vanish with respect to the initial state. We discuss possible realisations of this class of initial states in terms of the quasi-particle basis b_k^i in the next section, Sect. III.2.3.

Finally, the spin-spin correlation function for the spin in z-direction, $\langle S_z(t_1,0)\,S_z(t_2,y)\rangle$, can be obtained, since $S_z = \delta n_-/n_0 + O(\delta^2)$. With Eq. (III.28) evaluated at times t_1 and

t_2 we find

$$\langle S_z(0,t_1)\, S_z(y,t_2)\rangle = \mathcal{G}_{zz}(y,T,s) = \\ \frac{1}{2L}\sum_k \left\{ \langle S_z(k)S_z(-k)\rangle\big|_{t=0} \left[\cos\left(\omega_-(k,J^{\mathrm{f}})s\right) + \cos\left(2\omega_-(k,J^{\mathrm{f}})T\right)\right] \right. \\ \left. + \left\langle S_y(k)S_y(-k)\right\rangle\big|_{t=0} f_k(J^{\mathrm{f}})^4 \left[\cos\left(\omega_-(k,J^{\mathrm{f}})s\right) - \cos\left(2\omega_-(k,J^{\mathrm{f}})T\right)\right] \right\} \mathrm{e}^{\mathrm{i}\,ky}\,, \qquad \text{(III.30)}$$

where we have introduced central and relative time, $T = (t_1 + t_2)/2$ and $s = (t_1 - t_2)$ respectively.[4] The excitation spectrum ω_- and the mode function f_k are defined in Eq. (III.11) and Eq. (III.9).

The time evolution for $\langle \delta\theta(t_1,0)\delta\theta(t_2,y)\rangle$ can now be obtained easily using the operator relation $S_y(t,k) = \partial_t S_z(t,k)/f_k^2\omega_-)$. An expression similar to Eq. (III.30) emerges. Note that $\langle \delta\theta(0)\delta\theta(y)\rangle$ represents the connected correlation function for the spin in y-direction in Bogoliubov theory, as $S_y = \delta\theta_- + O(\delta^2)$. Since phase and density fluctuations are conjugate to each other both correlation functions are expected to contain the same information content concerning dynamics. However, beyond Bogoliubov theory it can be helpful to compute both observables, although they are still conjugate degrees of freedom, to evaluate expression Eq. (III.18). This can be used to either check how close to the linear regime the system evolves.

III.2.3 Initial states

In the ideal case of a sudden quench the characteristics of the quench hides in the choice of the initial spin correlation functions. The previous section, Sect. III.2.2, led us to an expression for the z-spin correlation function after a quench (Eq. (III.30)), which depends on the choice of the initial fluctuations of spins. Recall that, at the beginning of Sect. III.1, we needed to chose a meanfield, $\langle S_z\rangle \equiv \langle S_y\rangle \equiv 0$ and $\langle S_y\rangle \equiv 1$, to linearise the action. Since the Bogoliubov theory describes fluctuations around this meanfield (*cf.* Eq. (III.1)), the choice the meanfield constitutes a second important part of defining the pre-quench state. In our case, the choice of the meanfield pins the quench to start in the paramagnetic regime.

In practice, our choice of the initial fluctuations is motivated by the truncated Wigner formalism for the two-component Bose gas which leads in turn to coherent and squeezed spin states. In this section we want to discuss a more theoretical point of view which alludes to the treatment of the transverse field Ising model.

We introduce two specific realisations of the initial spin fluctuations, needed as input for Eq. (III.30), in this section and give an interpretation in terms of initial quasi-particle occupations. The first class of initial states, we discuss, is defined by the vacuum of initial quasi-particle operators b_k^{i} and leads to states of minimal uncertainty in the spin picture. The second class of initial states is defined by thermal occupations of initial quasi-particle modes.

[4] Note that there is an overlap in notation here with temperature and scale factors, which we will also denote with T and s. However, which definition to apply will be clear from the context or otherwise explicitly stated.

Initial Fluctuations with Minimal Uncertainty

Given a certain initial linear coupling, J_i , one can demand that the initial data corresponds to a vacuum state for the initial quasi-particle modes, $|\Omega\rangle_i = \otimes_k |0\rangle_k$ with $b_k|0\rangle_k = 0$. As this sets ${}_i\langle\Omega|b_k^\dagger b_k|\Omega\rangle_i = 0$ for all modes k on the left-hand side of Eq. (III.18) a straightforward choice in terms of the spin degrees of freedom which satisfies this demand is, for example,

$$\begin{aligned}\langle\delta n_-(0)\delta n_-(y)\rangle|_{t=0} &= \frac{1}{L}\sum_k e^{\mathrm{i}\,k(y-y')} f_k^2|_{J_\mathrm{i}} \frac{n_0}{2}\,,\\ \langle\delta\theta(0)\delta\theta(y)\rangle|_{t=0} &= \frac{1}{L}\sum_k e^{\mathrm{i}\,k(y-y')} \frac{1}{2n_0 f_k^2|_{J_\mathrm{i}}}\,.\end{aligned} \tag{III.31}$$

The state defined by Eq. (III.31) belongs to the class of states where the individual modes have minimal uncertainty,

$$\langle|\delta n_-(k)|^2\rangle \cdot \langle|\delta_-\theta(k)|^2\rangle = 1/4\,, \tag{III.32}$$

with $\delta n_-(k) = n_0 S_z(k) + O(\delta^2)$ and $\delta\theta_-(k) = S_y(k) + O(\delta^2)$.

Now, the quench primarily amounts to mapping this initial data via a Bogoliubov transformation to a new quasi-particle occupation at linear coupling J_f. We have discussed the mapping in detail in the first section of this chapter. One finds directly from Eq. (III.24)

$${}_i\langle\Omega|b_k^\dagger b_k|_{J_\mathrm{f}}|\Omega\rangle_i + \frac{1}{2} = \frac{1}{4}\left[\frac{f_k^2|_{J_\mathrm{i}}}{f_k^2|_{J_\mathrm{f}}} + \frac{f_k^2|_{J_\mathrm{f}}}{f_k^2|_{J_\mathrm{i}}}\right]\,. \tag{III.33}$$

We point out that the post-quench quasi-particle occupation numbers, ${}_i\langle\Omega|b_k^\dagger b_k|_{J_\mathrm{f}}|\Omega\rangle_i$, are conserved under the subsequent time evolution within Bogoliubov theory. See also Sect. III.2.1. We will discuss implications thereof in the last section of this chapter, Sect. III.4.

With the help of Eq. (III.19) one can find a straight-forward characterisation of the post-quench state. The equation connects the pre-quench quasi-particle operators with the post-quench operators via a standard Bogoliubov transformation. The same reasoning holds for the pre-quench vacuum state. In terms of the post-quench vacuum, it can be expressed as

$$|\Omega\rangle_i = \sum_k \exp\left(-\tanh(\eta_k) b_k^{\dagger\,\mathrm{f}} b_{-k}^{\dagger\,\mathrm{f}}\right)|0\rangle_{-k}\otimes|0\rangle_k\,, \tag{III.34}$$

which can be seen by acting with the right-hand side of equation Eq. (III.19) on it. This shows that the post-quench state is a two-mode squeezed vacuum state [178] and essentially is composed of coherent pairs of quasi-particles with moving with opposite momenta.

Thermal Initial Fluctuations

There exists another class of initial states which have a straight forward theoretical interpretation. One can choose the pre-quench quasi-particle occupation to be thermally

distributed at a certain finite temperature T, *i.e.* ${}_i\langle\Omega_{\text{th}}|b_k^\dagger b_k|\Omega_{\text{th}}\rangle_i = F_{\text{BE}}(\omega_-,T)$. For the distribution F_{BE} either the full Bose–Einstein distribution can be used or it can be approximated by a Rayleigh–Jeans distribution, $F_{\text{BE}} \approx T/\omega_-$. A possible application of such states is to study temperature quenches instead of quenches in the Hamiltonian parameter J or even combine both quench types. In Sect. III.4 we will use thermal states of fluctuations to compare the minimal uncertainty states to and as means to classify them in terms of effective temperatures.

To initialise the quench with thermally occupied initial Bogoliubov modes, the set of initial data from Eq. (III.31) has to be slightly modified,

$$\begin{aligned}\langle\delta n_-(0)\delta n_-(y)\rangle|_{t=0} &= \frac{1}{L}\sum_k e^{\mathrm{i}\,k(y-y')}\,(2F_{\text{BE}}|_{J_\text{i}}+1)\,f_k^2|_{J_\text{i}}\frac{n_0}{2}\,,\\ \langle\delta\theta(0)\delta\theta(y)\rangle|_{t=0} &= \frac{1}{L}\sum_k e^{\mathrm{i}\,k(y-y')}\,(2F_{\text{BE}}|_{J_\text{i}}+1)\,\frac{1}{2n_0 f_k^2|_{J_\text{i}}}\,,\end{aligned} \tag{III.35}$$

to yield eventually a post-quench Bogoliubov quasi-particle occupation associated with a finite pre-quench temperature,

$${}_i\langle\Omega_{\text{th}}|b_k^\dagger b_k|_{J_\text{f}}|\Omega_{\text{th}}\rangle_i + \frac{1}{2} = \frac{(2F_{\text{BE}}|_{J_\text{i}}+1)}{4}\left[\frac{f_k^2|_{J_\text{i}}}{f_k^2|_{J_\text{f}}}+\frac{f_k^2|_{J_\text{f}}}{f_k^2|_{J_\text{i}}}\right]\,. \tag{III.36}$$

It should be clear that the situation, and specifically the search for scaling behaviour, grows more complex the more phenomenology we add. Originally, the only energy scale for the dynamic situation was set by the energy gap and, thus, determined by the post-quench linear coupling J_f. In Eq. (III.31) we have introduced a second energy scale, J_i, coming from the characterisation of the pre-quench distribution. The thermal distribution from Eq. (III.35) introduces a third energy scale, set by the temperature. In any case, those scales set by initial fluctuations need to be taken into consideration when describing observables in terms of scaling laws.

We illustrate the outcomes of Eq. (III.36) and Eq. (III.33) for several examples in Fig. III.2. In particular, it can be observed that the qualitative difference between finite-temperature pre-quench states and zero-temperature are marginal. Both scales, T and J_i relative to J_f, control the number of 'created' quasi-particles for low momenta in the post-quench distribution.

In contrast to the standard treatment of the transverse Ising model (we give brief introduction at the beginning of chapter VI), here the spin system is only approximated by the Bogoliubov modes. Consequently, the groundstates and thermal states we used to find suitable pre-quench states are as well only of approximative nature. *Per se*, this is not a problem as we seek to set off non-trivial dynamics. But, since we will use this initial states also for the numerical treatment which reaches beyond the linear regime, it is necessary to keep in mind the approximation.

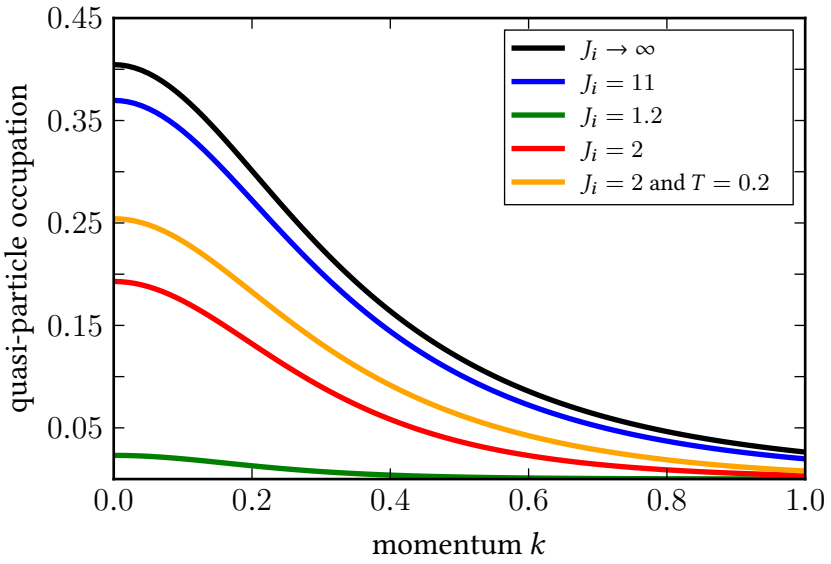

Figure III.2: The figure shows the post-quench quasi-particle occupation, ${}_i\langle\Omega|b_k^\dagger b_k|_{J_\mathrm{f}}|\Omega\rangle_i$, for several values of the initial linear coupling, J_i. All examples are computed for a quench to the final value $J_\mathrm{f} = 1.1\,(2J_\mathrm{c})$ of the linear coupling. The black, blue, green, and red curves correspond to a zero-temperature initial state while the orange curve is computed from initially Bose–Einstein distributed quasi-particles, at a temperature $T = 0.2\,(2J_\mathrm{c})$.

III.3 The Quest for Criticality

So far, we have computed the Bogoliubov solutions for the spin dynamics for various quench scenarios. In this section, we will analyse the structure of the obtained solutions in terms of critical behaviour. We adopt the temporary convention of "critical behaviour" equals "scaling laws" and, thus, we discuss in the following where scaling laws can be identified within the Bogoliubov time evolution of the z-spin correlation function.

As we are dealing with a theory of meanfield type, we do not start the search for scaling laws totally blank. As long as static critical exponents are concerned we can expect meanfield scaling to be valid. For the spin system, which shows the symmetries of the Ising universality class, one has the scaling of the correlation length $\xi = |\varepsilon|^{-\nu}$ and the scaling of the magnetic susceptibility $\chi = |\varepsilon|^{-\gamma}$. From the set of static scaling exponents, those two are most conveniently found from the correlation function. In addition, the hyperscaling relation, $(2-\eta)\nu = \gamma$, which connects the two exponents ν and γ is of interest. Within meanfield approximation, the three exponents are $\nu = 1/2$, $\gamma = 1$, and $\eta = 0$ (see Sect. II.2).

For the dynamic exponent, z, the reasoning is more involved. If viewed within the Halperin–Hohenberg classification [30], z defines the the scaling relation between time and space for relaxational dynamics and can be read of from the dispersion relation, $\omega \sim k^z$, at the critical point. If our model was purely of Ising class one would expect $z = 1$.

We discuss below in what sense that is true within the linear theory. One should also keep in mind that the spin sector is, beyond Bogoliubov theory, coupled to a conserved $U(1)$ field, which changes the dynamical class.

An additional level of complexity arises since we are not dealing with relaxational dynamics. We will study equal-time correlation functions as a function of the progressed time after the quench. However, z is, in the first place, connected to the time difference between the two correlated field operators. In this section, we clarify the role of the progressed post-quenched time in the scenario of criticality.

In this section, we analyse the equal-time z-spin correlation function $\mathcal{G}_{zz}(t_1 = t, t_2 = t, y)$ (see Eq. (III.27) and Eq. (III.30)) and its Fourier transform $\mathcal{G}_{zz}(t,k)$, *i. e.* the z-spin structure factor. As the goal is to identify scaling behaviour, we want to avoid a situation of a multi-scale initial state and, thus, concentrate on a zero-temperature pre-quench state with linear coupling $J_\mathrm{i} \to \infty$ (see Sect. III.2.3). From Eq. (III.31) we find, with $\lim_{J_\mathrm{i}\to\infty} f_k|_{J_\mathrm{i}} \to 1$, the initial conditions for that case

$$\begin{aligned} \langle \delta n_-(0)\delta n_-(y)\rangle|_{t=0} &= \frac{n_0}{2}\delta(y-y')\,, \\ \langle \delta\theta(0)\delta\theta(y)\rangle|_{t=0} &= \frac{1}{2n_0}\delta(y-y')\,, \end{aligned} \tag{III.37}$$

and consequently, using Eq. (III.30), the z-spin equal-time correlation function

$$\langle S_z(0)\, S_z(y)\rangle(t) = \frac{1}{L2n_0}\sum_k \left\{1 + \left[\frac{2J_\mathrm{c}}{\epsilon_k + 2J - 2J_\mathrm{c}}\right] \sin^2(\omega_-(k)\, t)\right\} \mathrm{e}^{\mathrm{i}\, ky}\,. \tag{III.38}$$

For the reminder of this chapter we substitute the post-quench coupling J_f with the distance of the meanfield critical coupling,

$$\varepsilon = (J_\mathrm{f} - J_\mathrm{c})/J_\mathrm{c}\,. \tag{III.39}$$

In addition, all dimensionful quantities, specifically time, space, momentum, and energy, will be expressed in appropriate units of the meanfield critical coupling[5], *cf.* Sect. B.1.

III.3.1 Scaling Regimes

For various reasons critical behaviour over all scales should not be expected. This is especially true for the Bogoliubov theory at hand, as the various expressions we encountered so far are square-roots of polynomials in ε and k. Thus, firstly we identify the relevant scaling regimes from the dispersion relation.

Expressed in natural units it reads

$$\omega_-(k,\varepsilon) = \sqrt{\Delta^2 + c_\mathrm{s}^2 k^2 + k^4}\,, \tag{III.40}$$

where the gap is $\Delta = \varepsilon(\varepsilon+1)$ and we introduced $c_\mathrm{s} = \sqrt{2\varepsilon+1}$. As can be directly

[5]For convenience, we define the natural unit system via $2J_\mathrm{c}$ to eliminate various factors of 2 in the expressions.

inferred, the dispersion is not a homogeneous function of momentum but rather shows three regimes in k: For $k \lesssim k_\mathrm{g} = \Delta/c_\mathrm{s}$, the spectrum is gapped and quadratic, $\omega_- \simeq \Delta + c_\mathrm{s}^2 k^2/(2\Delta)$. For $k_\mathrm{g}^2 \lesssim k^2 \lesssim c_\mathrm{s}^2$ it is linear, $\omega_- \simeq c_\mathrm{s} k$, and for $k^2 \gtrsim c_\mathrm{s}^2$ it is quadratic again, $\omega_- \simeq \Delta + k^2$. Note that the spectrum in the deep infrared always starts quadratic, unless the system is quenched directly to the critical point. Primarily, we are interested in the long range behaviour of the correlation functions. Therefore, we restrict the analysis to the momentum range $k \ll 1$ and neglect the term $\propto k^4$ in ω_-^2.

As can be seen from Eq. (III.40), the dispersion is not a homogeneous function of ε either. For the tuning parameter, two relevant regimes can be identified, $\varepsilon \gg 1$, such that $\omega_-^{(2)} = \sqrt{\varepsilon^2 + 2\epsilon k^2}$ and $\varepsilon \ll 1$, such that $\omega_-^{(1)} = \sqrt{\varepsilon + k^2}$. For the two approximative dispersion relations $\omega_-^{(1)}$ and $\omega_-^{(2)}$ scaling forms can be deduced. We find that

$$\omega_-^{(1)}(s\varepsilon, s^\nu k) = s^{1/2}\,\omega_-^{(1)}(\varepsilon, k)\ , \tag{III.41}$$

$$\omega_-^{(2)}(s\varepsilon, s^\nu k) = s^{1}\,\omega_-^{(2)}(\varepsilon, k)\ , \tag{III.42}$$

$$\tag{III.43}$$

if $\nu = 1/2$ is chosen for the rescaling of momenta and that only in this case the two functions $\omega^{(1,2)}$ are homogeneous in s.

The full scaling form of the dispersion relation, in presence of a energy scale, is expected to reflect the dynamical critical exponent. In particular, the scaling transformation $s^{-z\nu}\omega(s\varepsilon, s^\nu k)$ should leave the dispersion unchanged. Indeed, we find with Eq. (III.41) that $\omega_-^{(1)}$ is consistent with $z = 1$ and $\omega_-^{(2)}$ with $z = 2$. We point out that for the latter situation the reasoning is also valid if we include the quartic power of k in ω_-^2.

The consistency with a non-relativistic dynamical exponent away from the critical point is a remnant of the underlying non-relativistic bosonic field theory. The regime in which we find the 'relativistic' dynamical exponent, $z = 1$, *i. e.* for $\varepsilon \ll 1$ and $k \ll 1$, exhibits a peculiar dispersion relation equivalent to that of the transverse field Ising model[6]. For the Ising model, it is a well known fact that a relativistic dynamical behaviour emerges at the critical point, which is describable by a conformal field theory (see for example [128]). We discuss similarities of quench dynamics in the spinor Bose gas and the Ising chain in a transverse field in chapter VI

III.3.2 Scaling Properties of the Correlator

The central object of our studies is the equal-time correlation function of the spin in z-direction. Here, we discuss the properties of the specific realisation given in Eq. (III.38) in terms of scaling behaviour. As we have stated above, we have chosen an initial state corresponding to $J_\mathrm{i} \to \infty$ to eliminate the need to include a scale set by the initial state. By virtue of an emergent effective temperature this will nevertheless be an issue, as we discuss in Sect. III.4. But, for now, we adopt the point of view that $J_\mathrm{f} - J_\mathrm{c}$ is the only relevant energy scale.

[6] To be more precise, the dispersion relation $\omega = \sqrt{\Delta^2 + k^2}$ is found in the continuum limit of the transverse field Ising model see Sect. VI.1

We proceed as follows. First, we discuss the scaling behaviour and resulting critical exponents in the z-spin correlations, as they are reflected by the time evolution of the magnetic susceptibility and the structure factor $\mathcal{G}_{zz}(t,k)$. This can be done based on analytic expressions, as can be read off from the right-hand side of Eq. (III.38). Thereafter, we turn to scaling properties of the z-spin correlation function in real space $\mathcal{G}_{zz}(t,y)$ and of the corresponding correlation length. As the Fourier transform in Eq. (III.38) can not be evaluated in a closed form, we discuss an approximation for $\mathcal{G}_{zz}(t,y)$, obtained by the method of stationary phases. Scaling behaviour in the time evolution of the correlation length will be discussed based on a numerical evaluation of Eq. (III.38).

Scaling Properties of the Magnetic Susceptibility

We begin our analysis with the magnetic susceptibility, as it can be easily extracted from z-spin structure factor,

$$\chi(\varepsilon,t) = \langle S_z(-k)\, S_z(k)\rangle(t)|_{k=0} = \mathcal{G}_{zz}(t,k=0)\,, \tag{III.44}$$

Before going on, there is a technical issue to be discussed. The initial state given in Eq. (III.37) introduces an unregularised part to the correlation function, related to the quantum vacuum state of the quasi-particles (see Sect. III.2.3). On the left-hand side of Eq. (III.18) the additional '1/2' particle is a direct consequence of the imposed quantisation conditions for the Bogoliubov quasi-particles. In turn, it leads to an initial occupation of spin modes (*cf.* Eq. (III.37) at $t = 0$) which is constant over all modes. Consequently, the initial correlation function consists of a δ-distribution. As can be seen form Eq. (III.38), the δ-distribution is a persistent term. Although it will grow less important over time it makes the evaluation of Eq. (III.38) tedious. To overcome the problem, we define a regularised spin structure factor,

$$\langle S_z(0)\, S_z(y)\rangle(t)\rangle_{\text{reg}} = \langle S_z(0)\, S_z(y)\rangle(t) - 1/(2Ln_0)\,, \tag{III.45}$$

to study scaling features of all observables derived from the correlation function.

With Eq. (III.38) we find for the magnetic susceptibility

$$\chi(\varepsilon,t) = \frac{\sin^2(\Delta(\varepsilon)\,t)}{2Ln_0\,\varepsilon}\,, \tag{III.46}$$

after regularisation of the structure factor, *i. e.* applying Eq. (III.45) to Eq. (III.38). Since the sine-function by itself is not at all a homogeneous function, the susceptibility has no chance of being a homogeneous function of the tuning parameter at fixed time. Thus, a scaling transformation needs to include the time direction as well. Note that the time parameter here describes the time elapsed after the quench for both correlated operators in Eq. (III.38). We refer to it as 'central time' to distinguish it from the time difference within unequal-time correlation functions in the following.

Building on the discussion in the previous subsection, we can right away deduce the

scaling form of χ for the limiting cases $\varepsilon \ll 1$ and $\varepsilon \gg 1$,

$$\chi(s\varepsilon, s^{-\nu z}\, t) = s^{-1}\chi(\varepsilon, t)\,, \tag{III.47}$$

where a gap of either the form $\Delta^{(1)} = \varepsilon$ or $\Delta^{(2)} = \sqrt{\varepsilon}$ needs to be assumed. In both cases the scaling exponent $\gamma = 1$ can be identified if, as before, $\nu = 1/2$ and $z = 1$ or $z = 2$. Using the Fisher hyperscaling relation we find from $\gamma = (2 - \eta)\nu$, as expected for a meanfield theory, an anomalous dimension of $\eta = 0$.

Importantly, this discussion shows that the only way to achieve a consistent scaling transformation within Bogoliubov theory is to rescale the central time with the dynamical exponent z. This means that the post-quench time evolution reflects the dynamic universality class, for our quench setup.

Scaling Properties of the Structure Factor

At this point, we have already determined a full set of scaling exponents. The analysis of the scaling form of the dispersion ω_- (see Eq. (III.41)) yielded $\nu = 1/2$ and $z = 1$ ($\varepsilon \ll 1$) or $z = 2$ ($\varepsilon \gg 1$). These exponents lead to a consistent time-dependent scaling form for the magnetic susceptibility Eq. (III.47). Simultaneously, one obtains the third exponent $\eta = 0$.

The analysis of the z-spin structure factor for a full scaling form in t, ε and k,

$$\mathcal{G}_{zz,\,\mathrm{reg}}(s\varepsilon, s^{\nu}\, k, s^{-\nu z}\, t) = s^{-(2d-\eta)\nu}\mathcal{G}_{zz,\,\mathrm{reg}}(\varepsilon, k, t)\,, \tag{III.48}$$

now constitutes rather a consistency condition. The regularised structure factor reads (see Eq. (III.38) with Eq. (III.45))

$$\mathcal{G}_{zz,\,\mathrm{reg}}(t, k) = \frac{1}{2Ln_0(k^2 + \varepsilon)} \sin^2\left(\omega_-(k, \varepsilon)t\right)\,, \tag{III.49}$$

and, indeed, consistently fulfils the scaling form in Eq. (III.48) with the set of scaling exponents from above.

The important aspect to learn here is why it does so. As can be seen from Eq. (III.49), the structure factor is composed out of an oscillatory factor, carrying the time dependence, and an amplitude. The amplitude $\propto 1/(k^2 + \varepsilon)$ constitutes an independent static condition on the scaling exponents ν and η, enforcing in particular independently $\nu = 1/2$. Therefore, the full time-dependent scaling form in Eq. (III.48) is only fulfilled because the homogeneity in ε of the amplitude and the oscillation (the dispersion, specifically) fit to each other.

As a byproduct, one learns that already the amplitudes contain valuable information scaling properties, even if the full universal functions are hard to determine (for example from numerical or experimental data).

Furthermore, we find that the amplitudes are clean homogeneous functions of the tuning parameter ε. The restriction to $\varepsilon \gg> 1$ or $\varepsilon \ll 1$, to be able to apply the scaling forms, is only needed when the time dependence is to be included in the scaling transformation.

Correlation Function in Stationary Phase Approximation

Finally, we want to discuss the correlation length and the real-space correlation function. Although Bogoliubov theory allows deriving an expression for the z-spin correlation function (see Eq. (III.38)), it is not possible to evaluate it in closed form in real space (*i. e.* as function of y).

Nevertheless, approximations can be derived if the Fourier series is turned into an Fourier integral, $1/L\sum_k \to 1/(2\pi)\int \mathrm{d}k$ which is justified in the thermodynamic limit. A straight-forward way to solve the Fourier integral is to employ the method of stationary phases[7].

To apply the method, first, the squared sine function needs to be expressed in terms of exponential functions, $\sin^2(\omega t) = -\left(\mathrm{e}^{\mathrm{i}2\omega t} + e^{-\mathrm{i}2\omega t}\right)/4 + 1/2$. The constant part together with the amplitude of the squared sine function can be integrated right away, since the amplitude has the form of a unnormalised Cauchy-Lorentz distribution. From this one finds that the resulting correlation function is structurally of the form

$$\mathcal{G}_{zz}(t,y) \simeq \frac{1}{8n_0\sqrt{\varepsilon}}\mathrm{e}^{-\sqrt{\varepsilon}|y|} + \int_0^\infty \mathrm{d}k\, \frac{1}{2\pi}\left(\mathrm{e}^{\mathrm{i}2\omega t} + e^{-\mathrm{i}2\omega t}\right)\frac{\mathrm{e}^{\mathrm{i}\,ky}}{4}\,, \tag{III.50}$$

and it remains to approximate the oscillating part.

The strategy here is to combine the Fourier exponentials in with the remaining exponentials in the integrand of Eq. (III.50) and apply the stationary phase approximation. The structure of the integrand then is $\mathcal{F}(k)\mathrm{e}^{\mathrm{i}\Phi(t,k)}$, where the phase is given by

$$\Phi(k,t) = \pm 2\omega_-(k)t + ky\,. \tag{III.51}$$

The main contribution to the integral is generated by the saddle-points k_0, where the condition[8] $\partial_k\Phi(k,t)|_{k_0} = 0$ is fulfilled. Therefore, one can approximate $\mathcal{F}(k)$ by its value at the saddle point, $\mathcal{F}(k) \simeq \mathcal{F}(k_0)$ and $\Phi(k)$ with its second-order Taylor approximation around k_0 in the integral in Eq. (III.50).

Combining all ingredients and evaluating the remaining integral with Fresnel's formula yields

$$\mathcal{G}_{zz}(t,y) \simeq \frac{1}{8n_0\sqrt{\varepsilon}}\mathrm{e}^{-\sqrt{\varepsilon}\,|y|} - \frac{1}{4n_0}\mathcal{F}(k_0)\sqrt{\frac{1}{2\pi\partial_k^2\Phi(t,k_0)}}\cos\left(\Phi(k_0,t) - \frac{\pi}{4}\right), \tag{III.52}$$

where $\mathcal{F}(k) = 1/(k^2+\varepsilon)$, $\Phi(t,k) = 2\omega_- t + ky$, and $\partial_k^2\Phi(t,k)$ are to be evaluated at k_0, the momentum which renders the phase stationary. Since Φ is within this approximation respected up to second order only, it is reasonable to use a second-order approximation

[7] The credit for this idea goes to Isabelle Bouchoule (unpublished notes).

[8] If no real-valued solution exists the stationary phase approximation can not be employed.

also for ω_- to compute k_0. Here, we choose[9] $\omega_- \simeq \Delta + c_s^2 k^2/(2\Delta)$ and find with that

$$k_0 = -\frac{\Delta y}{2c_s^2 t}\,, \tag{III.53a}$$

$$\Phi(t,k_0) = 2\Delta t + \frac{\Delta y^2}{4c_s^2 t}\,, \tag{III.53b}$$

$$\partial_k^2 \Phi(t,k_0) = \frac{2c_s^2 t}{\Delta}\,, \tag{III.53c}$$

$$\mathcal{F}(k_0) = \frac{4c_s^4 t^2}{\Delta^2 y^2 + 4\varepsilon c_s^4 t^2}\,. \tag{III.53d}$$

Recall that $\Delta = \sqrt{\varepsilon(\varepsilon+1)}$ and $c_s = \sqrt{2\varepsilon+1}$, contributing the ε-dependence in the set of expressions Eq. (III.53).

In Fig. III.3 a comparison between the numerical evaluation of Eq. (III.38) and the direct evaluation of its approximation, Eq. (III.52), is shown. The oscillatory features are in general captured well by the approximation if $\varepsilon > 1$, since this is the regime where the small-k quadratic behaviour dominates the dispersion. Independently of ε, the logic of the stationary phase approximation is better applicable the larger y is as compared to $c_s t$. Fig. III.3 confirms that, even when the spatial oscillations are not reproduced well any more for $\varepsilon < 1$, the long-range decay of correlations is still reflected accurately by the approximation Eq. (III.52).

Combining the respective expression from Eq. (III.53) to form the amplitude $A(t,y,\varepsilon)$ in front of the cosine in Eq. (III.52) leads to

$$A(t,y,\varepsilon) = \frac{1}{4n_0}\mathcal{F}(k_0)\sqrt{\frac{1}{2\pi\partial_k^2\Phi(t,k_0)}} = \frac{1}{n_0}\frac{c_s^4 t^2}{\Delta^2 y^2 + 4\varepsilon c_s^4 t^2}\sqrt{\frac{\Delta}{2\pi c_s^2 t}}\,, \tag{III.54}$$

The amplitude decays in space algebraically, $A(t,y,\varepsilon) \sim y^{-2}$ if $y \gg c_s t$ and therefore constitutes no clear second characteristic scale for the spatial decay. Nevertheless, as long as the magnitude of $A(t,y,\varepsilon)$ is comparable in size to $1/\sqrt{\varepsilon}$, the oscillatory part in Eq. (III.52) will effectively contribute to the decay scale.

Concerning its time dependence, the amplitude of the oscillatory term in Eq. (III.52) is found to be proportional to $1/\sqrt{t}$ for $c_s t \gg y$ and, thus, suggests that the oscillations are suppressed algebraically in time. This is a consequence of dephasing quasi-particle modes and leads to a quasi-stationary spin correlator for $t \to \infty$, despite the fact that the quasi-particle mode occupation never changes in time. Note that the stationary phase approximation might over estimate the effect as the approximation itself relies on the dephasing of modes. But even if not, the suppression of the amplitude only with the square root of time makes the effect problematic to find on relevant time scales in experiment or simulations.

[9] Another possible choice would be $\omega_- = \Delta + c_s k + k^2$, which shifts the regime of validity of the approximation. In particular, the result can only be evaluated within a pseudo-lightcone, $c_s t > y$.

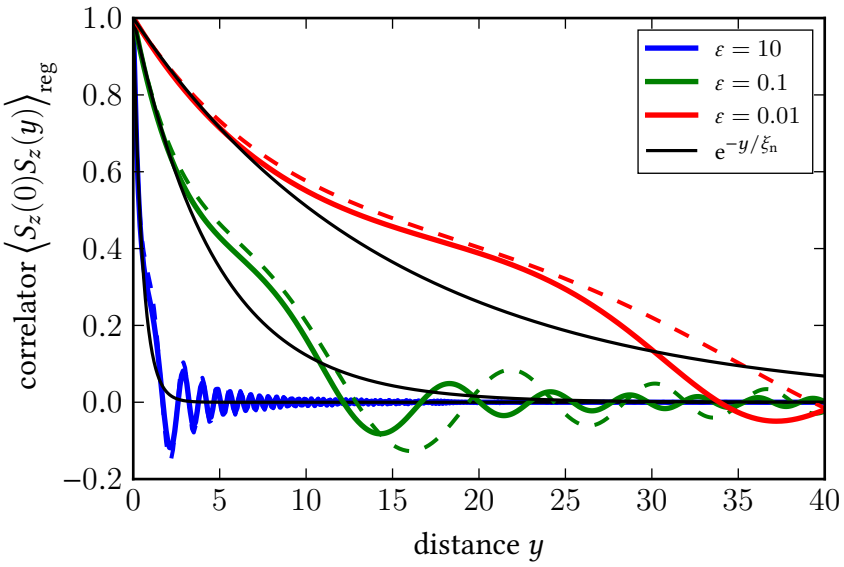

Figure III.3: The figure shows a comparison between the numerical evaluation (solid coloured lines) of the spin correlation function, Eq. (III.38), and the direct evaluation of its approximation (dashed coloured lines), Eq. (III.52), at various distances to the critical point. The correlators have been normalised such that $\langle S_z(0)\, S_z(y)\rangle_{\text{reg}}|_{y=0} = 1$. In addition, the decay length ξ_n has been determined from the integral over the numerically evaluated correlators. The result is depicted via the corresponding exponential decays, $e^{-|y|/\xi_n}$, (black solid lines).

Scaling Properties of the Correlation Length

The approximate expression for the spin correlation function we determined in Eq. (III.52) consists of a time independent exponential decay and a temporally and spatially oscillating algebraic decay. To determine an expression for the time-dependent correlation length from that is ambiguous, as the algebraic part has no proper scale.

The exponential part alone reflects a correlation length of $\xi = \varepsilon^{-1/2}$ which follows the expected scaling law but makes no statement about the time dependence. Thus, we follow the approach outlined in Sect. II.5.2 and compute the correlation length via the integral over the normalised correlation function. As the zero mode of the spin spectrum already gives the integral over the unnormalised correlation function, we are left with computing the norm, *i.e.* to evaluate Eq. (III.38) at $y = 0$. We find that the numerical result for the time dependent correlation function is described to a good degree by the square root of the susceptibility,

$$\xi(t,\varepsilon) = \frac{|\sin(\Delta t)|}{\sqrt{\varepsilon}}\,. \tag{III.55}$$

Consequently, similar to the magnetic susceptibility, we expect a scaling form $\xi(s^{\nu z}t, s\varepsilon) = s^{-1/2}\xi$ to be valid in the regimes $\varepsilon \ll 1$ and $\varepsilon \gg 1$ which allows to independently determine $\nu = 1/2$. In panel a of Fig. III.4 we show that for $\varepsilon \lesssim 0.1$ the numerically determined

correlation lengths as a function of time can be indeed collapsed to a single universal curve, which follows the described sinusoidal form of Eq. (III.55).

Again, it is the amplitude of the sinusoidal oscillations which carries information about the exponent ν . In panel b of Fig. III.4 we show independently the scaling of the amplitude in several subsequent periods of the oscillations. The figure confirms that the amplitude follows a scaling law

$$\xi(\tau_i) \sim \varepsilon^{-1/2}\,, \tag{III.56}$$

for $\varepsilon \lesssim 0.1$, with $\tau_i = (i + 1/2)\pi/\Delta$.

The figure also shows that the definition for the correlation length we employed produces a slight growth of the amplitude in time for early times which saturates for quickly for longer times. Within Bogoliubov theory, this is most likely an artefact of our definition of the correlation length and the numerical evaluation of Eq. (III.38) as the underlying quasi-particle occupation does not change.

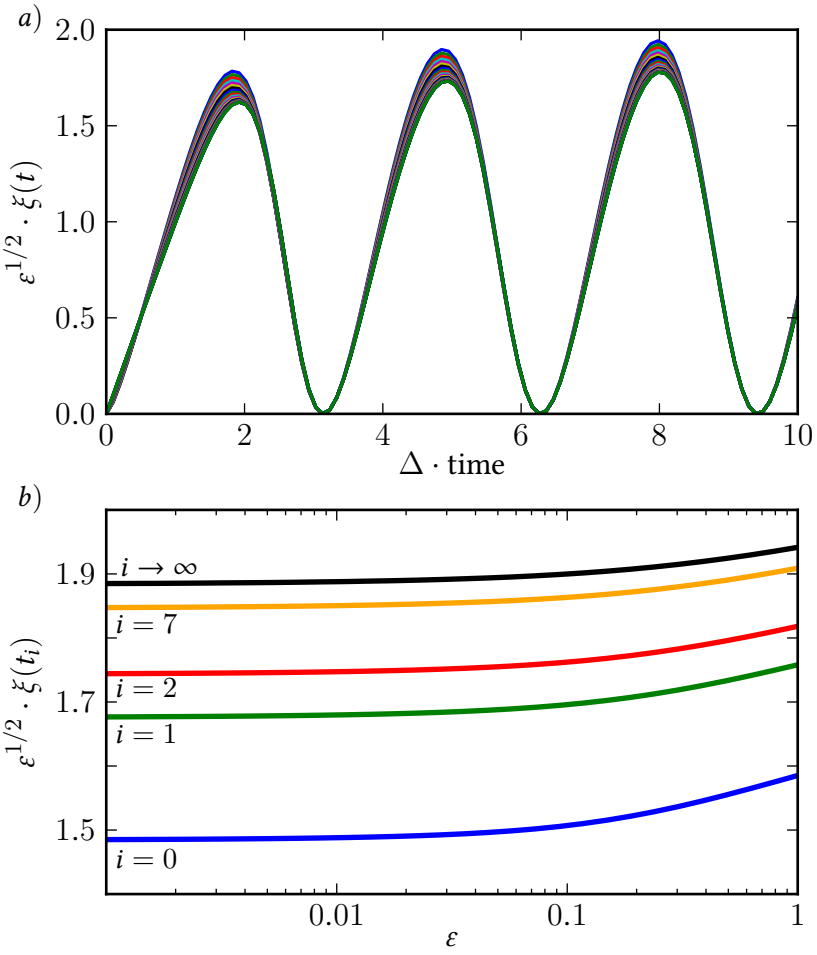

Figure III.4: The figure demonstrates the (partial) scaling collapse of the correlation length as a function of time and ε, for the whole temporal dependence (panel a), and at several characteristic times (panel b). In panel a, correlation lengths as a function of time are depicted for various ε, rescaled according to the scaling transformation $\xi \to \varepsilon^{1/2}\xi$ and $t \to \Delta t$ (which captures both scaling regimes simultaneously). The curves are evaluated for 30 logarithmic-equidistant ε between 1 and 0.001. The figure shows that the scaling transformation collapses the curves to one universal curve once $\varepsilon \lesssim 0.1$. In panel b, the correlation length is evaluated at $\tau_i = \pi/\Delta(i + 1/2)$ for each ε, which corresponds to the maxima of the correlation length in time. The figure verifies via rescaling that the correlation lengths behaves like $\xi \sim \varepsilon^{-1/2}$ for $\varepsilon < 1$ with a time dependent pre-factor.

III.4 Generalised Gibbs Ensemble and Effective Temperature

Its has been subject to extensive theoretical research if and how isolated quantum systems reach a stationary state, preferentially a state which is describable by a Gibbs or a generalised Gibbs ensemble [12]. If the latter can be proven for a system, it tremendously simplifies the task of studying universal or critical properties of the stationary state, as the theory of statistical ensembles is well understood. The question has drawn especially high attention for so-called integrable quantum systems. Those posses a infinite number of conserved local charges which heavily constrain the time evolution.

It has been put forward, first in [11], that integrable quantum systems do reach a generalised Gibbs state when subject to a sudden parameter quench, which can be *ab initio* predicted from local charges in the initial state. Subsequently, this has been demonstrated for various examples and the relaxation mechanisms have been extensively studied, primarily for 1D spin chains [4, 32, 90, 91, 179–182]. For a system similar[10] to ours, it has been shown recently in experiment [72] that a generalised Gibbs ensemble describes the post-quench stationary state which the system evolves to after a quench. It was furthermore reported, that it was sufficient to take only a small number of conserved charges into account to form the generalised ensemble.

In this section, we first introduce the concept of generalised Gibbs ensembles more detailed for the linearised spin system (described by the action $\mathcal{S}_-$ Eq. (III.3b)). In the context of quench dynamics (see Sect. III.2), we have shown that the post-quench distribution of Bogoliubov quasi-particles is conserved under the subsequent time evolution, (see Sect. III.2.1). In this section we discuss implications of that fact and how this leads naturally to a generalised Gibbs ensemble.

To formulate the statement more precise, one finds that every Bogoliubov mode on its own constitutes a conserved charge via $\partial_t \langle b_k^\dagger b_k |_{J_\mathrm{f}} \rangle_\mathrm{i} = 0$ for all k . We point out that these charges are not local but it can be argued that momentum modes for a non-interacting[11] integrable system are completely equivalent to the set of local charges [90]. Since our system evolves under the constraint of an infinite number of conserved charges it is integrable within Bogoliubov theory. Consequently, the spin system is a prime candidate for the application of the theory of generalised Gibbs ensembles.

We will furthermore demonstrate that the form of the quench protocol (see Sect. III.2.3), we apply, generates an ensemble which mimics the simple thermal Gibbs ensemble at a characteristic effective temperature. We derive the dependence of this effective temperature on the initial ($J = J_\mathrm{i}$) and finial ($J = J_\mathrm{f} < J_\mathrm{i}$) linear coupling, starting the quench in the Bogoliubov groundstate at J_i. As a main result here, we find that the effective temperature is set by the initial gap, $T_\mathrm{eff} = \Delta_\mathrm{i}/(4J_\mathrm{i})$ for strong quenches $J_\mathrm{f} \ll J_\mathrm{i}$ close to the critical point $J_\mathrm{f} \simeq 0$. For weak quenches, $J_\mathrm{f} \simeq J_\mathrm{f}$, the energy difference between final and initial gap sets the effective temperature, $T_\mathrm{eff} = (\Delta_\mathrm{i} - \Delta_\mathrm{f})/2$.

[10] In [72] the authors study quenches in a two-component Bose gas in $1d$, but with $g_{\uparrow\downarrow} = 0$ and for a decoupling quench, $J \neq 0 \to J = 0$

[11] There is a subtlety for integrable systems which are not mappable to non-interacting systems. To construct a the generalised Gibbs ensemble there it is necessary to include more than just local charges [182]

III.4.1 Generalised Gibbs Ensemble for the Spin System

We start by analysing the post-quench Bogoliubov particle distribution for the initial condition Eq. (III.37), we used in the last section,

$$n_{\mathrm{B}}\left(k, J_{\mathrm{f}}\right) = {}_{\mathrm{i}}\langle\Omega|b_k^{\dagger\,\mathrm{f}} b_k^{\mathrm{f}}|\Omega\rangle_{\mathrm{i}} = \frac{1}{4}\left(\sqrt{\frac{k^2+\varepsilon_{\mathrm{f}}+1}{k^2+\varepsilon_{\mathrm{f}}}} + \sqrt{\frac{k^2+\varepsilon_{\mathrm{f}}}{k^2+\varepsilon_{\mathrm{f}}+1}}\right) - \frac{1}{2}\,. \tag{III.57}$$

Recall, that this post-quench occupation was obtained by placing the spin system initially in the Bogoliubov groundstate of S_- at $J_{\mathrm{i}} \to \infty$. As in the last section, we use the natural unit system, defined by the energy scale $2J_{\mathrm{c}}$ (see Sect. B.1). In particular, $\varepsilon_{\mathrm{f,i}} = (J_{\mathrm{f,i}} - J_{\mathrm{c}})/J_{\mathrm{c}}$.

If every mode occupation is to be considered for the description of the system in terms of a generalised Gibbs ensemble every, every value $n_{\mathrm{B}}(k)$ requires a temperature, $T(k)$, to serve as a Lagrange multiplier. The generalised partition function for our bosonic Bogoliubov theory reads

$$Z_{\mathrm{GGE}} = \prod_k \frac{1}{1-\mathrm{e}^{-\lambda_k}}\,, \tag{III.58}$$

where the factors λ_k are to be chosen such that the ensemble produces the desired occupation,

$$n_{\mathrm{B}}(k) = -Z_{\mathrm{GGE}}^{-1}\partial_{\lambda_k} Z_{\mathrm{GGE}} \tag{III.59}$$

In turn, by comparison with an ordinary Gibbs ensemble the factors λ_k can be identified with a mode-dependent temperature,

$$\lambda_k = \omega_-(k)/T(k)\,. \tag{III.60}$$

This can be seen in analogy to a constant temperature $T(k) = \text{const}$ which would produce a ordinary Gibbs ensemble. Combining both ingredients, one finds for the mode temperatures

$$T(k) = \frac{\omega_-(k)}{\log\left(1 + n_{\mathrm{B}}^{-1}(k)\right)}\,. \tag{III.61}$$

It remains to calculate the spin two-point correlation functions which emerge from the ensemble Eq. (III.58). Note that, for our non-interacting Bogoliubov approximation, it is sufficient to study one- and two-point functions as there are no higher-order cumulants. But, in principle, the ansatz Eq. (III.58) for the ensemble would allow to deduce all correlation functions also in the interacting case, if one can solve for the mode temperatures.

With the expressions from the previous sections, we have already the means to deduce the two-point correlators. Take Eq. (III.18) at $J = J_{\mathrm{f}}$ and insert the ansatz

$$\begin{aligned}
\langle\delta n_-(0)\delta n_-(y)\rangle|_{\mathrm{GGE}} &= \frac{1}{L}\sum_k e^{\mathrm{i}\,k(y-y')}\left(2F_{\mathrm{GGE}}+1\right) f_k^2|_{J_{\mathrm{f}}}\frac{n_0}{2}\,,\\
\langle\delta\theta(0)\delta\theta(y)\rangle|_{\mathrm{GGE}} &= \frac{1}{L}\sum_k e^{\mathrm{i}\,k(y-y')}\left(2F_{\mathrm{GGE}}+1\right)\frac{1}{2n_0 f_k^2|_{J_{\mathrm{f}}}}\,,
\end{aligned} \tag{III.62}$$

where F_{GGE} can be any Bogoliubov occupation spectrum. One obtains ${}_{\mathrm{i}}\langle\Omega|b_k^{\dagger\,\mathrm{f}} b_k^{\mathrm{f}}|\Omega\rangle_{\mathrm{i}} = F_{\mathrm{GGE}}$. Turning the argument around, if one sets the Bogoliubov mode occupation numbers to $n_{\mathrm{B}}(k) = F_{\mathrm{GGE}}$ the corresponding spin correlation functions are given by Eq. (III.62).

Formally, F_{GGE} can be written in terms of a Bose–Einstein distribution, where the constant temperature is to be replaced by the mode temperatures $T(k)$ from Eq. (III.61), $F_{\mathrm{GGE}} = F_{\mathrm{BE}}(\omega_-(k, J_{\mathrm{f}}), T(k))$. In practice, we need just to set $F_{\mathrm{GGE}} = n_{\mathrm{i}}$ with n_{i} given in Eq. (III.57).

Before analysing the structure of the mode temperatures and, therewith, the structure of the generalised Gibbs state compared to an ordinary thermal Gibbs state, we provide a qualitative overview of what to expect. When looking at the dynamic spin structure factor $\mathcal{G}_{zz}(t,k)$, *i. e.* the expression within the curly brackets in Eq. (III.38) (or the regularised version Eq. (III.49)), it is obvious that the spectrum shows no sign of decay towards a stationary state. This is expected, as there is no scattering between modes which could provide a relaxation mechanism. On the other hand, it is believed that only observables which are local in position space should relax to a Gibbs state [15].

The stationary-phase approximation we found with expression Eq. (III.52) for the two-point correlation function in fact supports a stationary state since the oscillatory part decays in time. The decay mechanism for the local observable in the non-interacting theory is solely provided by dephasing of momentum modes, which justified the application of the stationary phase approximation in the first place. As a consequence, the correlator has no mathematically well-defined limit for $t \to \infty$ and the amplitude of the oscillatory part in Eq. (III.52) decays algebraically slow, with $\langle S_z(0) S_z(y)\rangle \simeq \mathrm{const} - A\cos(\Phi - \pi/4)/\sqrt{t}$.

However, a time average at late times yields a stationary state where the correlator is of the form

$$\langle S_z(0) S_z(y)\rangle_{t\to\infty} \sim \frac{\mathrm{e}^{-\sqrt{\varepsilon_{\mathrm{f}}}|y|}}{\sqrt{\varepsilon_{\mathrm{f}}}}\,. \tag{III.63}$$

In particular, the correlation length depends only on ε_{f}, via the meanfield scaling law. The evaluation of the full generalised Gibbs prediction for the corresponding correlator, starting from the occupation Eq. (III.57), has to be done numerically.

Anticipating the result of the next section, one can nevertheless provide qualitative arguments for the spin correlation functions in the generalised Gibbs state (Eq. (III.62)). We assume that the mode temperatures depend only weakly on momentum, such that they are effectively constant in the infrared region. Furthermore, for a sufficiently small ε_{f} the gap is sufficiently small to satisfy $\Delta/T \ll 1$ for any finite temperature. Thus, the Rayleigh–Jeans limit for the Bose–Einstein distribution will lead to a good estimate.

Combining this with Eq. (III.38) results, after regularisation, in a spin occupation of the form $\langle S_z(-k) S_z(k)\rangle \sim T/(k^2 + \varepsilon_{\mathrm{f}})$ which leads again to a spin correlation function of the form Eq. (III.63),

$$\langle S_z(0) S_z(y)\rangle \sim \frac{T\mathrm{e}^{-\sqrt{\varepsilon_{\mathrm{f}}}|y|}}{\sqrt{\varepsilon_{\mathrm{f}}}}\,. \tag{III.64}$$

except that the pre-factor is now temperature dependent. However, the dependence on the spatial separation $|y|$ and, in particular, the correlation length itself matches with the stationary limit from Eq. (III.63). In the next section, we show that the mode temperatures have a universal (ε_{f} independent) asymptotic limit for strong quenches. In this case, the

spin correlation function $\mathcal{G}_{zz}(t,y)$, as derived from the generalised Gibbs ensemble would fully match the stationary limit from Eq. (III.63) (provided that there is only one effective temperature relevant).

In summary, within the approximations which can be calculated analytically, we find that $\langle S_z(0)S_z(y)\rangle_{t\to\infty} = \langle S_z(0)S_z(y)\rangle_{\mathrm{GGE}}$ if the normed correlation function is considered. In particular this means for the correlation length that $\xi_{\mathrm{GGE}} \simeq \xi_{t\to\infty} = \varepsilon_{\mathrm{f}}^{-1/2}$. In the non-interacting theory, however, a truly stationary state is only approached in an algebraically slow manner. The stationary state contains, as expected, the meanfield scaling law of the underlying phase transition for the correlation length, which is not altered by a finite, possibly effective, temperature.

III.4.2 Effective Temperature

Even if the mode temperatures have no influence on the scaling laws or the criticality of the phase transition in the non-interacting spin system, they will play a crucial role when non-linearities are turned on. Thus, it is instructive to analyse the structure of mode temperatures which our quench protocol generates. We evaluate Eq. (III.61) for $T(k)$ for a quench where $J^{\mathrm{i}} = \infty$ (*i. e.* with $n_{\mathrm{i}}(k)$ from Eq. (III.57)) and J^{f} is close to the critical value.

Once again resorting to the Rayleigh–Jeans limit, *i. e.* expanding the logarithm for $n_{\mathrm{i}} \gg 1$, yields $T(k) = \omega_-(k)n_{\mathrm{i}}(k)$. With Eq. (III.57) one finds the mode temperatures for our setup,

$$T(k,\varepsilon_{\mathrm{f}}) = \frac{1}{2}\left(k^2 + \varepsilon_{\mathrm{f}} - \omega_-(k,\varepsilon_{\mathrm{f}} + \frac{1}{2})\right) . \tag{III.65}$$

As we have discussed in Sect. III.3.1, as long as the quench does not hit the critical point, *i. e.* as long as there remains a finite gap in the spectrum, the dispersion is quadratic in k for $k \ll 1$. The mode temperature Eq. (III.65) inherits this feature. In particular, expanding $T(k,\varepsilon_{\mathrm{f}})$ to quadratic order in k results in

$$T(k,\varepsilon_{\mathrm{f}}) \simeq \frac{1}{2}\left(1 - \frac{c_{\mathrm{s}}^2(\varepsilon_{\mathrm{f}})}{2\Delta(\varepsilon_{\mathrm{f}})}\right)\left(k^2 - \Delta(\varepsilon_{\mathrm{f}})\right) , \tag{III.66}$$

where $\Delta(\varepsilon) = \sqrt{\varepsilon(\varepsilon+1)}$ and $c_{\mathrm{s}} = \sqrt{2\varepsilon+1}$.

Consequently, for an infrared region which is determined by the gap via $k \lesssim \sqrt{\Delta}$ the mode temperatures can be considered constant. As the post-quench occupation number of quasi-particles drops fast to zero for $k > 1$, *cf.* Fig. III.2, the spin dynamics is mainly determined by those infrared modes and, thus, by the constant infrared mode temperature.

Moreover, the gap scales as $\Delta \sim \sqrt{\varepsilon}$ for small ε. As a consequence, even for small ε, *i. e.* strong quenches, the infrared momentum region $k < \sqrt{\Delta}$ depends only weakly on ε, such that the quasi-particle occupation there is to a good degree described by one effective temperature,

$$T_{\mathrm{eff}}(\varepsilon_{\mathrm{f}}) = \frac{1}{2}\left(\varepsilon_{\mathrm{f}} - \sqrt{\varepsilon_{\mathrm{f}}(\varepsilon_{\mathrm{f}}+1)} + 1/2\right) . \tag{III.67}$$

Examples for the mode temperature functions at different distances to the critical point,

in comparison to the the respective post-quench quasi-particle occupation are shown in Fig. III.5 (upper panel). This result implies that the generalised Gibbs state the system evolves to is, in fact, very close to a ordinary thermal Gibbs state at an effective temperature, given byEq. (III.67), set by the quench. We emphasise that this is not equivalent to a system which relaxes to a thermal state. What actually happens is that 'by chance' the non-equilibrium stationary states disguises as thermal state, when local observables are considered. This seems to be a rather generic outcome for strong bulk quenches in integrable systems and has also been reported in, *e. g.* [32, 183]. From the point of view of the magnetic susceptibility in Bogoliubov theory, for example, our system looks never thermal, except for isolated points in time, and certainly never reaches a stationary value.

The mode temperatures, $T(k)$, one finds from the generalised Gibbs approach constitute a quantitative characterisation of the scales inherent in the chosen pre-quench state. For an integrable theory, there are infinitely many of those scales which furthermore do not loose their relevance due to conservation. To obtain universal behaviour for, at least some, observables within the generalised Gibbs scenario, most of the conserved quantities need to be irrelevant or dominated by a few.

Beyond Bogoliubov theory the spin system profits form being not integrable. Our discussion of the Bogoliubov mode temperatures shows how the notion of universality can be realised even within the linearised time evolution. The presence of a finite gap leads to a plateau in the occupation numbers for the modes within the gap region ($k \lesssim \sqrt{\Delta}$). Outside the gap region, the occupation numbers are too small to constitute relevant scales although being conserved. Hence, the infrared limit of the mode temperatures, $T_{\text{eff}} = \lim_{k\to 0} T(k)$, remains as a scale to characterise the initial state. As this scale mimics an ordinary finite temperature, the scaling hypothesis remains valid if the effective temperature is included in the scaling forms. In particular, one finds from Eq. (III.67) that the effective temperature scales as $T_{\text{eff}} \sim \varepsilon_{\text{f}}^{-1}$ for large distances to the critical point and asymptotically reaches the universal constant $T_{\text{eff}} = 1/4$ for $\varepsilon_{\text{f}} \ll 1/4$ (and $J_{\text{i}} \to \infty$), *cf.* also Fig. III.5 (lower panel).

Before discussing how the effective temperature generalises to the case of arbitrary strong quenches, we pause a moment to analyse its origin further. As the phenomenon is intimately linked to the generation of quasi-particles, it needs to be clarified, first, how the quench produces quasi-particles at all and, second, why the resulting mode temperatures are approximately constant in the infrared.

For that reason, we start by introducing an alternative interpretation for the initial state. If the initial state Eq. (III.37) is inserted into Eq. (III.19) one finds that it represents a Bogoliubov vacuum state for $J/J_{\text{c}} \to \infty$. We have previously taken the point of view that the state Bogoliubov groundstate $|\Omega\rangle_{\text{i}}$, which corresponds to Eq. (III.37), is a groundstate at infinitely strong linear coupling. Actually, it is completely equivalent to view it as a Bogoliubov vacuum state for any finite linear coupling if $J_{\text{c}} = 0$.

To go on, we compare the energy spectrum of the Bogoliubov quasi-particles

$$\mathcal{E}(k) = \omega_{-}(k,\varepsilon)\left(\left\langle b_k^{\dagger} b_k \right\rangle + \frac{1}{2}\right) , \tag{III.68}$$

before and after the quench. The pre-quench state is a vacuum of the pre-quench quasi-particle operators, such that one finds for the initial energy spectrum $\mathcal{E}_\mathrm{i} = \omega_\mathrm{i}(k)/2 = \omega_-(k)|_{J_\mathrm{c}=0}/2$, to be constituted by the pre-quench vacuum energy. To get a finite energy spectrum for the pre-quench state, assume now $J_\mathrm{c} = 0$ and $J = J_\mathrm{f}$, to get $\mathcal{E}_\mathrm{i} = \epsilon_k/2 + J_\mathrm{f}$. This is equivalent to $J_\mathrm{i} \to \infty$ at finite J_c.

The quench, in this picture, is described now of setting J_c to a finite value at fixed $J = J_\mathrm{f}$. One finds for the spectrum of total energy after the quench, (including the post-quench vacuum energy) with Eq. (III.68), inserting $\omega_\mathrm{f}(k) = \omega_-(k, J_\mathrm{f})$ and $n_\mathrm{B}(k)$ from Eq. (III.57),

$$\mathcal{E}_\mathrm{f}(k) = \frac{1}{2}(\epsilon_k + J) - \frac{J_\mathrm{c}}{2} = \mathcal{E}_\mathrm{i} - \frac{J_\mathrm{c}}{2}\,. \tag{III.69}$$

This shows that the post-quench energy spectrum is shifted down by a momentum independent energy, $\mathcal{E}_\mathrm{f} = \mathcal{E}_\mathrm{i} - J_\mathrm{c}/2$. The quench, therefore, drains the pre-quench Bogoliubov vacuum energy, *cf.* Fig. III.6.

The total post-quench energy spectrum, contains also a contribution from vacuum energy. If there is a finite excess energy between $\mathcal{E}_\mathrm{f}(k)$ and the post-quench vacuum energy for a mode k, the excess energy is converted to quasi-particles for this mode. Associating this excess energy with a temperature $T(k) = \mathcal{E}_\mathrm{f} - \omega_-(k, J_\mathrm{f})/2$, yields together with Eq. (III.69)

$$T(k, \varepsilon_\mathrm{f}) = \mathcal{E}_\mathrm{f} - \frac{\omega_-(k, J_\mathrm{f})}{2} = \frac{\omega_-(k)|_{J_\mathrm{c}=0} - \omega_-(k, J_\mathrm{f})}{2} - \frac{J_\mathrm{c}}{2}\,. \tag{III.70}$$

The resulting expression is equal to $T(k, \varepsilon_\mathrm{f})$ from Eq. (III.65). The form of $T(k, \varepsilon_\mathrm{f})$ from Eq. (III.70) shows that the difference between pre- and post-quench quasi-particle dispersion is important for the mode dependence.

Energetically, quasi-particle creation is possible because the quench-induced energy loss is a universal, mode-independent constant, which can be seen as follows. Creation of quasi-particles happens where $T(k, \varepsilon_\mathrm{f}) > 0$ in Eq. (III.70). The pre-quench dispersion combines with the constant energy loss $-J_\mathrm{c}/2$ to the fixed infrared limit $J_\mathrm{f} - J_\mathrm{c}/2$ in Eq. (III.70) as $k \to 0$. The post-quench dispersion can be made arbitrarily small by the quench in the infrared region $k \to 0$. Therefore, there is always a region of momenta with $T(k, \varepsilon_\mathrm{f}) > 0$ (see Fig. III.6). The maximal possible effective temperature $T_\mathrm{eff} = J_\mathrm{c}/2$ also originates in this.

The second important ingredient is that the post-quench dispersion $\omega_-(k, J_\mathrm{f})$ is not only shifted down but also changed in shape, as compared to $\omega_-(k)|_{J_\mathrm{c}=0}$. Otherwise, the total post-quench energy is always devoured by the post-quench vacuum energy, leaving no space for quasi-particle excitations, as we explain as follows The initial dispersion goes together with unsqueezed Bogoliubov modes, *i. e.* the mode function is identically one, $f_k \equiv 1$. If the dispersion were just lowered by the quench, the mode function would not change and, consequently, the nature of the modes would not change. As the initial state is a vacuum state the final state would be also a vacuum state in this hypothetical situation. It is only the quench induced squeezing of the infrared modes (*i. e.* for $k < \sqrt{4mJ_\mathrm{c}}$) which allows for a finite excess energy in the infrared part of the energy spectrum. From the picture of dispersion relations, this means that the $\sim k^2$ particle-part of the dispersion is not changed by the quench while the set-in of the $\sim k$ quasi-particle part is shifted, see

the green solid line in Fig. III.6 in comparison to the black solid line.

Finally, it remains to be explained why the mode temperatures are constant in the infrared. This is simply a consequence of the finite gap which extends up to the momentum scale $k = \sqrt{4mJ_c}$ in the initial dispersion and remains finite in the post-quench dispersion. As the form of the mode temperature function is determined by the difference between the two, see Eq. (III.70), this is enough to ensure a infrared plateau in the mode temperature function together with a finite infrared limit. The weak dependence of the plateau on the final gap is caused by the squeezing and is, as we have argued, unavoidable for the phenomenon of quasi-particle generation out of a vacuum state.

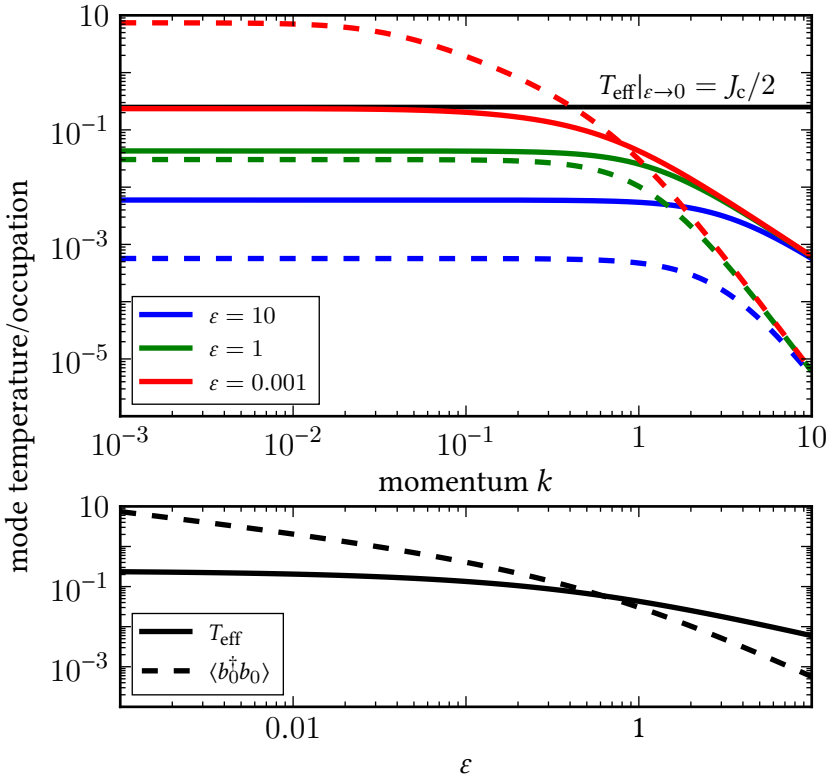

Figure III.5: The figure shows the generalised Gibbs mode temperatures (solid lines, in units of $2J_c$) and the post-quench occupation of Bogoliubov modes (dashed lines). The upper panel depicts the mode temperature $T(k, \varepsilon_f)$ (Eq. (III.65)) and the post-quench occupation of quasi-particles $\langle k^f b_k^f \rangle$ as a function of momentum at $\varepsilon = \{10, 1, 0.001\}$, concentrating on the infrared part of the spectrum, $k < \sqrt{4mJ_c}$. Note that the mode temperatures are to a good degree of approximation constant in this region and decay quadratically for higher momenta. The scale where quadratic behaviour sets in scales weakly with the distance to the critical point (see main text). The lower panel depicts the respective infrared limits as a function of distance to the critical point. The effective temperature reaches asymptotically the value $T_{\mathrm{eff}} = J_c/2$

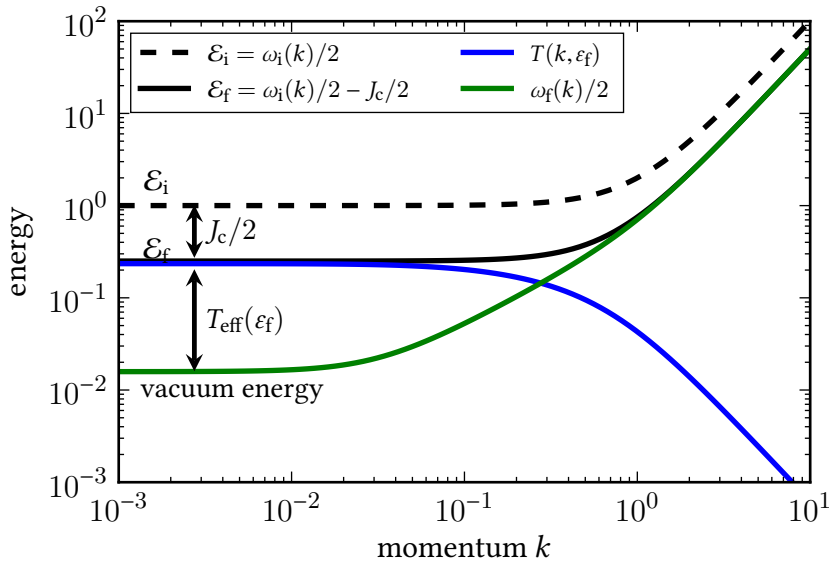

Figure III.6: The figure illustrates the energetic configuration before and after the quench at the example of a quench to $\varepsilon = 0.001$, which leads to a thermal post-quench quasi-particle occupation. The infrared parts of the pre-quench energy spectrum (dashed black line), $\mathcal{E}_\mathrm{i}$, which is identical to the pre-quench vacuum energy spectrum, the post-quench energy spectrum (solid black line), $\mathcal{E}_\mathrm{i}$, the post-quench vacuum energy spectrum (solid green line), and, finally, the resulting mode temperatures (solid blue line). Details are discussed in the main text.

III.4.3 Tuning the Effective Temperature

For the discussion of scaling laws we have deliberately chosen $J_\mathrm{i} \to \infty$. Following the previous reasoning, this ties the effective temperature solely to the post-quench distance from the critical point. On the other hand, in this way the effective temperature unavoidably changes with ε_f such that observables, as a function of ε_f, can not be studied at a fixed effective temperature and compared to finite-temperature results. In this section, we extend concept of the effective temperature to the case of a finite pre-quench coupling J_i. In this way, one obtains a knob to tune the temperature, to vary it at a fixed post-quench distance to the critical point.

In Sect. III.2.3 we have discussed initial states $|\Omega\rangle_\mathrm{i}$ which are a Bogoliubov ground-state for the action S_- at finite pre-quench linear coupling, $J = J_\mathrm{i} < \infty$. The initial spin correlation functions, corresponding to $|\Omega\rangle_\mathrm{i}$, are given in Eq. (III.31).

We identified this type of initial state as part of a class of initial states where spin fluctuations have minimal uncertainty, $\langle \delta n_-(-k)\delta n_-(k)\rangle\langle \delta\theta(-k)\delta\theta(k)\rangle = 1/4$ for all momentum modes k (see also Eq. (III.32)). The individual spin operator variances are modified with a mode dependent factor, either enhancing or diminishing the individual variances. Such a modification is commonly understood as squeezing [178]. In particular, Eq. (III.31) generates a mode dependent squeezing profile with the following asymptotic properties. For $k \gg 1$, one has $\langle \delta n_-(-k)\delta n_-(k)\rangle = n_0/2$ and $\langle \delta\theta(-k)\delta\theta(k)\rangle = 1/(2n_0)$. The squeezing profile mainly affects the infrared region, $k \ll 1$ where the density variance is enhanced by an additional factor of $J_\mathrm{i}/(J_\mathrm{i} - J_\mathrm{c})$ and the phase variance is diminished by the inverse factor.

The squeezing of infrared spin fluctuation modes influences strongly the post-quench occupation of Bogoliubov quasi-particles and with it the effective temperature, as we derive in the following. Qualitatively, it is clear that for $J_\mathrm{f} = J_\mathrm{i}$ no quasi-particles are created at all and, consequently, $T(k) \equiv 0$ and $T_\mathrm{eff} = 0$. Thus, one expects that smaller values of J_i, for which the initial state is prepared, lowers the effective temperature for a given quench to J_f.

To derive the effective temperature quantitatively we start, as before, from the post-quench occupation of Bogoliubov modes, $n_\mathrm{B}(k, \varepsilon_\mathrm{f}, \varepsilon_\mathrm{i}) = {}_\mathrm{i}\langle\Omega| b_k^{\dagger,\mathrm{f}} b_k^\mathrm{f} |\Omega\rangle_\mathrm{i}$. Here we assume that $b_k^\mathrm{i}|\Omega\rangle_\mathrm{i} = 0$ for all k, where b_k^i is the Bogoliubov basis diagonalising S_- (Eq. (III.3b)) at a finite J_i. In Sect. III.2.3 we derived the initial spin fluctuation correlation functions, given in Eq. (III.31), corresponding to $|\Omega\rangle_\mathrm{i}$. Using Eq. (III.18) for the occupation number operator at J_f and inserting the initial spin correlation functions from Eq. (III.31) yields

$$n_\mathrm{B}(k, \varepsilon_\mathrm{i}, \varepsilon_\mathrm{f}) = \frac{1}{4}\frac{\omega_-(k, \varepsilon_\mathrm{i})}{\omega_-(k, \varepsilon_\mathrm{f})}\left[\frac{k^2 + \varepsilon_\mathrm{f}}{k^2 + \varepsilon_\mathrm{i}} + \frac{k^2 + \varepsilon_\mathrm{f} + 1}{k^2 + \varepsilon_\mathrm{i} + 1}\right] - \frac{1}{2}\,. \tag{III.71}$$

The pre- and post-quench distance to the critical point are defined as $\varepsilon_\mathrm{e,f} = (J_\mathrm{e,f} - J_\mathrm{c})/J_\mathrm{e,f}$. We discuss all expressions in the following in the natural unit system (see Sect. B.1). To represent $n_\mathrm{B}(k, \varepsilon_\mathrm{i}, \varepsilon_\mathrm{f})$ more conveniently we made use of the relations $f_k^2 = \omega_-/(k^2+\varepsilon) = (k^2 + \varepsilon + 1)/\omega_-$ (see Eq. (III.11) and Eq. (III.9)).

From the expression Eq. (III.71) one finds, in particular, that the ratio between pre- and post-quench excitation spectrum mainly controls the occupation of quasi-particles if

$\varepsilon_\mathrm{f} \simeq \varepsilon_\mathrm{i}$, since the term in square brackets then is approximately constant in k. Examples for $n_\mathrm{B}(k, \varepsilon_\mathrm{i}, \varepsilon_\mathrm{f})$ for several finite ε_i at fixed $\varepsilon_\mathrm{f} = 0.001$ are shown in Fig. III.7 (dashed lines). The figure shows, as expected, that the number of created quasi-particles in the infrared momentum region continuously gets less when ε_i approaches ε_f.

The mode temperatures, required to describe $n_\mathrm{B}(k, \varepsilon_\mathrm{i}, \varepsilon_\mathrm{f})$ as a generalised Gibbs ensemble, can be derived right away in the Rayleigh–Jeans approximation (see previous section Sect. III.4.2). With $T(k, \varepsilon_\mathrm{i}, \varepsilon_\mathrm{f}) \simeq \omega_-(k, \varepsilon_\mathrm{f}) n_\mathrm{B}(k, \varepsilon_\mathrm{i}, \varepsilon_\mathrm{f})$ one obtains

$$T(k, \varepsilon_\mathrm{i}, \varepsilon_\mathrm{f}) = \frac{1}{4}\omega_-(k, \varepsilon_\mathrm{i}) \left[\frac{k^2 + \varepsilon_\mathrm{f}}{k^2 + \varepsilon_\mathrm{i}} + \frac{k^2 + \varepsilon_\mathrm{f} + 1}{k^2 + \varepsilon_\mathrm{i} + 1} \right] - \frac{1}{2}\omega_-(k, ef) \,. \tag{III.72}$$

For $\varepsilon_\mathrm{i} \to \infty$, the expression for $T(k, \varepsilon_\mathrm{i}, \varepsilon_\mathrm{f})$ is equal to our result for $T(k, \varepsilon_\mathrm{f})$ (Eq. (III.65)) from the previous section. The leading-order divergence $\omega_-(k, \varepsilon_\mathrm{i}) \sim \varepsilon_\mathrm{i}$ for $\varepsilon_\mathrm{i} \to \infty$ is cancelled by the term in square brackets in Eq. (III.72). In the other limit $\varepsilon_\mathrm{i} \simeq \varepsilon_\mathrm{f}$, one finds from Eq. (III.72) that the mode temperatures are approximately set by the difference between the pre- and post-quench excitation frequencies, $T(k, \varepsilon_\mathrm{i}, \varepsilon_\mathrm{f}) \simeq (\omega_-(k, \varepsilon_\mathrm{i}) - \omega_-(k, \varepsilon_\mathrm{f}))/2$.

Examples for the form of $T(k, \varepsilon_\mathrm{i}, \varepsilon_\mathrm{f})$ in comparison to $T(k, \varepsilon_\mathrm{f})$ (*i. e.* at $\varepsilon_\mathrm{f} \to \infty$) are shown in Fig. III.7 (solid lines). We find that $T(k, \varepsilon_\mathrm{f})$ constitutes the maximal reachable mode temperatures. Lowering ε_i lowers the mode temperatures as a whole. Simultaneously, the plateau region in $T(k, \varepsilon_\mathrm{i}, \varepsilon_\mathrm{f})$ in the infrared moves towards lower momenta when $\varepsilon_\mathrm{i} \simeq \varepsilon_\mathrm{f}$. The effect is, however, rather weak. Lowering ε_i three orders of magnitudes shifts the plateau just by roughly one order of magnitude down in magnitude and to the infrared in k. Therefore, we find that the mode temperatures are dominated by a single effective temperature $T_\mathrm{eff}(\varepsilon_\mathrm{i}, \varepsilon_\mathrm{f}) = T(k, \varepsilon_\mathrm{i}, \varepsilon_\mathrm{f})|_{k \to 0}$ for a wide range of finite pre-quench distances to the critical point.

The effective temperature itself is easily found from Eq. (III.72) and conveniently expressed in terms of the pre-quench gap $\Delta_\mathrm{i} = \sqrt{\varepsilon_\mathrm{i}(\varepsilon_\mathrm{i} + 1)}$ and and the post-quench gap $\Delta_\mathrm{f} = \sqrt{\varepsilon_\mathrm{f}(\varepsilon_\mathrm{f} + 1)}$ in the Bogoliubov excitation spectra. We find with Eq. (III.72)

$$T_\mathrm{eff}(\varepsilon_\mathrm{i}, \varepsilon_\mathrm{f}) = T(k, \varepsilon_\mathrm{i}, \varepsilon_\mathrm{f})|_{k \to 0} = \frac{1}{4}\Delta_\mathrm{i} \left[\frac{\varepsilon_\mathrm{f}}{\varepsilon_\mathrm{i}} + \frac{\varepsilon_\mathrm{f} + 1}{\varepsilon_\mathrm{i} + 1} \right] - \frac{1}{2}\Delta_\mathrm{f} \,. \tag{III.73}$$

In the form of Eq. (III.73) for the effective temperature, several interesting limits can be read off conveniently. For quenches close to the critical point, $\varepsilon_\mathrm{f} \simeq 0$, we determined in Sectteffinf that the effective temperature is dominated by the constant value $T_\mathrm{eff} = 1/4$. From Eq. (III.73) we find that this generalises to

$$T_\mathrm{eff}|_{\varepsilon_\mathrm{f} \simeq 0} = \frac{\Delta_\mathrm{i}}{4(\varepsilon_\mathrm{i} + 1)} \simeq \frac{\Delta_\mathrm{i}}{4} \,, \tag{III.74}$$

where the second equality is an approximation for $\varepsilon_\mathrm{i} \ll 1$. Thus, for quenches close to criticality, the pre-quench gap determines the effective temperature. If the quench is strong, in addition (*i. e.* $\gg 1$), the effective temperature is universally set by $T_\mathrm{eff} = 1/4$, as this is the leading-order asymptotic behaviour of Eq. (III.74) for $\varepsilon_\mathrm{i} \to \infty$.

For strong quenches in general (*i. e.* $\gg 1$ and $1 < \varepsilon_\mathrm{f} <$ *i. e.*), the effective temperature is approximately (*i. e.* leading-order in *i. e.* $\to \infty$) given by $T_\mathrm{eff}(\varepsilon_\mathrm{f})$ (Eq. (III.67)).

On the other hand, for weak quenches $\varepsilon_\mathrm{i} \simeq \varepsilon_\mathrm{f}$, one finds from Eq. (III.74) that the difference between the pre- and the post-quench gap determines the effective temperature

$$T_\mathrm{eff}(\varepsilon_\mathrm{i}, \varepsilon_\mathrm{f}) \simeq \frac{\Delta_\mathrm{i} - \Delta_\mathrm{f}}{2} \,. \tag{III.75}$$

This completes our understanding of the emergence of the effective temperature in terms of relevant energy scales from the quench.

As a last remark we comment on the practical relevance of the possibility to tune T_eff via ε_i. Following our qualitative discussion in Sect. III.4.1 it is within Bogoliubov theory not expected that the spin correlation length (in the stationary state) changes with the effective temperature. Therefore, the correlation length will also not change with ε_i, as long as the Gibbs ensemble at temperature T_eff is a good approximation for the generalised Gibbs stationary state.

Nevertheless, the effective temperature has strong influence on quench dynamics of bulk quantities (such as the correlation length) beyond the linearised regime, as we will discuss in chapter VI. Within that context, we will find that the effective temperature determines the scale where the Bogoliubov scaling $\xi = \varepsilon_\mathrm{f}^{-1/2}$ turns into a crossover. In a certain sense, the scale set by the effective temperature determines up to which distance to the critical point Bogoliubov theory is valid. Therefore, a second independently adjustable parameter is helpful for controlling scaling regimes and testing scaling hypotheses beyond Bogoliubov theory.

III.5 Summary

In this chapter, we have discuss an implementation of Bogoliubov theory for the spinor Bose gas as defined by the model Eq. (II.1). Based on a description in terms of relative and absolute phase and density fields for the Bose gas Eq. (II.4), we found that spin and absolute degrees of freedom decouple on the Bogoliubov level. Thereafter, we diagonalised the quadratic spin action S_- Eq. (III.3) and derived the corresponding Bogoliubov quasi-particle basis. From this procedure we obtained, most importantly for subsequent chapters, the Bogoliubov excitation spectrum of quasi-particles $\omega_-(k, \varepsilon)$ Eq. (III.11).

The quasi-particle basis allowed us in Sect. III.2 to methodically define the quench within Bogoliubov theory and derive the post-quench time evolution of the full z-spin two-time correlation function Eq. (III.30). Thereafter we discussed possible initial states from which to quench and their physical interpretation. In particular important for subsequent chapters will be the class of initial states defined by Eq. (III.31), where the quench starts in a groundstate of the Bogoliubov quasi-particle basis b_k^i which diagonalises the spin action for a specific value of the linear coupling J_i.

For this quench scenario, we analysed in Sect. III.3 the scaling behaviour within the dynamic evolution of the z-spin structure factor and correlation function. We find that the structure factor follows a full scaling form including the post-quench time dependence $\mathcal{G}_{zz,\,\mathrm{reg}}(s\varepsilon, s^\nu k, s^{-\nu z} t) = s^{-(2d-\eta)\nu} \mathcal{G}_{zz,\,\mathrm{reg}}(\varepsilon, k, t)$, if concentrating to either small $\varepsilon_\mathrm{f} \ll 1$ or large $\varepsilon_\mathrm{f} \gg 1$ distance to the critical point. The scaling form is fulfilled for the static meanfield scaling exponents $\nu = 1/2$ and $\eta = 0$ and the dynamical critical exponent

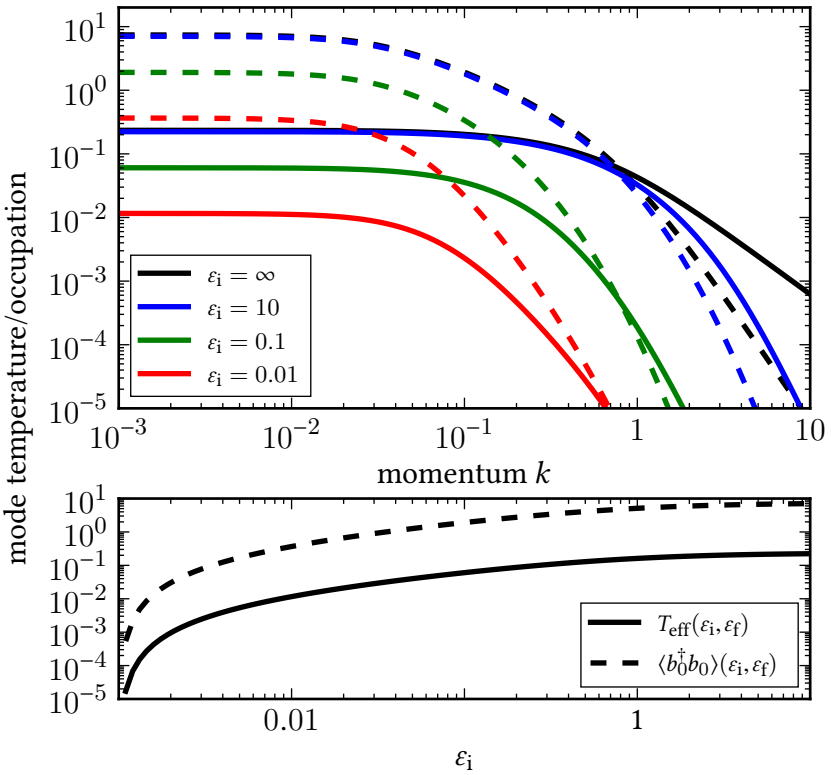

Figure III.7: The figure shows the generalised Gibbs mode temperatures (solid lines, in units of $2J_c$) and the post-quench occupation of Bogoliubov modes (dashed lines). The initial state is prepared as a Bogoliubov groundstate at a finite pre-quench distance to the critical point ε_i. The post-quench distance is chosen $\varepsilon_f = 0.001$ for all curves. The upper panel depicts the mode temperature $T(k, \varepsilon_i, \varepsilon_f)$ (Eq. (III.72)) and the post-quench occupation of quasi-particles $\langle b_k^f b_k^f \rangle$ as a function of momentum at $\varepsilon_i = \{10, 1, 0.001\}$, concentrating on the infrared part of the spectrum, $k < \sqrt{4mJ_c}$. The black solid and dashed curve in the upper panel corresponds to the red curves in Fig. III.5. The lower panel depicts the respective infrared limits, $T(k = 0, \varepsilon_i, \varepsilon_f)$ and $\langle b_0^f b_0^f \rangle$, as a function of distance to the critical point. A finite pre-quench linear coupling decreases the effective temperature and the mode temperatures as a whole.

$z = 1$ ($\varepsilon_f \ll 1$) or $z = 2$ ($\varepsilon_f \gg 1$). These exponents do not need to be determined by full rescaling of the structure factor but can be obtained from independent rescaling amplitudes and oscillation frequencies of individual modes in the structure factor. We use this knowledge in subsequent chapters to analyse the results from full simulation for the structure factor for the scaling predictions and determine deviations from meanfield scaling.

In the last section Sect. III.4 we applied the concept of generalised Gibbs ensembles [11–14] to the Bogoliubov formulation of the spin sector, which is naturally an integrable theory. As main result in this chapter, we derived that the generalised Gibbs ensemble, required to describe the post-quench occupation of Bogoliubov modes, can be replaced by a regular Gibbs ensemble. If concentrating on infrared modes $k < 1$, which is the important momentum region for critical behaviour, a Bose–Einstein distribution at a single, mode-independent temperature describes the post-quench quasi-particle occupation. This means that the employed quench protocol erases details of the pre-quench state, such that only one relevant scale, the effective temperature $T_{\text{eff}}(\varepsilon_{\text{f}}, \varepsilon_{\text{i}})$ Eq. (III.73) is left. The scale is a consequence of the quench itself, together with spectral properties of the system, as it is set by the pre-quench excitation gap $T_{\text{eff}} = \Delta_{\text{i}}/4$ for strong quenches $\Delta_{\text{f}} \ll \Delta_{\text{i}}$.

We have argued that correlations in the generalised Gibbs stationary state of the Bogoliubov theory are insensitive to the temperature and always follow the scaling law $\xi \sim \varepsilon_{\text{f}}^{-1/2}$. Nevertheless, we will discuss in chapter VI that the effective temperature has strong influence on quench dynamics of bulk quantities (such as the correlation length) beyond the linearised regime. Within that context, we will find that the effective temperature determines the scale where the Bogoliubov scaling $\xi = \varepsilon_{\text{f}}^{-1/2}$ turns into a crossover.

IV Comparison to the Experiment

Multi-component quantum gases, of bosonic or fermionic nature, offer a vast playground for theory and experiment alike. Especially in the world of alkaline atom species, where reaching quantum degeneracy is a long-known art since the groundbreaking works by Cornell, Wieman [184] and Ketterle [185] , multi-component gases are nowadays often used to mimic completely different systems from the condensed matter or even high-energy physics realm. As they allow for *in situ* imaging of densities, an important application for example is spin pattern formation and dynamic spin mixing(see [74, 152, 164, 174, 175, 186–191] for a collection of experiments in that context). For being clean and controllable multi-level systems multi-component condensates of alkaline atoms as well often employed in the context of quantum information and spin entanglement experiments,see for example [192–198]. And, for all those properties, multi-component alkaline gases have been proposed as construction kit for simulators of non-abelian gauge theories [199–201].

In the subsequent chapters V and VI, we present simulations for quench dynamics in the two-component Bose gas in one spatial dimension. A substantial part of the motivation for the numerical work we carried out for precisely that system comes from the experiments presented in Refs. [118, 202] by the Oberthaler group. In this chapter, we review the recent experimental results on quenches in the $1d$ spinor Bose gas from Ref. [73]. As main result, we[1] find in Ref. [73] that the current experimental realisation lies within the Bogoliubov scaling regime but is at the verge of going beyond the Bogoliubov regime.

The purpose of this chapter is to motivate why to study quenches in the spinor Bose gas, instead of theoretically simpler models. In contrast to, for example, the Ising chain or a $O(N)$-symmetric field theory which are typically effective descriptions, the model we use, defined by Eq. (II.1), directly reflects the experiment. For the spinor gas, the experiment has a similar control over interaction parameters as the simulation. For observables, the experiment is able to measure realisations of the spin density field *in situ*, such that, in principle, all equal-time correlations functions of the spin fields can be retrieved as ensemble averages. Therefore, apart from practical issues, the spinor Bose gas allows comparing simulation and experiment of the same quench dynamics directly.

IV.1 Experimental Realisation

In the experiment in Ref. [73], the two-component gas is prepared in a quasi-condensate, where the atoms are in two hyperfine states, which we denote as $|\downarrow\rangle = |F = 2, m_F = -1\rangle$ and $|\uparrow\rangle = |F = 1, m_F = 1\rangle$. The system is described by the model Hamiltonian

[1] For Ref. [73], I contributed to the theoretical analysis and the interpretation of the experimental data and provided data from direct numerical simulation.

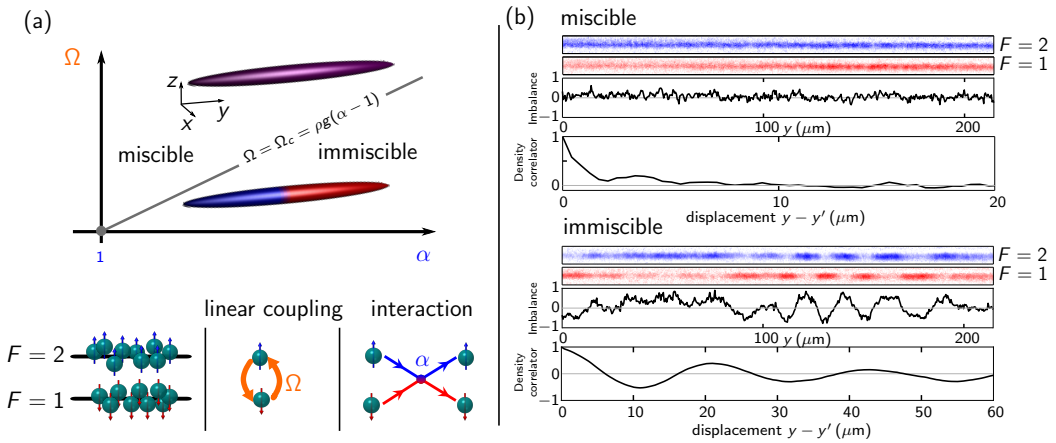

Figure IV.1: Details of the experimental system. (a) Phase diagram, distinguishing miscible and immiscible phases of the elongated degenerate Bose gas of rubidium atoms in $F = 2$ (blue) and $F = 1$ (red) hyperfine states. The state of the system is controlled by linear coupling of the levels, with Rabi frequency Ω, and by tuning the collisional interaction between atoms in the hyperfine states, quantified by the relative strength $\alpha = a_{\uparrow\downarrow}/\sqrt{a_{\uparrow\uparrow}a_{\downarrow\downarrow}}$ of inter- and intra-species scattering lengths (experimentally fixed to $\alpha \approx 1.23$). A quantum phase transition occurs at $\Omega_c = n_0 g(\alpha - 1)$, with 1D atom density n_0 and intra-species coupling constant g. (b) The system is initially prepared far in the miscible regime, and then Ω quenched close to Ω_c. After different evolution times the two species are absorption imaged. Snapshots of the patterns emerging on either side of the transition are shown, with corresponding normalised density imbalance $(n_\uparrow(y) - n_\downarrow(y))/n_0$ and density correlation functions between spatially separated points y and y'. The correlations on the miscible side exhibit decay on a characteristic length scale, while oscillations on the immiscible side reflect domain formation as seen in the density. Figure adapted from [73]

Eq. (II.1). The collisional interaction between atoms in these states is tuned by use of an inter-species Feshbach resonance [195, 203] such that the system is in the immiscible regime, as discussed in Sect. II.1.2. The situation is illustrated in Fig. IV.1a (*cf.* also Fig. II.1).

Specifically, the interspecies scattering length $a_{\uparrow\downarrow}$ is chosen larger than the intraspecies scattering lengths $a_{\uparrow\uparrow}$ and $a_{\downarrow\downarrow}$. In the experiment, the ratio α (see Eq. (II.3)) is set to $\alpha = a_{\uparrow\downarrow}/\sqrt{a_{\uparrow\uparrow}a_{\downarrow\downarrow}} \approx 1.23$. De-mixing of such kind has already been observed experimentally [74, 75, 118] and studied theoretically [87, 113, 119, 191, 196, 204] Varying the strength of linear Rabi coupling[2] $\Omega = 2J$ between the two atomic species allows tuning across the quantum phase transition between the immiscible and miscible regimes. Note

[2] In the experimental context, it is more common to formulate the linear coupling term in Eq. (II.1) in terms of $\Omega = 2J$, as it is realised by a Rabi coupling. Theoretically on the other hand, it is a Josephson-type coupling term. We will discuss the experiment in terms of the Rabi coupling Ω but the relation $\Omega = 2J$ can be assumed at any point for any plot or expression.

that we use $\Omega = 2J$ for the linear coupling in this chapter and present data in physical units (and not in natural units).

The experiment studies, the dynamics after a sudden change, *i. e.* quench, of the linear coupling, observing the time evolution of the spatially resolved density patterns of the two components $n_\uparrow(y)$ and $n_\downarrow(y)$ along the extended axis of the trap, on either side of the miscible-immiscible transition (Fig. IV.1b). Due to the repulsive interactions between the individual components, the local atomic density $\rho(y) = n_\uparrow(y) + n_\downarrow(y)$ is to a very good approximation constant, such that only the density difference $n_\uparrow(y) - n_\downarrow(y)$ fluctuates. Consequently, the gas can be considered as a homogeneously distributed, coupled collective spin ensemble, characterised by a continuous angular-momentum field $\mathbf{S}(y)$ (Fig. IV.2a).

The longitudinal extension of the cloud of $\sim 200\,\mu$m allows exploring the miscible regime where the expected length scales are of the order of a few microns, as well as the immiscible side, with expected domain sizes of a few tens of microns. As the densities of the individual components can be measured, the z-component $S_z(y) = [n_\uparrow(y) - n_\downarrow(y)]/\rho(y)$ (see also Eq. (II.2)) of the 'Schwinger spin' normalised to the total density can be obtained from the density differences. Finally, the equal-time spin correlation function

$$\mathcal{G}_{zz}(y, y', t) = \langle S_z(y) S_z(y') \rangle_t \,, \tag{IV.1}$$

between different points y, y' can be determined from the density patterns. Examples of realisations of the density fields, the S_z-spin field and the obtained correlation function Eq. (IV.1) are depicted in panel Fig. IV.1b. In particular, the lower part of Fig. IV.1b displays spin domains which have formed after a quench across the critical point.

Initial state in the Experiment

Before we turn to results on scaling behaviour, we describe the initial state in the experiment. Both hyperfine-modes $j = \uparrow$ and $\downarrow$ are initially occupied equally with zero relative phase, *i. e.* the system is fully polarised along the positive spin x-axis. In this state, the spin degrees of freedom can, to a good approximation, be considered in the zero-spin-temperature groundstate while the symmetric sector is equilibrated at a temperature on the order of $T \simeq 30\,$nK.

The spin, pointing initially into the negative z-direction, as only the $|\uparrow\rangle$ state is populated, is rotated into the x-direction, *i. e.* to $(\Theta, \theta_-) = (0, 0)$, with a $\pi/2$-pulse in the linear coupling at high coupling strength $\Omega \gg \Omega_c$. The initial superposition of $|\downarrow\rangle$ and $|\uparrow\rangle$ states can be, to a good approximation, considered being prepared at infinite linear coupling strength. As a consequence, the initial spin and relative phase fluctuations can be considered to be Gaussian and delta-correlated in space,

$$\begin{aligned} \mathcal{G}_{zz}(y, y'; t = 0) &= \langle S_x(y) S_x(y') \rangle_0 = (2n_0)^{-1} \delta(y - y') \\ &= \langle \theta_-(y) \theta_-(y') \rangle_0 = \mathcal{G}_{yy}(y, y'; t = 0) \,. \end{aligned} \tag{IV.2}$$

We have used this initial state (see also Sect. III.2.3) for computing quench dynamics and scaling behaviour within Bogoliubov theory (see Sect. III.3 and Eq. (III.37)). These cor-

relations determine the quasiparticle occupation numbers which form the diagonal elements of the density matrix in the quasi-particle basis and represent the conserved quantities during the ensuing evolution, as long as the system stays in the linear regime, see Sect. III.4.

After this preparation procedure, the Rabi coupling strength is quenched close to the critical coupling strength, with distances in the range $\varepsilon \simeq \{0.1 \ldots 1\}$, on a time scale much faster than the pre- or post-quench gap period.

Details on the Experimental Procedure

To understand the relation to the simulations from subsequent chapters better, we provide details on experimental parameters and employed procedures in the following, *cf.* also [73]. The condensate is prepared with $N \approx 4 \times 10^4$ Rubidium-87 atoms in the $|\uparrow\rangle = |F = 1, m_F = 1\rangle$ hyperfine state of the $5S_{1/2}$ hyperfine manifold, in an elongated optical trapping potential with $(\omega_y, \omega_\perp) = 2\pi \times (1.9, 128)$ Hz. The resulting density in the trap centre is therefore $n_{1\mathrm{D}} \simeq 230\,\mu\mathrm{m}^{-1}$. The trapping potential is harmonic to a good degree of approximation, $V(\mathbf{r}) = m\omega_y^2 y^2/2 + m\omega_\perp^2 |\mathbf{r}_\perp|^2/2$. The Feshbach resonance between $|\uparrow\rangle$ and $|\downarrow\rangle = |F = 2, m_F = -1\rangle$ at 9.10 G is used to tune the inter-species scattering length to $a_{\downarrow\uparrow} \approx 120\, a_{\mathrm{Bohr}}$ at 9.08 G while the intra-species scattering lengths are fixed, $(a_{\uparrow\uparrow}, a_{\downarrow\downarrow}) = (95, 100)\, a_{\mathrm{Bohr}}$. At this magnetic field, the bare system is immiscible. By applying resonant two-photon linear coupling, the system can be rendered miscible. The phase transition occurs at a critical Rabi frequency $\Omega_\mathrm{c} = 2J_\mathrm{c}$. In mean-field and uniform-gas approximation, it is given by $\Omega_\mathrm{c} = -2n_+ g_s \approx 2\pi \times 70$ Hz where $g_s = \hbar\omega_\perp(a_{\uparrow\uparrow} + a_{\downarrow\downarrow} - 2a_{\downarrow\uparrow})$ is the effective 1D coupling of the spin degrees of freedom, and $2n_+$ the $1d$ density of the whole gas. Note that g_s is the generalisation of g_- if $g_{\uparrow\uparrow} \neq g_{\downarrow\downarrow}$. After the initial preparation of all atoms in $|\uparrow\rangle$, a $\pi/2$ pulse of combined microwave and radio frequency magnetic fields with a Rabi frequency $\Omega \approx 2\pi \times 340$ Hz, creates an equal superposition of $|\uparrow\rangle$ and $|\downarrow\rangle$. Subsequently, the phase of the radio frequency is switched by $\pi/2$ ($3\pi/2$ for $\epsilon < -1$), and Ω is quenched to a final value above or below the critical value Ω_c.

After the following evolution time, the two components are sequentially detected using in-situ absorption imaging at 9.08 G. Due to the proximity of the Feshbach resonance, atoms are lost with a $1/\mathrm{e}$ lifetime of ≈ 30 ms, and the density decreases with time. The resulting change of Ω_c was compensated by dynamically adjusting the Rabi frequency Ω during the evolution time. When discussing the results all given values for Ω will refer to the initial value. Other effects of atom loss such as the change in the spin healing length ξ_s remain. To ensure resonance of the two-photon coupling, the independently determined AC Zeeman shift, resulting from the detuning of 200 kHz to the intermediate $|F = 2, m_F = 0\rangle$ state, is compensated by adjusting the frequency of the radio frequency driving δ (*cf.* Eq. (II.1)). The average of the density dependent meanfield shift $\propto (g_{\uparrow\uparrow} - g_{\downarrow\downarrow})2n_+$ is compensated in the same way. However, we point out that this compensation mechanism works based on the meanfield approximation and effects of $g_{\uparrow\uparrow} \neq g_{\downarrow\downarrow}$ might become relevant again if the results are compared to beyond-meanfield predictions.

In the analysis of the in-situ images the centre of the cloud is selected to reduce effects of cloud inhomogeneity and position. Images with an integrated population imbalance

$|N_\uparrow - N_\downarrow|/(N_\uparrow + N_\downarrow) > 0.2$ are not taken into account, as well as images with large imaging noise. The longitudinal extension of $\sim 200\,\mu$m allows to explore the miscible regime, where the length scales are of the order of a few microns, as well as the length scales of a few tens of microns on the immiscible side. The transverse extension of the atomic cloud is $\approx 2\,\mu$m (while the chemical potential is $\mu \approx 2\pi \times 300\,$Hz) and is comparable to the spin healing length $\xi_s(\Omega) = \hbar/\sqrt{m(2g_s n_+ + \hbar\Omega)} = \sqrt{\hbar/m\Omega_c\varepsilon}$ for $|\varepsilon| \sim 1$. Thus the system close to quantum criticality is effectively one-dimensional for the spin degree of freedom. The experimental data is analysed with respect to the linear density profiles $n_{\uparrow,\downarrow}(y)$ of each component from which the spin profile $S_z(y)$ and its longitudinal correlations $\mathcal{G}_{zz}(y,y',t) = \langle S_z(y)S_z(y')\rangle_t$ between different points y, y' along the axis of the trap are computed, and averaged over ~ 20 experimental realisations. As observables from the experiment are computed within the approximately homogeneous trap centre, results from our simulations or Bogoliubov theory alike can be compared by means of the physical value of the critical coupling in the trap centre, $\Omega_c \simeq 2\pi \times 70\,$Hz. This allows to convert the J_c-based unit system, we employed so far for calculations, back to physical values.

In [73] it has been shown, by comparing the described experiment with Bogoliubov theory and our non-perturbative results from simulation (these will be discussed in detail in chapter V and chapter VI), that the experiment is still in the meanfield regime but right at the brink for its smallest reachable distances from the critical point. It is also argue that spatial resolution and reachable hold times are already sufficient to witness critical dynamics beyond the meanfield approximation, despite atom loss and trap-generated spatial inhomogeneity, if smaller distances to the critical point can be stabilised.

IV.2 Time Evolution of Correlations

The experiment studies quenches in Ω to the miscible as well as to the immiscible regime, starting in the miscible regime as described above, and measures the post-quench correlation function $\mathcal{G}_{zz}(y,t)$ and corresponding correlation length $\xi(t)$. The goal is finally to determine scaling behaviour of those quantities (as we have done within Bogoliubov theory in Sect. III.3). In this section, we briefly show the time evolution of correlations for quenches on the miscible side, as measured in the experiment. We have discussed the prediction from Bogoliubov theory for the corresponding case in Sect. III.2.

The long-wavelength dynamics of the effective spin fluid is under the conditions of the experiment described, to a good approximation, by a translationally invariant nonlinear XXX-type Heisenberg Hamiltonian density (see also Eq. (II.6) with $\Omega = 2J$)

$$\mathcal{H} = \left[|\partial_y \mathbf{S}|^2/4 + \Omega S_x - \Omega_c S_z^2/2\right] n_0/2. \tag{IV.3}$$

The correlations $\mathcal{G}_{zz}(y,t;\varepsilon)$ developing on the miscible side ($\varepsilon > 0$) are shown in Fig. IV.2b, in comparison with homogeneous Bogoliubov-de Gennes theory predictions.

The Bogoliubov expression for $\mathcal{G}_{zz}(y,t;\varepsilon)$ is, in principal, given by the expression Eq. (III.38) we have also derived in Sect. III.3. To compare to the experiment, however, there are additional effects included (see also the supplementary materials in [73]). The Bogoliubov expression is averaged over the density inhomogeneity in the trap. To do

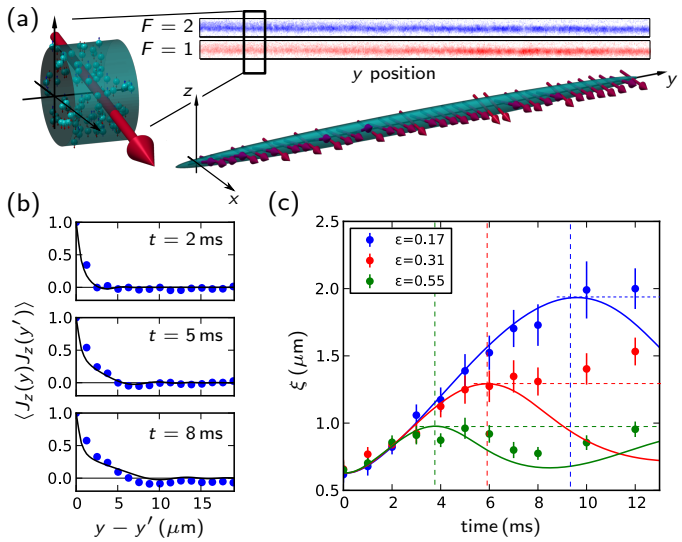

Figure IV.2: Time evolution of correlations after quench to the miscible side of the quantum phase transition. (a) Two-component gas as a coupled collective spin ensemble. The spatially resolved density difference between $F = 1$ and $F = 2$ allows the extraction of the local z-component of the collective spin vector $\mathbf{S}(y)$. (b) Measured spin correlation function $\mathcal{G}_{zz}(y,y',t) = \langle J_z(y)J_z(y')\rangle_t$ at three different times after a quench to $\varepsilon = \Omega/\Omega_c - 1 = 0.17$, showing build-up of spatial correlations. Solid black lines show Bogoliubov-de Gennes mean-field predictions. (c) Time-evolution of the correlation length $\xi(t;\varepsilon)$, for three different ε, deduced by fitting an exponential to the extracted correlation data. The Bogoliubov evolution (solid lines) recovers the initial near-linear rise of ξ, with slope given by the speed of (spin-wave) sound, and captures the maximum correlation length at a characteristic time depending on ε. The predicted oscillatory behaviour is experimentally observed for larger ε, while the maximum correlation length reached at short times is robustly detected in all cases. Dashed lines serve as a guide to the eye, marking the predicted first maxima. For the scaling analysis of the data, the correlation lengths are compared at a fixed time, see Fig. IV.3. Figure adapted from [73]

so, one replaces the homogeneous density n_0 in Eq. (III.38) with the trap density profile $n_0 \to n(y)$ and averages the resulting function over $n(y)$. Additionally, the resulting Bogoliubov correlation function is convoluted with the optical point spread function of the imaging system.

Fitting an exponential to the observed correlation functions, a correlation length $\xi(t;\varepsilon)$ is extracted. The post-quench time evolution of $\xi(t;\varepsilon)$ shows near-linear growth after the initial quench (see Fig. IV.2c). The Bogoliubov prediction for $\xi(t;\varepsilon)$, which is extracted in the same way from the adapted Bogoliubov correlation functions, (solid lines) qualitatively reproduces this rise as well as the oscillations seen for larger ε. The damping of the oscillations seen at smaller ε is attributed to effects of the transverse trapping potential.

Thus, Bogoliubov theory describes the quench dynamics on the miscible side to a good degree, including the full correlation functions (see Fig. IV.2b), up to the first maximum in the correlation. Thereafter, most likely effects from the trap lead to deviations, not (alone) interaction effects [73].

IV.3 Scaling Behaviour of Correlations

Up to the first maximum in correlation, it is therefore reasonable to test for the meanfield scaling predictions for the z-spin correlations (see Sect. III.3). Using the theoretically expected exponent of 0.5 for rescaling the measured correlation functions at a fixed time ($t = 12\,\mathrm{ms}$) they all fall on a universal curve (see Fig. IV.3a, upper panels).

The maximum correlation length for different ε is then extracted, within the first $12\,\mathrm{ms}$ after the quench, where this observable is still weakly affected by the atom loss or effects of the trapping. Extracting characteristic length scales, as described in Sect. IV.2, scaling according to the meanfield prediction

$$\xi(t_{\mathrm{ref}}, \varepsilon) \sim \varepsilon^{-\nu}\,, \tag{IV.4}$$

is found (see lower panels of Fig. IV.3a).

The exponent extracted from a linear fit of ξ on a double-log scale is $\nu = 0.51 \pm 0.06$ (Fig. IV.3a, lower right panel). The scaling exponent furthermore found to be robust. Varying the range of the exponential fit of the correlation functions or the reference time $t_{\mathrm{ref}} < 12\,\mathrm{ms}$ after the initial linear rise does not affect the scaling exponent ν.

Although the dynamic evolution was not recorded for quenches to the immiscible regime, scaling behaviour is analysed after a hold time. As the quenches reach deep into the immiscible regime $\varepsilon < -1/2$, a dynamical instability is triggered which nucleates domains in the z-spin (see Sect. II.4). The domains come with a characteristic size L_{d}, which provides an equivalent to the correlation length in the immiscible regime.

In Fig. IV.3a (lower left panel) the measurements of $L_{\mathrm{d}}(\varepsilon)$ for quenches in the immiscible regime are shown. The domain size is determined after a hold time sufficiently long for domains having fully grown. From a fit the scaling exponent of $\nu = 0.51 \pm 0.04$ (Fig. IV.3a, lower left panel) is found, with $L_{\mathrm{d}}(\varepsilon) \sim \varepsilon^{-\nu}$. It meets the prediction from Bogoliubov theory (see Sect. II.4 and Eq. (II.37)), when identifying the domain size with the most unstable mode via $L_{\mathrm{d}} \sim 1/k_{\mathrm{m}}$.

As a result, in both, the miscible and immiscible regimes, the experimental observations displays self similarity under rescaling $y \to \varepsilon^{\nu} y$ with $\nu = 1/2$, with correlations following different universal functions.

Since for quenches in the miscible regime the full time evolution of correlation functions has been measured, a dynamical critical exponent can be determined. To obtain the dynamical exponent z, the observed time dependence of the correlation functions are analysed.

A characteristic time scale can be defined when focusing on the point of time τ where $\xi(t)$ levels off after the initial linear rise (Fig. IV.3b, upper panel). To find τ from data, crossing point of two independent linear fits to the short and long-time behaviour is determined. The resulting dependence of $\tau(\varepsilon)$ is compared, on a double-log scale to a power

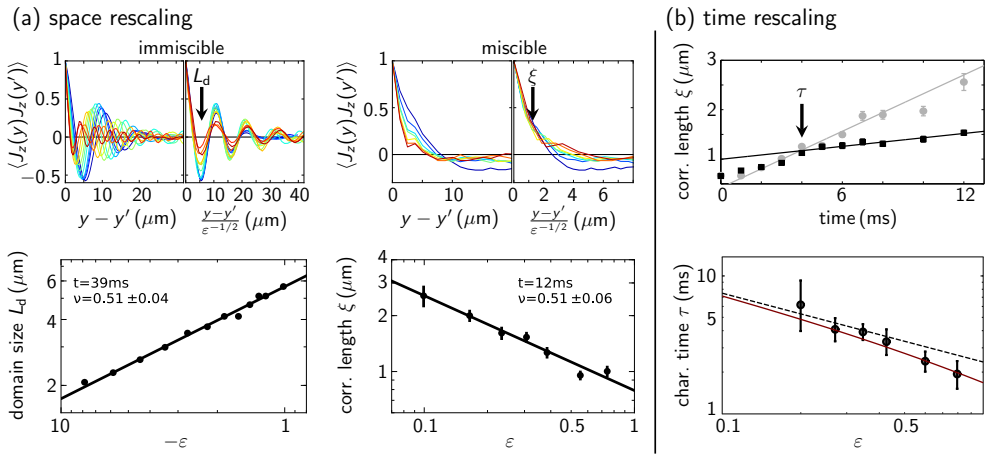

Figure IV.3: Spatial and temporal scaling of the spin-spin correlations. (a) Spatial correlations after quenches to different proximities ε from the critical point (colour-coded), on the immiscible (left panels, at $t = 39\,\mathrm{ms}$) and miscible side (right, $t = 12\,\mathrm{ms}$). Top row: The correlation functions, under a rescaling $y \to y\varepsilon^{\nu}$ of the distance dependence with mean-field exponent $\nu = 1/2$, fall on a universal curve. Bottom row: ε-dependence (double-log scale) of the characteristic length scales deduced from the correlation functions. The straight lines reveal values for the critical exponent $\nu = 0.51(4)$ on the immiscible and $\nu = 0.51(6)$ on the miscible side of the transition. (b) Temporal scaling of the spin-spin correlations. The characteristic time τ for different ε is obtained as the intersection point of the linear fits to the initial rise of $\xi(t)$ (grey symbols for $\varepsilon = 0.1$) and to the behaviour after ξ deviates from this rise. The procedure of determining the intersection is exemplarily shown in the upper panel for $\varepsilon = 0.23$. In the lower panel we compare the extracted $\tau(\varepsilon)$ to a mean-field scaling with $\nu z = 1/2$ (dashed line) and to the Bogoliubov prediction $\tau \sim 1/\Delta$, with gap $\Delta(\varepsilon) = \Omega_c\sqrt{\varepsilon(\varepsilon+1)}$, also applicable at larger $\varepsilon \gtrsim 1$ (solid line). Figure adapted from [73].

law with exponent $\nu z = 1/2$ (see Fig. IV.3b, lower panel, dashed line), from Bogoliubov prediction (*cf.* Sect. III.3). The deviation of the data from this power law for large ε can be understood within Bogoliubov theory which predicts $\xi(t;\varepsilon) = (2m\Omega_c\varepsilon)^{-1/2}|\sin(\Delta(\varepsilon)t)|$ The time $t_{1,\varepsilon}$ of the first maximum (solid line in Fig. IV.3b, lower panel), related to the characteristic time τ, is inversely proportional to the gap, *i. e.*, zero-momentum-mode frequency $\Delta(\varepsilon) = \Omega_c\sqrt{\varepsilon(\varepsilon+1)}$.

IV.4 Outlook

On either side of $\varepsilon = 0$, the miscible and the immiscible, z-spin correlations as measured from experiment display scaling behaviour. The critical exponents extracted from experimental data are thereby consistent with Bogoliubov-de Gennes mean-field predictions.

To reveal the limitations of mean-field theory and study the effects due to the excita-

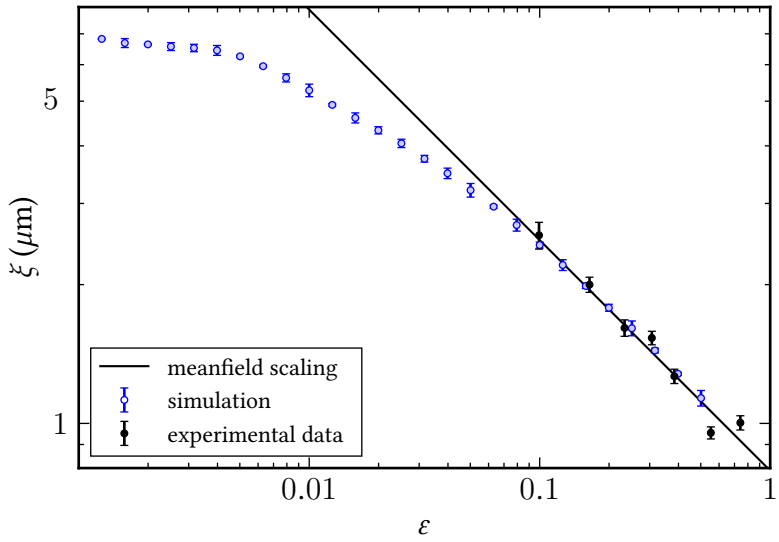

Figure IV.4: (Color online) Scaling analysis at short times after the quench. Correlation length $\xi_0(t;\varepsilon)$ on the miscible side of the transition, at the time of the first maximum of ξ_0 after the quench. The solid black line marks the Bogoliubov prediction $\xi_{\mathrm{Bog}} = \sqrt{\hbar/(2m\Omega_c\varepsilon)}$ also shown in Fig. IV.3a. Closer to the critical point, the open coloured symbols show results of semi-classical simulations of the quench dynamics. In the experimental range ($\varepsilon \gtrsim 0.1$) simulation data and Bogoliubov mean-field prediction and experimental data (black filled symbols) agree. For $\varepsilon \lesssim 0.1$, the simulations demonstrate a deviation from the mean-field power law and saturation for $\varepsilon \to 0$. Figure adapted from [73]

tion of total-density fluctuations, we have performed for [73] semi-classical simulations (see Sect. II.5.1). We discuss the numerical results in detail in the subsequent chapters V and VI. Before going on, we give an outlook of what to expect with respect to the scaling behaviour of the experimentally determined correlation length.

We define a correlation length ξ_0 in terms of the zero-momentum limit of the Fourier transform of the normalised spin-spin autocorrelation function, $\xi(t,\varepsilon) = \mathcal{G}_{zz}(k,t;\varepsilon) = \int \mathrm{d}y \exp\{-\mathrm{i}\,ky\}\mathcal{G}_{zz}(y,t;\varepsilon)$ (see also Sect. II.5.2). As for the experiment, we analyse the correlation length obtained from full simulation at its first maximum in the miscible regime, $\xi_0(\varepsilon) = \max\xi(t,\varepsilon)$ for $\varepsilon > 0$, as a function of ε (see Fig. IV.4).

For $\varepsilon > 0.1$, we find very good agreement of the computed correlation length at the first maximum (blue points in Fig. IV.4) with meanfield scaling (solid black line) and experimental data (black points, see also Fig. IV.3a). The numerical data shows that, for $\varepsilon \lesssim 0.05$, the extracted correlation length scale at the first maximum deviates from a simple mean-field power law and saturates to a finite value at vanishing ε. This ε-dependence of ξ_0 shows crossover behaviour reminiscent of an equilibrium one-dimensional Ising model [89].

As one of the main results of this work, we quantify this relation between the crossover in the spinor Bose gas for quench dynamics in terms of an effective temperature and the universal crossover Ising crossover functions in chapter VI. The purpose of this chapter is to show that the experiment is not far away from actually measuring the crossover. The experimental data stops at $\varepsilon \simeq 0.1$, as it was in the realisation used in [73] not possible to stabilise a smaller distance to the critical point against atom losses. It seems realistic to overcome this problem[3], for example, by using other states in the hyperfine manifold of ^{87}Rubidium and to, finally, explore the crossover regime with an improved version of the experimental setup.

[3]Personal communication with the other authors of [73]

V Paramagnetic Quench Dynamics Beyond the Linear Regime

In this and the following chapter VI, we present a thorough numerical analysis of the dynamical response of the two-component Bose gas when quenched into the vicinity of the quantum critical point J_c. Thereby, we concentrate on real-time dynamics of spin correlation functions after a quench in one spatial dimension, since this is the situation which is directly accessible by experiments (*cf.* chapter IV and [73]).

Phase transitions in one spatial dimensions usually come with a catch. In $1d$, fluctuations always destroy true long-range order, in the sense of a diverging correlation length. Consequently, critical scaling is not expected in (classical) one dimensional systems. On the other hand, in the realm of quantum physics it turns out that not only the fluctuations in spatial directions are important. For equilibrium physics, the time direction has the exact same meaning as any spatial direction, increasing effectively the dimensions for the phase transition. This can be easily seen when an euclidean path integral formalism is applied (see for example [127] or [128] for an introduction to quantum phase transitions). In the field-theoretical description of a spatially one-dimensional quantum system, the temperature T constitutes a second euclidean dimension with finite extent $\sim 1/T$. Thus, at zero temperature one is back at the classical system in the thermodynamic limit in two-spatial dimensions, including critical scaling.

The phase transition in the quantum Ising chain in a transverse field [89, 205] provides expectations for the influence of non-zero temperature on critical scaling. Scaling behaviour with exponents from the Ising universality class in $2d$ appears in observables for larger distances to the critical point. But, at any non-zero temperature, close to the critical point observables such as the correlation length stay analytic (do not diverge). This implies deviation from critical scaling in favour of a crossover, which appears when temperature is on the order of the excitation gap. We discuss the transverse-field Ising model and its relevance for the spinor gas in more detail in the next chapter VI.

In this chapter, we analyse when, in time and distance to the critical point, the full semi-classical simulation (see Sect. II.5.1) of the spinor Bose gas starts to deviate from the Bogoliubov behaviour, presented in chapter III. In particular, we are concerned with the question what happens to the meanfield scaling predictions (see Sect. III.3.2) for the structure factor beyond Bogoliubov theory. Therefore, we concentrate on the scenario of a sudden parameter quench in J on the paramagnetic side, as introduced in Sect. III.2. and analyse the system mainly in terms of observables which are directly accessible by the experiment [73].

Naturally, one expects to find a regime in time and distance to the critical point where the Bogoliubov results of chapter III are valid, in particular the predictions for $\mathcal{G}_{zz}(t,k)$ (see Sect. III.2). In particular, we find that meanfield scaling stops being valid for quenches

to distances to the critical point smaller than $\varepsilon_\mathrm{f} \lesssim 0.1$. For smaller distances, scaling behaviour is replaced by a crossover-like behaviour, similar to the expectations for a thermal system in one spatial dimension.

In this chapter, we concentrate on identifying the deviations of the full simulation from Bogoliubov theory from the point of view of observables in momentum space. The next chapter VI is dedicated to the question if the quench dynamics of position space correlations can nevertheless be formulated in terms of universal functions. To answer it we will use the similarity of our model to the transverse-field Ising chain and exploit its analytically computable universal scaling functions.

In both chapters (this and VI), we present simulation results obtained from applying the Truncated Wigner method [83, 84], discussed in Sect. II.5.1, to the full model for two-component Bose gas (Eq. (II.1)). Additional details on the simulations are described in Appendix B and, in particular, numerical parameters are described in detail in Sect. B.3. Figures are presented in natural units of $2J_\mathrm{c}$ (see Sect. B.1).

V.1 Sampling of the Initial State

Before we present and discuss the results from semi-classical simulations, we discuss the sampling procedure of the initial state. The final goal is to implement a parameter quench in J, as discussed in Sect. III.2, with a well defined (in terms of spin fluctuations) initial state. As the time evolution itself in the semi-classical approximation is simply generated by the classical equations of motions, the post-quench coupling, J_f, can be directly set in the equations Eq. (II.42). The quench scenario is then defined by the choice of the initial spin fluctuations. Apart from the fact that the Wigner function of the initial state needs to be known in advance, an additional complication is thereby that we need to sample fluctuations in the fundamental fields $\phi_i(k, t_0)$, $\phi_i^\dagger(k, t_0)$ (see Sect. II.5.1). Therefore, the initial fluctuations in the spin fields can not be set directly.

We proceed as follows. First, we discuss how we sample in practice the fundamental classical fields $\phi_i(k, t_0)$, $\phi_i^\dagger(k, t_0)$, to initialise the simulations from a well defined initial state in the language of Wigner functions. Thereafter, we derive to which initial state for the spin fluctuations this maps. Finally, we summarise the quench setup which is implemented in simulation. Essentially, the initial state which is sampled in the numerical simulations corresponds to the groundstate of the spin sector at $J = J_\mathrm{i} \to \infty$, including quantum fluctuations.

Initial State in the Fundamental Field Picture

The quality of the truncated Wigner approximation depends to a high degree on the sampled initial Wigner distribution. In general, it is beneficial if the exact analytic form of the distribution is known which is for example the case for the non-interacting homogeneous Bose gas at zero temperature.

Here, we take advantage of that fact and choose to sample the initial field configurations for each component independently from the Wigner distribution of a non-interacting zero-temperature gas. Expanding the field in the momentum basis it implies that the non-zero momentum modes have to be seeded with complex numbers drawn from a complex

Gaussian probability distribution. The zero mode needs to be filled deterministically with the remaining particles, reassembling the condensate. The initial field realisations for each component are therefore given by

$$\phi_i(k) = \sqrt{\mathcal{N}_i}\delta_{k,0} + c_{k\neq 0}\,, \tag{V.1}$$

where c_k are Gaussian random numbers with $\langle c_k\rangle = 0$ and $\langle c_k^* c_k\rangle = 0.5$. The deterministic part $\mathcal{N}_i$ is to be chosen such that $\sum_k \langle \phi_i^*(k)\phi_i(k)\rangle = N_i$. The standard deviation of the c_k leads to half a particle per non-zero momentum mode on average which is the classical statistical representation of the quantum vacuum at zero temperature.

The subsequent time evolution of the fields is computed with the classical equations of motion Eq. (II.42) at non-zero linear and non-linear coupling constants. Thus, from the point of view of the two-component Bose gas, all couplings $g_\uparrow$, $g_\downarrow$, $g_{\uparrow\downarrow}$, and J are quenched instantaneously to a non-zero value, where 'instantaneously' here means on the time scale of the numerical temporal resolution.

Initial State in the Spin Picture

It is equally important how the above described initial field distribution is represented in the spin picture. When the distribution is transformed from the Fourier mode expansion to position space, the Gaussian distributed non-zero modes are incoherently added to the zero mode. This results in a complex Gaussian[1] distribution for the fields, at every site of the position-space grid, with a non-zero mean, $\langle\phi_i(y)\rangle = \sqrt{n_0 - 1/2}$, and variance $1/2$.

The density and phase fields do, strictly speaking, not follow a Gaussian distribution. However, for high mean densities $n_0 \gg 1$ a Gaussian distribution is a good approximation for both fields. One finds then the mean of the density field distribution, being equal to the second moment of the complex field distribution, $\langle n_i(y)\rangle = n_0$, and a variance for the density field distribution of $\Delta n_i(y) = n_0$.

Under the assumption of high mean densities, the z-projection of the spin field can also be taken to be Gaussian distributed at every grid point, as one has then approximately $S_z = (n_\uparrow - n_\downarrow)/(n_\uparrow + n_\downarrow) \simeq (n_\uparrow - n_\downarrow)/2n_0$. By virtue of Gaussian error propagation, the variance of the z spin distribution is consequently $\Delta S_z(y) = [\Delta n_\uparrow(y) + \Delta n_\downarrow(y)]/4n_0^2 = 1/2n_0$.

Similar considerations for the condensate density field, $n_+ = (n_\uparrow + n_\downarrow)/2$, lead to a variance of $\Delta n_+(y) = n_0/2$. The means are $\langle S_z(y)\rangle = 0$ for the spin field and $\langle n_+(y)\rangle = n_0$ for the condensate field, respectively. The position-space distribution of the phase fields has a well defined mean and variance due to the deterministic phase of the zero mode. Otherwise, the phase fields would be uniformly distributed.

For high mean density, the phase fields of the individual components are approximately determined by $\theta_i = \sin\left(\mathrm{Im}\,\phi_i/\sqrt{\phi_i^*\phi}\right) \simeq \mathrm{Im}\,\phi_i/\sqrt{n_0}$. Within that approximation the phase fields can be considered to be distributed according to a Gaussian at every point of the grid, since the imaginary part of the complex field is so, too. Thus, the variances are

[1] If $\bar{\phi}(y)$ is the mean and σ^2 the variance the complex normal distribution we refer to is of the form $\mathcal{P}[\phi^*(y),\phi(y)] = \prod_y \frac{1}{\pi\sigma^2}\exp\left\{-\sigma^{-2}\left[\phi(y) - \bar{\phi}(y)\right]^2\right\}$.

$\Delta\theta_i(y) = \Delta \operatorname{Im}\phi_i/n_0 = 1/4n_0$.

As the two phase fields are statistically independent, naturally, their symmetric and anti-symmetric combination is, within the approximation $n_0 \gg 1$, as well Gaussian distributed with zero mean values, $\langle\theta_-(y)\rangle = \langle\theta_+(y)\rangle$. The variances are again obtained by means of Gaussian error propagation, $\Delta\theta_-(y) = \Delta\theta_+(y) = 1/2n_0$. Note that the distribution of θ_- is connected to the distribution of the spin fields on the equator of the Bloch sphere.

For small fluctuations of S_z and θ_-, which is the case for the initial conditions we describe here, the spin projection in y direction, $S_y = \sqrt{(1-S_z^2)}\sin\theta_-$, is to lowest non-trivial order approximated by $S_y \simeq \theta_-$. Therefore, the variances are directly equal, $\Delta S_y(y) = \Delta\theta_-(y)$, to quadratic order in the fluctuating fields (*cf.* also chapter III). At the same level of approximation, the x projection of the spin needs to be assumed non-fluctuating, $\langle S_x(y)\rangle = 1$ and $\Delta S_x(y) = 0$, as the linearised mapping between relative phase and density and spin does not take the curvature of the Bloch sphere into account.

Quench Setup in the Simulations

The initial state, in terms the Wigner distribution for the uncoupled system at zero temperature, is defined as a product of probability distributions which are completely local in momentum or position space. Consequently, the local variances determine the connected second order correlation functions via $G_X(y-y') = \Delta X\,\delta(y-y')$. Due to the Gaussianity of the field distribution, correlation functions of higher order have no non-zero connected contribution.

From the perspective of the spin sector, the initial state appears as follows. The mean field configuration is given by $\langle S_z(y)\rangle = \langle S_y(y)\rangle = 0$ and $\langle S_z(y)\rangle = 1$, resembling the configuration for which we carried out the Bogoliubov transformation in chapter III. The initial two-point correlation functions in the spin sector read

$$\begin{aligned}\langle S_z(y)S_z(y')\rangle &= \frac{1}{2n_0}\delta(y-y')\,,\\ \langle\theta_-(y)\theta_-(y')\rangle &= \frac{1}{2n_0}\delta(y-y')\,.\end{aligned} \tag{V.2}$$

In Sect. III.3 we have used this particular state to set off the Bogoliubov dynamics and have also argued that this state is the Bogoliubov groundstate[2] for $J \to \infty$. Here, we have found that the state emerges quite naturally when choosing two uncoupled Bose gases at zero temperature as initial state. Thus, as far as it concerns the spin sector, it is equivalent to either suddenly switch on $g_{\uparrow\downarrow}$ and J for two uncoupled gases or prepare a superposition at $J = \infty$ and then change J to a finite value.

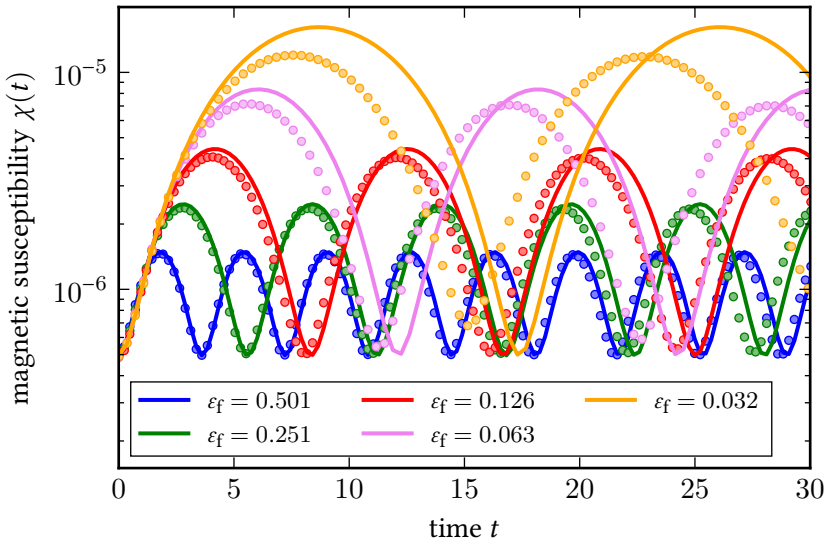

Figure V.1: Time evolution of the magnetic susceptibility $\chi(t)$ (Eq. (V.3)) after a deep quench to the meanfield distance ε_f from the critical point. Data points correspond to simulation data, where averages have been taken over $\mathcal{N} = 8192$ realisations and parameters from Table B.2 have been used. Solid lines show the corresponding Bogoliubov predictions from Eq. (III.46) at corresponding ε_f. Note the logarithmic y-axis. In this and in all following figures numerical data is plotted in natural units, defined in terms of $2J_c$ (see Sect. B.1).

V.2 Quench Dynamics of the Susceptibility

We start the discussion of our numerical results by comparing the data from the non-perturbative dynamics drawn from the simulation to the Bogoliubov dynamics (see Sect. III.2) for the magnetic susceptibility.

Throughout this chapter and the next VI, we work with the following numerical parameters if not stated otherwise. The system is resolved with 2^{14} Fourier modes, where the ultra-violet cut-off is set at $k_{UV} = 11\sqrt{2mn_+g}$ and the infrared cut-off at $k_{IR} = 0.003\sqrt{2mn_+g}$. Ensemble averages as required by the Truncated Wigner method (see Sect. II.5.1) are taken over $\mathcal{N} = 8192$ realisations. We keep the inter- to intra-species ratio of the coupling strengths at the value $\alpha = g_{\uparrow\downarrow}/g = 1.23$ (see Eq. (II.1)) as it is the case in the experimental setup of [73]. The numerical realisation of the quench, as we described it in the previous section, also resembles the situation in that experiment.

On general grounds, it is expected that any form of fluctuations, quantum, thermal, or classical-statistical, grow more influential as the system is parametrically tuned to the critical coupling. In turn, one should expect the Bogoliubov analysis to be valid close to $\varepsilon_f \simeq 1$. For a similar reason, the system can be expected to stay in the linear regime for

[2] As the system is effectively linear for $J \to \infty$, the Bogoliubov groundstate actually equals the true ground-state

early times, $t \ll 1/\Delta$. We set the stage for that with the magnetic susceptibility, as it is a comparatively simple observable but allows already identifying the important effects of the non-linearities. The quantity is extracted from the infrared limit of the numerically computed spin occupation spectrum (see also Eq. (III.44) and Sect. III.3.2),

$$\chi(t) = \lim_{k\to 0} \mathcal{G}_{zz}(t,k)\,. \tag{V.3}$$

Examples for the time evolution of $\chi(t)$ after a quench to ε_f as computed from direct numerical simulation are shown in Fig. V.1 (coloured data points). As compared to the Bogoliubov prediction Eq. (III.46), which is also shown in Fig. V.1, one finds that Eq. (III.46) describes the data for $\varepsilon_\mathrm{f} \gtrsim 1$ and for $t \lesssim \pi/2\Delta_\mathrm{f}$ to a good degree. Recall, that the gap Δ_f in the post-quench dispersion sets the oscillation frequency in $\chi(t)$ in the Bogoliubov time evolution (see Eq. (III.46)). On the other hand, we find that the oscillation period, which should be set by the spectral gap, quickly detunes from the Bogoliubov prediction as ε_f decreases. In the next section, we will find that this detuning can be mapped to a time-independent change of the oscillation frequency.

The amplitude of the susceptibility undershoots the Bogoliubov scaling prediction $\chi \sim \varepsilon_\mathrm{f}^{-1}$ (see discussion in Sect. III.3.2) as ε_f decreases. Although it is not yet a dominating effect on the timescale we show in Fig. V.1, the amplitude is not a static quantity any more but decays towards a stationary value for ε_f close to the critical point.

Scaling of the Susceptibility

We analyse the time evolution of the amplitude and its scaling behaviour further in Fig. V.2. As determined from Bogoliubov theory, the amplitude should display scaling behaviour, $\chi(\tau_i, \varepsilon_\mathrm{f}) \sim \varepsilon_\mathrm{f}^{-\nu(2-\eta)}$, allowing to disentangle spatial and temporal rescaling. Here, we therefore analyse the times τ_i where $\chi(\tau_i, \varepsilon_\mathrm{f}) = \max\chi(t, \varepsilon_\mathrm{f})$ has a local maximum, but do so for subsequent maxima. At each τ_i one can individually test the scaling prediction in ε_f and simultaneously analyse the effects from the decay in time (see Fig. V.1).

For $\varepsilon_\mathrm{f} \simeq 1$ in Fig. V.2, the amplitude of the susceptibility follows indeed the meanfield scaling prediction, $\chi_\mathrm{max} \sim \varepsilon_\mathrm{f}^{-1}$. Closer to the meanfield critical point, however, the behaviour deviates from a power law. In fact, the susceptibility seems to saturate towards a finite value at the critical point rather than to diverge.

This comes not unexpected for a interacting theory in one spatial dimension, as critical scaling is typically destroyed by fluctuations. In the full simulation, the non-linear interactions are quenched (suddenly switched on), amplifying the energy contained in the small initial fluctuations of high-momentum mode occupations. These fluctuations can be expected to have similar consequences for scaling behaviour as finite-temperature fluctuations.

In Fig. V.2, we find that the amplitudes $\chi(\tau_i, \varepsilon_\mathrm{f})$ decay in time close to the critical point $\varepsilon_\mathrm{f} \to 0$. In the scaling region $\varepsilon_\mathrm{f} \gtrsim 0.1$, the amplitudes are time independent, as predicted by Bogoliubov theory. The inset in Fig. V.2 shows the decay of the saturation plateau in time beyond the first four maxima for small ε_f. In particular, the saturation plateau for small distances to the critical point decays exponentially in time (note logarithmic scale) within the first 10 oscillation maxima. The decay then seems to slow down before

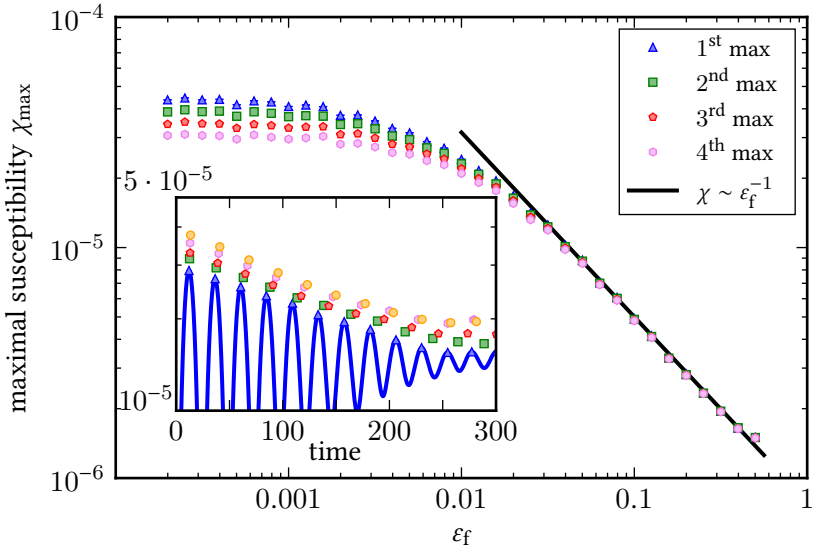

Figure V.2: The maximal magnetic susceptibility at the first four consecutive maxima (*cf.* Fig. V.1) is shown as a function of distance to the meanfield critical point. Note the double-logarithmic scale. The same dataset is shown as in Fig. V.1, with a largely extended number values for ε_f. The scaling with ε_f follows the Bogoliubov prediction for $\varepsilon_f \simeq 1$. Thereafter the amplitude of the susceptibility deviates from a power-law behaviour and seemingly saturates as $\varepsilon_f \to 0$. The saturation plateau additionally decays in time, *i. e.* for small ε_f. Inset: Decay of the plateau as a function of time. Note the logarithmic y-axis. The decaying envelope of the susceptibility is depicted for five different values of ε_f within the plateau region. For $\varepsilon_f = 0.004$ the whole functional dependence is shown in addition (blue line). The decay proceeds initially exponential and slows down thereafter.

reaching a stationary value. Note that the simulation data we show in Fig. V.2 are at the limit concerning the total simulation time with the parameters of Table B.2. Thereafter, recurrence effects on the finite periodic simulation domain set in, leading to a revival of the amplitude of the susceptibility.

Frequency Shift in the Susceptibility

We turn back to the temporal behaviour of the magnetic susceptibility, as shown in Fig. V.1. In Bogoliubov theory, the oscillations are a direct consequence of the finite spectral gap and its value sets the oscillation period (*cf.* Eq. (III.46)). Assuming that interactions let this dependency intact but change the value of the gap itself, a shift of the gap can be computed from simulation data and analysed for scaling behaviour in ε_f.

The simulation data used for Fig. V.1 allows us to extract the time τ_i at which the maximal susceptibility is achieved, $\chi(\tau_i) = \chi_{\max,i}$, without knowing the exact properties of

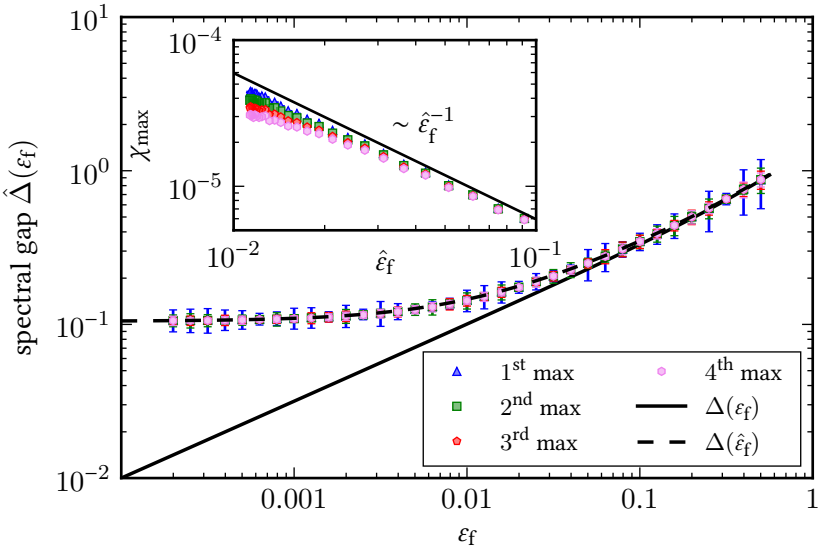

Figure V.3: The figure shows the spectral gap $\hat{\Delta}_f(\varepsilon_f)$, which is numerically determined from the oscillation period of the magnetic susceptibility (see discussion in the main text), as a function of the distance to the meanfield critical point ε_f. The same data set is analysed as in Fig. V.1 and Fig. V.2. Coloured data points represent the shifted gap as determined from the first four subsequent maxima of $\chi(t)$. Within numerical errors, there is no dependence on the maximal times τ_i. The solid black line represents the Bogoliubov prediction Eq. (II.43) for the gap, evaluated with respect to the distance ε_f to the meanfield critical coupling J_c. The dashed black line represents the same function evaluated with respect to the distance $\hat{\varepsilon}_f$ to a shifted critical coupling aJ_c (see Eq. (V.6)). The shift is determined by a fit which yields $a = 0.989 \pm 0.0005$. The inset shows the maximal magnetic susceptibility at the first four maxima (coloured points, same colour code as in main figure), equivalent to Fig. V.2, with respect to the shifted distance $\hat{\varepsilon}_f$, together with the scaling prediction $\chi_{max} \sim hef^{-1}$ (solid black line in inset).

the decaying envelope of the oscillations. As $\chi(t) \sim \sin(\Delta t)^2$ by assumption, one finds the shifted spectral gap from numerical data

$$\hat{\Delta}_f = \left(i + \frac{1}{2}\right) \pi \tau_i^{-1}, \tag{V.4}$$

with $i \in \mathbb{N}_0$.

The result of this analysis for the simulation data presented in Fig. V.1 and Fig. V.2 is shown in Fig. V.3, where $\hat{\Delta}_f$ is extracted from several successive maxima of the susceptibility. We find that the quantity we extract from the oscillation period is independent from the analysed maximum. This strengthens the assumption that the $\sin^2$ form of oscillations for susceptibility is still given beyond Bogoliubov theory, with one ε_f-dependent

but time-independent period.

The oscillation period, however, acquires a strong shift as compared to the Bogoliubov prediction, as was already qualitatively visible from Fig. V.1. The numerically extracted values $\hat{\Delta}_\mathrm{f}(\varepsilon_\mathrm{f})$ from Fig. V.3 allow us to quantify that further. The shift leads to higher values of the gap as the distance to the meanfield critical point decreases (*cf.* coloured data points and solid black line in Fig. V.3). In particular, the shifted gap $\hat{\Delta}_\mathrm{f}(\varepsilon_\mathrm{f})$ bends away from the Bogoliubov scaling behaviour $\Delta_\mathrm{f}(\varepsilon_\mathrm{f}) \sim \varepsilon_\mathrm{f}^{1/2}$ for $\varepsilon_\mathrm{f} \lesssim 0.1$. If the oscillation period of the susceptibility indeed reflects the effective, *i. e.* by fluctuations renormalised, spectral gap, it is expected that it keeps a non-zero value when crossing the transition in one spatial dimension.

The behaviour of the numerically extracted shifted gap in Fig. V.3, on the other hand, can also be consistent with a static shift of the location of the critical point with respect to the Bogoliubov prediction. In particular, it can be tested if the shift in the gap is described by a shift in the distance from the critical point

$$\hat{\Delta}_\mathrm{f}(\varepsilon_\mathrm{f}) = \sqrt{\hat{\varepsilon}_\mathrm{f}(\hat{\varepsilon}_\mathrm{f}+1)}\,, \tag{V.5}$$

if the Bogoliubov functions are kept.

Assume that the zero-temperature critical point is actually located at $\hat{J}_\mathrm{c} = aJ_\mathrm{c} = -ag_- n_0$. Then ε_f and $\hat{\varepsilon}_\mathrm{f}$ are connected via

$$\hat{\varepsilon}_\mathrm{f} = \frac{J-\hat{J}_\mathrm{c}}{\hat{J}_\mathrm{c}} = \frac{\varepsilon_\mathrm{f}+1}{a} - 1\,. \tag{V.6}$$

Numerically, one can ask the question if there is a shift parameter a such that the Bogoliubov prediction at $\hat{\varepsilon}_\mathrm{f}$, *i. e.* Eq. (V.5), describes the numerically extracted value for $\hat{\Delta}_\mathrm{f}$. For the simulation data presented in Fig. V.3 this is possible, with a shift parameter $a = 0.989 \pm 0.0005$. Thus, we find that the assumption $\hat{\Delta}_\mathrm{f}(\varepsilon_\mathrm{f})$ from Eq. (V.5) consistently describes the data in Fig. V.3 with Eq. (V.6) and $a = 0.989 \pm 0.0005$. This would imply that the shifted gap is zero for quenches to $J_\mathrm{f} = aJ_\mathrm{c}$ and oscillations in $\chi(t)$ vanish there. However, from currently available data it can not be decided if this description in terms of a shifted critical point remains valid when going to smaller values of $\varepsilon_\mathrm{f} \ll 0.0002$.

The inset in Fig. V.3 shows that re-evaluating the data for $\chi(\tau_i, \varepsilon_\mathrm{f})$ with respect to $\hat{\varepsilon}_\mathrm{f}$ does not fully explain the behaviour of the magnetic susceptibility in terms of the Bogoliubov scaling. In the inset of Fig. V.3 the scaling of the maximal magnetic susceptibility is analysed with respect to $\hat{\varepsilon}_\mathrm{f}$. We find that, although the effect is not as dominant as in Fig. V.2, the amplitude of the magnetic susceptibility turns away from the scaling prediction, towards a finite value also at $\hat{\varepsilon}_\mathrm{f} = 0$. This implies that there a renormalisation effects beyond a static shift of the critical point alone.

V.3 The Quasi-Particle Excitation Spectrum

Our results so far suggest that the influence of non-linear interactions in our setup can be grouped in two parts, which can be analysed separately. The rather obvious part consists of a modification of quasi-particle properties, *i. e.* the dispersion relation ω_- and the

mode function f_k. A change of the latter can capture deviations in the amplitude of mode occupations. The second part concerns the stability of the quasi-particles. The decay we have identified for the susceptibility most likely originates in a change of quasi-particle mode occupations over time, which can be generated through quasi-particle scattering, a finite life time, or quasi-particle creation through coupling to the symmetric sector.

In this section, we analyse the change of spectral properties of the Bogoliubov quasi-particles when subject to interactions. In doing so, we rely on the assumption that observables still evolve close to the functional dependencies deduced from Bogoliubov theory. Similar to the approach of perturbative Wilsonian renormalisation group (see for example [127]), we rather quantify the consequences of interactions of Bogoliubov particles by shifts of parameters, *i. e.* the spectral gap, the speed of sound, and the dynamical exponent z.

So far we have extracted information on the excitation spectrum purely by relying on Bogoliubov functions and using only the zero mode of the full spin-spin correlation function. We point out that the approach from the last section is in particular feasible for experimental setups, as only knowledge about equal-time correlation function of the spin in one direction is required. The results raise the question how the whole quasi-particle excitation spectrum $\omega_-(k,t)$, beyond the gapped momentum region, changes under interactions. To answer it, we use a different approach to calculate the mode energies. Although it is in principle possible to determine oscillation periods from non-zero momentum modes of the correlation function, its impractical from a numerical point of view. Furthermore, a scheme which requires less input from Bogoliubov theory is advantageous for a consistency check.

Ideally, one would compute spectral functions for the spin degrees of freedom to, first, confirm the existence of quasi-particles and, second, compute their energy spectrum. The classical-statistical approach requires then to compute Poisson brackets of the spin fields which in turn implies to compute functional derivatives. It is questionable if this can be done in a numerically stable way and is in any case an unfeasibly demanding numerical procedure.

Instead, assuming that there are dominant quasi-particle excitations present in the interacting system, information on their energy spectrum can also be retrieved from the two-time correlation functions. In [206] for example, it is argued for relativistic $O(N)$ models that a two-time derivative of the form

$$|\omega(k,t)|^2 = \frac{\partial_{t_1}\partial_{t_2}F(t_1,t_2,k)}{F(t_1,t_2,k)}\Big|_{t_1=t_2=t}, \tag{V.7}$$

returns the squared modulus of the dispersion relation $\omega(k)$ for the order parameter field $\phi(t,k)$, if $F(t_1,t_2,k) = \langle\{\phi(t_1,k),\phi^\dagger(t_2,k)\}\rangle/2$ is the statistical two-point correlation function at times t_1 and t_2.

We can apply a similar reasoning here for the spin fields, when correcting for the different relation between fields and conjugate momenta. For the Bogoliubov operators of the spin fields we have shown that $\partial_t\delta n_k(t) = n_0 f_k^2\omega_-(k)\delta\theta_k(t)$ and similarly $\partial_t\delta\theta_k(t) = \omega_-(k)\delta n_k(t)/(n_0 f_k^2)$ (see Eq. (III.30) and subsequent text). Thus, for the two-time correlation function of the z-spin field and its conjugate field one finds within Bo-

goliubov dynamics

$$\partial_{t_1}\partial_{t_2}\langle S_z(t_1,k)S_z(t_2,k)\rangle = \omega_-^2(k) f_k^4 \langle \theta(t_1,k)\theta(t_2,k)\rangle \,,$$
$$\partial_{t_1}\partial_{t_2}\langle \theta(t_1,k)\theta(t_2,k)\rangle = \frac{\omega_-^2(k)}{f_k^4}\langle S_z(t_1,k)S_z(t_2,k)\rangle \,. \tag{V.8}$$

This implies that the denominator in Eq. (V.7) is to be replaced by the correlation function of the conjugate momenta. But even then, Eq. (V.7) would not fall back on to the Bogoliubov spin dispersion relation but rather yield one half-axis of the squeezing ellipse of mode k. Therefore, we combine the two-time derivatives in the form of Eq. (V.7) of the two-time correlation functions of both spin fields to obtain the dispersion relation independently

$$\omega_-^4(k,t) = \frac{\partial_{t_1}\partial_{t_2}G_{zz}(t_1,t_2,k)\partial_{t_1}\partial_{t_2}G_{\theta\theta}(t_1,t_2,k)}{G_{zz}(t_1,t_2,k)G_{\theta\theta}(t_1,t_2,k)}\Big|_{t_1=t_2}, \tag{V.9}$$

with central time $t = (t_1 + t_2)/2$. This quantity falls back on to the Bogoliubov spin dispersion $\omega_-(k)$ if the correlation functions evolve close to the Bogoliubov prediction, without requiring any prior knowledge.

The expression Eq. (V.9) can be computed independently from the statistical fields S_z and θ obtained from simulation and yields a time dependent quasi-particle dispersion relation at any instance in total time T. Additionally, as it is computed from time derivatives at time T, the two-time correlation functions need to be known only close to the central line $t_1 = t_2$. This is not only advantageous for a numerical treatment but also for measurements from experiment. If a procedure can be implemented which non-destructively retrieves subsequent spin density profiles, it will be certainly more feasible to do this for small time differences and only a few subsequent time steps. The expressions Eq. (V.9) and Eq. (V.7) can phenomenologically be viewed as locating the maximum of the statistical correlation functions in the coordinate space of relative time $s = t_1 - t_2$ and momentum k and then attributing a frequency ω to the relative time s. This will inevitably fail if there is no dominant quasi-particle branch present. In any case, there is no statement about the stability or lifetime of the quasi-particles retrievable.

For the remainder of this section, we put Eq. (V.9) to practical application for our quench setup in the spinor Bose gas. To calculate the expression for $\omega_-(k,t)$ in practice, the two-time derivatives in Eq. (V.9) are approximated by discrete central derivatives,

$$\partial_{t_1}\partial_{t_2}F(t_1,t_2)|_{t_1=t_2=T} \to$$
$$\frac{F(T+h,T+h) - F(T+h,T-h) - F(T-h,T+h) + F(T-h,T-h)}{4h}, \tag{V.10}$$

where h is the timestep of the simulation. Thus, in addition to the equal-time correlation function at central time t only the off-diagonal elements of the correlation functions at $t \pm h$ need to be evaluated.

For the computing $\omega_-(k,t)$ in the following from our simulation, we choose parameters for the simulation from Table B.3. Due to the involvement of unequal-time cor-

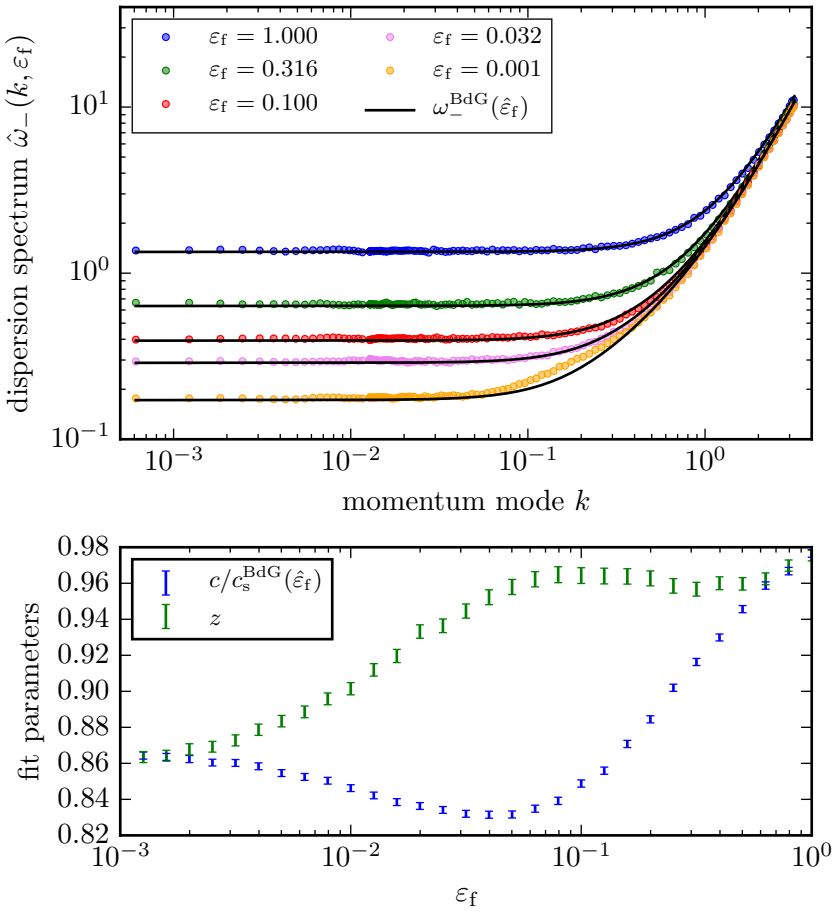

Figure V.4: Upper panel: Dispersion relation $\hat{\omega}_-(\varepsilon_f, k)$ as directly determined from simulation via the two-time derivative of unequal-time spin correlation functions (see Eq. (V.9)) for quenches to the distance ε_f from the meanfield critical point (as given in the legend). Coloured data point correspond to the temporally averaged (over central time) dispersion $\hat{\omega}_-(\varepsilon_f, k)$ (see Eq. (V.11) and main text). Black lines next to the coloured data points correspond to the evaluation of the Bogoliubov dispersion (Eq. (III.11)) at a shifted distance $\hat{\varepsilon}_f$. The shift is determined from the gap as discussed in the context of Fig. V.3 (see main text). Lower panel: The function $\omega_-^{fit}(k, c, z)$, given in Eq. (V.12), is fitted to the data for $\hat{\omega}_-(\varepsilon_f, k)$ to fit a speed of sound c and a dynamical exponent z as a function of ε_f (see main text). The result is displayed in the lower panel. The gap in the dispersion is determined independently (see main text). For reasons of visibility we display in the upper panel five example curves out of the full data set consisting of 30 values for ε_f (as displayed the lower panel). Numerical parameters given in Table B.3 have been used.

relation functions, the observable is more sensitive to noise as compared to equal-time structure factors. To compensate for that, it is advantageous to divert a larger fraction of the momentum-space computational grid to the infrared region $k < 1$. Additionally, we average the numerically determined $\omega_-(k,t)$ over several successive central times t.

In practice, it turns out that $\omega_-(k,t)$ is only weakly time-dependent. Within the window for ε_f and central time from Fig. V.3 there was no change in time t of $\omega_-(k,t)$ determinable within the numerical accuracy. This is consistent with Fig. V.3, where also no time independence of the numerically determined gap was found within the first four oscillations.

Therefore, in the following we present data for the temporally averaged dispersion functions

$$\hat{\omega}_-(\varepsilon_\mathrm{f},k) = \sum_i \frac{\omega_-(\varepsilon_\mathrm{f},k,t_i)}{\mathcal{N}}\,, \tag{V.11}$$

are shown for different distances to the meanfield critical point. We choose $\mathcal{N} = 100$ linear equidistant times t_i between $t = 0$ and $t = \tau_4$, the fourth oscillation maximum of the corresponding susceptibility $\chi(\varepsilon_\mathrm{f},\tau_4)$, *cf.* Fig. V.1.

We find in Fig. V.4 that the numerical dispersion functions follow qualitatively the general Bogoliubov form. This means that they start gapped, $\lim_{k\to 0}\hat{\omega}_-(\varepsilon_\mathrm{f},k) > 0$. Thereafter a momentum region follows where $\hat{\omega}_-(\varepsilon_\mathrm{f},k) \sim k^z$ with $z < 2$. Finally the dispersion relations turn towards the free-particle form, $\hat{\omega}_-(k) \sim k^2$, beyond the infrared momentum region $k \gtrsim 1$.

Consistently with the results from Fig. V.3, a quantitative analysis of the numerical data for $\hat{\omega}_-(\varepsilon_\mathrm{f},k)$ yields that the gap acquires a shift as compared to the Bogoliubov prediction, $\hat{\omega}_-(\varepsilon_\mathrm{f},k\to 0) > \Delta(\varepsilon_\mathrm{f})$. As has been discussed for Fig. V.3, one can adopt the point of view that the Bogoliubov functions are usable as skeletons, where the parameters gap, speed of sound, and distance to the critical point can shift.

Also here, the simplest scenario is to assume a shift of $\varepsilon_\mathrm{f} \to \hat{\varepsilon}_\mathrm{f}$ and check that for consistency. The black lines in Fig. V.4 close to the coloured data points for $\hat{\omega}_-(\varepsilon_\mathrm{f},k)$ represent this consistency check. First, the effective gap parameter $\hat{\Delta}_\mathrm{f}$ is determined as described with Fig. V.3 and then converted to an effective distance $\hat{\varepsilon}_\mathrm{f}$ via $\hat{\Delta}_\mathrm{f} = \sqrt{\hat{\varepsilon}_\mathrm{f}(\hat{\varepsilon}_\mathrm{f}+1)}$.

This is inserted in the Bogoliubov dispersion function and displayed as the black lines in Fig. V.4. They therefore show the function $\omega_- = \sqrt{\Delta^2(\hat{\varepsilon}_\mathrm{f}) + c_\mathrm{s}^2(\hat{\varepsilon}_\mathrm{f})k^2 + k^4}$, where $c_\mathrm{s}(\hat{\varepsilon}_\mathrm{f}) = \sqrt{2\hat{\varepsilon}_\mathrm{f}+1}$. We find that the effective gap parameter is consistently described over the whole range of tested ε_f whereas the parameter describing the speed of sound is not. In the momentum region of the linear part in the dispersion function, a clear deviation between numerical data and the Bogoliubov dispersion $\omega_-(\hat{\varepsilon}_\mathrm{f},k)$ function, evaluated at $\hat{\varepsilon}_\mathrm{f}$, is found.

We find that it is possible to fit the simulation data for $\hat{\omega}_-(\varepsilon_\mathrm{f},k)$ in Fig. V.4 if two additional free parameters are allowed for in the Bogoliubov dispersion function,

$$\omega_-^\mathrm{fit}(k,c,z) = \sqrt{\Delta^2(\hat{\varepsilon}_\mathrm{f}) + c^2\kappa^{2z} + k^4}\,. \tag{V.12}$$

In the lower part of Fig. V.4, the result for fitting an effective speed of sound parameter c and dynamical exponent z to the whole dataset for $\hat{\omega}_-(\varepsilon_\mathrm{f},k)$ is shown. From that we

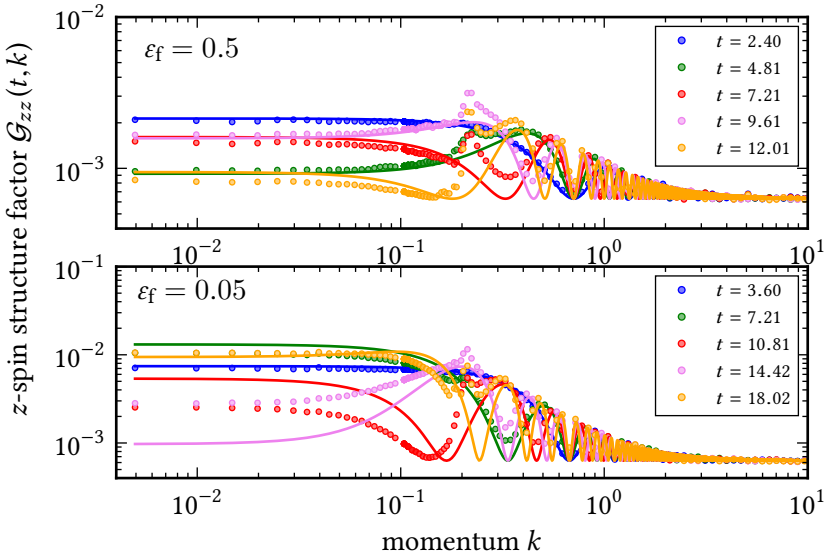

Figure V.5: Examples for the post-quench time evolution of the z-spin structure factor $\mathcal{G}_{zz}(k,t)$ for two different distance to the critical point $\varepsilon_f = 0.5$ (upper panel) and $\varepsilon_f = 0.05$ (lower panel). Coloured data points correspond to data from simulation at different times (see legend). Coloured solid lines show the correspondingly evaluated Bogoliubov structure factor Eq. (III.49). Simulation parameters from Table B.2.

find that not only c starts to differ from $c_s(\hat{\varepsilon}_f)$ as $\varepsilon_f \to 0$ but also the dynamical exponent changes.

Both fit parameters seem to reach a common limit value for $\varepsilon_f \to 0$. However, from the currently available data set it is not clear if the values for z and c truly reach a limit or further decrease. It is a realistic scenario that one of the parameters further decreases and reaches 0, meaning that the dispersion would renormalise under interactions to a gapped free-particle dispersion. If both parameters stay non-zero, it is most likely a coincidence that $c/c_s^{BdG} \simeq z$ for $\varepsilon_f \simeq 0.001$, as the two parameters have different physical meaning. To interpret these results further, analytic predictions beyond Bogoliubov theory are required.

V.4 Dynamics of the Structure Factor

With the magnetic susceptibility $\chi(t)$, we have already analysed the quench dynamics and scaling properties of the infrared part of the z-spin structure factor (see Eq. (V.3)). In this section, we complete the analysis by discussing the post-quench dynamics of the full structure factor $\mathcal{G}_{zz}(k,t)$.

In the upper panel of Fig. V.5 we show the time evolution of the spin structure factor $\mathcal{G}_{zz}(t,k)$ after a quench to $\varepsilon_f = 0.1$ for early times, as obtained from full simulations. In general, the Bogoliubov form for the spin structure factor, *i. e.* expression Eq. (III.49),

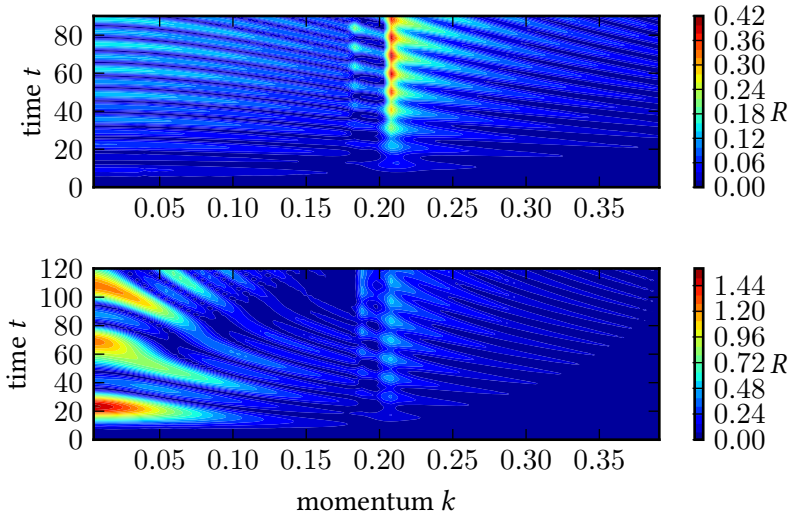

Figure V.6: The figure shows, exemplary for two values of ε_f, the deviation between full simulation and the Bogoliubov prediction for the z-spin spectrum in the whole time-momentum plane. The quantity $R = |\mathcal{G}_{zz}(k,t) - \mathcal{G}_{zz}^{\mathrm{BdG}}(k,t)|/\mathcal{G}_{zz}(k,t)$ is depicted in colour projection, where the upper panel is computed at a meanfield value of $\varepsilon_f = 0.05$ and the lower panel at $\varepsilon_f = 0.005$. The same dataset is used for this figure as for Fig. V.2 and Fig. V.1. The depicted momentum range is restricted to a region where a significant relative deviation is visible. We find a distinctively large peak of deviation R at momentum $k \simeq 0.2$, starting to appear at time $t \simeq 20$. This feature is independent of the value of ε_f. This deviation is possibly caused by a non-linear dynamical instability of momentum modes in this region, which is not present in the Bogoliubov theory. Simulation parameters from Table B.2

describes the data from simulation to a good degree (compare coloured solid lines and coloured data points in the upper panel of Fig. V.5). As can be also seen from the comparison, shifts from interactions affect the deep infrared part of the spin occupation spectrum first. The temporal oscillation frequency of the plateau in the spectrum from simulation at $k \ll \sqrt{\varepsilon_f}$ is already slightly detuned from the Bogoliubov spectrum. A second dominant discrepancy between Bogoliubov theory and full simulation in the spin occupation spectrum is the development of a large peak structure around the scale $k = \sqrt{\varepsilon_f}$. This happens already for very early times, when the plateau is still described by Bogoliubov theory.

In the lower panel of Fig. V.5 we show for comparison the time evolution for the spin occupation spectrum $\mathcal{G}_{zz}(t,k)$ after a quench to $\varepsilon_f = 0.01$ for similarly early times. Here, we find that oscillation frequencies of all modes in the infrared $k < 1$ are already strongly detuned as compared to Bogoliubov theory. The peak structure at $k = 0.2$ is also visible and has not shifted due to the changed ε_f.

For both distanced to the critical point in Fig. V.5, spatial and temporal oscillation patterns in the spin occupation spectrum match between Bogoliubov theory and full simulation for high momentum modes $k \gg 1$. This means that interactions do not affect the free-particle modes in the high momentum region. This is consistent with the numerically computed excitation spectra (see Fig. V.4).

Finally, we illustrate the difference between Bogoliubov theory and direct numerical simulation for the entire z-spin occupation spectrum for examples of ε_f. To do so, the relative difference between the z-spin spectrum from Bogoliubov theory, $\mathcal{G}_{zz}^{\mathrm{BdG}}(k,t)$ (*cf.* Eq. (III.49)), and from full simulation, $\mathcal{G}_{zz}(k,t)$, is computed. In Fig. V.6 the relative difference defined via $R = |\mathcal{G}_{zz}(k,t) - \mathcal{G}_{zz}^{\mathrm{BdG}}(k,t)|/\mathcal{G}_{zz}(k,t)$ is shown, where we use again the distance from the meanfield critical point as basis for the comparison. The results are shown for two values of ε_f, one near the end of scaling region of χ and one near the beginning of the plateau region.

As can be seen in Fig. V.6, the deviations from the linear theory we identified for the susceptibility extend into the whole infrared region of the occupation spectrum. The oscillatory structure is inherited from the oscillations of occupation modes. Interaction effects thus mainly lead to a detuning between Bogoliubov and actual mode frequencies in the deep infrared region of the spectrum. This comes with a difference in the oscillation amplitude of infrared modes the closer the system is quenched to the critical point.

The structure of R in the full time-momentum plane reveals an additional interaction effect which is apparently quench-independent. As can be seen from Fig. V.6, there is a significant relative deviation R at momentum $k = 0.2$ appearing at time $t = 20$, independently of the quench parameter. However, the effect is less dominant for strong quenches as compared to the strong deviations in the deep infrared region (*cf.* lower panel in Fig. V.6). The independence of the related time and momentum scales of ε_f rules out that the effect is due to an interaction between quasi-particles of the symmetric and spin sector. If such an interaction was present at a perturbative level, the related momentum scale would be the momentum where $\omega_-(k)$ and $\omega_+(k)$ cross, which depends on the quench.

V.5 Summary

In this chapter, we investigated quench dynamics in the spinor gas numerically, be means of semi-classical simulations (see Sect. II.5.1). Our particular interest was to extend the knowledge about scaling behaviour within the post-quench dynamics evolution beyond the meanfield predictions (*cf.* Sect. III.3). We initialise the dynamics with the Bogoliubov groundstate at $J_\mathrm{i} \to \infty$ and show in Sect. V.1 that this state is naturally described by a classical statistical ensemble of fields with Gaussian fluctuations, in the language of the fundamental fields. This allowed us to formulate the quantum state in terms of Wigner functions, which is in turn an important requirement to approximate the quantum system with the Truncated Wigner method [83, 84].

By analysing the dynamics and scaling of the magnetic susceptibility (Sect. V.2), we found that scaling behaviour, in time and distance to the critical point, stops generically for distances to the critical point smaller than $\varepsilon_\mathrm{f} \lesssim 0.1$. Here, it turns out that, instead

of a change from meanfield exponents to different critical exponents, scaling behaviour simply does not appear to describe the observables closer to the critical point. On a phenomenological level, this is understandable as the quench magnifies the energy contribution from initial fluctuations. These tend, similar to temperature fluctuations, to destroy critical behaviour in one spatial dimension.

We used in Sect. V.2 the oscillatory structure of the magnetic susceptibility to extract information on the excitation gap, as the magnetic susceptibility reflects the zero mode and, with it, a large infrared plateau in the structure factor (see Sect. V.4). We found that the numerically determined gap displays a deviation from Bogoliubov scaling. We find that this deviation can be mapped to a static shift in the critical point $\varepsilon_{\mathrm{f}} \to \hat{\varepsilon}_{\mathrm{f}}$, which describes the numerically determined gap consistently but not the scaling deviation of the amplitude of the magnetic susceptibility.

In Sect. V.2 we proposed a method to compute numerically the whole excitation spectrum of (spin-) quasi-particle modes from two-time spin correlation functions (see Eq. (V.9)). With this we corroborated the findings for the shifted gap from oscillations in the magnetic susceptibility. At the same time, the numerically determined excitation spectrum revealed further parameter shifts. In particular, we find that the dynamic critical exponent z and the speed of sound c shift towards smaller values as compared to the Bogoliubov prediction. This constitutes an interesting starting point for analytic studies using a renormalisation group approach, possibly along the lines of [183, 207, 208]

Our method to extract the excitation spectrum is especially feasible for an experimental implementation. If non-destructive measurements can be implemented for an experimental setup (as for example in [209]) to retrieve the spin fields, the unequal-time correlation functions for Eq. (V.9) can be evaluated as we did numerically. The fact that only a small number of unequal time correlators with small difference in time is required is advantageous for experiment and simulation alike.

VI Crossover Behaviour in Quench Dynamics

The results for the interacting spinor Bose gas in one spatial dimension from the previous chapter V show that spin observables avoid critical divergences when quenched towards the phase transition. Qualitatively, this is expected for a phase transition in $1d$ when classical fluctuations are introduced into the system. In Sect. III.4 we argued that the energy distribution the quench produces initially can be characterised by a single effective temperature, since it resembles a thermal energy distribution for infrared quasi-particle momentum modes. In this chapter, we discuss the question if this effective temperature can be identified from the point of view of correlations beyond the Bogoliubov regime and held responsible for the deviation from critical scaling in the spin observables.

For this question to be addressed, a model for the spin sector is required for which analytic statements on its thermal behaviour beyond the linearised theory can be made. For the full model described by Eq. (II.1) there are currently no analytic solutions beyond Bogoliubov theory available, neither for quench dynamics nor for thermal equilibrium. There have been similar but simpler models studied with effective action and renormalisation group techniques for quench dynamics, for example within Luttinger liquids [210, 211] and relativistic $O(N)$ models [183, 207, 208]. Although the methods seem adaptable to our model, a direct comparison to these results is difficult as it is not clear how to map the fully interacting spinor Bose gas (in the form of Eq. (II.1) or Eq. (II.4)) or the non-linear restriction to the spin sector (see Eq. (II.15)) to them.

Instead, we concentrate here on fundamental models for quantum spin chains. In particular, the spin sector of our model shares its structure with the Ising chain in a transverse field. As explained in Sect. II.1.2, anisotropies break the full rotational symmetry in spin space such that only a discrete Z_2 symmetry remains[1]. An energetic competition between two spin direction leads to spontaneous breaking of this symmetry, generating the phase transition. On a more quantitative level, in [116] it has been demonstrated that the the miscible–immiscible transition in the two-component Bose gas in the Mott insulating phase falls into the static universality class of the transverse field Ising model. As there exist additionally analytic solutions for a variety of observables, for the dynamic as well as the thermal transverse-field Ising model, it provides a good starting point to compare and contrast the behaviour of the spinor Bose gas with.

In this chapter, we first introduce the relevant aspects of the transverse-field Ising model, in particular its properties in thermal equilibrium following [89, 128]. Second, we briefly discuss results [91, 92, 212] on quenches in the paramagnetic phase in the Ising model. In particular, we calculate the post-quench dynamics of the correlation length

[1] Actually, a discrete $Z_2 \times Z_2$ symmetry remains. But, since one requires a simultaneous sign change in the external field J (see Sect. II.1.2), the relevant Z_2 symmetry is $S_z \to -S_z$

and specifically the approach to the stationary state. We will demonstrate that the post-quench stationary state is reached extremely fast (for finite spin chains). We will furthermore argue that the correlation length in the stationary state follows a thermal crossover, as function of the post-quench gap, although the occupation of quasi-particles is not thermal. The way the integrable and exactly solvable Ising model approaches the stationary state after a quench will provide a point of comparison for our analysis of the spinor Bose gas.

The main part of this chapter is concerned with the behaviour of correlations after a quench in the spinor Bose gas. We analyse our simulation results for the same quench setup as in chapter V with respect to the equal-time z-spin correlation function (in position space) and corresponding correlation length. As highlighted throughout the previous chapters, we find that the correlations are not described by the generalised Gibbs ensemble from Bogoliubov theory beyond a specific energy scale, as far es it concerns scaling behaviour. Nevertheless, we will demonstrate that the effective temperature derived from the generalised Gibbs ensemble (see Sect. III.4) provides the energy scale where the deviation from Bogoliubov scaling takes place.

As a main result, we find from this analysis that the deviation of the correlation length from Bogoliubov scaling is describable by the finite temperature crossover function of the transverse Ising chain. Specifically, we find that the maximal correlation length during early times of the post-quench time evolution follows a Ising crossover function, when the anomalous dimension is adapted in time.

VI.1 The Quantum Ising Chain in a Transverse Field

The Hamiltonian of the one-dimensional quantum Ising model in a transverse field is given by

$$H(h) = -J \sum_{n=1}^{N} \sigma_n^x \sigma_{n+1}^x - h \sum_{n=1}^{N} \sigma_n^z, \tag{VI.1}$$

describing a chain of N spin-$1/2$ degrees of freedom with periodic boundary conditions[2]. The parameter $h \in \mathbb{R}$ denotes an external magnetic field in z direction, and $J > 0$ is the strength of a ferromagnetic exchange coupling in x direction. Without loss of generality we set $J = 1$, which fixes the energy scale. At zero temperature in the thermodynamic limit the model has quantum phase transitions at $|h| = h_c$, separating a ferromagnetic phase at $|h| < 1$ from paramagnetic phases at $|h| > 1$, where $\langle \sigma_n^x \rangle$ is the order parameter of the transition.

VI.1.1 Exact Diagonalisation of the Ising Chain

The Hamiltonian Eq. (VI.1) can be mapped onto non-interacting fermions, and eigenvalues and eigenstates can be computed analytically [88]. We briefly outline the procedure here and refer the reader to [91, 128, 212] for details. The fist step is to map the spin operators

[2] For simplicity we assume N to be even. See [212] for N odd and details on the difference between even and odd.

σ_i^μ via a Jordan–Wigner transformation [213] to one species of, *i. e.* spin-less, fermions c_i,

$$\begin{aligned}\sigma_i^x &= 1 - 2c_i^\dagger c_i\,,\\ \sigma_i^z &= -\prod_{i<j}\left(1-2c_j^\dagger c_j\right)\left(c_i + c_i^\dagger\right)\,.\end{aligned} \tag{VI.2}$$

The Jordan–Wigner transform thereby maps the fermion anti-commutator algebra, $\{c_i, c_j^\dagger\} = \delta_{ij}$, $\{c_i, c_j\} = 0$, and $\{c_i^\dagger, c_j^\dagger\} = 0$ to the spin commutator algebra, $[\sigma_i^\mu, \sigma_j^\nu] = 2\mathrm{i}\delta_{ij}\epsilon_{\mu\nu\lambda}\sigma_i^\lambda$. Inserting Eq. (VI.2) into the spin Hamiltonian Eq. (VI.1) yields a quadratic Hamiltonian in c_j,

$$H(h) = -\sum_n \left(c_n^\dagger c_{n+1} + c_{n+1}^\dagger c_n + c_{n+1}c_n - 2hc_n^\dagger c_n + h\right)\,, \tag{VI.3}$$

which requires still diagonalisation. This can be achieved by a simultaneous Bogoliubov and Fourier transform, in a similar way we have already discussed for the linearised spin sector S_- of the spinor gas in Sect. III.1 (*cf.* Eq. (III.3) and Eq. (III.4)). Introducing Bogoliubov fermions γ_k at lattice momenta $k = 2\pi j/N$ with $j \in [-(N-1)/2, (N-1)/2]$ and a the lattice constant, one defines

$$\gamma_k = \frac{1}{\sqrt{N}}\sum_j \mathrm{e}^{-\mathrm{i}kj}\left(u_k c_j - \mathrm{i}v_k c_j^\dagger\right)\,. \tag{VI.4}$$

The Bogoliubov transformation here needs to be unitary to conserve the fermion anti-commutator relations, in contrast to Sect. III.1, and therefore $u_k^2 + v_k^2 = 1$. Inverting Eq. (VI.4) and inserting it into Eq. (VI.3) yields a diagonal Hamiltonian for non-interacting fermions,

$$H(h) = \sum_k \epsilon_k\left(\gamma_k^\dagger\gamma_k - \frac{1}{2}\right)\,, \tag{VI.5}$$

together with Bogoliubov mode functions $u_k = \cos(\eta_k/2)$ and $v_k = \sin(\eta_k/2)$. The Bogoliubov angle η_k then needs to fulfil the relation

$$\tan(\eta_k) = \frac{\sin(k)}{h - \cos(k)}\,, \tag{VI.6}$$

to obtain the diagonal Hamiltonian Eq. (VI.5). Together with Eq. (VI.6) one finds a bounded single-fermion excitation spectrum

$$\epsilon_k = 2\sqrt{1 + h^2 - 2h\cos(k)}\,. \tag{VI.7}$$

As this spectrum is bounded from below with $\epsilon_k \geq \epsilon_0 = \Delta = 2|1-h|$, the groundstate is the state with zero occupancy of Bogoliubov fermions.

The lattice Hamiltonian Eq. (VI.3) can also be extrapolated to the continuum (scaling) limit, by introducing a lattice constant a in fermion operators $\Psi(a\cdot i) = c_i/\sqrt{a}$. After the diagonalisation, the limit $a \to 0$ and $N \to \infty$ can be evaluated under the condition

$aN = \text{const}$. In particular, the fermion spectrum Eq. (VI.7) extrapolates to [128]

$$\epsilon(k) = \sqrt{\Delta^2 + c^2 k^2}\,, \tag{VI.8}$$

where $\Delta = 2(1-h)$. The constant c appears through the continuum limit replacing the hopping energy constant J via $c = 2Ja$, since the hopping energy J needs to diverge if $a \to 0$. From Eq. (VI.8) one finds that there is a finite spectral gap, $\epsilon(k \to 0) = 2|\Delta|$, in the continuum limit at zero temperature, which vanishes only at $h = h_c = 1$. This indicates that there is a second order phase transition in the model at $h = 1$. A more rigorous argument is provided via the groundstate energy in the limit $N \to \infty$, which has non-analytic point at $h = 1$ [88]. In contrast, the free energy of the model is analytic at any finite temperature [88], meaning that the phase transition exists only at zero temperature. Nevertheless, it has been demonstrated in [89] that observables follow universal behaviour also at finite temperature, as a direct consequence of the zero-temperature critical point.

VI.1.2 Finite Temperature Properties

In principle, in the basis of Bogoliubov fermions γ_k any observable can be retrieved without much effort. In particular, the thermal properties are set, as the occupation of Bogoliubov modes are given in terms of the Fermi–Dirac distribution. The time evolution can be solved for on the operator level. The actual problem is to invert the sequence of mappings to go back to the spin operators and finally obtain correlation functions of Ising spins.

Going back to the original fermion basis, c_i, follows the same logic as we have discussed for the conversion between Bogoliubov quasi-particles and Bose gas pseudo spin in Sect. III.1[3]. Since the c_i and γ_k are related by a linear and local transformation this can be done on the level of operators.

In contrast, the non-local Jordan–Wigner transformation is typically inverted directly for specific spin correlation functions. The two-point spin correlation function $C^{xx}(\ell) = \langle \sigma_n^x \sigma_{n+\ell}^x \rangle$, for example, which we will discuss here, is expressible in form of a Toeplitz determinants [88]. The on the lattice, the components of the related Toeplitz matrix can be obtained as analytic expressions, for thermal system [88] and likewise for sudden quenches [91]. This allows to retrieve observables on finite lattices by means of direct computation with efficient numerical linear algebra routines.

For example, for a quench from h_0 to h and an infinite chain, calculating the dynamics of equal-time correlations $C^{xx}(\ell) = \langle \sigma_n^x \sigma_{n+\ell}^x \rangle$ between sites that are a distance ℓ apart can be reduced to computing the determinant of an $\ell \times \ell$ matrix [91]. In the next section, we present calculations for quenches in finite discrete chains from [212], where also the required analytic expressions for the Toeplitz determinants can be found.

As key feature of the transverse field Ising chain, for various observables, and in particular the spin-spin correlation function $C^{xx}(\ell) = \langle \sigma_n^x \sigma_{n+\ell}^x \rangle$, closed analytic expressions can be obtained in the scaling or thermodynamic limit. For quench dynamics, this has been achieved in [91, 92], as we discuss in the next section, while finite temperature correlation functions in the scaling limit have been derived in [89].

[3] Despite that the transformation here is unitary instead of symplectic, there is literally no difference.

The equal time spin-spin correlation function, which we are interested in, can be given in the full temperature-Δ plane,

$$\lim_{r\to\infty} C^{xx}(r) = ZT^{\eta} G_I(\Delta/T) \exp\left(-|r|\frac{T}{c} F_I(\Delta/T)\right), \tag{VI.9}$$

where Z is a non-universal renormalisation factor and η is the anomalous dimension, which is $\eta = 1/4$ for the Ising chain. The limit on the right-hand side of Eq. (VI.9) is to be understood as the leading-order behaviour of $C^{xx}(r)$ as $r \to \infty$. Note that for the expressions in the following, we use the gap parameter $\Delta = 2(1-h)$ including the sign. In accordance with common literature, *e. g.* [128], $\Delta < 0$ indicates the paramagnetic side of the zero-temperature phase transition while $\Delta > 0$ signals the ferromagnetic side.

Most importantly, the correlation function in Eq. (VI.9) is set in terms of two universal functions, $G_I(s)$ and $F_I(s)$, for which only the dimensionless ratio Δ/T is required as input. Both functions are analytic for all s and expressions for the functional dependence on s are known. The function $F_I(s)$ describes the universal crossover of the correlation length,

$$\xi_{\text{th}}^{-1} = \frac{T}{c} F_I\left(\frac{\Delta}{T}\right), \tag{VI.10}$$

and

$$F_I(s) = |s|\Theta(-s) - \frac{4\eta}{\pi}\int_0^\infty \mathrm{d}y \, \log\tanh\frac{\sqrt{y^2+s^2}}{2}. \tag{VI.11}$$

The integral appearing in Eq. (VI.11) needs to be evaluated numerically in general. However, at $s = 0$ one finds analytically $F_I(0) = \pi\eta$ and with that the correlation length at vanishing gap,

$$\xi_{\text{th}} = \frac{c}{\pi\eta T}. \tag{VI.12}$$

At vanishing temperature and vanishing gap the exponential decay of the correlation function Eq. (VI.9) turns into an algebraic decay, $C^{xx}(r) \sim (r/c)^{-\eta}$. This goes together with the divergence $\xi_{\text{th}} \to \infty$ as $T \to 0$ and is a sign of the quantum critical point at $T = 0$ and $\Delta = 0$.

VI.2 Quench Dynamics and Stationary States in the Ising chain

In this section, we[4] discuss sudden quenches within the paramagnetic phase of the Ising chain in a transverse magnetic field. Here, the possibility to express the Ising Hamiltonian in a diagonal form (see Sect. VI.1.1) allows implementing sudden quenches and calculating the time evolution of observables in a analytically exact way. Here, we consider as initial state a paramagnetic groundstate of the Ising Hamiltonian for a transverse field $h = h_{\text{i}} > 1$ (see Eq. (VI.1)). The quench then is simply implemented by evolving a observable in time

[4] This section partially contains results from the Master's thesis [212]. I co-advised the project and contributed to the interpretation of the results. For computing observables of the finite Ising chain, a code package was used written by the author of [212] in the course of his work.

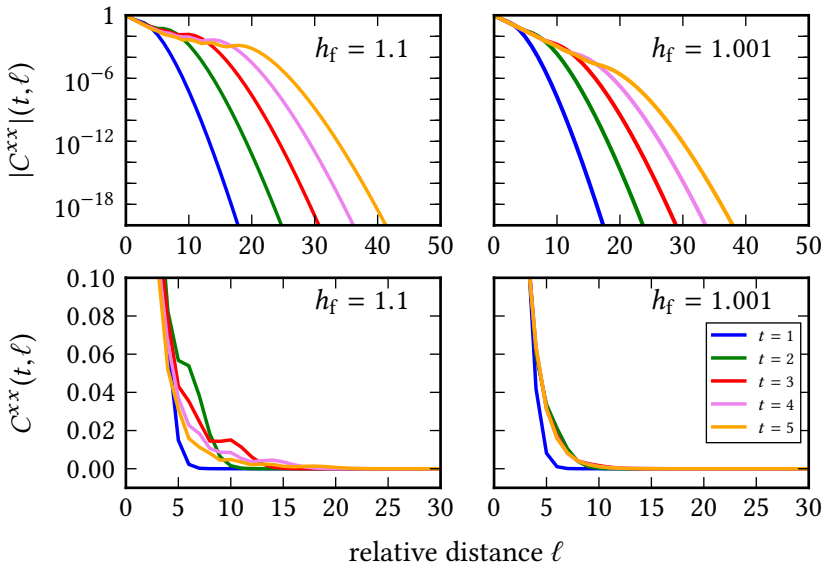

Figure VI.1: Equal-time spin correlation function $C^{xx}(t,\ell)$ (see Eq. (VI.14)) for quenches within the paramagnetic phase of the transverse field Ising chain, as a function of the spin–spin distance ℓ for different times t after the quench. The correlation functions are computed for a discrete spin system with $N = 200$ spins and for a quench to a transverse field $h_f = 1.1$ (left panel) and $h_f = 1.001$ (right panel), starting with the groundstate at a finite high transverse field $h_i = 1000$ in both cases.

with the Ising Hamiltonian at a different (the post-quench) transverse field $h = h_\mathrm{f} > 1$, still in the paramagnetic phase,

$$\partial_t O(t) = [O, H(h_\mathrm{f})] \ . \tag{VI.13}$$

Expectation values of the observable are analysed with respect to the pre-quench density matrix, *i. e.*, for our case, with respect to the groundstate of $H(h_\mathrm{i})$.

We point out that the logic the implementation of the quench follows for the Ising model is in complete analogy to the quench within the Bogoliubov theory for the spinor gas (see Sect. III.2). The complication for the Ising model (rendering the Ising spins non-linearly 'interacting') lies in the non-local map between fermions and spin operators (Eq. (VI.2)).

To match the quench setup for the Ising chain to the quench setup in the spinor Bose gas which we implement in simulations (see chapter V), we chose[5] $h_\mathrm{i} \to \infty$. In this case, the pre-quench groundstate is a fully z-polarised state. As in the spinor Bose gas, for the quench, transverse fields $h_\mathrm{f} = \varepsilon_\mathrm{f} + 1$ close to the critical point $h_\mathrm{c} = 1$ with $\varepsilon_\mathrm{f} < 1$ are analysed in this section.

For finite spin chains, it is possible to express correlation functions and, in particular, the equal-time spin correlation function

$$C^{xx}(t,\ell) = \left\langle \sigma_0^x(t)\sigma_\ell^x(t) \right\rangle_\mathrm{i} \ , \tag{VI.14}$$

in terms of Toeplitz determinants (see for example [88]), which allows for an efficient calculation.

In this section, we analyse the post-quench time evolution of the equal-time correlation function $C^{xx}(t,\ell)$, as obtained for finite spin chains, and compare to analytic expressions in the thermodynamic limit and scaling limit, which have been found in [91, 92]. We find that the post-quench spin correlation function and, specifically, correlation lengths derived from it reach a non-equilibrium stationary state (corroborating the results from [91, 92]). We demonstrate that a stationary state is reached even for small system sizes within short time periods of post-quench evolution. If a bulk measure such as the correlation length is considered, this stationary state appears thermal for quenches close to the critical point, at a temperature universally set by the quench. See also [212].

VI.2.1 Quench dynamics

For quenches to $\varepsilon_\mathrm{f} \gtrsim 0$ in the transverse Ising chain, *i. e.*, within the paramagnetic phase and into the close vicinity of the quantum critical point, the correlation function $C^{xx}(t,\ell)$ (see Eq. (VI.14)) shows overdamped dynamics as can be seen from the right panel in Fig. VI.1. At least for those distances ℓ where C^{xx} is large enough to be detected experimentally, correlations approach their stationary value already on a time scale of the order of $1/J$, where J is the spin coupling in the Ising chain (see Eq. (VI.1)) which we set to $J = 1$ in practice. This finding comes as a surprise, as theoretical arguments (in a slightly different context) indicate that full stationarity is reached only at times several

[5] For finite spin chains, we evaluate numerical expressions at $h_\mathrm{i} = 1000 \gg h_\mathrm{f}$

orders longer, and even up to $10^{20}/J$ [91, 92].

For quenches that end further away from the quantum critical point, like the one in the left panel of Fig. VI.1 for $ef = 0.1$, oscillations are superimposed on the build-up of correlations. Relaxation time scales are somewhat longer in that case, in the range of a few or even tens of $1/J$, but the short-distance decay of the C^{xx} again reaches its stationary values at a time of the order of $1/J$.

The rapid convergence to stationarity can be explained by considering the (suitably improved [212]) analytic expressions for $C^{xx}(t,\ell)$ conjectured in [91, 92], which are rigorously valid only at late times t and large distances ℓ (in the sense of leading-order asymptotic behaviour). Based on the results of [91, 92] the author of [212] puts forward the expression

$$C^{xx}(t,\ell) \sim E(h_\mathrm{f},\mathrm{i})\mathrm{e}^{-\ell/\xi_1} + (h_\mathrm{f}^2-1)^{1/4}\sqrt{4h_\mathrm{f}}\int_{-\pi}^{\pi}\frac{\mathrm{d}k}{\pi}\frac{K(k,h_\mathrm{f},h_\mathrm{i})}{\omega_k(h_\mathrm{f})}\sin\left(2t\omega_k(h_\mathrm{f})-k\ell\right)$$
$$\times\exp\left(\int_0^{\pi}\frac{\mathrm{d}k}{\pi}\log|1-2n_\mathrm{BF}(k,h_\mathrm{f},h_\mathrm{i})|[\ell+\Theta(\ell-2v(k,h_\mathrm{f})t)(2v(k,h_\mathrm{f})t-r)]\right) \quad \text{(VI.15)}$$

for the analytic form of the spin correlation function in the thermodynamic limit. In Eq. (VI.15), $\omega_k(h_\mathrm{f})$ is the post-quench energy spectrum of Bogoliubov fermions, $\omega_k(h_\mathrm{f}) = \epsilon_k|_{h_\mathrm{f}}$ (see Eq. (VI.7)), and the function $K(k,h_\mathrm{f},h_\mathrm{i})$ is set in terms of the post-quench occupation of Bogoliubov fermions, $n_\mathrm{BF}(k,h_\mathrm{f},h_\mathrm{i})$, via $K = K^2/(1+K^2)$. The function $v(k,h_\mathrm{f}) = \partial_k\omega_k(h_\mathrm{f})$ describes the group velocities of Bogoliubov fermion modes. The constant E is, for our case $h_\mathrm{i} > h_\mathrm{f} > 1$, independent of time and space given by [92]

$$E(h_\mathrm{f},h_\mathrm{i}) = \sqrt{\frac{h_\mathrm{f}(h_\mathrm{i}-h_\mathrm{f})\sqrt{h_\mathrm{i}^2-1}}{(h_\mathrm{f}+h_\mathrm{i})(h_\mathrm{f}h_\mathrm{i}-1)}}\,, \quad \text{(VI.16)}$$

The correlation function from Eq. (VI.15) is composed similar to the Bogoliubov form of the corresponding spinor Bose gas correlation function (see Eq. (III.52)). It consists out of a time-independent decaying exponential, which defines the short distance behaviour and a sinusoidal term which oscillates in time and space. The amplitude in front of the oscillation term in Eq. (VI.15) is multiplied by a second exponential function which constitutes a second characteristic length scale [91]. It was shown [91, 212] that the oscillating term in Eq. (VI.15) dominates outside a lightcone, $\ell \gtrsim \max_k(v(k,h_\mathrm{f}))t$. Inside the lightcone, the static first term dominates with a characteristic decay scale ξ_1. This implies also that the oscillating term vanishes asymptotically, leaving the first term $C^{xx}(t,\ell) \sim \mathrm{e}^{-\ell/\xi_1}$ as stationary limit.

From the evaluation of the discrete spin chain (see also [212]) we find that the spin correlation function in the Ising model approaches at short distances $\ell \lesssim \zeta(t)$, the long-time behaviour $C^{xx}(t,\ell) \sim \exp(-\ell/\xi_1)$ to a very good approximation, *cf.* Fig. VI.2, panels (a)

and (b). Here,

$$\xi_1^{-1} = \Theta\left(h_\mathrm{f}-1\right)\Theta\left(h_\mathrm{i}-1\right)\log\min\left\{h_\mathrm{i},h_1\right\} - \frac{1}{2\pi}\int_{-\pi}^{\pi}\log\left|1-2n_\mathrm{BF}(k)\right|\,\mathrm{d}k\,, \tag{VI.17}$$

defines the long-time inverse correlation length, where Θ denotes the Heaviside step function and

$$h_1 = \frac{1+h_\mathrm{f}h_\mathrm{i}+\sqrt{\left(h_\mathrm{f}^2-1\right)\left(h_\mathrm{i}^2-1\right)}}{h_\mathrm{f}+h_\mathrm{i}}\,. \tag{VI.18}$$

The mode occupation numbers of the Bogoliubov fermions after the quench from $h_\mathrm{i} > 1$ to $h_\mathrm{f} > 1$ are defined as

$$n_\mathrm{BF}(k;h_\mathrm{f},h_\mathrm{i}) = 1/2 - 2[h_\mathrm{i}h_\mathrm{f}+1-(h_\mathrm{i}+h_\mathrm{f})\cos(k)][\omega_\mathrm{BF}(k;h_\mathrm{f})\omega_\mathrm{BF}(k;h_\mathrm{i})]^{-1}\,, \tag{VI.19}$$

with mode frequencies $\omega_\mathrm{BF}(k;h_\mathrm{f}) = \epsilon_k|_{h_\mathrm{f}}$ given by the post-quench fermion energy spectrum (see Eq. (VI.7)), *cf.* Ref. [91, 92].

Furthermore, the analytic expression for the correlation function, given in Eq. (VI.15), yields

$$\xi_2^{-1} = -\frac{1}{2\pi}\int_{-\pi}^{\pi}\log\left|1-2n_\mathrm{BF}(k)\right|\,\mathrm{d}k\,, \tag{VI.20}$$

for the fall-off scale of the correlations beyond $\zeta(t)$, $|C^{xx}(t,\ell \gg \zeta(t))| \sim \exp(-\ell/\xi_2)$. The amplitude of the oscillatory term in Eq. (VI.15) decays in space on this characteristic scale.

In the limit $h_\mathrm{f} \to \infty$, the correlation lengths simplify to

$$\xi_1^{-1} = \log(2h_\mathrm{f})\,, \tag{VI.21}$$

$$\xi_2^{-1} = \log(2h_\mathrm{f}) - \Theta(h_\mathrm{f}-1)\,\mathrm{arcosh}\,(h_\mathrm{f})\,. \tag{VI.22}$$

The scale ζ, dividing the two regimes, increases logarithmically in time, $\zeta(t) \sim (3\xi_1/2)\log(t/t_0)$, in accordance with (40) in [92, 212].

VI.2.2 Correlation lengths

We extract the correlation lengths $\xi_{1,2}$ from the data in Fig. VI.1 by fitting exponential functions to the short- and long-distance decay of C^{xx}, as obtained for a finite spin chain ($N = 200$ spins). The time-dependence of ξ_1 is shown, for various ε, in Fig. VI.2 (right inset), where stationarity is observed around times $t = 4$ for small ε_f, and only at later times for larger ε_f. At $t \simeq 40$ the correlation length has reached its stationary regime for all ε_f considered. In Fig. VI.2 (right) the correlation length $\xi(t = 40)$ is shown as a function of the quench parameter ε_f (red points). The ε_f-dependence of $\xi_1(t = 40)$ confirms the analytic expression (VI.17) shown as a blue line.

Since the lower critical dimension of the model is 2, the correlation length, in equilibrium, does not diverge at the critical magnetic field $h = 1$ and for non-zero temperatures.

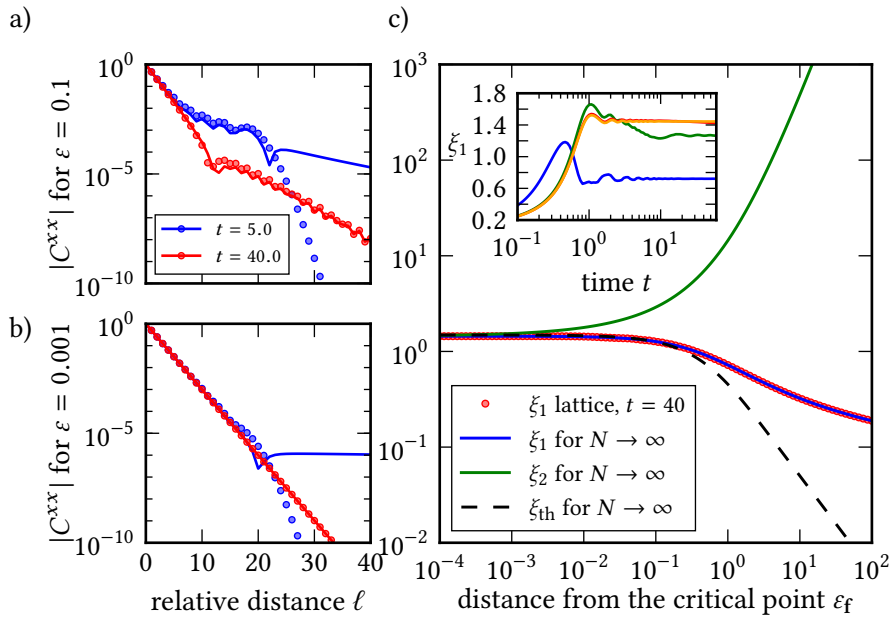

Figure VI.2: Longitudinal spin correlation functions and correlation length after a quench on the paramagnetic side of the phase transition close to the critical point in the transverse field Ising model. (a) Correlation function $|C^{xx}(\ell)|$ at two different times t after the quench from $h_0 \to \infty$ to $\varepsilon_{\rm f} = h_{\rm f} - 1 = 0.1$. Note the logarithmic scale. Data points correspond to a finite spin chain ($N = 200$). Solid lines correspond to a evaluation of $|C^{xx}(\ell)|$ in the thermodynamic limit Eq. (VI.15). (b) Same correlation function after a quench to $\varepsilon_{\rm f} = 0.001$. (c) Inset: Time evolution of the correlation length ξ_1 of the short-distance fall-off of $|C^{xx}(\ell)| \sim \exp(-\ell/\xi_1)$ defined in Eq. (VI.17), for the finite spin chain ($N = 200$ spins) and three different quenches. Main graph: The resulting correlation length $\xi_1(40/J; \varepsilon_{\rm f})$ as a function of the final $\varepsilon_{\rm f}$ (red points), in comparison with the analytical expression $\xi_1(t \to \infty; \varepsilon_{\rm f}) = [\log(2 + 2\varepsilon_{\rm f})]^{-1}$ (blue line) in the thermodynamic limit. The green line shows the asymptotic correlation length $\xi_2(t \to \infty; \varepsilon_{\rm f})$. The black dashed line shows for comparison $\xi_{\rm th}(T, \varepsilon_{\rm f})$ (in the thermodynamic limit,see Eq. (VI.23)) at temperature $T \simeq 1.58$, chosen to match ξ_1 at $\varepsilon_{\rm f} = 0$.

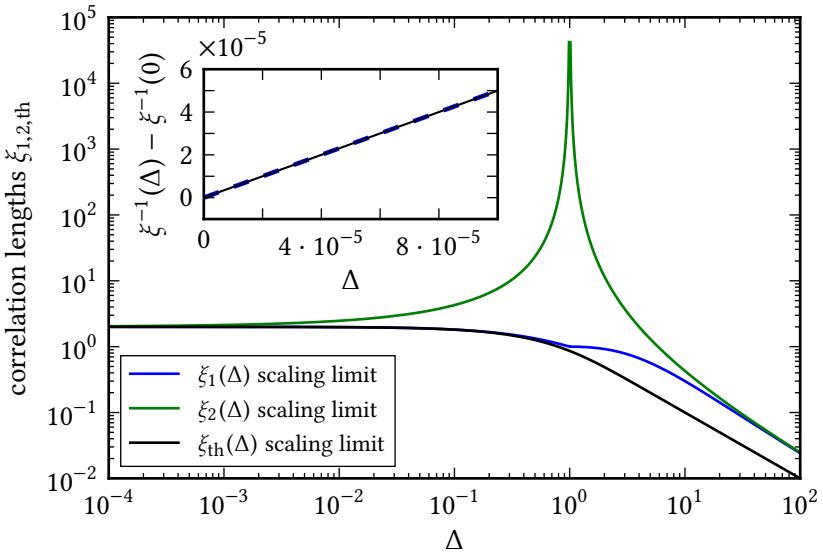

Figure VI.3: Main graph: Asymptotic post-quench correlation lengths $\xi_{1,2}(t \to \infty; \Delta_\mathrm{f})$ (blue and green lines, respectively) after a quench from $\Delta_\mathrm{i} = 1$ in comparison with the thermal correlation length ξ_th (in the scaling limit Eq. (VI.10)), for the same ε and a temperature $T_s = 2\Delta_\mathrm{i}/\pi$ ensuring that it saturates at the same value as the post-quench lengths, $\xi_{T=2\Delta_\mathrm{i}/\pi}(0) = \xi_{1,2}(t \to \infty; 0)$. The inset shows that within a scaling window of small $\Delta_\mathrm{f}/\Delta_\mathrm{i} \ll 1$ the same linear corrections apply to ξ_1 and ξ_th.

The same qualitative crossover behaviour is seen here. For comparison, we show the dependence of the equilibrium correlation length ξ_th on h, defined by

$$\xi_\mathrm{th}^{-1}(h_\mathrm{f}) = \Theta\,(h_\mathrm{f} - 1)\,2(h_\mathrm{f} - 1) - (2\pi)^{-1} \int_{-\pi}^{\pi} \mathrm{d}k \log[1 - 2n_\mathrm{th}(k; h_\mathrm{f})]\,, \tag{VI.23}$$

with Bogoliubov fermion distribution $n_\mathrm{th}(k; h_\mathrm{f}) = \{\exp[\omega_\mathrm{BF}(k; h_\mathrm{f})/T] + 1\}^{-1}$ [89], for a temperature $T \simeq 1.58$ which is chosen such as to give the same saturation value at $h = 1$ (dashed line in Fig. VI.2). The thermal correlation length given in Eq. (VI.23) is evaluated in the thermodynamic limit ($N \to \infty$) while the form for ξ_th in Eq. (VI.10) constitutes the scaling limit.

Note that, other than $\xi_\mathrm{th}(h_\mathrm{f})$, the correlation length $\xi_1(h_\mathrm{f}; t \to \infty) = 1/\log(2h_\mathrm{f})$ decays logarithmically for $h_\mathrm{f} \gg 1$. The reason for these discrepancies is that for any initial ε_i and final ε_f, the post-quench spectrum rather defines a generalized Gibbs ensemble [90–92] and hence cannot lead to the full thermal crossover behaviour of ξ_th. Nevertheless, a temperature can be found to match the crossover behaviour of $\xi_\mathrm{th}(\varepsilon_\mathrm{f}, T)$ and $\xi_1(\varepsilon_\mathrm{f}, \varepsilon_\mathrm{i})$ for quenches close to the critical point $\varepsilon_\mathrm{f} \simeq 0$.

VI.2.3 Continuum and scaling limits

In view of the comparison with the continuous Bose gas (in the following section), we consider the transverse field Ising chain in the continuum limit, assuming the spins to reside on a lattice with spacing a and taking the lattice spacing to zero. Keeping the speed of sound $c = 2Ja$ and the post-quench gap energy $\Delta_\mathrm{f} = 2|h_\mathrm{f} - J|$ finite, implies that J diverges as a^{-1} and the scaling limit must be taken, with $\lambda = h_\mathrm{f}/J \to 1^+$ as $\lambda - 1 = \Delta_\mathrm{f}/2J = a\Delta_\mathrm{f}/c \to 0$. The fermion frequencies reduce to $\omega_\mathrm{BF}(k, \Delta_\mathrm{f}) = \sqrt{\Delta_\mathrm{f}^2 + (ck)^2} = \Delta_\mathrm{i}\sqrt{\varepsilon^2 + \kappa^2}$, where we now define $\varepsilon = \Delta_\mathrm{f}/\Delta_\mathrm{i}$ and $\kappa = ck/\Delta_\mathrm{i}$. The mode occupations after a quench from Δ_i to Δ_f in this scaling limit read $n_\mathrm{BF}(k; \Delta_\mathrm{f}, \Delta_\mathrm{i}) = \{1 - [\varepsilon\varepsilon_\mathrm{i} + \kappa^2]/[\omega_\mathrm{BF}(k, \varepsilon)\omega_\mathrm{BF}(k, \Delta_\mathrm{i})]\}/2$. Clearly, Δ_i (or Δ_f) now takes over the role to set the scale in units of which all quantities can be expressed. Inserting the above and $2J\log(h_1) = \sqrt{\Delta_\mathrm{f}\Delta_\mathrm{i}}$ into Eqs. (VI.17) and (VI.20), the post-quench correlation lengths result as (*cf.* [91], Eq. (271))

$$\begin{aligned}\xi_1 &= \frac{2c\,\Theta(\Delta_\mathrm{i} - \Delta_\mathrm{f})}{\Delta_\mathrm{i} + \Delta_\mathrm{f}} + \frac{c\,\Theta(\Delta_\mathrm{f} - \Delta_\mathrm{i})}{\Delta_\mathrm{i} + c/\xi_2}, \\ \xi_2 &= 2c\,(\sqrt{\Delta_\mathrm{f}} - \sqrt{\Delta_\mathrm{i}})^{-2}. \end{aligned} \tag{VI.24}$$

Hence, at $\Delta_\mathrm{f} = 0$, one has $\xi_1 = 2c/\Delta_\mathrm{i}$, and this to coincide with the thermal critical length scale $\xi_\mathrm{th}(\Delta_\mathrm{f} = 0) = 4c/(\pi T)$ [89] requires a temperature $T_s = 2\Delta_\mathrm{i}/\pi$ which only depends on the initial-state gap scale. Fig. VI.2d shows the crossover-behaviour of the post-quench correlation lengths $\xi_{1,2}(\Delta_\mathrm{f}, \Delta_\mathrm{i})$ as well as the thermal length $\xi_\mathrm{th}(\Delta_\mathrm{f})$ [89] as functions of Δ_f, with the temperature set to T_s. We find, that all three length scales fall of as $(\Delta_\mathrm{f}/\Delta_\mathrm{i})^{-1}$ for $\Delta_\mathrm{f} \gg \Delta_\mathrm{i}$ but that there is a factor of two difference between the post-quench and the thermal lengths, respectively. In the scaling window near the critical point, $0 \leq \Delta_\mathrm{f} \ll \Delta_\mathrm{i}$, both, deviations of ξ_1^{-1} and ξ_{th}^{-1} from the critical value $\Delta_\mathrm{i}/(2c)$ are, to linear order equal to $\Delta_\mathrm{f}/(2c)$, see the inset of Fig. VI.2d, while only the thermal one receives additional corrections in even powers of Δ_f [89].

VI.3 Crossover in the Spinor Bose Gas

For the remainder of this chapter, we turn back to quench dynamics in the two-component Bose gas. In the previous chapter V, we have already presented results from full simulation for quenches of $h = J/J_\mathrm{c}$ close to the critical coupling, staying on the z-unpolarised side of the transition. As pre-quench state a ground state in the spin sector at infinitely high linear coupling, $h_\mathrm{i} = J_\mathrm{i}/J_\mathrm{c} = \infty$, was chosen. Therefore, the quench setup in chapter V for the spinor gas is the same as we discussed for the transverse Ising chain in the previous section VI.2.

In this section, we present results on the dynamics of correlation functions and correlation lengths, as obtained from the simulations also presented in chapter V. In particular, the quench we implement for the Bose gas thereby starts in the (non-interacting) ground-state at high linear coupling $J = J_\mathrm{i} \to \infty$. The simulation data we present in this section is obtained with numerical parameters as given in Table B.2.

With this, we are in the position to discuss similarities and differences between the Bose gases' pseudo-spin dynamics and the dynamics of actual spins in the transverse Ising chain from the point of view of local observables. As our main result from this comparison, we find that the behaviour of the spin correlation length of the Bose gas beyond Bogoliubov theory can be explained in terms of the transverse Ising chain's universal crossover function (see Eq. (VI.10) and Eq. (VI.11)). The scale which takes the role of temperature is universally set by the quench. It turns out to be set by the effective temperature from the generalised Gibbs ensemble for the Bogoliubov spin modes (see Sect. III.4).

VI.3.1 Dynamics of Correlations

Before presenting calculations for the Bose gas, a technical remark is in order. When comparing the model for the Ising chain from Eq. (VI.1) and the spin description of the Bose gas from Eq. (II.6), one finds the transverse field pointing in different directions in spin space, in x-direction for the Bose gas and in z-direction for the Ising chain.

This difference is superficial, insofar it is due to a different choice of the quantisation axis in spin space, and does not change physical properties. In both models a rotation around the y spin axis could be performed, $\sigma^z \to \sigma^x$ and $\sigma^z \to -\sigma^x$, to match the definitions. In accordance with common literature on both sides we use both models as given in Eq. (II.6) and Eq. (VI.1).

Then, of course, different correlation functions need to be compared to be on equal physical footing. As we have analysed the correlation function C^{xx} of the Z_2 symmetry-breaking order parameter field in the transverse Ising chain in Sect. VI.2 we need to analyse the z-spin two point correlation function

$$G^{zz}(t,r) = \frac{\langle S^z(t,0)S^z(t,r)\rangle}{\langle S^z(t,0)^2\rangle}\,, \tag{VI.25}$$

for the Bose gas. Note that G^{zz} in Eq. (VI.25) has to be normalised[6] 'by hand' to $G^{zz}(r \to 0) = 1$, since it is derived from a continuous spin density field, whereas the calculations of the discrete spin correlation C^{xx} in Sect. VI.2 do not require additional normalisation.

We point out that, even within the same model, spin correlation functions in different spin directions can thermalise on very different time scales, see for example [32]. Therefore, out of equilibrium it is vital to compare the spin correlation functions with same physical meaning in the two models.

VI.3.2 Details of the Spin Correlation Function

Typical examples for the time evolution of the z spin correlation function G^{zz} of the Bose gas are shown in Fig. VI.4. Similar to Fig. VI.1 we concentrate on early times, meaning within the first two oscillation periods of the magnetic susceptibility (*cf.* Fig. V.1), and

[6] We reserve the symbol G for the normalised spin correlation functions (or structure factors) of the spinor gas, while the symbol $\mathcal{G}$ is used for the unnormalised ones. As before, we denote with the symbol C spin correlation functions of the transverse Ising chain.

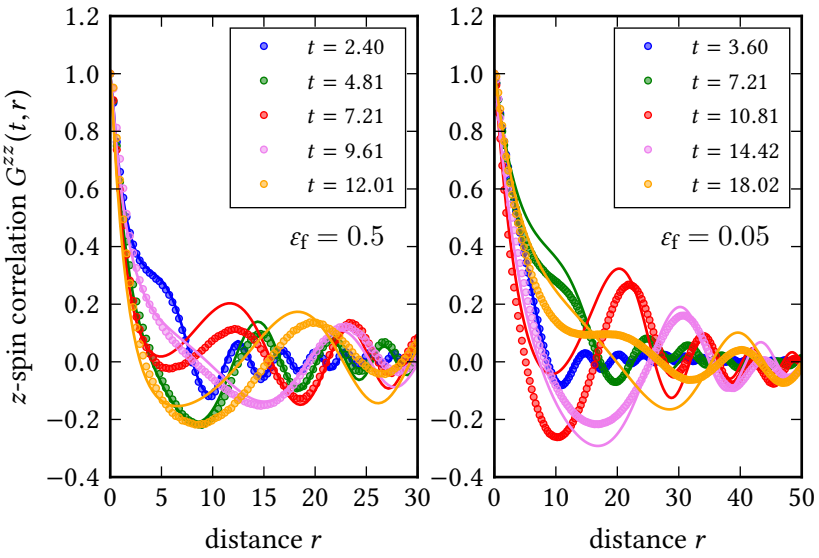

Figure VI.4: Examples for the equal-time spin correlation function $G^{zz}(t,r)$ (see Eq. (VI.25)) after a quench in the Bose gas. The left panel depicts a quench from $h_i \to \infty$ to a large post-quench distance to the meanfield critical point $\varepsilon_f = 0.5$ while the right panel depicts a quench to a small distance $\varepsilon_f = 0.05$, in both cases with $h_f = (1 + \varepsilon_f)$. Both panels show simulation data (coloured symbols) for early times (see legends) together with the Bogoliubov prediction (coloured solid lines), as given in Eq. (III.38), for the corresponding times (same colour as symbols) and post-quench distances to the meanfield critical point. For that, the Fourier transform in Eq. (III.38) is evaluated numerically on the simulation's momentum space grid. In both panels, a small window is shown, to concentrate on short distance properties. The full system size in the simulations (see parameters in Table B.2) is $L = 1293$ in natural units (see Sect. B.1)

compare the evolution for two different post-quenches distances to the meanfield critical point.

The equal-time correlation functions follow the general structure of being composed out of a short-ranged decay for small distances r, overlaid with spatial oscillations. To set the general behaviour into context, we compare the simulation data for $G^{zz}(t,r)$ (coloured symbols in Fig. VI.4) with the corresponding evaluation of the Bogoliubov equal-time correlation functions (coloured lines in Fig. VI.4). To do so, the expression Eq. (III.38) is evaluated on the simulation's momentum space grid at corresponding times and meanfield distances from the critical point.

From the comparison in Fig. VI.4, we find that Bogoliubov dynamics is a good description only for very early times at comparatively large distance $\varepsilon_f = 0.5$. Then, the Bogoliubov correlation functions capture the structure of the simulation data in detail, *i. e.* the decay together with matching period and amplitude of spatial oscillations, (*cf.* blue and green data points and lines in left panel of Fig. VI.4).

The decay of the correlation function on small scales, on the other hand, is described well by Bogoliubov theory for all times and both values of ε_{f} shown in Fig. VI.4. Thus, as time progresses or distance to the critical point decreases, large-scale properties of the correlation function are strongly changed by interactions as compared to Bogoliubov theory. The short-ranged decay is described by Bogoliubov theory in a larger window of time and distance to the critical point.

Similar to the behaviour of the corresponding correlation function in the transverse field Ising chain $C^{xx}(t,\ell)$ (*cf.* Fig. VI.1), the decay on small scales r of $G^{zz}(t,r)$ is found to be nearly static. However, there is not such a clear separation between a small-scale decay and a long-distance decay as we found for $C^{xx}(t,\ell)$ in Fig. VI.1.

The difference can be understood as follows. As we have discussed in Sect. VI.2, the turning point between the long-range and the short-range exponential decay of C^{xx} moves towards larger spatial scales in time, therewith growing the extend of the static short-distance exponential decay, $C^{xx}(t,\ell) \sim \exp(-\ell/\xi_1)$. If a fixed window in ℓ is analysed, as in Fig. VI.1, the oscillatory part of C^{xx} moves out of this window, leaving back the static exponential decay of the generalised Gibbs state.

The behaviour of the spin correlation function in the Bose gas is already different when it is considered within the Bogoliubov regime, where a relaxation towards a stationary generalised Gibbs state takes place. As discussed in Sect. III.3.2, the correlation function $G(t,r)$ within Bogoliubov theory is schematically given by a static exponential decay plus a spatially oscillating function,

$$G^{zz}(t,r) \sim e^{-r/\xi_1} + \frac{1}{\sqrt{t}}\frac{1}{r^2}\cos\left(\Phi(\varepsilon_{\mathrm{f}},t,r) - \frac{\pi}{4}\right) . \tag{VI.26}$$

Note that, for the sake of the argument, we focus in Eq. (VI.26) on the leading-order asymptotic behaviour of $G(t,r)$ in time and space, found from Bogoliubov theory and stationary phase approximation. The full expression can be found in Eq. (III.52) together with Eq. (III.53).

The crucial difference to C^{xx} in the Ising chain (*cf.* Eq. (VI.15)) is that the time dependent part in Eq. (VI.26) does not contain a second characteristic decay length, such as ξ_2 in C^{xx}. The oscillatory part of the correlation length in the spinor gas at fixed time t decays only algebraically in space and is, therefore, at any finite time present on all scales. As a consequence, the oscillatory part decays as a whole in time $\propto 1/\sqrt{t}$ instead of moving out of the spatial window. At sufficiently large times an approximately static correlation function $G^{zz}(t,r) \sim e^{-r/\xi_1}$ with $\xi_1 = \varepsilon_{\mathrm{f}}^{-1/2}$ would be expected. We turn back to this question when analysing the correlation lengths.

From Fig. VI.4 we find that the general form for $G(t,r)$, as given Eq. (VI.26), is not changed fundamentally by interactions. In particular, also beyond Bogoliubov theory there is no exponentially fast decay of the oscillatory part found, neither in time or space. It can be seen that (spatial) oscillation frequencies and amplitudes get shifted as compared to Bogoliubov theory. This is expected to affect mainly the long-distance properties of the spatial decay of correlations at fixed time t.

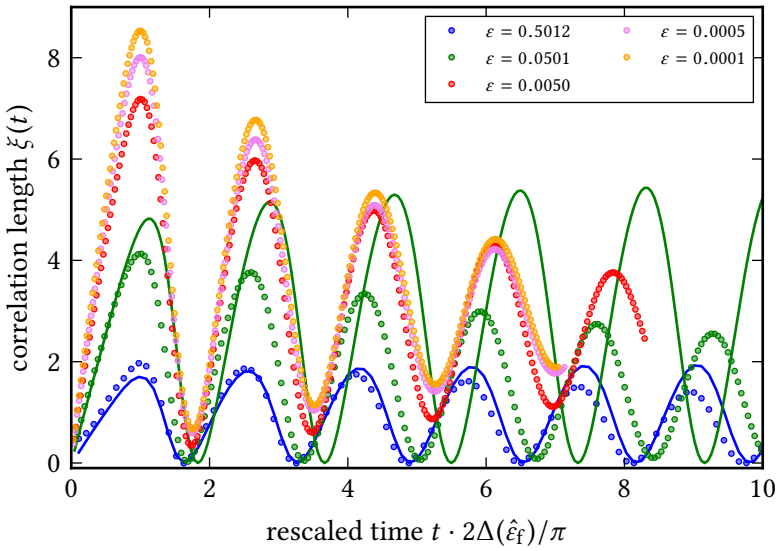

Figure VI.5: Time evolution of the long-distance spin correlation length $\xi(t)$ (see Eq. (VI.27)) of the spinor Bose gas as a function of post-quench time. The correlation length $\xi(t)$, as computed from numerical simulation (coloured symbols), is shown for five different values (see legend) of the distance ε_f to the meanfield critical point. The time axis is rescaled with the time $\tau_1 = \pi/(2\Delta(\hat{\varepsilon}_\mathrm{f}))$ at which the first maximum of the magnetic susceptibility was determined in Sect. V.3 (see Fig. V.3 and discussion in main text). The solid blue and green line represent the long-distance correlation length, as obtained evaluating Eq. (VI.27) with the Bogoliubov correlation functions for corresponding ε_f. The maximum correlation length within Bogoliubov theory scales with $\xi_1 \sim \sqrt{\varepsilon_\mathrm{f}}$ whereas the maximal correlation length from simulation saturates. For reasons of visibility, we plot the Bogoliubov lines therefore only for the two smallest values of ε_f.

VI.3.3 Long-Distance Correlation Length

To analyse the time dependence of spin correlations in the Bose gas further and, in addition, for smaller distances to the critical point, we turn to the correlation length as observable. Since there is no clear separation between a short-distance decay and second characteristic scale for the spatial decay of oscillations in $G^{zz}(t,r)$, we use the integral

$$\xi(t) = \int_0^L \mathrm{d}r\, G^{zz}(t,r)\,. \tag{VI.27}$$

as a bulk measure for the decaying spin correlations. Note that the total system size for our simulations is $L = 1293\,(1/\sqrt{4mJ_\mathrm{c}})$ which is much larger than the characteristic decay of correlation functions. Finite size effects from the spatial integral in the definition Eq. (VI.27) can be neglected.

The length scale $\xi(t)$ in Eq. (VI.27) reflects the overall-decay of the correlation function, including the oscillatory part, as it averages over neighbouring negative and positive re-

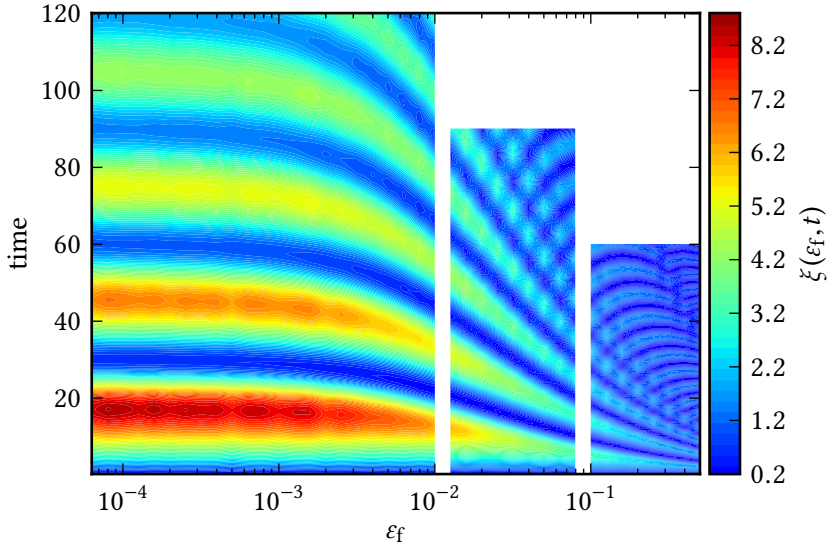

Figure VI.6: Time evolution of the long-distance spin correlation length $\xi(t)$ (see Eq. (VI.27)) in the spinor Bose gas after a quench from $h_i \to \infty$ to distance ε_f from the meanfield critical point in the whole time-ε_f plane. Note the logarithmic scale for the ε_f axis. The value of $\xi(t)$ is encoded in the colour projection. Fig. VI.5 displays slices at fixed values of ε_f.

gions. From Eq. (VI.27), one finds that the long distance correlation length is equal to the zero mode of the *normalised* structure factor, $\xi(t) = G^{zz}(t, k = 0)/2$. With that, the quantity is similar to the magnetic susceptibility, we defined as the zero mode of the *unnormalised* structure factor $\chi(t) = \mathcal{G}^{zz}(t, k = 0)$. Nevertheless, the inclusion of the normalisation factor will lead to different behaviour, as it is time- and ε_f-dependent on its own. In the Bogoliubov scaling regime one expects $\xi \sim \sqrt{\chi}$ due to the Fisher hyperscaling relation.

If $G^{zz}(t, r)$ is dominated by a decay of the form $G^{zz}(t, r) \sim \mathrm{e}^{-r/\xi}$, the definition of ξ in Eq. (VI.27) yields the scale of the exponential decay, $\xi(t) \to \xi_1$. See Sect. II.5.2 for further discussion. Thus, if a stationary state is approached in time with a dominating exponential decay of correlations, one expects $\xi(t) \to \xi_1$ for $t \to \infty$.

As discussed in Sect. II.5.2, the computation of $\xi(t)$ includes in practice also a coarse-graining procedure, to reduce artificial influence of noise from high momentum modes. Note that the length scale $\xi(t)$ defined in Eq. (VI.27) can turn negative for strong anti-correlations (*i. e.* high negative values) at the first oscillation minimum in $G^{zz}(t, r)$, for example for the red curves in both panels of Fig. VI.4.

Examples of the post-quench time evolution of $\xi(t)$ from Eq. (VI.27) for various distances to the meanfield critical point on the paramagnetic side in the spinor Bose gas are shown in Fig. VI.5 (coloured symbols). An overview over the time evolution of $\xi(t)$ in the whole time-ε_f plane is provided in Fig. VI.6, where a colour projection encodes the value of the correlation length.

The long-distance correlation length initially grows in time, reaches a first dominant maximum, and thereafter oscillates. We find that the oscillation maxima of the long-distance correlation length from simulation decay, even for large distances to the critical point $\varepsilon_\mathrm{f} \simeq 0.5$ (in contrast to $\chi(t)$ where the decay appears only for smaller distances, *cf.* Fig. V.1).

The temporal structure of the oscillations follows the same pattern as for the magnetic susceptibility in Fig. V.1. To demonstrate this, the time axis in Fig. VI.5 is rescaled with the time of the first maximum of the magnetic susceptibility. We use the numerically determined value $\tau_1 = \pi/(2\Delta(\hat{\varepsilon}_\mathrm{f}))$ (see Sect. V.3, together with Fig. V.3). Upon expressing time in units of τ_1 for the respective distance to the critical point, the oscillation maxima and minima in the correlation length $\xi(t)$ fall approximately onto each other for the first two periods and then detune again. Thus, the oscillation period of $\xi(t)$ is close to the frequency set by the (shifted) gap. As $\xi(t)$ receives contributions from higher k modes in the structure factor $\mathcal{G}_{zz}$ (via the normalisation of the correlation function), it is understandable that oscillations in $\xi(t)$ reflect not purely the gap frequency.

In contrast to the correlation length ξ_1, defined in Eq. (VI.17), in the Ising model (*cf.* inset c in Fig. VI.2), the damping of the oscillations of the correlation length in the Bose gas is much less pronounced. In fact, within times accessible to simulations and for the distances to the critical point we find in Fig. VI.5 the system does not reach the stationary state, whereas the oscillations are essentially over-damped in the Ising model for $\varepsilon_\mathrm{f} \lesssim 1$.

From the fact that the minima in $\xi(t)$ grow in time while the maxima decay for small distances to the critical point ($\varepsilon_\mathrm{f} > 0.05$ in Fig. VI.5 or Fig. VI.6) the existence of plateau in $\xi(t)$ for times much later times can be deduced.

However, the four maxima and minima for the relevant small values of ε_f do neither allow to extrapolate the data, to obtain a value for the correlation length at this plateau, nor is it possible to decide of the plateau is approached algebraically or exponentially in time. For this reason we analyse the maxima of the correlation length for scaling behaviour in the following, instead of a stationary plateau as for the Ising model in Fig. VI.2.

For the distances to the meanfield critical point $\varepsilon_\mathrm{f} = 0.5$ and $\varepsilon_\mathrm{f} = 0.05$, for which the correlation functions are displayed in Fig. VI.4, the time evolution of the long-distance correlation length $\xi(t)$ as obtained from the Bogoliubov correlation functions is also shown in Fig. VI.5 (see blue and green solid lines in comparison to data points of same colour).

We find that the decay of the oscillations in $\xi(t)$ obtained from full simulation is a pure non-linear effect, when the long-distance correlation length is regarded. Although the oscillation period matches for $\varepsilon_\mathrm{f} = 0.5$ and approximately matches for $\varepsilon_\mathrm{f} = 0.05$, the long-distance correlation length in Bogoliubov theory shows no sign of approaching a stationary plateau.

In light of the asymptotic form of the Bogoliubov correlation function Eq. (VI.26) a comment is in order here. Due to this form, one expects the Bogoliubov correlation length to decay at some point in time (although algebraically slow). But one needs to take into account that the algebraic decay of the oscillatory term in Eq. (VI.26) is obtained within the continuum limit, where complete dephasing of quasi-particle modes is possible (*cf.* also Eq. (III.52) and the corresponding discussion).

The Bogoliubov correlation functions and lengths displayed in Fig. VI.7 and Fig. VI.5, however, are evaluated on a discrete momentum- and position-space grid with discrete

mode frequencies $\omega_{-}(k_i)$. Therefore, quasi-particle modes do not dephase completely and oscillations in the correlation function do not completely decay. As the integral in Eq. (VI.27) always integrates over the whole position-space region, the maximum in $\xi(t)$ does not change much over time and clearly does not visibly decay. It seems even to rise slightly initially. In turn, this shows that the decay of the correlation length in full simulation (which lives on the same finite lattice) is an effect beyond simple dephasing.

VI.3.4 Effective Temperature Crossover

To characterise the scaling behaviour hidden in the post-quench time evolution of the long-distance correlation length further, without knowing the stationary plateau, we analyse the values $\xi(\tau_i) = \max(\xi(t))$ of the correlation length at successive maxima as a function of the distance to the critical point. We demonstrated, in Sect. III.3.2 and Fig. III.4, that successive maxima of the long-distance correlation length in Bogoliubov theory follow the scaling relation

$$\xi(\tau_i) = a(\tau_i)\varepsilon_{\mathrm{f}}^{-1/2}\,, \tag{VI.28}$$

with a slowly varying, time-dependent pre-factor $a(\tau_i)$. However, the results presented in chapter V, in particular, the scaling behaviour of the magnetic susceptibility (see Fig. V.2) already let expect that $\xi(\tau_i)$ deviates from the power law behaviour of the Bogoliubov prediction in Eq. (VI.28).

The results for the maximal long-distance spin correlation length for quenches in the spinor Bose gas from $h_{\mathrm{i}} \to \infty$ to a distance ε_{f} to the meanfield critical point on the paramagnetic side, as obtained from simulation, are shown in Fig. VI.7. For this, the maximal values $\xi_i = \xi$ of $\xi(t;\varepsilon_{\mathrm{f}})$, as displayed in Fig. VI.6, are determined directly numerically, instead of relying on the times $\tau_i = (i+1/2)\pi/\Delta(\hat{\epsilon})$ of maximal magnetic susceptibility (*cf.* Sect. V.3).

As expected, we find in Fig. VI.7 that the maximal long-distance correlation length turns away from the Bogoliubov scaling prediction already at the first maximum ξ_1 for $\varepsilon_{\mathrm{f}} \lesssim 0.1$ (compare black solid line and blue coloured symbols in Fig. VI.7). Instead, the correlation length saturates and turns towards a finite value as $\varepsilon_{\mathrm{f}} \to 0$.

As already found from Fig. VI.5 and Fig. VI.6, the maximal values of the long-distance correlation length additionally decreases in time for all $\varepsilon_{\mathrm{f}} < 1$. From Fig. VI.7 it is apparent, that the decay of the maximal correlation length proceeds faster closer to the critical point. This means that the maximal correlation lengths $\xi_i(\varepsilon_{\mathrm{f}})$ can not simply be rescaled to a universal curve by introducing a τ_i-dependent pre-factor, $\xi_i(\varepsilon_{\mathrm{f}}) = Z_i\xi(\varepsilon_{\mathrm{f}})$.

The behaviour of the post-quench correlation length $\xi(t)$ at its successive maxima $\xi_i(\varepsilon_{\mathrm{f}})$ as a function of the quench parameter, as shown in Fig. VI.7, is very similar to the behaviour of the Ising model's correlation length at a finite temperature (see Eq. (VI.10) and black line in Fig. VI.3). In the following, we argue that this similarity can be turned into a quantitative description for the crossover of $\xi_i(\varepsilon_{\mathrm{f}})$. In Fig. VI.7, we demonstrate that it is possible to fit the crossover of $\xi_i(\varepsilon_{\mathrm{f}})$ with the Ising model's finite temperature crossover function $\xi_{\mathrm{th}}(\varepsilon_{\mathrm{f}}, T)$ (coloured solid lines in Fig. VI.7) from Eq. (VI.10). To do so, three key steps are required, as follows.

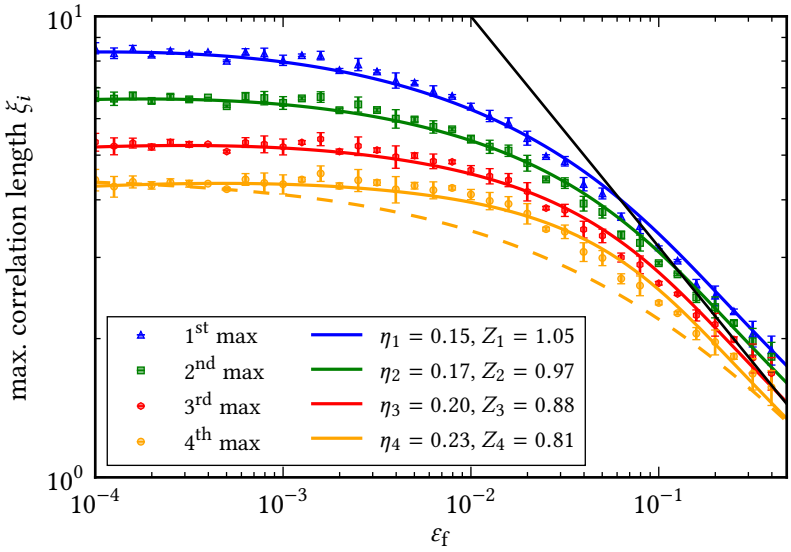

Figure VI.7: Maximal long-distance spin correlation lengths $\xi_i = \xi(\tau_i)$ in the spinor Bose gas as a function of the post-quench distance ε_f to the meanfield critical point. Different colours refer to different successive maxima, the first (blue), second (green), third (violet), and fourth (red), attained after the quench. Coloured data points represent the numerically extracted maximal values of $\xi(t, \varepsilon_f)$, the data for which is shown in Fig. VI.6. The solid black line shows the scaling prediction computed from equilibrium Bogoliubov theory, $\xi \sim \varepsilon_f^{-1/2}$, for comparison. Coloured solid lines represent an evaluation of the expression Eq. (VI.10) for ξ_{th}, the finite temperature correlation length in the Ising chain. The expression Eq. (VI.10) for ξ_{th} is evaluated with gap $\Delta(\varepsilon_f)$ and speed of sound $c(\varepsilon_f)$ from the Bogoliubov spin dispersion of the Bose gas. The temperature is set by the effective temperature (see Eq. (VI.29)) which determines the post-quench occupation of Bogoliubov spin quasi-particles (see Sect. III.4). Additionally, for the different maxima the anomalous dimension appearing in Eq. (VI.10) is adapted as a fit parameter, together with an overall constant Z_i, to correct for the decay of $\xi(\tau_i)$ for $\varepsilon_f \to 1$. Obtained values η_i (error from fit is $\pm 0.02\eta_i$) and Z_i (error from fit is $\pm 0.02 Z_i$) are given in the legend. The dashed line shows ξ_{th} at η_4 and Z_4 at a *constant* temperature $T = 1/4$. We find that the ε_f-dependent profile of $T_{\text{eff}}(\varepsilon_f)$ is vital for being able to fit the numerical data with ξ_{th}. See the main text for further discussion.

First, Eq. (VI.10) for xi_{th} requires properties of the quasi-particle dispersion as input, the excitation gap Δ and the speed of sound c_s. It is reasonable that these properties need to be adapted to the dispersion $\omega_-(k, \varepsilon_f)$ (Eq. (III.11)) of the quasi-particles describing the spin sector of the Bose gas. Thus, for the coloured lines in Fig. VI.7 we insert the Bogoliubov expression, $\Delta = \Delta(\varepsilon_f) = 2\sqrt{\varepsilon_f(\varepsilon_f + 1)}$ and $c = c_s(\varepsilon_f) = \sqrt{2(2\varepsilon_f + 1)}$ for the evaluation of Eq. (VI.10). This means in particular, that the Bogoliubov speed of sound produces an

additional ε_f-dependence as compared to the Ising model.

The second step concerns the temperature scale which enters, in particular, the universal scaling function F_I in ratio to the gap. The ratio Δ/T in $F_\mathrm{I}(\Delta/T)$ locates where the correlation length actually bends away from a pure scaling form and thus determines the crossover feature. As discussed in Sect. III.4, within Bogoliubov theory for the spin sector, the initial state we utilise here can be reduced to a single scale $T_\mathrm{eff}(\varepsilon_\mathrm{f})$ in the infrared momentum region. Adapting the post-quench occupation of Bogoliubov modes to a thermal occupation for momenta $k \ll 1$, one is able to map the scale from the initial state to a ε_f-dependent effective temperature (see Sect. III.4.2 and Eq. (III.67)),

$$T_\mathrm{eff}(\varepsilon_\mathrm{f}) = \frac{1}{2}\left(\varepsilon_\mathrm{f} - \sqrt{\varepsilon_\mathrm{f}(\varepsilon_\mathrm{f}+1)} + 1/2\right) . \tag{VI.29}$$

We insert this expression as temperature in the expression Eq. (VI.10) for the crossover of the correlation length to evaluate it for the coloured solid lines in Fig. VI.7. This demonstrates that the energy scale T_eff has an influence beyond defining a generalised Gibbs state in the Bogoliubov approximation. It determines the energy scale, and with that the distance to the critical point, where interaction effects set in.

Equally important, we find that a constant temperature does not suffice to describe the crossover of $\xi_i(\varepsilon_\mathrm{f})$ in the region $\varepsilon_\mathrm{f} \in [0.1, 0.001]$. An example is given with the dashed yellow line in Fig. VI.7, which is ξ_th at fixed temperature $T = 1/4$. Recall that this is the limiting maximal effective temperature for $\varepsilon_\mathrm{f} \to 0$ (see Sect. III.4.2). We emphasise that, although not shown, attempts to fit a *constant* effective temperature in ξ_th (Eq. (VI.10)) to describe the data for $\xi_i(\varepsilon_\mathrm{f})$ over the whole ε_f-region fail.

In the third step, one needs to compensate for the change of the long-distance correlation length $\xi_i(\varepsilon_\mathrm{f})$ in time. The maximal values of the post-quench correlation length decay in time, see Fig. VI.7 or Fig. VI.5, which is not captured naturally by the finite temperature crossover function from Eq. (VI.10).

It is reasonable that one needs to allow for a non-universal, possibly time-dependent, constant (in the spirit of a renormalisation constants) in the comparison between Ising model and Bose gas correlation length, *i. e.* $\xi_\mathrm{th}(\varepsilon_\mathrm{f}) \to Z(\tau_i)\xi_\mathrm{th}(\varepsilon_\mathrm{f}) = x i_i(\varepsilon_\mathrm{f})$. This overall constant can be used to compensate the decay of the correlation length in the Bogoliubov scaling regime for $\varepsilon_\mathrm{f} \to 1$.

However, as can be seen from Fig. VI.7 and argued before, for $\varepsilon_\mathrm{f} \to 0$, the decay of the correlation length (*i. e.* the shift downwards) is stronger than for $\varepsilon_\mathrm{f} \to 1$. Therefore, the limit $\lim_{s\to 0} F_\mathrm{I}$ (see Eq. (VI.12)) needs to be different for different maxima, as compared to the thermal Ising crossover function. A change of this limit can be attained by assuming a different anomalous dimension $\eta \to \eta_i$ entering the expression Eq. (VI.10) for ξ_th, see also Eq. (VI.12).

To achieve the four different coloured lines in Fig. VI.7, the overall constant Z_i is fixed from the limit $\lim_{\varepsilon_\mathrm{f}\to 1} \xi_i$. The anomalous dimension η_i is then determined by a fit of

$$\xi_i(\varepsilon_\mathrm{f}) = Z_i \xi_\mathrm{th}\left(\eta_i, T_\mathrm{eff}, \Delta(\varepsilon_\mathrm{f}), c_\mathrm{s}(\varepsilon_\mathrm{f})\right) , \tag{VI.30}$$

to the data points of the maximal correlation length $\xi_i(\varepsilon_\mathrm{f})$. We point out, that the form of the crossover (the ε_f-dependence in ξ_i) is set by *a priori* knowledge. It is determined by

inserting the ε_f-dependent effective temperature together with the Bogoliubov gap and the Bogoliubov speed of sound into the Ising crossover function.

From this procedure, we find that the values for η_i are considerably smaller than the anomalous dimension of the Ising model, $\eta_i < 1/4$ (see legend in Fig. VI.7). It is, at this point unclear, if the η_i assume the meaning of a dynamical anomalous dimension (in the sense of critical exponents) for the spin sector of spinor Bose gas. One can take the point of view, that the appearance of η_i in Eq. (VI.30) constitutes a second non-universal fit parameter, which is required since the Bose gas is at the maxima displayed in Fig. VI.7 still far away from a stationary plateau. Then, the progression of the values of η_i (see values for η_i in the legend of Fig. VI.7) towards $\eta = 1/4$, the anomalous dimension of the Ising model, suggests that the stationary state in the Bose gas indeed would be described by the thermal crossover function of the Ising model.

In summary, we find that the maximal long-distance correlation length can be described by the universal crossover function for the thermal correlation length of the Ising model, see Eq. (VI.30). This requires to introduce two time-dependent parameters, η_i and Z_i. This however is a consequence of studying a very early stage in the post-quench time evolution. The main result is that the ε_f-dependence of the (maximal) correlation lengths $\xi_i(\varepsilon_\mathrm{f})$ is set by the universal crossover function of the Ising model. For this one needs to evaluate the crossover function with the Bogoliubov quasi-particle dispersion of the spinor gas, and, intriguingly, the effective temperature $T_\mathrm{eff}(\varepsilon_\mathrm{f})$ (including its full ε_f-dependence) found from the generalised Gibbs ensemble describing the Bogoliubov quasi-particles.

VI.4 Self-Similar Evolution within Quench Dynamics

Finally, we turn to the question if a quench in the spinor Bose gas within the paramagnetic regime hosts self-similar time evolution of occupation spectra. In particular, if time itself acts as an additional critical tuning parameter after the quench one expects a general scaling form

$$\mathcal{G}\left(s^{-1/\beta}t, sk, s^c\varepsilon\right) = s^{-\alpha/\beta}\mathcal{G}\left(t,k,\varepsilon\right) , \tag{VI.31}$$

for a equal-time correlation function to hold. For our quench setup, the scaling form can include ε_f, ε_i or even more scales of the initial state (generically represented by $s^c\varepsilon$ in Eq. (VI.31)). Such a scaling form allows to eliminate the explicit dependence of $\mathcal{G}$ on one of the variables, as the scaling form holds for arbitrary values of s. For example, choose $s = (t/t_\mathrm{ref})^\beta$ such that $ts^{-1/\beta} = t_\mathrm{ref}$ and insert on both side of expression Eq. (VI.31) to get

$$\mathcal{G}\left(t,k,\varepsilon_\mathrm{f}\right) = t^\alpha\mathcal{G}\left(t_\mathrm{ref}, (t/t_\mathrm{ref})^\beta k, (t/t_\mathrm{ref})^{\beta c}\varepsilon_\mathrm{f}\right) . \tag{VI.32}$$

This essentially means that, via the scaling form Eq. (VI.31), the spectrum at any time t is connected to the spectrum at an arbitrary reference time t_ref. Thus, the full time dependence is generated by rescaling a universal function.

In Sect. III.3 we found that the spin structure factor $\mathcal{G}_{zz}$ fulfils a scaling form Eq. (VI.31) if $\varepsilon \gg 1$ or $\varepsilon \ll 1$. In chapter V, we found that this scaling behaviour is destroyed when quenching to values $\varepsilon \lesssim 1$.

In this section, we show that there are nevertheless occupation spectra for specific or-

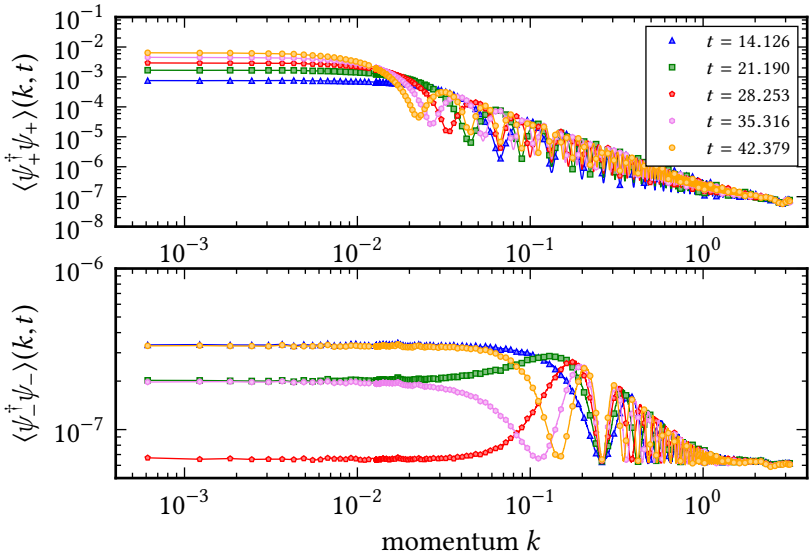

Figure VI.8: Examples for the post-quench time evolution of the symmetric occupation spectrum $\mathcal{G}_{++}(k,t)$ (upper panel) and the anti-symmetric occupation spectrum $\mathcal{G}_{--}(k,t)$ (lower panel), see Eq. (VI.33). Coloured data points correspond to data from simulation at different times (see legend) for a quench to a distance $\varepsilon_\mathrm{f} = 0.1$ from the critical point. Coloured solid lines are plotted as guide for the eye. Simulation parameters from Table B.3.

der parameter fields in the spinor Bose gas, which fulfil a time-dependent scaling form Eq. (VI.31) for quenches close to the critical point. This is especially important, as behaviour of the structure factor or occupation spectrum following Eq. (VI.32) is typically taken as a signal for critical dynamics. In particular, concrete realisation of Eq. (VI.32) with $c = 0$ are found in the context of phase ordering kinetics (see [54] for a review) and have been put forward as a signature of non-thermal fixed points in the context of transport phenomena [47]. This will be addressed in more detail in chapter VII.

In this section, we analyse occupation number spectra of the fundamental Bose fields $\Phi_j(k,t)$ (see Eq. (II.1)) for scaling forms. It is convenient to define the combinations $\psi_\pm = \Phi_\uparrow \pm \Phi_\downarrow$ (see Appendix A for a corresponding representation of the full spinor gas Eq. (II.1)). Then, the observables of interest read

$$\begin{aligned}\mathcal{G}_{\pm\pm}(k,t) = \langle\psi_+^\dagger(k,t)\psi_+(k,t)\rangle \\ \langle\Phi_\uparrow^\dagger(k,t)\Phi_\uparrow(k,t)\rangle + \langle\Phi_\downarrow^\dagger(k,t)\Phi_\downarrow(k,t)\rangle \pm 2\mathrm{Re}\langle\Phi_\uparrow^\dagger(k,t)\Phi_\downarrow(k,t)\rangle\end{aligned} \tag{VI.33}$$

which are combinations of the occupation spectra of the single components $\langle\Phi_j^\dagger(k,t)\Phi_j(k,t)\rangle$ with the overlap spectrum $\langle\Phi_\uparrow^\dagger(k,t)\Phi_\downarrow(k,t)\rangle$.

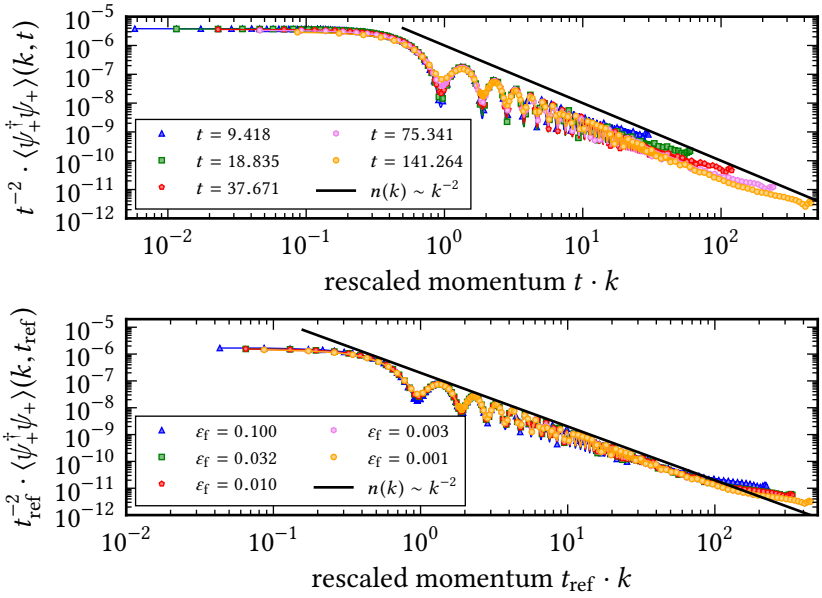

Figure VI.9: Rescaled symmetric occupation spectrum $t^{-\alpha}\mathcal{G}_{++}(k,t)$ as a function of rescaled momentum $t^{\beta}k$, to demonstrate the scaling collapse of $t^{-\alpha}\mathcal{G}_{++}(k,t)$ according to the scaling form Eq. (VI.32). Upper panel: Scaling collapse with $\alpha = 2$ and $\beta = 1$ at fixed $\varepsilon_{\mathrm{f}} = 0.1$ (see unscaled data in Fig. VI.8), where five exemplary times (see legend) are shown at logarithmically equidistant times. Lower panel: rescaled symmetric occupation spectrum $t_{\mathrm{ref}}^{-\alpha}\mathcal{G}_{++}(k,t_{\mathrm{ref}})$ as function of $t_{\mathrm{ref}}^{\beta}k$ at reference time $t_{\mathrm{ref}} = 141.264$ (*cf.* orange curve in upper panel) for several distances to the critical point ε_{f} (see legend). Coloured data points correspond to simulation data and coloured solid lines are plotted as guide for the eye. Note that the reference time t_{ref} is ε_{f}-independent, rendering the scaling collapse quench independent. Simulation parameters from Table B.3.

Occupation spectra of Fundamental Fields

Examples for the time evolution of $\mathcal{G}_{++}(k,t)$ and the corresponding spectrum are shown in Fig. VI.8. We show the post-quench time evolution for our standard quench scenario (as employed in Sect. VI.3) to $\varepsilon_{\mathrm{f}} = 0.1$ for early times. The numerical parameters are given in Table B.3, which are chosen to resolve mainly the momentum region $k \in [0,1]$.

We find that $\mathcal{G}_{--}(k,t)$ (lower panel in Fig. VI.8) displays a behaviour very similar to the time evolution of the z-spin structure factor $\mathcal{G}_{zz}(k,t)$ (*cf.* Fig. V.5). This is not surprising, as ψ_- is a antisymmetric combination similar to the z-spin field. In particular, $\mathcal{G}_{--}(k,t)$ has a heavily oscillating plateau in the infrared momentum region. The scale, at which this plateau goes over into a decay in k, is fixed for fixed ε_{f}. Likewise, the amplitude of the temporal oscillation of the plateau does not change at fixed ε_{f}.

The behaviour of the spectrum $\mathcal{G}_{++}(k,t)$ (upper panel in Fig. VI.8) is drastically different. We find that $\mathcal{G}_{++}(k,t)$ is in general several orders of magnitudes larger than $\mathcal{G}_{--}(k,t)$. According to Eq. (VI.33), this means that the real part of the overlap occupation spectrum

is on the order of the occupation spectra of the single components. The symmetric spectrum $\mathcal{G}_{++}(k,t)$ displays also a plateau for infrared momenta. But in contrast to $\mathcal{G}_{--}(k,t)$ this plateau in $\mathcal{G}_{++}(k,t)$ does not oscillate in time. It grows in time towards higher occupation numbers and simultaneously moves further towards $k = 0$ in time. This shifts the whole occupation spectrum upwards and towards the infrared.

Universal Scaling Forms

The type of time dependence described above is typical for cascades and for scaling forms according to Eq. (VI.32). To analyse this further, we test the scaling prediction Eq. (VI.32) by plotting the rescaled symmetric occupation spectrum $t^{-\alpha}\mathcal{G}_{++}(k,t)$ as a function of rescaled momentum $t^{\beta}k$. The result is shown in Fig. VI.9. In the upper panel, we depict the result after rescaling the same data for the symmetric occupation spectrum as is shown unscaled in Fig. VI.8 (upper panel), *i. e.* at fixed $\varepsilon_{\mathrm{f}} = 0.1$. Note that the times are at which $\mathcal{G}_{++}(k,t)$ is evaluated are different and, in particular, extend to a bigger range of times at logarithmically equidistant steps.

We find that, at fixed ε_{f}, the spectrum $\mathcal{G}_{++}(k,t)$ can be collapsed to a single curve, apart from a high momentum tail. The scaling form in Eq. (VI.32) holds if

$$\begin{aligned} \alpha &\simeq 2 \\ \beta &\simeq 1\,. \end{aligned} \tag{VI.34}$$

In the lower panel of Fig. VI.9 we analyse the ε_{f}-dependence of the scaling form. We compute the rescaled occupation spectrum at a reference time for different quenches, *i. e.* different values of ε_{f}. As a reference time we choose $t_{\mathrm{ref}} = 141.264$, which is the latest time displayed in the upper panel. From this, we find that there is no dependence on ε_{f} in the scaling form, meaning $c = 0$ in Eq. (VI.32). This means that the post-quench time evolution of the symmetric occupation spectrum $\mathcal{G}_{++}(k,t)$ can be generated from a universal function $\mathcal{G}_{++}(k)$ via a scaling transformation Eq. (VI.32) and exponents $\alpha = 2$, $\beta = 1$, and $c = 0$. In particular, the universal function is does not depend on the quench. We emphasise that we have tested this for all available reference times and did not find any dependence of α and β on ε_{f} either.

The universal curve $\mathcal{G}_{++}(k)$ decays after the plateau in the infrared algebraically, approximately with a power law $\mathcal{G}_{++}(k) \sim k^{-2}$ (see black lines Fig. VI.9). The power law stops at a scale k_λ, which moves in time to the infrared following a power law itself, $k_\lambda \sim t^{-\beta}$ (due to the scaling form Eq. (VI.32)). This means that the spectrum evolves algebraically (critically) slow in time.

Fig. VI.9 shows that oscillations in k are superimposed on the decay of the spectrum $\mathcal{G}_{++}(k)$ for $k > k_\lambda$. It is peculiar that the oscillations in k are consistently rescaled by the scaling transformation Eq. (VI.32) and collapsed to a single curve. This implies that there is a second k-space scale (the period of the oscillations) which is not quench dependent. To clarify this, a further analytic analysis of the origin of the scaling form is required.

Finally, we comment on the values of the exponents α and β Eq. (VI.34), which are realised in the scaling form. For our concrete realisation of the spinor Bose gas, there are currently no analytic predictions available, due to the structure of couplings. However,

the critical dynamical evolution of the symmetric occupation spectrum $\mathcal{G}_{++}(k,t)$ seems rather insensitive the quench (*i. e.* details of the coupling structure).

For $O(N)$-symmetric field theories, however, there exist predictions and it seems reasonable to compare to them. In particular, in [47] out-of-equilibrium dynamics for $O(N)$-symmetric field theories is studied with effective Boltzmann transport equations and two-particle irreducible effective action techniques. The authors find possible realisations of scaling forms for the statistical correlation function together with predictions for α and β. The realisations depend on the type of local transport (particle or energy) assumed and if the theory is relativistic (see Eq. 91 and Eq, 92 in [47]) or non-relativistic (see Eq. 81 and Eq, 82 in [47]).

Assuming now, that the calculations for a $O(N)$-symmetric theory are applicable to the symmetric occupation spectrum[7] $\mathcal{G}_{++}(k,t)$, we find that there is only one scenario from [47] consistent with the numerical values of α and β Eq. (VI.34). One needs to assume local energy transport in a relativistic theory, which comes with exponents

$$\begin{aligned} \alpha &= \frac{d+z}{2-\eta-z} \\ \beta &= \frac{1}{2-\eta-z}\,. \end{aligned} \tag{VI.35}$$

This yields, $\alpha = 2$ and $\beta = 1$, *i. e.* the values required for the scaling collapse of $\mathcal{G}_{++}(k,t)$ in Fig. VI.9, with $z = 1$ and for zero anomalous exponent $\eta = 0$. This would imply that the critical dynamical evolution of $\mathcal{G}_{++}(k,t)$ in Fig. VI.9, together with the temporal scaling collapse, is connected to a local transport of energy towards the infrared. An analytic analysis of the correlation function $\mathcal{G}_{++}$ within a non-perturbative approximation of our model Eq. (II.1) is required to clarify this further.

VI.5 Summary

In this chapter, we argued that the Ising model in a transverse Field is the best starting point to compare the non-linear quench dynamics of the spinor gas to. The results from [116] show that the static universality class of the Ising phase transition applies at least in one regime (the Mott insulating regime) of the full phase diagram of the spinor gas.

Consequently, we reviewed recent results [90–92, 212] on quenches within the paramagnetic phase of the transverse Ising chain. The quench protocol, starting in the ground-state of the quasi-particle basis at one parameter value and computing the Hamiltonian time evolution with a different parameter, is thereby the same as we implement for the spinor gas (see Sect. V.1).

The situation for the Ising model is as follows. As the post-quench stationary state of the Ising model is fully described by a generalised Gibbs ensemble [90–95] and, thus, correlation functions quickly relax to this stationary state. We find that this is even the case for small finite spin chains within a view periods of the characteristic gap frequency.

[7] $\mathcal{G}_{++}(k,t)$ is the equal-time contribution to the statistical correlation function $\langle\{\psi_+(k,t_1)\psi_+(k,t_2)\}\rangle$ of the symmetric field ψ_+.

The spin correlation length follows a crossover function towards the critical point. In the scaling limit and close to the critical point (leading and next-to-leading order in the gap ratio $\Delta_\mathrm{f}/\Delta_\mathrm{i}$), the crossover function can be matched to the thermal crossover function (Eq. (VI.30), [89]), if a effective temperature $T_s = 2\Delta_\mathrm{i}/\pi$ is chosen (see Sect. VI.2.3). However, this effective temperature is rather a characteristic scale for the bulk energy and derives not naturally from the quasi-particle occupation numbers. As a direct consequence it describes not the full crossover function in the steady state, when going to larger distances to the critical point.

The situation in spinor Bose gas is superficially similar, but comes with a number of striking differences when details are considered. First, we find that the correlation lengths or functions approach a steady state on much longer time scales (in units of gap periods) for similar distances to the critical point ε_f. This can be understood, as the parameter ε_f simply does not need to be comparable on a 'value by value' basis. Even if renormalisation effects are not taken into account for the Bose gas (*cf.* Sect. V.3), the gaps in both models already scales differently with ε_f.

Nevertheless, we demonstrated that it is possible to extract a meaningful correlation length as function of the distance to the critical point, by concentrating on maximal values of the correlation lengths (see Sect. VI.3.4). We find from this procedure that the maximal long-distance correlation length follows a crossover function, which scales according to the Bogoliubov prediction for large ε_f but saturates towards a finite value close to the critical point.

As main result of this chapter, we find that this crossover can be described by the universal crossover function for the thermal correlation length of the Ising model, see Eq. (VI.30). This requires to introduce two parameters, η_i and Z_i, which depend on the maximum which is evaluated, to capture the overall decay of the correlation length. This is necessary as we analyse a very early stage in the post-quench time evolution. The important point is that the ε_f-dependence of the (maximal) correlation lengths $\xi_i(\varepsilon_\mathrm{f})$ is set by the universal *thermal* crossover function of the Ising model over the whole range of ε_f if the effective temperature $T_\mathrm{eff}(\varepsilon_\mathrm{f})$ Eq. (VI.29) is used in the universal function. But, as we have determined in Sect. III.4, the effective temperature of the Bose derives naturally from the generalised Gibbs ensemble for the post-quench Bogoliubov quasi-particle occupation.

All together, this brings back the notion of universality to the post-quench behaviour of the spinor Bose gas. If one corrects for the decay to an unknown steady-state, correlations follow in the bulk (measured by the maximal long-distance correlation length) a universal function which carries the ε_f dependence only via ratios of energy scales. The energy scales derive naturally, as one comes from the excitation gap after the quench and one essentially from the pre-quench excitation gap (see Sect. III.4).

It is an equally striking observation, that one can measure the crossover behaviour long before the spinor gas has reached a form of stationary state (be it equilibrium or non-equilibrium). Due to the fact that the spinor Bose gas is not integrable for the fully interacting dynamics but starts initially very close to the integrable theory, it is expected to encounter the phenomenon of prethermalisation [34, 35], instead of relaxation to a truly steady state [214].

In the context of prethermalisation out results for the spinor gas can be interpreted in

the following way. The crossover in the bulk correlations appears after kinetic prethermalisation (in the language of [35]), meaning, after the Bogoliubov modes have sufficiently dephased to let the energy stored in the infrared Bogoliubov occupation numbers define an effective temperature. At the same instance, interactions between quasi-particle modes become relevant, which let correlations evolve towards a prethermalisation plateau. If the plateau is reached, the correlation function displays universal behaviour of the underlying equilibrium universality class at a possibly different effective temperature.

In the last section Sect. VI.4, we have demonstrated that the Bose, gas viewed not in the language of pseudo-spins but in terms of the actual quantum gas, displays critical dynamics (critical scaling in time) after the quench insensitive to the distance to the critical point. We have demonstrated that single-component occupation number distributions evolve self-similar in time after the quench $\mathcal{G}_{++}(t,k) \sim t^{\alpha} f(t^{\beta}k)$, with critical exponents $\alpha = 2$ and $\beta = 1$. This implies, in particular, a critical slow down in the post-quench time evolution. In [47] this kind of behaviour has been put forward as criterion for the presence of a non-thermal fixed point for the time evolution. In the light of these findings, we have argued that the critical scaling in single-component occupation distributions of the spinor gas can be attributed to a non-thermal fixed point which is connected to a (an effectively) relativistic local energy transport. This is in particular interesting, as quenches to the immiscible regime, or in general, quenches which provoke structure formation (see Sect. II.6), lead typically to fixed point behaviour in the context of inverse particle cascades [60].

VII Non-equilibrium Steady States in the Bose Gas

In the final part of this thesis we address the question if the Bose gas can host truly steady states with a distinctly non-thermal signature[1]. So far, we have discussed non-thermal fixed points in the isolated two-component Bose gas and identified them via non-thermal scaling laws in power spectra and, in particular, via a critical slow-down of the time evolution. The latter means that the state evolves arbitrarily slow in time, being in proximity to a renormalisation group fixed point, but nevertheless do not become perfectly stationary. Since otherwise the thermalisation hypothesis would be violated, such a behaviour lies within expectations for non-integrable isolated systems. Actually, for our findings for the spinor Bose gas, the property 'isolated' is already a matter of the point of view one wants to adopt. We have mainly analysed the spin sub-sector and ignored the symmetric sector as it stays in its Gaussian state. However, the symmetric sector will act as a bath for the spin degrees of freedom, rendering the effective dynamics on the spin sector non-isolated. To make this explicit in an analytic treatment one would just have to integrate out the symmetric degrees of freedom in a path integral formalism to obtain an effective action [215] for the spin sector. The coupling between the 'bath' and the spin sector in this scenario is self-consistent and, thus, hardly controllable from the outside. The same is true for the statistics of fluctuations of the 'bath', although a thermal behaviour can be considered unlikely.

In this and the following chapter, we open the single-component Bose gas in two spatial dimensions to an external environment by explicitly introducing a stochastic bath with which the Bose gas can interact. With that, the isolation is broken in a controlled way which allows to engineer the fluctuation statistics of the bath. First, we introduce a different method to probe the fixed point structure in the isolated one-component Bose gas, using ensembles of topological defects in the initial state (see also [65]). With that we reveal a new, strongly anomalous, non-thermal fixed point in the dynamics of the isolated Bose gas. It comes with an anomalous slow evolution in time which tremendously stabilises the non-thermal state, bringing it closer to a non-equilibrium steady state. In the second part of this chapter, we expose the Bose gas to a thermal environment, within the same setups which evolve close to a non-thermal fixed point when studied without the thermal bath. The exposure to the thermal bath in this case will exceed the 'parasitical' coupling to environment which is usually encountered in experiments with alkaline atoms. On the other hand, the coupling strength will still be 'weak' as compared for example to the holographic treatment of the Bose gas from [65].

In the next chapter VIII, we utilise couplings to stochastic baths with strong non-

[1] For simplicity and in accordance with common literature we speak of 'non-equilibrium steady state (NESS)' in the following

thermal features. This allows to probe the structure of fixed points of the Bose gas from outside, by trying to drive the system directly into different non-equilibrium steady states. To do so, the stochastic properties of the fluctuations in the bath and the initial state which is coupled to the bath serve both as tuning knobs. *A priori*, it is not clear if every fixed point of the isolated Bose gas is in one-to-one correspondence with a non-equilibrium steady state. As a major result, we succeed in identifying one non-thermal fixed point of the isolated Bose gas which has a direct counterpart in form of a non-equilibrium steady state. In addition, we identify a new class of steady states which are presumably connected to the Kardar–Parisi–Zhang dynamic universality class.

VII.1 Stochastic dynamics of the Bose gas

In this section, we summarise the description of non-equilibrium dynamics of a driven-dissipative ultra cold Bose gas by means of stochastic semi-classical field simulations. The method constitutes a variation of the truncated Wigner-type semi-classical field simulations we employed so far for the isolated Bose gas, where the sampling over a stochastic *initial* field distribution is traded for a sampling over a time dependent stochastic driving force. Introducing additionally dissipation via imaginary coupling constants allows to capture, for example, the physics of a Bose gas in a thermal environment [160–162] or a non-equilibrium situation as it occurs for exciton–polariton condensates [109, 216, 217]. After introducing the driven-dissipative Gross-Pitaevskii theory we recall its relation to the hydrodynamic description involving a continuity equation for the density as well as the Kardar-Parisi-Zhang equation for the condensate phase.

VII.1.1 Driven-dissipative Gross-Pitaevskii equation

A two-dimensional dilute interacting Bose gas coupled to a particle bath and a driving force field can be described by the stochastic driven-dissipative Gross-Pitaevskii equation [162]

$$i\partial_t\psi(\boldsymbol{x},t) = \frac{\delta H}{\delta\psi^*(\boldsymbol{x},t)} + \frac{\delta H_\mathrm{d}}{\delta\psi^*(\boldsymbol{x},t)} + \zeta(\boldsymbol{x},t)\,, \tag{VII.1}$$

where H denotes the standard Gross-Pitaevskii Hamiltonian,

$$\frac{\delta H}{\delta\psi^*(\boldsymbol{x},t)} = \left[-\frac{1}{2m}\nabla^2 + g\,|\psi(\boldsymbol{x},t)|^2 - \mu\right]\psi(\boldsymbol{x},t)\,, \tag{VII.2}$$

with particle mass m, real-valued part of the coupling constant g, expressed in two dimensions in terms of the s-wave scattering length a as $g = -(4\pi/m)[\ln(\mu m a^2/4)]^{-1}$, with chemical potential μ. This describes the energy and particle-conserving part of the dynamics and is the one-component analogue of what we have used so far. H_d accounts for the dissipative part of the dynamics,

$$\frac{\delta H_\mathrm{d}}{\delta\psi^*(\boldsymbol{x},t)} = i\left[\nu\nabla^2 - g_\mathrm{d}\,|\psi(\boldsymbol{x},t)|^2 + \mu_\mathrm{d}\right]\psi(\boldsymbol{x},t)\,, \tag{VII.3}$$

defined in terms of the diffusion constant ν and the imaginary parts of the coupling, g_d, and chemical potential, μ_d. If the latter quantities are positive, $g_\mathrm{d} > 0$, $\mu_\mathrm{d} > 0$, the term proportional to g_d accounts for non-linear particle loss, while the linear term quantified by μ_d describes a source of particles. In this chapter, we restrict our numerical study to the case $g_\mathrm{d} > 0$, $\mu_\mathrm{d} > 0$.

The external force ζ is a stochastic complex quantity vanishing in the mean, $\langle\zeta(\boldsymbol{x},t)\rangle \equiv 0$. It represents a stochastic driving force, as for example generated by a laser which incoherently pumps an exciton-polariton condensate. Without loss of generality ζ can be chosen to have Gaussian statistics. Here, we choose ζ uncorrelated in time but correlated in a characteristic manner in space. We demand the power spectrum to follow a generalised Cauchy distribution

$$\langle\zeta^*(\boldsymbol{k},t)\zeta(\boldsymbol{k},t')\rangle = \frac{\gamma}{1+(k\lambda)^\upsilon}\delta(t-t')\,, \tag{VII.4}$$

with a length scale λ and the driving strength γ. This sets the second-order correlation function of ζ and defines the stochastic properties of the bath as we choose it Gaussian. In our simulations, γ is a constant in time and space. The setup generates in general a strong non-equilibrium coupling to a non-thermal bath. However, a special choice of the parameter set renders the setup thermal, along the lines of the idea of the stochastically projected Gross–Pitaevskii equation [162]. The bath itself needs to follow white-noise spatial correlations, achieved by $\upsilon = 0$, if it is not dynamically simulated on its own. Furthermore, the complex coupling constants $1/2m+\mathrm{i}\nu$, $g+\mathrm{i}g_\mathrm{d}$, and $\mu+\mathrm{i}\mu_\mathrm{d}$ have to assume the same phase in the complex plane to fulfil a detailed balance condition [109]. Then, the classical-statistical fluctuation-dissipation theorem allows to deduce a temperature [162],

$$T = 2k_\mathrm{B}\alpha/\gamma\,, \tag{VII.5}$$

where $\alpha = g_\mathrm{d}/g = \mu_\mathrm{d}/\mu = 2m\nu$ is a constant set by the ratio between imaginary and real part of the complex coupling constants.

VII.1.2 Hydrodynamic Description and Kardar–Parisi–Zhang Equation

A hydrodynamic formulation of the stochastic driven-dissipative Gross–Pitaevskii equation is found by again resorting to the phase-density parametrisation $\psi = \sqrt{n}\exp[\mathrm{i}\theta]$ in terms of the fluid density n and velocity field $\boldsymbol{v} = m^{-1}\nabla\theta$. Inserting this parametrisation in Eq. (VII.2) and Eq. (VII.3) one finds n and θ to obey

$$\begin{aligned}\partial_t\theta + \frac{1}{2m}(\nabla\theta)^2 - \nu\nabla^2\theta &= U\,,\\ \partial_t n + \frac{1}{m}\nabla(n\nabla\theta) &= S\,.\end{aligned} \tag{VII.6}$$

These equations generalise the hydrodynamic equations equivalent to the conservative Gross–Pitaevskii equation, introducing inhomogeneities and a dissipative term to the

equation for θ,

$$U = \frac{1}{4m\sqrt{n}}\nabla\cdot\left(\frac{\nabla n}{\sqrt{n}}\right) + \frac{\nu}{n}\nabla n\cdot\nabla\theta + \mu - gn - \frac{\mathrm{Re}(\zeta\,\mathrm{e}^{-\mathrm{i}\theta})}{\sqrt{n}}\,,$$
$$S = \nu\sqrt{n}\nabla\cdot\left(\frac{\nabla n}{\sqrt{n}}\right) - 2\nu n\,(\nabla\theta)^2 - 2\mu_{\mathrm{d}}n - 2g_{\mathrm{d}}n^2 + 2\sqrt{n}\,\mathrm{Im}(\zeta\,\mathrm{e}^{-\mathrm{i}\theta}). \tag{VII.7}$$

Recall that we derived equations similar to Eq. (VII.6) for the hydrodynamic description of the symmetric sector of the two-component Bose gas, where in that case U and S receive contributions from the spin sector instead of the stochastic bath. The above coupled set of non-linear Langevin equations can be simplified if the fluctuations of the density are sub-dominant to the fluctuations of the phase which is generically the case at low momenta in the degenerate regime. In this case, the equations decouple, with U playing the role of the potential of a stochastic forcing $\mathrm{f} = m^{-1}\nabla U$ in the hydrodynamic equation for the fluid velocity $\boldsymbol{v} = m^{-1}\nabla\theta$, with noise correlator

$$\langle U(\omega,\boldsymbol{k})U(\omega',\boldsymbol{k}')\rangle = \delta(\omega+\omega')\,\delta\left(\boldsymbol{k}+\boldsymbol{k}'\right)\,u(\omega,\boldsymbol{k}). \tag{VII.8}$$

This describes particles being injected and removed as amplitude fluctuations, such that the system reaches a state where they can be described by a (not necessarily thermal) distribution and feed energy to the phase fluctuations. As argued in [110, 217] and in [218] the equation for the phase angle θ, Eq. (VII.6), reassembles the Kardar–Parisi–Zhang equation [105] if the density fluctuations can be considered sub-dominant. Then, U constitutes a self-consistent and self-adjusting effective forcing term for the an effective Kardar–Parisi–Zhang equation, which can be computed from the dynamics of the driven-dissipative Bose gas. Results from [218] as well as the results we will present in this chapter suggest that, to exploit the mapping to the Kardar–Parisi–Zhang equation for describing the dynamics of the Bose gas, the Bose gas is additionally required to be free of phase defects. This is understandable from a phenomenological point of view, as the Kardar–Parisi–Zhang equation actually describes the height of surfaces and, thus, calculations do not take topological sectors into account, whereas Eq. (VII.6) describes a phase field which can live in different distinct topological sectors. Calculations should only be compared if the phase field is restricted to zero winding number. In a dynamical setup, correspondingly the nucleation of local phase defects has to be excluded.

VII.2 An Anomalous Non-thermal Fixed Point

The cubic non-linearity in $\nabla\theta$ in the Kardar–Parisi–Zhang Hamiltonian can lead to an instability. For typical parameter choices, however, the Kardar–Parisi–Zhang equation describes surface growth and smoothing [105], and a steady state is reached when the driving and dissipation compensate each other. Shocks in the velocity field, corresponding to cusps in the surface, develop and grow. The dynamics described by the stochastic Gross–Pitaevskii equation, however, is in general different as the phase θ lives on the compact circle. Moreover, the Gross–Pitaevskii equation supports solitary wave solutions, in particular (quasi) topological defects such as vortices, see Sect. II.3. Velocity shock waves

created due to the non-linearity typically lead to the formation of such defects.

It was shown in [55–57] that the formation of turbulent ensembles of vortices can be associated with the isolated system approaching a non-thermal fixed point [44–46] where the time evolution is critically slowed down before the system eventually thermalises [47, 59]. Signatures of such turbulent behaviour and critical slowing down are a characteristic scaling behaviour of correlation functions such as the angle-averaged single-particle momentum spectrum

$$n(k,t) = \int \mathrm{d}\Omega_k \, \langle \Phi^\dagger(\boldsymbol{k},t)\Phi(\boldsymbol{k},t)\rangle \,. \tag{VII.9}$$

It was shown [55–57] that typically, a, *e. g.*, instability-induced overpopulation of momenta at scales on the order of the inverse healing length $k_\xi = \sqrt{2gnm}$, where n is the bulk density of the gas, can subsequently drive the system to a non-thermal fixed point. This happens because the particles in the overpopulated regime of momenta are being transported in momentum space to modes with lower eigenenergy in self-similar fashion, exhibiting scaling in space and time [47],

$$n(k,t) = (t/t_0)^\alpha n([t/t_0]^\beta k, t_0). \tag{VII.10}$$

At the same time, energy conservation forces a few particles to be transported to higher momentum modes, forming a direct wave-turbulent cascade and eventually a non-condensed thermalised fraction of the gas [55–57, 59]. In the long-wavelength regime of particles scattered to lower momenta the momentum distribution was found to exhibit characteristic scaling[2] $n \sim k^{-\zeta}$ in momentum space,

$$n(k,t) \sim k^{-4} \,, \tag{VII.11}$$

in $d = 2$, cutoff in the infrared at a certain scale k_λ to ensure non-divergence of the overall particle density. More precisely, the scaling evolution Eq. (VII.10) predicts that $n(k,t)$ forms a universal scaling function in the regime of momenta carrying the inverse transport. The scaling exponents which characterise the self-similar evolution corresponding to Eq. (VII.11) have been found to be $\alpha = 1$ and $\beta = 1/2$ [219]. This self-similar build-up of momentum mode occupations in the infrared reflects a coarsening dynamics of the ensemble of vortices interacting with background sound waves, leading to a dilution of the vortex defects through mutual annihilation. Eventually, when the last defects have disappeared, long-range order is established and phase coherence of the Bose condensed particles is maximised. In the next section, we discuss how this picture, which is established and numerically demonstrated at many examples for the isolated Bose gas, adapts to the case of a coupling to thermal and non-thermal bath.

VII.2.1 Defect Configurations as Initial States

In the remainder of this section, we present numerical results on a to date unexplored non-thermal fixed point in the non-relativistic isolated Bose gas which is tightly con-

[2] The symbol *zeta* will denote scaling exponent and stochastic force likewise, as both is the convention in the respective literature. Which definition to apply will be clear from the context or clarified explicitly

nected to highly correlated vortex ensembles. The numerical findings are obtained from semi-classical truncated Wigner-type simulations for the isolated one-component Bose gas in two spatial dimensions, in complete analogy to the techniques employed so far for the two-component gas and in [59]. However, here we set off dynamics with completely different initial conditions. The parameters for the simulations presented in this chapter are summarised in Table B.4. All imaginary parts of the couplings are set to zero. Numerical data is presented in units set by appropriate powers of the healing length, $\xi = 1/\sqrt{2mng}$, throughout this and the following sections. We set $\hbar = k_{\mathrm{B}} = 1$ and $m = 1/2$ in the numerical treatment.

From a hydrodynamic point of view, it seems obvious that vortices need to build like-sign clusters for the Bose gas to bear the energy spectrum or velocity statistics of classical turbulence. On the other hand, in [59] it was found that the defects tend to arrange in randomly distributed bound vortex–anti-vortex pairs, for the overpopulation scenario and for periodic simulation domains. This state was identified responsible for the fixed point properties explained above, in particular the scaling law in the occupation number Eq. (VII.11). There are indications [220] that vortex ensembles indeed cluster for a short transient period in time on periodic domains, independently from their initial distribution. To obtain, however, a significant persistent effect, here, we place vortex clusters in the initial conditions, similar to [65, 221]. To do so, homogeneous field configurations including the $1/2$ particle per mode of truncated Wigner noise are sampled and afterwards vortices with winding number $w = \pm 6$ are multiplied into the sampled configurations. Their arrangement is chosen on a regular lattice with alternating signs of the winding number, see panel a) in Fig. VII.1. Due to the instability of non-elementary vortices this configuration eventually decays. But, as it turns out, the decay process takes a substantial amount of time in the isolated system. In a first stage, the non-elementary vortices decay to tightly bound clusters of like-signed elementary vortices, see panel b) in Fig. VII.1. The cluster configuration then screens the vortex–anti-vortex attraction, such that the clusters resist further decay. Over time, the vortex configuration undergoes then a dilution process, *cf.* panels c) and d) in Fig. VII.1, upon entering a self-similar universal stage of time evolution. We discuss the universal character of the evolution when analysing the time evolution of the occupation number (see Fig. VII.3) which corresponds to the dynamic process illustrated in Fig. VII.1. We compare the vortex lattice initial state to a second class of vortex-containing initial field configurations. Elementary vortices, *i. e.* with a winding number of $w = \pm 1$, are placed into a noisy homogeneous background field, where the positions are chosen uniformly random (*cf.* also [65]). Each realisation is topologically neutral, *i. e.* contains as much vortices as anti-vortices, and the number of initial vortices and anti-vortices is individually matched to the vortex lattice initial condition. When calculating observables in the random vortex scenario, we average over the truncated Wigner noise and the randomly chosen initial positions likewise. The random vortex scenario is studied with the overpopulation scenario in mind. As discussed in [59], properties such as the power law $\zeta = 4$ in the occupation number emerge as a consequence of dilute random vortex configurations.

That the universal stage within the evolution of the vortex lattice scenario is fundamentally different from what has been found before from the overpopulation-scenario can be seen on a phenomenological level from Fig. VII.2. Realisations of the hydrodynamic ve-

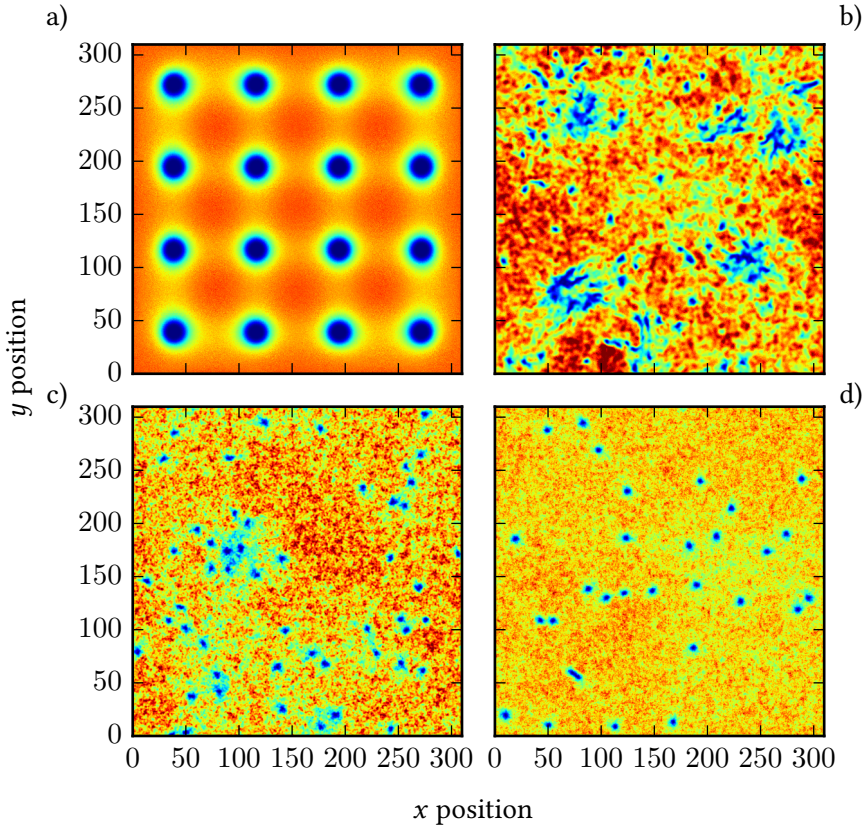

Figure VII.1: Illustration of the vortex lattice configuration (panel a) and the different stages of the decay thereof (panels b-d). Snapshots of the normed real-space density $|\psi|^2/n$ at different times of a single realisation are shown colour-coded (from $|\psi|^2/n = 0$ (dark-blue) to $|\psi|^2/n = 1.2$ (orange)). Panel a) depicts an initial vortex lattice configuration at $t = 0$ with $4x4$ vortices of winding number ± 6, placed with alternating signs in a checker-board manner. Panel b) ($t = 2746\,\xi^2$) shows strongly clustered vortex configuration at a time during the early, non-universal stage. Panels c) ($t = 9155\,\xi^2$) and d) ($t = 82397\,\xi^2$) show configurations during the intermediate and late stage of universal time evolution. Simulation parameters are given in Table B.4

locity field $\boldsymbol{v} = \nabla\theta$ late during the self-similar stage of time evolution are computed for both scenarios. We find that the vortex configuration is essentially clustered, although strongly diluted, even beyond the simulation times displayed in Fig. VII.1. As a direct consequence, the hydrodynamic velocity field builds up a strongly coherent structure over the whole simulation domain, see panel a) in Fig. VII.2. In the other scenario (panel b in Fig. VII.2), the vortex configuration consists of bound pairs, as reported also in [59] which concentrate the hydrodynamic flux circularly around them.

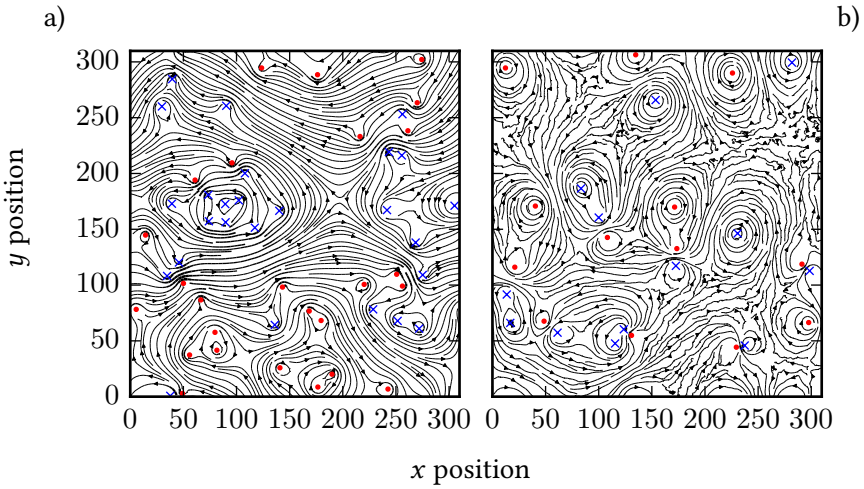

Figure VII.2: Realisations of vortex configuration in the universal stage of time evolution are shown, together with the corresponding hydrodynamic velocity field $\boldsymbol{v}$ by means of flow lines of the vector field. Black directed lines visualise the direction of the velocity field and the line thickness is proportional to the modulus $|\boldsymbol{v}|$. The positions of vortices and anti-vortices are marked by blue crosses and red dots, respectively. Both panels show a typical single-run realisation at an late instance in time, well within the universal stage of time evolution close to the fixed point. For the realisation in panel a), dynamics was initialised with a regular vortex lattice which leads to vortex clusters and a strong coherent hydrodynamic flow. For comparison, panel b) shows the resulting configuration when dynamics is instead initialised with an overpopulation of infrared momentum modes, as has been studied in detail in [59].

VII.2.2 Self-Similar Coarsening

The time evolution of the occupation number spectrum for the vortex lattice scenario, shown in Fig. VII.3, demonstrates the typical self-similar evolution, heralding the presence of a non-thermal fixed point. After an initial stage of time evolution, corresponding to the stage where the non-elementary vortices decay, a power law builds up in an infrared momentum region of the occupation number which is cut at a scale k_λ deep in the infrared. The scale moves algebraically in time towards lower momenta dragging the occupation in the deep-infrared upwards, while the occupation in the scaling region gets lower. The evolution signals the typical local particle transport towards the condensate mode, together with a re-condensation process. The inset in Fig. VII.3 demonstrates that the time evolution of the occupation spectrum can indeed be rescaled to collapse to a single curve, within numerical precision, according to Eq. (VII.10). The scaling exponents needed to do so are found by a fit to be

$$\begin{aligned} \alpha_{\mathrm{VL}} &= 0.40 \pm 0.05\,, \\ \beta_{\mathrm{VL}} &= 0.20 \pm 0.05\,. \end{aligned} \tag{VII.12}$$

The remaining universal curve $n(k)$ follows in the infrared a generalised Cauchy distribution and, thus, contains a power law $n(k) \sim k^{-\zeta}$. The exponent ζ is also determined by fit, yielding

$$\zeta_{\mathrm{VL}} = 6.0 \pm 0.3\,. \tag{VII.13}$$

The scaling region in the spectrum can be interpreted as turbulent (inverse particle) cascade in an inertial range, see for example [55–57, 59]. Adopting the same point of view, we find here a power-law characterising the turbulent state which is substantially steeper than what has been identified before for the Bose gas in two spatial dimensions. It exceeds the exponent $\zeta = 4$, which characterises the universal state attained within the overpopulation scenario, and even the classical Kolmogorov-$5/3$ power-law (corresponding to $\zeta = 4.66$ when translated to the occupation number spectrum). The time evolution of the infrared cut-off scale, $k_\lambda \sim t^{-\beta}$, signals a coarsening process. We discuss that further in Sect. VII.4, linking the coarsening process to the dilution of the defect ensemble and phase ordering kinetics.

The scaling exponents α and β have been calculated analytically for relativistic and non-relativistic scalar field theories in [47, 219] within a scheme based on effective quantum Boltzmann equations, together with an effective scattering matrix obtained form 2-particle-irreducible effective action techniques (similar to [44–46]). For the non-relativistic case under the assumption of local particle transport, [47, 219] predicts

$$\begin{aligned} \alpha &= \frac{d}{2-\eta}\,, \\ \beta &= \frac{1}{2-\eta}\,, \end{aligned} \tag{VII.14}$$

where d is the spatial dimension and η an anomalous scaling of the spectral function. Assuming this to be applicable to our system, as was done for the overpopulation scenario in [47, 219], yields a consistent answer if we attribute a strong anomalous scaling exponent of $\eta \simeq -3$ to the fixed point addressed by the vortex lattice scenario. In addition, our values for α and β are only consistent with the predictions from [219] if a particle cascade is assumed, not with the case of an energy cascade. The value of the scaling exponent of the universal curve, ζ, is not consistent with the calculations of [46] if our value of η is inserted. However, the whole set of scaling exponents including ζ is consistent if a conjecture from [48] is taken into account. Comparing the Bose gas and Kardar-Parisi-Zhang dynamics with renormalisation group methods, it was argued that the scaling exponent ζ is composed from two contributions, $\zeta = \zeta_{\mathrm{c}} - \eta$. One contribution, ζ_{c}, characterises compressible turbulence generated by sound waves and the other captures the influence of vortical hydrodynamic fluxes, directly identifiable with the anomalous exponent. In [222] it was demonstrated that the compressible contribution to the occupation number spectrum for the vortex lattice scenario is sub-dominant but hosts an infrared scaling regime with $\zeta_{\mathrm{c}} = 3$. Adding our anomalous exponent, which we extracted with Eq. (VII.14) from our data in Fig. VII.3, we obtain $\zeta \simeq 6$ in accordance with our numerical result from Fig. VII.3.

In Fig. VII.4 we analyse the time evolution of the occupation spectrum obtained in the random vortex scenario for self-similar coarsening, analogue to Fig. VII.3. As before, there

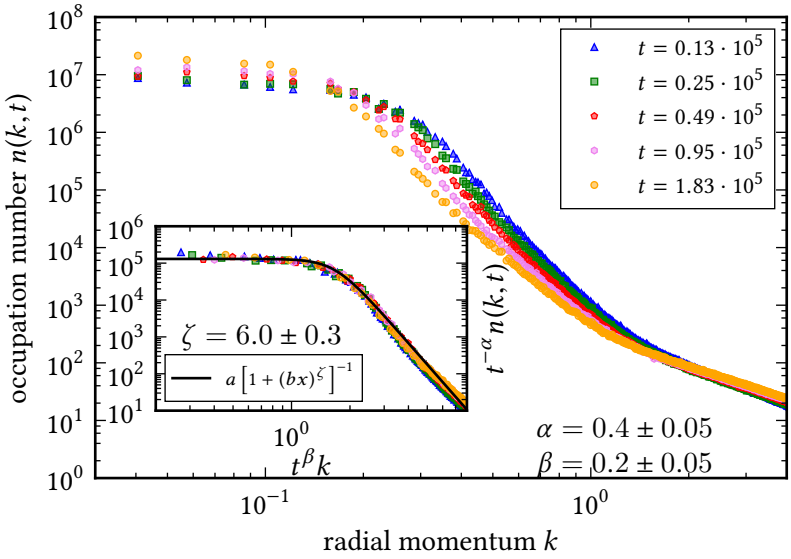

Figure VII.3: Particle occupation spectrum (coloured markers) at several times (different colours as given in the legend) during the universal stage of time evolution for the *vortex lattice* initial conditions. The spectrum evolves in the typical self-similar way of a particle cascade (see main text for discussion). The inset demonstrates the scaling collapse of the spectrum according to $n(t,k) = (t/t_0)^{-\alpha} n((t/t_0)^{\beta} k)$. The simulation data from the main plot is depicted (coloured points with the same colour-coding as in main figure), plotting $t^{-\alpha} n(k,t)$ on the y-axis versus rescaled momentum $t^{\beta} k$ on the x-axis. The used exponents are determined by fit which yields $\alpha = 0.4 \pm 0.05$ and $\beta = 0.2 \pm 0.05$. The universal curve obtained from the scaling collapse (black line in the inset) has a scaling region with scaling exponent $\zeta = 6.0 \pm 0.3$, which was also determined by a fit. For reasons of visibility we show five exemplary curves but want to emphasise that the scaling collapse and fits are performed for the whole dataset, consisting of spectra at 300 logarithmic equidistant times within the universal stage of time evolution.

is a late stage of time evolution, $t > 10^4 \xi^2$, in which the spectrum evolves in a universal self-similar way (see upper panel in Fig. VII.4). The scaling exponents are found to be

$$\begin{aligned} \alpha_{\mathrm{RV}} &= 1.0 \pm 0.02\,, \\ \beta_{\mathrm{RV}} &= 0.5 \pm 0.02\,. \end{aligned} \tag{VII.15}$$

which is again only consistent with local particle transport, when compared to the predictions from [47] (see Eq. (VII.14)). The difference to what we found above is that for the random vortex scenario the set of numerically determined exponents is consistent with Eq. (VII.14) for $\eta = 0$. In particular, the vanishing anomalous exponent leads to a much faster turbulent re-condensation. In turn this means that the finite system spends consid-

erably less time in the universal regime near the non-thermal fixed point, before thermalising. In contrast, in the lower panel of Fig. VII.4 we find that even before the universal stage the occupation spectrum in the random vortex scenario demonstrates self-similar coarsening. Although the effect is less pronounced than in the universal stage, between times $t \simeq 10^3 \xi^2$ and $t \simeq 10^4 \xi^2$ the spectrum evolves approximately self-similar and can be collapsed to a single curve. The exponents, in this transient stage, are consistent with the anomalous exponents from Eq. (VII.12), $\alpha = \alpha_{\mathrm{VL}}$ and $\beta = \beta_{\mathrm{VL}}$. In both stages in the random vortex scenario the spatial scaling exponent ζ is considerably flatter than in the vortex lattice scenario. We find $\zeta = 4$ in the universal stage, consistent with [59]. The scaling exponent $\zeta = 4$ is expected for dilute ensemble of randomly distributed vortices in $d = 2$, for geometrical reasons (see also Sect. VII.4). In the intermediate stage, ζ is close to $\zeta = 4$ but clearly steeper, $\zeta \simeq 4.5$. The results provide strong evidence that there are two non-thermal fixed points, a anomalous and a non-anomalous, which can act as universal attractor for the dynamics in the one-component Bose gas. We will develop this picture further in Sect. VII.4.

While the turbulent condensation process [55, 57, 59] described above is a consequence of the particular non-equilibrium state and the closure of the system, turbulent transport is generically possible also in continuously driven systems. In chapter VIII we study the case that particles are fed into the system in a characteristic way, favoring low-k modes over high-k ones and vice versa. At the same time, dissipation leads to particle and energy loss, allowing for transport being induced between different momentum scales, and the ensuing buildup of characteristic scaling laws. Scaling solutions of the driven-dissipative Kardar–Parisi–Zhang equation have been studied in detail in the literature, both perturbatively [105, 106] and in non-perturbative approximations [48, 107, 108].

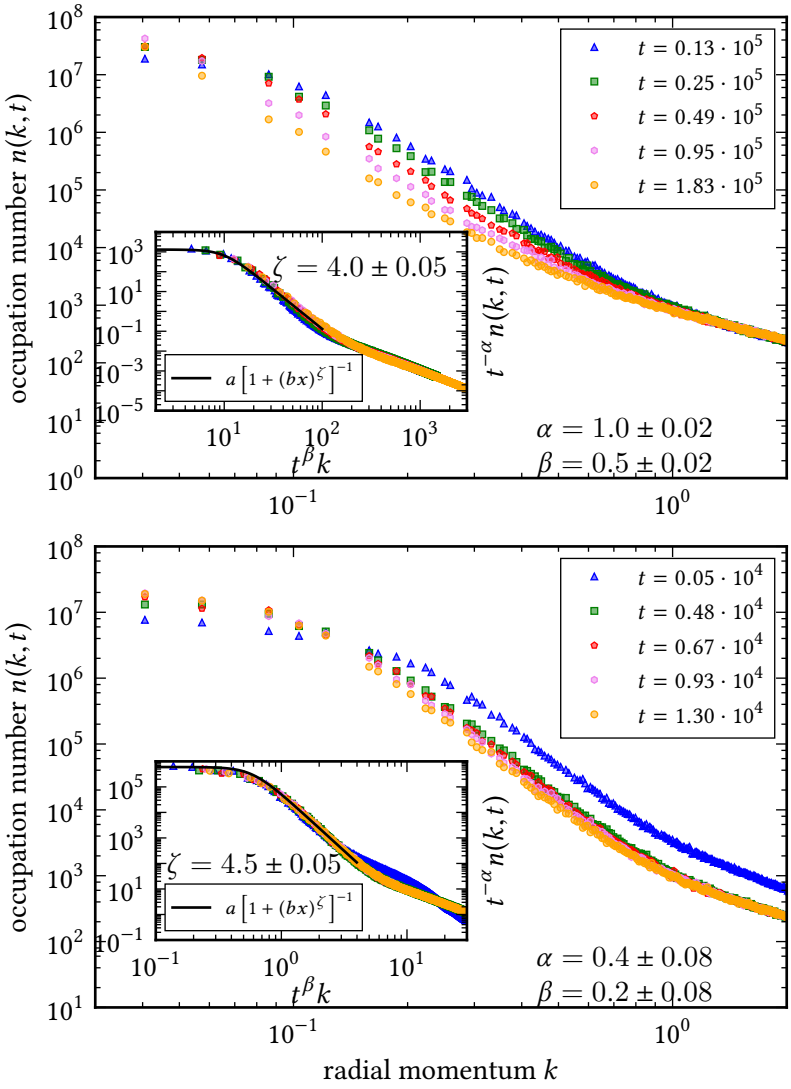

Figure VII.4: Upper panel: Particle occupation spectrum (coloured markers) at several times (different colours as given in the legend) during the universal stage of time evolution for the *random vortex* initial conditions. The spectrum evolves in the typical self-similar way of a particle cascade (see main text for discussion). The inset demonstrates the scaling collapse of the spectrum, see Fig. VII.3. The simulation data from the main plot is depicted (coloured points with the same colour-coding as in main figure), plotting $t^{-\alpha} n(k,t)$ on the y-axis versus rescaled momentum $t^\beta k$ on the x-axis. The used exponents are determined by fit which yields $\alpha = 1.0 \pm 0.02$ and $\beta = 0.5 \pm 0.02$. The universal curve obtained from the scaling collapse (black line in the inset) has a scaling region with scaling exponent $\zeta = 4.0 \pm 0.05$, which was also determined by a fit. Lower panel: time evolution, as in upper panel, of the occupation spectrum for intermediate times, *cf.* red line in Fig. VII.5 from $t = 10^3 \xi^2$ to $10^4 \xi^2$. Inset in lower panel: Scaling collapse and universal curve, as in upper panel, for intermediate times. The fits yield $\alpha = 0.4 \pm 0.08$, $\alpha = 0.2 \pm 0.08$, and $\zeta = 4.5 \pm 0.05$.

VII.3 Coupling to a Thermal Environment

To bridge the previous studies for the isolated system to the case of driven-dissipative situations, we start out by briefly addressing what happens if the fixed point scenarios are coupled to a thermal environment. To do so, we choose $H_\mathrm{d} = aH$ in Eq. (VII.1) otherwise keeping the parameters from Table B.4, and set $v = 0$. The parameters γ is adjusted to yield a temperature $T = 20\xi^{-2}$ (see Sect. VII.1.1 and Eq. (VII.5)) at $\alpha = 0.5$, *i. e.* energetically on the order of the microscopic interaction energy. This places the system deep in the quasi-ordered regime of the Berezinskii–Kosterlitz–Thouless transition[3] [223, 224] in the 2d Bose gas. As a consequence, any vortex-containing state is expected to be of transient nature.

VII.3.1 Evolution of the Vortex Ensemble

The number of vortex defects in the gas as a function of the time elapsed after coupling the system to the thermal bath serves as a instructive measure to capture the state of the system on its way to complete thermalisation. We use this quantity to compare the behaviour of two different classes of initial conditions, the vortex lattice scenario and random distributions of elementary vortices (see Sect. VII.2.1), both classes isolated as well as coupled to the bath. A comparison of the time evolution of the vortex ensemble for the four cases is shown in Fig. VII.5. We find that, in any case, the average number of vortices contained in the system decays and does so approximately algebraically,

$$N_\mathrm{v}(t) \sim t^{-2\beta'} \,. \tag{VII.16}$$

The main difference between the thermal and the isolated setups concerns the speed of the decay. If the Bose gas is coupled to a thermal bath, the defect decay follows closely the prediction of phase-ordering kinetics [54], especially if the initial vortex distribution is completely random (*cf.* blue datapoints and blue solid line in Fig. VII.5). Bray predicts in [225] for a field order parameter with two real-valued components in two-spatial dimensions a average defect spacing which evolves as $L_\mathrm{v}(t) = 1/N_\mathrm{v}^{1/2} \sim (t/t_0 \log t/t_0)^{1/2}$, if no additional conserved quantities are present (see also Sect. VII.4). If the initial vortex distribution is not random but clustered, as illustrated in Fig. VII.1, the behaviour initially deviates from the phase-ordering prediction but falls into this class again after details of initial state had time to decay. In both cases, the power-law decay of the vortex number stops once the total number of vortices is of order one. This is a consequence of the finite total number of vortices in our finite simulation box and therefore a finite-size effect. The value of the scaling exponent $\beta' = 0.5$ in the stage of algebraic decay marks a diffusive motion of the vortices on a thermal background, as argued in [65]. It suggests that vortex–vortex and vortex–anti-vortex interaction effects are suppressed by thermal fluctuations.

The decay of the random vortex distribution in an isolated gas (see red datapoints in Fig. VII.5) corroborates that point. Once the thermal background is gone, Helmholtz mo-

[3] The Berezinskii–Kosterlitz–Thouless transition temperature evaluates to $T_\mathrm{BKT} = 574\xi^{-2}$ with the parameters from Table B.4, using a meanfield approximation $T = \pi\sqrt{n_0}/2m$ [146]

tion of vortex pairs together with scattering of those pairs slows down the decay process [59], yielding a smaller value of $\beta' < 0.5$. Finally, we find that the decay of the vortex lattice in the isolated gas proceeds slowest with $\beta' = 0.2$ and follows a pure power-law after a non-universal initial stage. The stage of algebraic decay coincides with the universal stage of time evolution close to the non-thermal fixed point, as discussed in Sect. VII.2. In particular, one has $\beta = \beta'$, signalling that the power-law in the scaling form of the occupation spectrum (see Fig. VII.3) is cut off at the inverse inter-vortex spacing, as both, the cut-off scale k_λ and $1/L_\mathrm{v}$, follow the same scaling law in the universal stage. For the random vortex initial conditions (see red datapoints in Fig. VII.5), we find that there is an intermediate stage from $t \simeq 10^3\, \xi^2$ to $t \simeq 10^4\, xi^2$, where a scaling law can be attributed to the decay. The scaling exponent in this stage is approximately $\beta' \simeq 0.2$ which equals within error bounds the corresponding value of β in the intermediate stage (*cf.* Fig. VII.4). Beyond $t \simeq 10^4\, \xi^2$ the red curve in Fig. VII.5 turns towards a scaling law with exponent $\beta' = 0.5$. This falls together with the change in the self-similar progression of the occupation spectrum we determined in Fig. VII.4. Therefore, we find also from the point of view of the vortex distribution that there is a crossing between two self-similar stages in the time evolution of the random vortex initial conditions. In both stages, k_λ and L_v follow the same scaling law with $\beta' = \beta$. Note that for the overpopulation scenario in [59], a change in the scaling exponent β' from $\beta' \simeq 0.5$ to a considerably smaller value (β' between 0.15 and 0.2) has been observed but the corresponding values of β have not been determined. On the other hand, in [219] the value $\beta = 0.5$ is determined in the overpopulation scenario for the occupation spectrum but the corresponding vortex distributions are not analysed.

VII.3.2 Coarsening in Presence of a Thermal Bath

We complete the picture of the thermally coupled gas by studying the occupation number spectrum analogous to Sect. VII.2.2. Examples of the occupation number during the approach to the thermal state are shown in Fig. VII.6, where the times are mainly situated in the algebraic stage of the decay of the vortex ensemble (*cf.* Fig. VII.5). The final thermal occupation number is expected to be distributed according to a Rayleigh–Jeans distribution, $n(k) = T/\omega(k)$, due to the semi-classical nature of the simulation method. The occupation spectrum at the latest time in Fig. VII.5 is close to the thermal occupation, assuming a Bogoliubov dispersion for $\omega(k)$, but has not yet converged totally. At first sight, it seems that the self-similar evolution of the occupation spectrum is destroyed by the presence of the thermal bath, although there is a steep power law in the infrared momentum region present. However, this impression is created by the fact that the infrared cut-off scale of the power-law seems to be below the infrared cut-off of the simulation grid, $k_\lambda < 1/L$. Analysing the spectrum for a universal scaling form according to Eq. (VII.10) shows that the occupation spectrum evolves indeed self-similar, as long as the steep infrared scaling law is present. As a consequence, the steep power law in the infrared part of the spectrum does not decay towards a the thermal occupation but shifts towards the deep-infrared momentum region, keeping the non-thermal scaling exponent $\zeta > 2$. Once the vortex ensemble has decayed to a point where there is less than one vortex pair on average the self-similar evolution is replaced by an evolution which

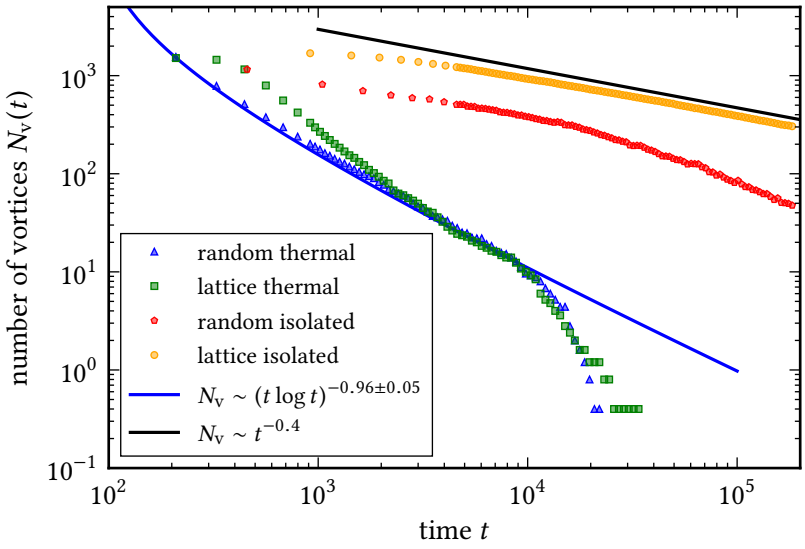

Figure VII.5: Total number of vortices N_v as a function of time for four different setups, comparing two classes of initial conditions in the isolated gas with the corresponding initial conditions subjected to a thermal bath at $T = 20\xi^{-2}$. 'Lattice' reveres to regular vortex lattices of non-elementary vortices (the same as discussed in Sect. VII.2. 'Random' refers to initially randomly placed elementary vortices). The vortex number is averaged over 20 realisations of: stochastic driving ζ (lattice thermal, green markers), stochastic driving ζ and initial vortex positions (random thermal, blue markers), truncated Wigner noise (lattice isolated, yellow markers), truncated Wigner noise and initial vortex position (random isolated, blue markers). Parameters from Table B.4. The blue solid line is an analytic prediction from phase ordering kinetics [225], see main text.

asymptotically approaches the thermal occupation. The inset in Fig. VII.6 demonstrates that a scaling collapse is possible, yielding the scaling exponents

$$\begin{aligned} \alpha_{\text{th}} &= 1.0 \pm 0.05\,, \\ \beta_{\text{th}} &= 0.5 \pm 0.05\,, \end{aligned} \tag{VII.17}$$

which are the same as for the non-anomalous non-thermal fixed point (see Eq. (VII.15)). The infrared power law in the universal scaling form has the value $\zeta = 4.0 \pm 0.1$, also the same as identified in [59] for the non-anomalous fixed point. We point out that these results for the self-similar evolution of the thermally coupled gas are the same for both classes of initial conditions, the vortex lattice setup as well as the initially randomly distributed vortices. Therewith we find numerical evidence that the fixed point behaviour which has been found for the isolated Bose gas is not completely destroyed by a thermal environment. However, the transient nature of the non-thermal universal stage of time evolution makes now the crucial difference. In the isolated case, vortex–anti-vortex in-

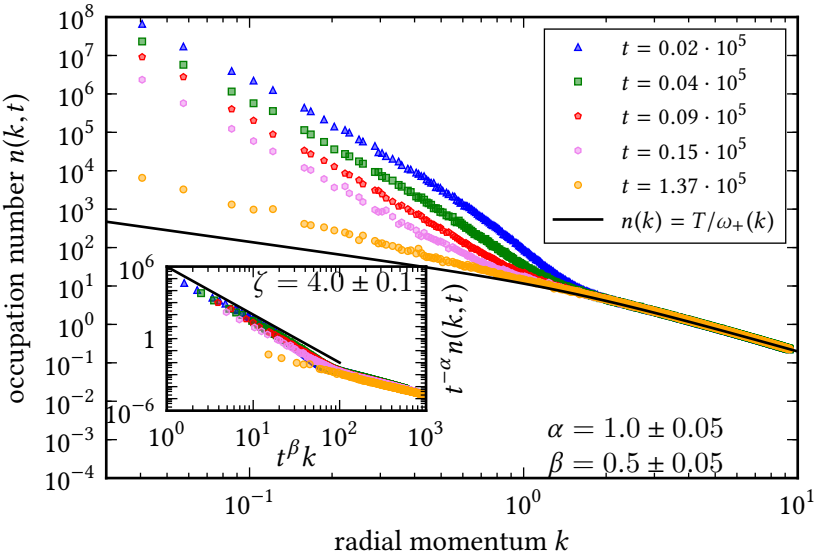

Figure VII.6: Particle occupation spectrum (coloured markers) at several times (different colours as given in the legend) during the universal stage of time evolution for the vortex lattice initial conditions, when subjected to a thermal bath at $T = 20\xi^{-2}$. The spectrum evolves in a self-similar way as long as the steep power-law in the infrared momentum region is present (see main text for discussion) and approaches a thermal Rayleigh–Jeans occupation thereafter T/ω. The solid black line gives correspondingly T/ω with $\omega(k) = \omega_+(k)$ the Bogoliubov dispersion. The inset demonstrates the scaling collapse of the spectrum, as was done Fig. VII.3. The used exponents are determined by fit which yields $\alpha = 1.0 \pm 0.05$ and $\beta = 0.5 \pm 0.05$. The universal curve obtained from the scaling collapse has a scaling region with scaling exponent $\zeta = 4.0 \pm 0.1$ (black line in inset).

teractions and clustering effects where able to slow down the decay or even to change the whole set of scaling exponents, substantially elongating the universal non-thermal stage. In particular, three-body collisions between defects, happening when two vortex–antivortex pairs meet, have been argued to be the dominant mechanism for slowing down the vortex decay [59]. In the thermal case, the transient universal stage is bound to a quickly decaying, because diffusively diluting, vortex ensemble.

VII.4 Non-thermal Fixed Points and Phase Ordering Kinetics

Our findings allow establish a connection between non-thermal fixed points in the one-component Bose and the theory of phase ordering kinetics. In particular, we can use the results of this chapter to compare the temporal scaling form, *i. e.* Eq. (VII.10), at a non-

thermal fixed point with the scaling forms obtained from topological defect properties, as discussed in [225–228] (see [54] for a review). This is in particular helpful, as for defect coarsening a more rigorous renormalisation group approach was developed, see for example [229–231].

By means of power counting, a universal scaling form for the structure factor of a defect-containing order-parameter field can be obtained. Assuming a defect ensemble with a mean defect distance L in an order parameter field with n real-valued components, Porod's law [167, 168] (or rather a generalisation thereof to arbitrary n [227]) predicts a scaling form for the structure factor

$$S(k) \sim L^d/(Lk)^{d+n} \,. \tag{VII.18}$$

If concentrating on a momentum range between the inverse defect distance and an ultraviolet cut-off from the internal defect structure, $1/L \ll k \ll 1/\xi$, Eq. (VII.18) basically is derived from the d dimensional Fourier transform of a $d-n$ dimensional but otherwise structure-less defect in the order parameter field.

Further arguments, based on classical dynamics[4] of the order parameter field [227] or based on a renormalisation group approach [54, 229, 230], additionally allow to predict temporal scaling properties for the defect scale, $L(t) \sim t^{\beta'}$. The exponent β' characterises the speed of progression of the coarsening, which is influenced by conservation laws in the order parameter field. For dynamics of the order parameter field which can be cast into the form

$$\left(\frac{1}{ak^\mu} + \frac{1}{\Gamma}\right) \partial_t \phi(\boldsymbol{k},t) = \frac{\delta F[\phi]}{\delta \phi(-\boldsymbol{k},t)} \,, \tag{VII.19}$$

where $F[\phi]$ is the free energy for the order parameter field defining the model, the parameter μ defines the nature of the conservation law. In particular, $\mu = 0$ addressed the class of the purely dissipative model A from [30]. For dynamics in the form of Eq. (VII.19) together with models from the Halperin–Hohenberg classification, Bray finds (see for example [54] and figure 24 therein) $\beta' = 1/(2+\mu)$ if $n > 2$, with logarithmic corrections for $n = 2$ as we have used in Fig. VII.5.

Inserting the temporal scaling prediction in the spatial scaling form Eq. (VII.18) results in a scaling form for the structure factor,

$$S(t,k) \sim \frac{t^{d\beta'}}{1 + (t^{\beta'}k)^{d+n}} \,, \tag{VII.20}$$

including a simple infrared cut-off in the scaling form. If this is to describe the same self-similar evolution as has been predicted for the non-thermal fixed point, Eq. (VII.10), in [47] one needs to assume particle transport at the non-thermal fixed point to get $\alpha = d\beta$. In addition, the temporal evolution in the structure factor (which is the occupation number spectrum for the Bose gas) needs to be governed by the average defect spacing, to have $\beta = \beta'$. If both is true, the local transport process towards infrared momenta, which is described by the non-thermal fixed point in the case of exponents Eq. (VII.14), is in one to one correspondence with coarsening (in a renormalisation group sense) of a

[4] The calculations assume $O(N)$ models from the Halperin–Hohenberg classification [30]

defect-containing order parameter field.

Turning back to our numerical results for the non-relativistic Bose gas in Fig. VII.6, Fig. VII.4, and Fig. VII.3 together with Fig. VII.5, we find that both non-thermal fixed points, the non-anomalous and the anomalous fulfil the conditions $\alpha = d\beta$ and $\beta = \beta'$. For the thermally coupled situation, we have determined $\beta' = \beta \simeq 0.5$, $\alpha = d\beta' \simeq 1$. These values are within Bray's prediction, $\beta' = 1/(n + \mu)$, if purely dissipative dynamics ($\mu = 0$) is assumed for the order parameter field. As has been argued in [99] this is expected, if vortex–anti-vortex interaction is suppressed sufficiently, since the Bose gas then is described by model A. Furthermore, this allows to attribute the two stages of decay of the random vortex initial conditions to two different phases of coarsening. Correspondingly, the transport process is dominated subsequently by both non-thermal fixed point. In the first stage, high vortex densities and the absence of a thermal bath produces the anomalous slow exponent $\beta' = \beta \simeq 0.2$. In the second stage, a thermal background provided by the high-momentum modes and low vortex density change the exponent $\beta' = \beta$ towards its non-anomalous value, which is also identifiable with purely dissipative dynamics.

The anomalous value for we found for β in Fig. VII.3, however, is not as unambiguously explainable from phase ordering kinetics. Associating the self-similar evolution of the spectrum with phase ordering kinetics and taking the predictions for β and β' literally, the anomalous exponent we identified numerically, $\eta \simeq -3$, then maps to an effective conservation parameter $\mu = 3$. The renormalisation group approach for defect coarsening [54, 229, 230] allows for a more intuitive interpretation. An ansatz for the scaling forms requires the introduction of a dynamical critical exponent z, defining a relation between temporal and spatial scales of the renormalisation flow of the order parameter field[5]. Naturally, the temporal scaling of $L(t)$ provides that relation, such that

$$z = 1/\beta' \,, \tag{VII.21}$$

where z defines the dynamic universality class of the the effective, defect-hosting order parameter field. Thus, we find for the anomalous non-thermal fixed point in the Bose gas an anomalous high value of the dynamical critical exponent, $z \simeq 5$. In contrast, for example, thermally diffusing vortices come with $z = 2$ and studies for thermal quenches in the superfluid phase of the Bose gas in [99] find $z = 1$. In fact, such high values as $z = 5$ for the dynamical exponent are not found within the models from the Halperin–Hohenberg classification [30]. However, anomalous slow ordering is typically a characteristic of glasses and glass phases for vortex ensembles have been proposed. In particular, in type-II superconductors experimental evidence has been found for a transition from a vortex lattice phase to a vortex glass phase [100, 101], supporting $z \approx 5$ in the glass phase. Numerical studies [102] corroborate that findings and theoretical models for the vortex glass phase in superconductors have been proposed [103, 104]. An epsilon expansion (around $d = 6$), discussed in [104], yields a value $z = 2(2 + \epsilon/6)$ to first order, which

[5] *A priori* z here relates to the defect-hosting order parameter field and dos not necessarily equal the dynamical critical exponent considered for the calculations in [47] for the non-thermal fixed point. However, the dependency on the microscopic dynamical critical exponent drop out for the particle-transport exponents Eq. (VII.14)

extrapolates to a dynamical exponent $z = 5.33$ in $d = 2$.

The origin of the the spatial scaling exponent $\zeta \simeq 6$ at the anomalous fixed point supports the identification of the anomaly with glassy coarsening dynamics from a phenomenological point of view. In the other studied cases, the thermal case and the isolated random vortex scenario, the spatial scaling law $\zeta \simeq 4$ can be attributed to the generalised Porod law Eq. (VII.18). An explanation for the considerably higher value $\zeta \simeq 6$ is that the geometrical scaling from a point defect is to be replaced by the scaling properties of the vortex core. Based on our observations from Fig. VII.2 it is reasonable as multiple like-sign vortices are confined to clusters during the self-similar stage of time evolution. The tail in the structure factor mostly relates to scales within the clusters. The self-similar coarsening is then dominated by dynamics of defects in a dense like-sign cluster, where dilution is hindered by screening effects. It is reasonable that the distribution then rather evolves glassy instead of diluting diffusively.

VII.5 Summary

In the first part of this chapter, Sect. VII.2, we have presented numerical evidence for a new non-thermal fixed point in the one-component Bose gas with a distinctly different set of scaling exponents, $\alpha = 0.4 \pm 0.05$, $\beta = 0.2 \pm 0.05$, and $\zeta = 6.0 \pm 0.3$, (see Eq. (VII.12) and Fig. VII.3). It coexists with the non-anomalous fixed point in the $2d$ Bose gas with exponents, $\alpha = 1$, $\beta = 0.5$ [219] and $\zeta = 4$ [59] (see Eq. (VII.15) and Fig. VII.4), previously reported on in the literature. We emphasise that this no contradiction to the universality property one assigns to non-thermal fixed points, as we have also used a distinctly different class of initial conditions to let the system approach it. In fact, we have demonstrated that it is possible to have the dynamic evolution be attracted by both fixed points successively. Since the anomalous fixed point we identified seems closely connected to non-trivial vortex clustering and macroscopic hydrodynamic fluxes, it seems reasonable that present analytic calculations [44–47] can not fully reproduce the scaling exponents, as they are not selective for topological structures or sectors. However, if interpreted along the lines of [47] together with [218], a strong anomalous scaling exponent of $\eta \simeq -3$ can be consistently attributed to the fixed point. To our knowledge, this is the first example for demonstrating anomalous scaling at a non-thermal fixed point.

Coupling the fixed point scenarios to a thermal bath in Sect. VII.3, at a temperature below the Berezinskii–Kosterlitz-Thouless transition temperature, we demonstrated that the self-similarity in the time evolution at a non-thermal fixed point is not destroyed by thermal fluctuations. Rather, the defining scaling exponents are changed such that, firstly, the critical slow-down is much less pronounced and, secondly, the self-similar evolution falls consistently into the class of phase ordering kinetics [54]. The set of exponents in the thermally coupled system was found $\alpha = 1$, $\beta = 0.5 = \beta'$, and $\zeta = 4$ (see Eq. (VII.17) and Fig. VII.6), irrespective of the class of initial conditions. As a byproduct we demonstrated also, that the fixed point behaviour in the Bose gas for both classes of initial conditions, overpopulation and vortex lattices, is in one to one correspondence with self-similar coarsening of the defect-hosting order parameter field. This allows to convert the fixed point scaling exponent β to the dynamical critical exponent associated with the

coarsening process, $z = 1/\beta$. With that we find a anomalous high dynamical exponent $z \simeq 5$ for the coarsening dynamics at the anomalous fixed point. In light of findings for vortex glass phases in type-II superconductors [100–104] we attribute the anomalous slow coarsening in the Bose gas, we identified, to a glass-like phase of the vortex ensemble.

Our findings in Sect. VII.3 also add to the notion of universality associated with the dynamics at non-thermal fixed points, when interpreted in light of our results from [65] for holographic superfluids. The model for a superfluid studied in [65] describes a relativistic superfluid coupled to a thermal bath in a specific strong-coupling limit. *A priori* it has nothing in common with our system from Sect. VII.3, apart from being subject to a thermal bath and being a superfluid. The latter is ensured in the model by constructing a superfluid's $U(1)$-symmetry. Nevertheless, in [65] a non-thermal fixed point is identified with $\zeta = 4$ and $\beta' = 0.5$ which is insensitive to the difference between vortex clusters and random vortex distributions in the initial state. The dynamics of the abstract strongly coupled superfluid from [65] shares vital universal properties with the weakly thermally coupled Bose gas from Sect. VII.3.

VIII Scaling in the strongly driven-dissipative 2D Bose gas

In this chapter, we[1] analyse numerically the dissipative ultra cold Bose gas in two spatial dimensions, when subjected to strong stochastic driving forces. The stochastic properties of the driving force Eq. (VII.4) allow us to tune strength (via γ) and spatial coherence (via λ and mainly υ) of the driving, such that we can methodically explore the structure of non-equilibrium stationary states and their universal properties. At the same time, the forcing term employed corresponds to a simple incoherent particle pump which should be realisable in experiment, including our tuning parameters.

It turns out that our setup has two entirely different regimes, depending on the magnitude of the initial condensate density $n_0 = \langle\psi^\dagger\psi\rangle|_{k=0,t=0}$. Since n_0 acts as stiffness for phase fluctuations, the magnitude controls the mechanism of vortex nucleation. If n_0 is small compared to the condensate density in the steady state, n_f, even small and totally incoherent phase fluctuations can and will be wound into phase defects, which subsequently turn into full-grown vortices when the background density rises. On the other hand, for a high initial condensate value, the energy costs for the build-up of a phase defect in the background density should suppress vortex nucleation. Note that we sample the driving force such that the coherence parameters λ and υ affect only the amplitude of the stochastic forcing ζ. The phase correlations of ζ, on the other hand, are parameter-independent. The phase of the stochastic forcing field is constituted by incoherent white noise.

In the first part of this chapter, we analyse the structure of non-equilibrium steady states in the regime where the driving does not lead to the creation of vortices. We have empirically determined that $n_0 = 0.1 n_\mathrm{f}$ as choice for the initial condensate prevents vortex nucleation completely for the different setups of driving parameters we will discuss. In a second part of this section, we allow for the generation of vortices through stochastic driving. We will demonstrate that then the nucleation process, and in particular vortex density and the timescale for the process, is controlled by the coherence parameters of the forcing and by the dissipation strength. However, the late time properties, *i. e.*, the stationary state becomes independent thereof.

In this section, we present numerical results from simulations of the model Eq. (VII.1) with a setting as follows. The computational grid is rectangular with 1024×1024 lattice points and periodic boundary conditions together with parameters from Table B.4. With

[1] The numerical data presented here has partially been reported on and obtained in the course of the Master's thesis [220]. I co-advised the project, guided the numerical work, and provided the numerical code. Figures which have been taken from [220] are marked accordingly. For all other figures, I analysed the data anew or carried out new simulations. The interpretation of the results presented here extends the work [220].

that, the non-dissipative part of the system's dynamics is determined by the same parameters as we have used in the previous chapter VII. The dissipative and stochastic parts of the model, however, are now tuned to a explicitly non-thermal setting. As compared to the setting of Sect. VII.3, this requires mutually different phases of all complex couplings and will include different degrees of spatial coherence in the stochastic forcing. For the two-point correlation function of the stochastic driving force (Eq. (VII.4)) we set $\gamma = 0.01$, $\lambda = 10\xi$. Consequently, we focus on the steepness of the power-law tail, set by v, as the main tuning parameter of the forcing characteristics. The deterministic pumping term in Eq. (VII.3) (*i. e.* the term proportional to μ_d) together with the driving strength γ determines the magnitude of the condensate n_f in the stationary state. We choose $\mu_\mathrm{d} = -g_\mathrm{d}\hat{n}_\mathrm{f}$ together with $\hat{n}_\mathrm{f} = 3052$ particles per lattice cell. The magnitude of the non-linear dissipation constant is set to $g_\mathrm{d} = g/9$, to be on the order of the scattering coupling g. Therewith, we control the condensate in the stationary state in the absence of stochastic driving. Since $\gamma \ll \hat{n}_\mathrm{f}$, $\hat{n}_\mathrm{f}$ constitutes a good *a priori* approximation for n_f, while its true value can be determined from simulation. Note that, throughout this section, all numerical data is presented in units of appropriate powers of the healing length, $\xi = 1/\sqrt{2mg\hat{n}_\mathrm{f}}$, in the steady state.

VIII.1 Vortex-less Non-equilibrium Steady State

We start out by analysing the situation when vortex nucleation is strongly suppressed. For that, an deterministic initial field configuration is set in the form of

$$\phi(\boldsymbol{x}, t = 0) \equiv \sqrt{n_0}\,, \tag{VIII.1}$$

where $n_0 = 0.1\hat{n}_\mathrm{f}$. With this, the stochastic differential equation Eq. (VII.1) is solved numerically by solving the equation for 20 realisations of the stochastic driving force ζ. Thereafter we calculate observables as ensemble averages $\langle\,\cdot\,\rangle = \langle\,\cdot\,\rangle_\zeta$ over the the realisations of the forcing. The initial condensate density is large enough to prevent efficiently vortex formation but is still small enough to allow stochastic forcing to influence the time evolution of the system in a non-perturbative manner.

After a short period of time evolution, subject to the driving, we find that the bulk density of the gas grows to a stationary value which we take as indication that the system has reached a non-equilibrium stationary state. In this state, we analyse the radial particle occupation spectrum as before, see Eq. (VII.9), and in addition the radial spectrum of hydrodynamic kinetic energy,

$$\epsilon(k) = \int \mathrm{d}\Omega_k \, \langle \boldsymbol{v}(-\boldsymbol{k})\boldsymbol{v}(\boldsymbol{k})\rangle_\zeta \,. \tag{VIII.2}$$

The second type of spectrum provides a link between the Bose gas and the effective Kardar–Parisi–Zhang equation, see Eq. (VII.6), in addition to the effective force correlator $u(\omega, \boldsymbol{k})$, Eq. (VII.8). For the latter, we concentrate on the equal-time angle-averaged

forcing correlator,

$$u(k) = \int \mathrm{d}\Omega_k \frac{\mathrm{d}\omega}{\sqrt{2\pi}} u(\omega, \boldsymbol{k}) = \int \mathrm{d}\Omega_k \, \langle U(t, -\boldsymbol{k}) U(t, \boldsymbol{k}) \rangle_\zeta \,. \tag{VIII.3}$$

VIII.1.1 Steady States in the Power Spectrum

Our results in the previous chapter allow to anticipate that one should especially search for non-trivial power laws in the infrared region of the occupation spectrum. To obtain a comprehensive view on the situation, we compute the infrared power law in the occupation number spectrum as a function of time for different choices of the forcing power-law v. The result is shown in Fig. VIII.1 for integer values of v between $v = 0$ and $v = 8$. The widths of the coloured lines represent the statistical errors of the fit procedure and the solid black lines show the fitted value of the infrared power law, see [220] for details. Note that, in principle, also non-integer or negative values of v can be utilised. We restrict this study to positive values of v. With this, the forcing term injects particles more dominantly in the infrared momentum region without introducing much energy per particle.

As can be seen from Fig. VIII.1, the infrared power law in the occupation spectrum quickly builds up, after a short period of non-universal time evolution, for the whole range of driving power-laws. Beyond time $t \simeq 3000\, \xi^2$ a non-equilibrium steady state is reached. The form of the occupation spectrum in the this steady state is shown in Fig. VIII.2. The power law which is attained in the infrared part of the occupation spectrum in the steady state is found to be dependent on the shape of the forcing term. From this point of view, the identified scaling behaviour in the spectrum seems to be non-universal, as the power law can be manufactured at will by just choosing a certain form of driving. However, Fig. VIII.1 as well as Fig. VIII.2 show also that the infrared power law in the steady state does not simply equal the driving power law v but is steeper. The inset in Fig. VIII.1 illustrates the dependence of the infrared power law on v. We find that there is a universal, *i. e.* forcing independent, offset between the scaling exponents,

$$\zeta_\mathrm{f}(v) - v = 1.4 \,. \tag{VIII.4}$$

In contrast, the power law which forms in the ultra-violet tail of the occupation spectrum does reassemble the driving power law, see Fig. VIII.2. Therefore, we find that, even without vortices, there is a non-trivial non-equilibrium steady state building up, where the occupation spectrum follows a multi-modal scaling form. The scaling law which appears in the infrared part of the spectrum is universal, if the ratio between occupation spectrum and power spectrum of the stochastic driving is considered.

The universal character of the offset can be understood in terms of the effective forcing U (see Eq. (VII.7)), linking the driven dissipative Gross–Pitaevskii model and the Kardar–Parisi–Zhang equation. As discussed in Sect. VII.1.2, without topological defects and for negligible density fluctuations, the driven-dissipative Bose gas model can be mapped to the driven Kardar–Parisi–Zhang equation. The mapping between the two models relies on an effective forcing potential U, see Eq. (VII.6), which can be calculated from the stochastic driving of the Bose gas together with the evolving order parameter field $\psi(t, \boldsymbol{x})$. Our simulations for the driven-dissipative Bose gas allow to calculate the time-dependent

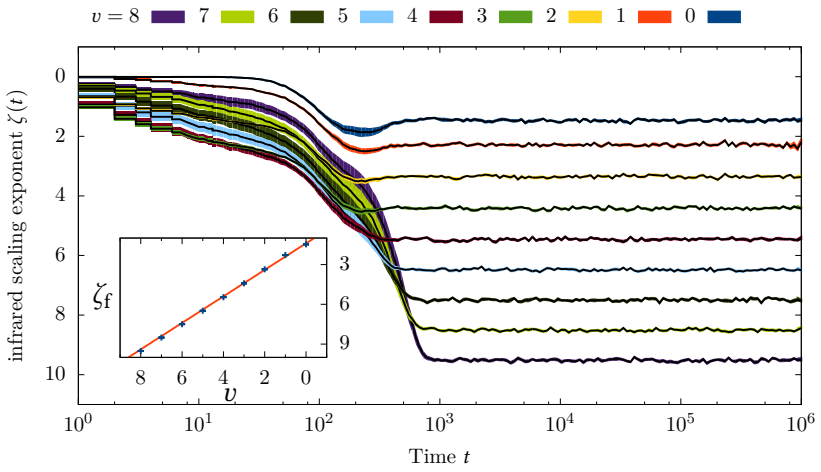

Figure VIII.1: The infrared scaling exponent ζ of the occupation spectrum as a function of time t for different degrees of coherence v in the stochastic forcing. The forcing is switched on starting from a finite low bulk density of the Bose gas, to prevent vortex nucleation (see main text for details). A fitting procedure is used to determine three characteristic regions in the occupation spectrum, a deep-infrared, an infrared, and an ultra-violet region at every timestep, and fits a scaling law $n(k) \sim k^{-\zeta}$ to the infrared region. Thereby, it is assumed that the spectrum is flat in the deep-infrared and follows the driving power-law in the ultraviolet (see [220] for additional details). Coloured bands show the uncertainty of the fit of ζ (different colours for different values of v) while the black lines within show the value of ζ. The scaling exponent ζ of the spectrum in the steady state turns out to be proportional to v but has a clearly visible offset. The inset illustrates the linear dependence of the steady-state power-law in the occupation spectrum (blue data points) on the power-law of the forcing $\zeta_f(v) = v + 1.4$ (red solid line). All simulations are average over 20 realisations of the stochastic forcing. Figure adapted from [220].

radial power spectrum $u(t,k)$, see Eq. (VIII.3), of the effective forcing potential, using Eq. (VII.7) on a single realisation. In Fig. VIII.3, the resulting power spectrum $u(k)$ for the steady state is shown for different values of v. We find that the effective Kardar-Parisi-Zhang forcing follows a v-independent scaling law,

$$u(k) \sim k^{-\gamma}\,, \tag{VIII.5}$$

in an infrared region, where the value of the scaling exponent $\gamma \simeq 1.4$ reflects the universal offset we have determined above. Thus, our data suggests a relation

$$\gamma = \zeta - v\,, \tag{VIII.6}$$

between the scaling exponents of the effective forcing and the occupation spectrum. The

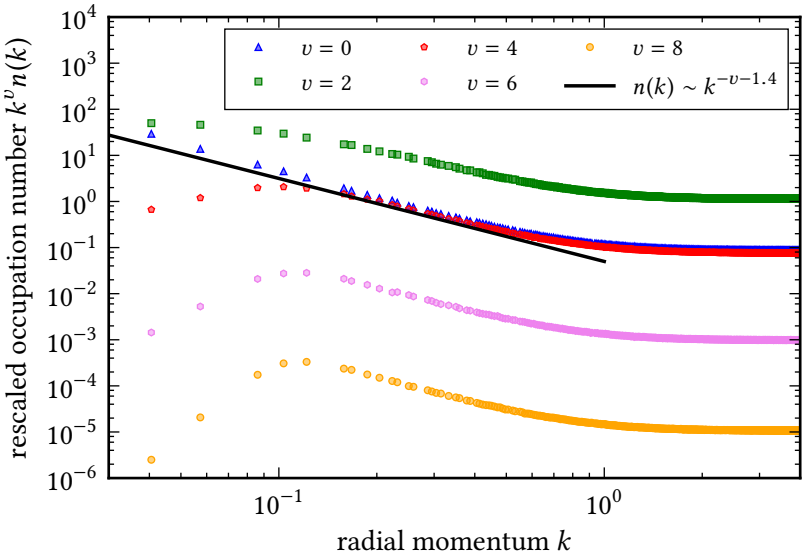

Figure VIII.2: The occupation spectrum in vortex-free non-equilibrium steady state shown for different power-laws v (different colours) in the stochastic forcing. We show occupation spectra at $t = 5000\,\xi^2$ from the same dataset as has been used for Fig. VIII.1. Note that the y-axis is rescaled with the driving power-law to highlight the steeper power-law building up in the infrared. The spectra generally have three different momentum regions, to each of which a scaling law is attributable. The in the deep-infrared the spectrum typically follows $n(k) \sim k^0$ while it follows the driving power-law $n(k) \sim k^v$ in the ultra-violet. This is employed as input for the fitting procedure to determine the infrared scaling exponent ζ in Fig. VIII.1.

momentum region where this is valid depends on the level of coherence in the driving power spectrum of the Bose gas. For power law tails in the Bose gas power spectrum steeper than $v > 2$ the effective power spectrum $u(k)$ demonstrates the scaling form clearly and falls on a universal curve. For less coherent stochastic driving forces in the Bose gas, density excitations dominate in the expression for U and, with that, the power spectrum $u(k)$ [220]. In particular, it has been found in [220] that the term $\propto 1/4m\sqrt{n}\nabla \cdot (\nabla n/\sqrt{n})$ in U (see Eq. (VII.7)),is responsible for the non-universal flat tails in $u(k)$ in Fig. VIII.3.

VIII.1.2 Scaling Laws in the Hydrodynamic Energy

Finally, we analyse the hydrodynamic character of the excitations in the Bose gas in the vortex-less non-equilibrium steady state to make contact to superfluid turbulence. To do so, we switch from the occupation number spectrum to the kinetic energy spectrum, as defined in Eq. (VIII.2). As a bridge between Bose gas and Kardar-Parisi-Zhang physics, we use the hydrodynamic velocity field in the form $\boldsymbol{v} = \sqrt{n}\nabla\theta$, as introduced by [165, 166].

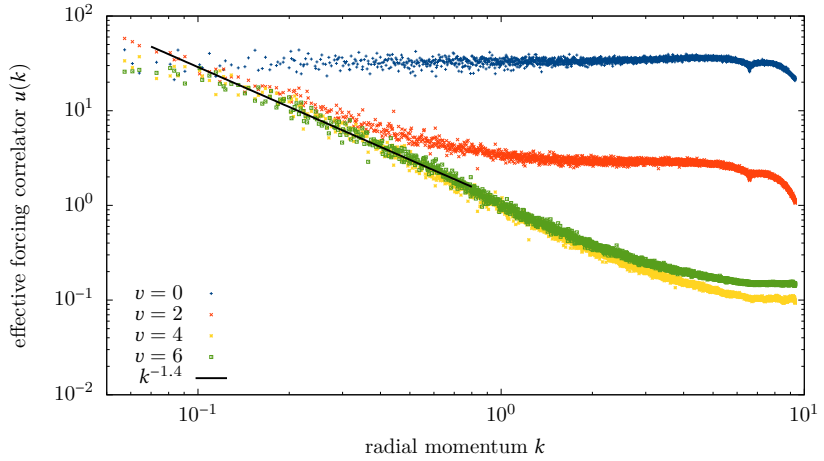

Figure VIII.3: Radial power spectrum $u(k)$ (see Eq. (VIII.7)) of the effective Kardar–Parisi–Zhang forcing potential U (see Eq. (VII.7)), calculated in the vortex-less steady state of the Bose gas for different driving power-laws v, corresponding to Fig. VIII.2. The spectrum follows a scaling law in an infrared momentum region, $u(k) \sim k^{-\gamma}$ with $\gamma = 1.4$, where the scaling exponent reflects the offset scaling exponent, $\gamma = \zeta - v$, found in Fig. VIII.2 and Fig. VIII.1. The extend of the infrared momentum region depends on the shape of the driving power spectrum (see main text). Figure adapted from [220].

On the one side, the kinetic energy spectrum in the form of Eq. (VIII.2) is then approximately equal to the kinetic energy spectrum of the Bose gas [165, 166], $\epsilon(k) \simeq k^2 n(k)$, if gradients in the gas density are small. On the other side, under the same condition, the relation $\epsilon(k) \simeq k^2 \langle \theta(-k)\theta(k) \rangle_\zeta$ approximately holds, linking the energy spectrum to the phase field appearing in the effective Kardar-Parisi-Zhang equation. We furthermore employ a decomposition of the velocity field in a compressible and an incompressible component, $\boldsymbol{v} = \boldsymbol{v}_\mathrm{c} + \boldsymbol{v}_\mathrm{i}$, with $\nabla \cdot \boldsymbol{v}_\mathrm{i} = 0$ and $\nabla \times \boldsymbol{v}_\mathrm{c} = 0$. Following [165, 166] this allows to divide the hydrodynamic energy spectrum accordingly in a compressible and an incompressible part $\epsilon(k)_{\mathrm{c,i}}$, by inserting the decomposed velocity fields in Eq. (VIII.2). The resulting hydrodynamic kinetic energy spectra in the vortex-less steady state are shown in Fig. VIII.4 for high values of $v > 2$, where the effective forcing attains the v-independent scaling form. First of all, we find that the compressible contribution to the spectrum dominates by more than four orders of magnitude and reassembles closely the form of the occupation spectrum. The additional scaling by a factor k^2 simply captures the difference between kinetic energy and occupation number. This corroborates that non-topological, *i. e.* small perturbative, excitations of the phase field are responsible for the universal properties of the non-equilibrium steady state, including the scaling exponent $\zeta = v + 1.4$. But the decomposition reveals also that there is an incompressible part in the energy spectrum building up in the steady state, which follows a scaling law with the same universal offset as the compressible part. The momentum region where the power law is attained in the incompressible spectrum even extends far beyond the typical infrared region we have

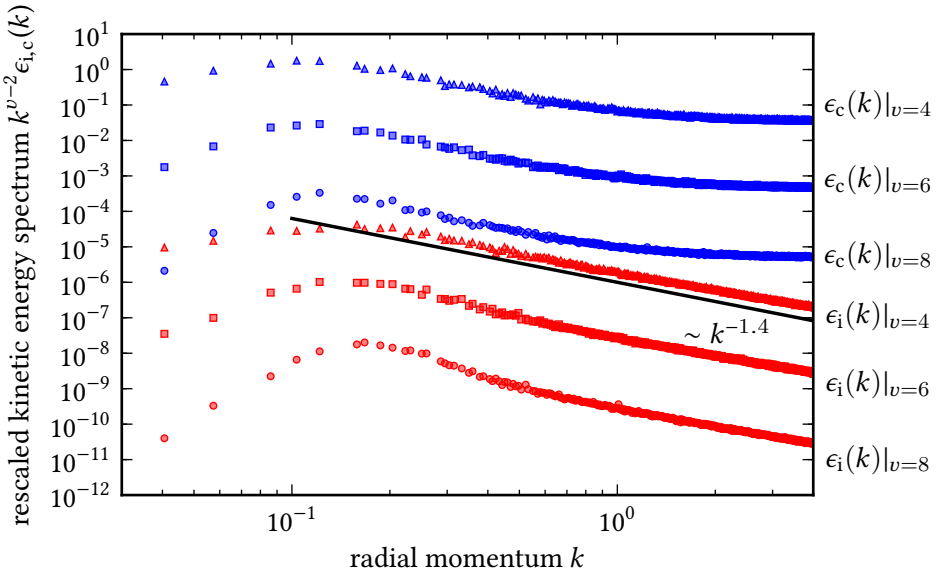

Figure VIII.4: Hydrodynamic kinetic energy spectra in the vortex-less steady state are shown for values of $v = \{4, 6, 8\}$. Note that the y-axis is rescaled with a factor k^{v-2}, to compensate for the forcing power law which builds up in the ultra-violet (*cf.* Fig. VIII.2). The additional factor k^2 originates in the difference in physical dimensions between energy and occupation spectrum. Blue symbols show the compressible part of the hydrodynamic kinetic energy, $\epsilon_c(k)$, while red symbols show the incompressible, $\epsilon_i(k)$. The black solid line illustrates the scaling law $\epsilon(k) \sim k^{-1.4-v+2}$. Time and simulation parameters correspond to Fig. VIII.2.

encountered in the other observables so far. This can be understood in the following way. Even in the absence of vortices, the curl of the velocity field we use is non-zero, due to the additional factor of $\sqrt{n}$, $\nabla \times \boldsymbol{v} = \nabla\sqrt{n} \times \nabla\theta$. This shows that the incompressible energy spectrum in Fig. VIII.4 also captures a contribution from phase fluctuations. However, only those phase fluctuations contribute the gradients of which are disaligned with the density gradients. This suggest that, to disentangle phase and density fluctuations in the Bose gas for mapping it to the Kardar–Parisi–Zhang equation, one needs to project out the transverse phase excitations $\nabla\theta_\perp = \boldsymbol{e}_{\nabla n} \times \nabla\theta$. Integrating $\nabla\theta_\perp$ then yields a phase field with a clean scaling law in its power spectrum in the steady state. For the scaling law, still the linear dependence $\zeta(v) = \gamma + v$ holds. Thus, we find numerical evidence that the structure of steady states is determined by a fixed line (rather than a fixed point) of the underlying Kardar–Parisi–Zhang dynamics. Such structures, although in a different context, have been identified in non-perturbative renormalisation group flows for the driven Kardar–Parisi–Zhang equation in [218].

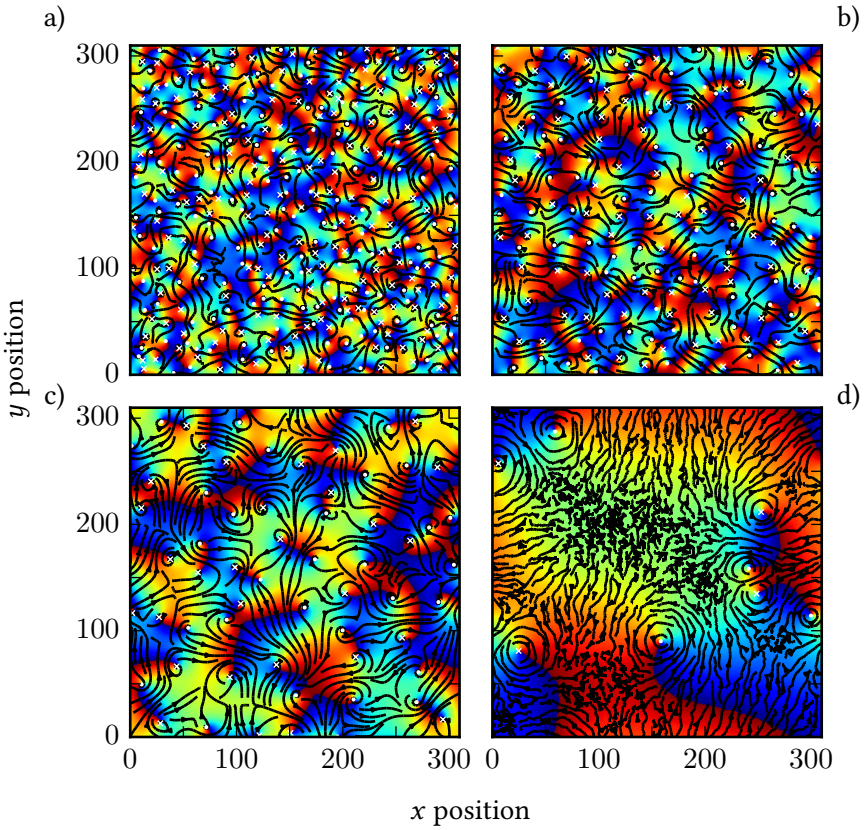

Figure VIII.5: Examples of vortex configurations in the non-equilibrium steady state (a-c) for different values of $v = \{0, 4, 8\}$, when vortex nucleation is allowed for via initial conditions. For comparison, panel d) shows a realisation from a thermally coupled situation, during the transient vortex-containing stage, from the simulations discussed in Sect. VII.3. Single realisations of the phase θ of ψ are depicted colour-coded (from blue $-\pi$ to red π) at simulation time $t = 500\,\xi^2$, which is well within the steady state for panels a)-d). Vortex defects are marked with white symbols, dots for vortices and crosses for anti-vortices. Black solid lines illustrate the normed hydrodynamic flow field $\boldsymbol{v}/|\boldsymbol{v}|$ where $\boldsymbol{v} = \sqrt{n}\nabla\theta$.

VIII.2 Vortex Nucleation from Stochastic Driving

The behaviour of the driven-dissipative Bose gas changes dramatically when the the dynamic evolution is initialised with an empty condensate mode, just putting half a particle occupation on average in all non-zero momentum modes,

$$\langle \psi^\dagger \psi \rangle_{\mathrm{i}}(\mathbf{k}) = 1/2\,. \tag{VIII.7}$$

The gas is then, initially, subject solely to the external drive, where the finite imaginary part of the chemical potential enforces an exponentially fast build-up of a finite bulk density. In light of the initially negligible local gas density, large phase fluctuations can form, without being imposed by the driving force, and eventually wind into local topological phase defects. This provides a natural mechanism to produce random vortex configurations in the gas. Examples thereof for different driving schemes are depicted in Fig. VIII.5. The figure shows examples of field realisations in the attained non-equilibrium steady state for three different values of the driving power law (panels a to c). The fourth panel depicts, for comparison, a realisation from a thermally coupled situation during the transient vortex-containing stage, from the simulations discussed in Sect. VII.3. The non-equilibrium drive builds up vortex configurations which produce hydrodynamic velocity fields with large-scale structures (see black lines in Fig. VIII.5), very similar to what we have found in the vortex lattice scenario (*cf.* Sect. VII.2 and Fig. VII.2). In contrast, the hydrodynamic flow concentrates around vortex pairs in the thermally coupled system and staggers in large areas in between the pairs.

We find that, under the condition of $n_\mathrm{i} \simeq 0$, every driving scheme we utilised produces vortex configurations with vortex quantisation $w = \pm 1$, together with highly coherent hydrodynamic velocity fields. However, the time this process needs and the number of vortices forming is dependent on the driving scheme. We assume a phase defect to be a true vortex if a vortex core is identifiable within the gas bulk density. With this, we can define a timescale for vortex creation, τ_v, via the average bulk density

$$n(t) = \frac{1}{V} \int \mathrm{d}^2 x \, \langle \psi^\dagger \psi \rangle \, . \tag{VIII.8}$$

Assuming that a minimum of $n(t) = 0.1 n_\mathrm{f}$ average bulk density is required to identify the vortex core, we define

$$n(\tau_\mathrm{v}) = 0.1 n_\mathrm{f} \, , \tag{VIII.9}$$

and count the number of vortices N_v^i at this instance in time. The behaviour of τ_v and the initial vortex density $n_\mathrm{v}^\mathrm{i} = N_\mathrm{v}^\mathrm{i}/V$ as a function of the power law in the driving force v we obtain is shown in Fig. VIII.6 (upper panel). Both quantities are in one-to-one correspondence and demonstrate a crossover behaviour from small to high values of v. On a qualitative level, the crossover behaviour for the initial vortex density can be explained. If the vortex density is turned into a length scale, $L_\mathrm{v}^\mathrm{i} = (n_\mathrm{v}^\mathrm{i})^{-1/2}$, we find $L_\mathrm{v}^\mathrm{i} \simeq 3.1\xi \simeq 1/\sqrt{2mn_f g_\mathrm{d}}$ for the limit $v = 0$. In the other limiting case, $v = 8$, the initial average defect distance is set by the infrared cut-off in the driving $L_\mathrm{v}^\mathrm{i} \simeq 10\xi \simeq \lambda$ (*cf.* Eq. (VII.4)). Therefore, the initial vortex nucleation undergoes a crossover from a dissipation-dominated process to forcing-dominated process, which is understandable since the forcing becomes increasingly coherent at a scale set by λ as v increases. When the forcing has no inherent scale, *i. e.* at $v = 0$, on the other hand, vortices are created as dense as possible. If two phase defects of opposite winding number are nucleated with a separation closer than $1/\sqrt{2mn_f g_\mathrm{d}}$, *i. e.* the characteristic scale of the non-linear dissipation, they simply decay instead of forming density defects. The lower panel in Fig. VIII.6 shows that there is a linear dependence between the characteristic vortex formation time tau_v and the initial vortex density n_v^i in the crossover regime. With this, we have iden-

tified a reliable and easily realisable mechanism to engineer vortex distributions via the choice of the driving scheme.

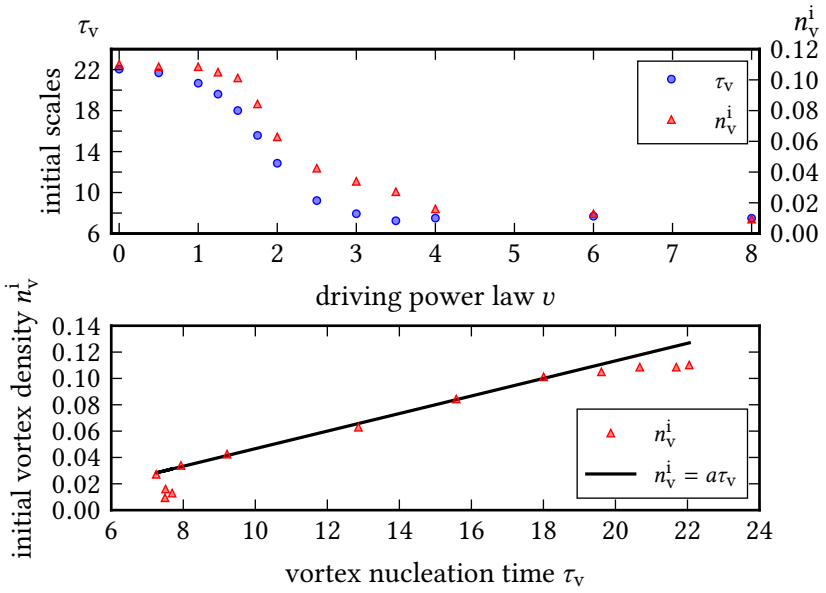

Figure VIII.6: Upper panel: the timescale for vortex creation τ_v (blue circles, left axis), defined via $n(\tau_v) = 0.1 n_f$, and the corresponding density of initially nucleated vortices, N_v^i (red triangles, right axis) is shown as a function of the power-law v in the driving force. We find a crossover between a dissipation-dominated nucleation of vortices and a forcing-dominated one. See main text for details. Lower panel: initial vortex density as a function of the characteristic vortex formation time. There is a linear dependence $n_v^i \propto \tau_v$ (see black line) between the density and the timescale in the crossover region. Simulation data from [220]

Not only the initial number of vortices but also their number as a function of time is influenced by the forcing mechanism. The time evolution of the vortex density $n_v(t)$ is shown in Fig. VIII.7 for several forcing power laws. There are apparently three possible stages of the vortex time evolution, depending on the vortex density. For very high densities, there is a fast non-universal decay at early times (*cf.* coloured symbols and grey lines for $v \in [0, 2]$ in Fig. VIII.7). This corresponds to the values of v where the nucleation process is dissipation-dominated. This initial stage is followed by a slow universal stage of decay, where the number of vortices reduces algebraically,

$$n_v(t) \sim t^{-0.14} . \tag{VIII.10}$$

Even then, the exponent of the power law decay is considerably weaker as has been identified in previous studies, in isolated Bose gases [55, 59] (see also Fig. VII.5), the thermally coupled gas as discussed in Sect. VII.3, or strongly-coupled dissipative systems [65]. We point out that the decay in Fig. VIII.7 is universal not only in the sense that the power law

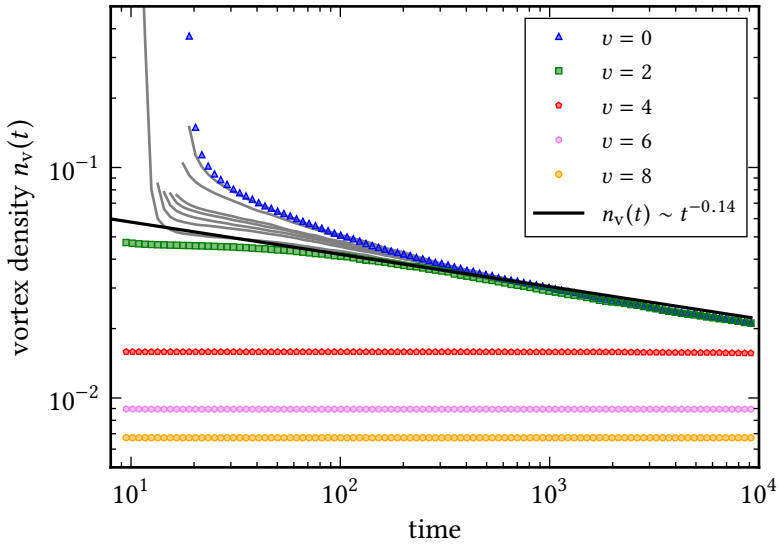

Figure VIII.7: Vortex density $n_v(t)$ (coloured lines) as a function of time for different values of of the forcing power law υ. Coloured symbols represent integer values of υ as given in the legend. Grey solid lines show the vortex density, from simulation data, for additional non-integer values of $\upsilon = [1.5, 1.75, 1.8, 1.85, 1.9, 2.1, 2.2]$, demonstrating that the behaviour of the vortex number is continuous in υ (*cf.* also Fig. VIII.6). The black solid line corresponds to a $n_v \sim k^{-0.14}$ power law. For small to intermediate values of υ, $n_v(t)$ approaches a universal curve, whereas there is no visible decay for the highest values of υ we have simulated. The crossover we have discussed in Fig. VIII.6 manifests itself also here in the initial non-universal behaviour. If the nucleation of vortices is dissipation-dominated there is extremely fast decay present. Simulation data from [220]

is independent of υ but in addition also the pre-factor is. Therefore, after non-universal dependencies from the initial stage of evolution have damped out, all curves fall on one universal curve without additional re-scaling. For highly coherent driving forces (*cf.* $\upsilon = 8$ in Fig. VIII.7), however, there is no decay of the vortex distribution observable, for times accessible in the simulations. In this case, the nucleation process is dominated by the driving scale alone, such that the vortex configuration is created in a statistically stationary state from the outset. We point out that vortices in our simulations always are created in pairs and removed in pairs. The defect structure proves remarkably stable even against strong external perturbations. Thus, a decay of the vortex distribution can only proceed via mutual annihilation of pairs and stops if the defects are pinned by the stochastic forcing. The question remains, which we can not answer with our current numerical implementation, if the decay for intermediate values of υ in practice halts completely once the vortex density is sufficiently low. But even if not, the decay is sufficiently weak to deduce the existence of a non-equilibrium stationary state in this phase. In general, the

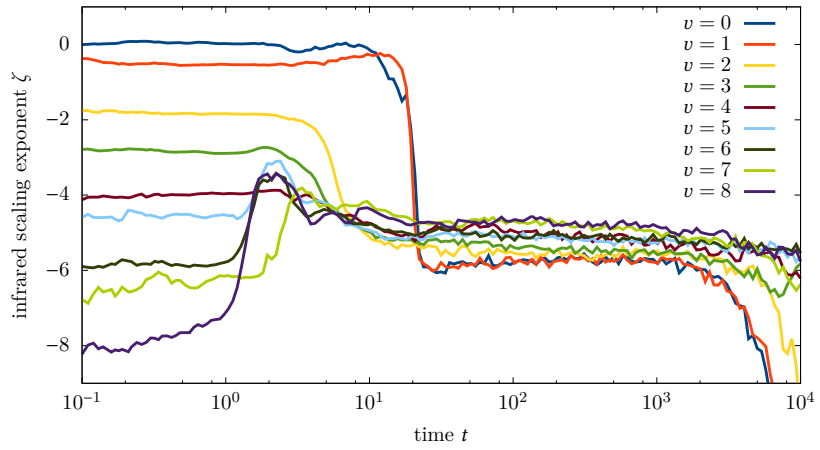

Figure VIII.8: The infrared scaling exponent $\zeta(t)$ of the occupation spectrum in the vortex-containing non-equilibrium steady state as a function of time t. Different coloured solid lines correspond to different values v of the forcing power-law. The fitting procedure employed to determine the scaling exponent is similar to that discussed in Fig. VIII.1. The scaling exponent ζ of the spectrum in the steady state converges nearly v-independent to a narrow band between $\zeta = 5.4$ and $\zeta = 6$. Corresponding occupation spectra in the steady state are depicted in Fig. VIII.9. Figure adapted from [220].

stochastic forcing tremendously stabilises the vortex-containing state of the Bose gas, as it counteracts the Magnus force and the attractive force between vortex–anti-vortex pairs likewise.

VIII.3 Vortex Influence on the Non-equilibrium Steady State

The scaling properties of the non-equilibrium steady state change equally drastically, in comparison to the case discussed in Sect. VIII.1, when vortices are allowed to form out of the stochastic driving process. We again anticipate the existence of a scaling law in some infrared momentum region of the occupation spectrum and apply a similar fitting procedure as discussed in Fig. VIII.1 to determine the time evolution $\zeta(t)$ of the corresponding scaling exponent. The result for different power laws in the driving force is shown in Fig. VIII.8. Here, it is the early stage of time evolution where the occupation spectrum is shaped by the driving power law. This is of course expected, as one literally computes the power spectrum of the driving force at early times with $n(k)$, if the condensate mode is zero initially. But in contrast to the case of the vortex-free steady state, the system here enters thereafter a steady state where the infrared scaling exponent in the occupation number is drawn to a narrow band between $\zeta = 5.4$ and $\zeta = 6$. The time window $10\xi^2 \lesssim t \lesssim 100\xi^2$ in which this happens is consistent with the transition from non-universal fast decay to the universal stage in the time evolution of the vortex number, see Fig. VIII.7.

Before we go on, we comment on the temporal limitation our simulation setup is subject to. As can be seen from the curves for $v = \{0, 1, 2\}$ in Fig. VIII.8, at times beyond $t \simeq 2 \cdot 10^3 \xi^2$ the infrared power law begins to steepen further. This originates in the periodic boundary conditions of our simulation domain. At this point, the Bose gas has developed a persistent superfluid current, under the influence of the driving force, flowing around one of the circles of the torus of the simulation domain. In this state, the vortex configuration is ordered into a regular lattice on the torus and the hydrodynamic velocity field $\boldsymbol{v}$ acquires a constant direction and value, being subject to a quantised flux. Although this effect constitutes a good starting point for investigating the influence of boundary conditions on the structure of non-equilibrium steady states and non-thermal fixed points, we will not pursue it further in this work and consider it as a limitation for the total simulation time.

The (nearly) v-independent infrared power-law in the vortex-containing non-equilibrium steady state, together with the coherent hydrodynamic velocity fields in this state (see Fig. VIII.5), are reminiscent of our findings for the anomalous fixed point in the isolated gas, see Sect. VII.2. The functional form of the occupation number spectra in the steady state, shown in Fig. VIII.9, demonstrates also on a quantitative level the similarity of the steady state here to the anomalous non-thermal fixed point, see for comparison Fig. VII.3. The infrared and deep-infrared momentum region follows the typical form of a generalised Cauchy distribution, we have also identified the scaling forms with in Fig. VII.3. In the upper panel of Fig. VIII.9, we show the spectrum determined from simulation (coloured data points) together with corresponding fits (coloured lines) of the function

$$S(k) = \frac{a}{b^\zeta + k^\zeta}\,, \tag{VIII.11}$$

to the infrared and deep-infrared momentum region $k < 1/\xi$. Note that the spectra $n(k)$ depicted Fig. VIII.9 represent temporal averages over several times within the stationary plateau in Fig. VIII.9. In the lower panel of Fig. VIII.9, the corresponding scaling exponents ζ is depicted, as determined from the fit of the function Eq. (VIII.11) to the temporally averaged spectrum $n(k)$ in the steady state. The scaling exponent ζ undergoes a crossover from $\zeta = 6$ for less coherent driving to $\zeta = 5.4$ for highly coherent driving, similar to Fig. VIII.6. But, within numerical error bounds, the scaling exponents $\zeta(v)$ exceed Porod's scaling law, $\zeta(v) > 4$, and approximately equal the scaling exponent attained near the anomalous non-thermal fixed, $\zeta \simeq 6$ (*cf.* Fig. VII.3).

The remaining v dependence of the spectrum in Fig. VIII.9 can again be analysed for a universal scaling form. An obvious v-dependent effect on the occupation spectrum originates in different particle numbers N_f in the stationary state, as our definition of the field ψ and the occupation spectrum (see Eq. (VII.9)) leads to

$$\int \mathrm{d}k\, k n_\mathrm{f}(k) = N_\mathrm{f}\,. \tag{VIII.12}$$

Since the particle number the system converges to in the steady state is not fixed by our numerical procedure, we normalise the occupation spectrum to $N_\mathrm{f}(v)$, via $n(k) \to n(k)/N_\mathrm{f}$. The upper panel in Fig. VIII.9 (which shows the *normalised* spectra) demonstrates that there remains a v-dependent scale in the spectrum after normalisation to N_f.

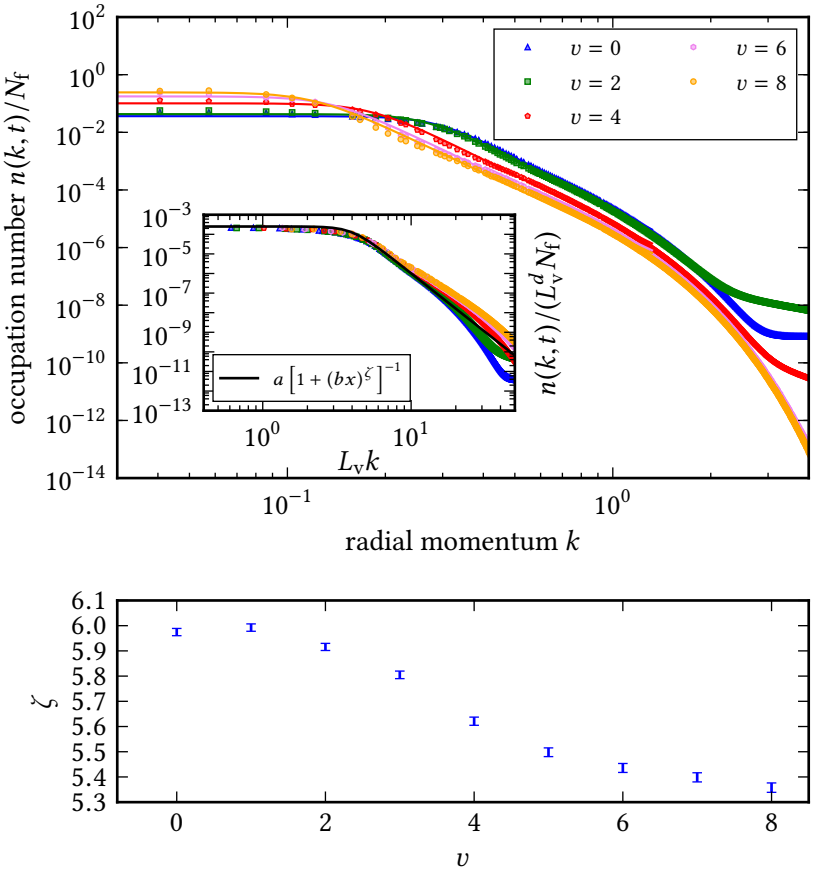

Figure VIII.9: Upper panel: the occupation spectrum in vortex-containing non-equilibrium steady state shown for different power laws v (different colours) in the stochastic forcing. Note that the spectrum is normalised to the total number of particles in the steady state N_v^f. Coloured datapoints show simulation data $n(k)/N_\mathrm{v}$, where a temporal average over $n(k,t)$ at 50 logarithmic-equidistant time steps within the steady steady state (*cf.* $t = 40\,\xi^2$ to $t = 10^3 \cdot \xi^2$ in Fig. VIII.8) is computed. The corresponding coloured lines represent fits of a generalised Cauchy distribution, (see Eq. (VIII.11)), to the infrared and deep-infrared part $k < 1/\xi$ of the occupation spectra. Lower panel: fit parameter ζ, as obtained from fitting Eq. (VIII.11) to the occupation spectra, as a function of v The inset in the upper panel shows the scaling collapse of the normalised occupation spectrum according to Eq. (VIII.14), using the average vortex distance (see Eq. (VIII.13)) in the steady state as scale v-dependent scale. The scaling form contains a power law with ζ between 5.4 and 6. The inset shows a generalised Cauchy distribution with $\zeta = 6$ (black line).

Note that in chapter VII this was not an issue for scaling forms, as we did not compare situations with differing total particle number.

Turning back to the scaling hypothesis from Eq. (VII.18) in the context of phase ordering kinetics (see discussion in Sect. VII.4), the average defect distance in the steady state,

$$L_{\mathrm{v}}^{\mathrm{f}} = \frac{1}{\sqrt{n_{\mathrm{v}}^{\mathrm{f}}}}\,, \tag{VIII.13}$$

is expected to provide the relevant scale in the occupation spectrum, *i. e.* the structure factor. We have already determined in Fig. VIII.7 that the quantity $L_{\mathrm{v}}(t)$ is driving dependent, even in the stationary state. The inset in the upper panel of Fig. VIII.9, demonstrates that the normalised spectrum in the steady state can indeed be collapsed to a single curve according to a scaling form

$$S(k) \simeq \frac{L_{\mathrm{v}}^{\mathrm{f}}(v)^d}{1 + (L_{\mathrm{v}}^{\mathrm{f}}(v)k)^{\zeta}}\,. \tag{VIII.14}$$

The length scale $L_{\mathrm{v}}^{\mathrm{f}}$ can be determined independently from the data used for Fig. VIII.7. We find that the collapse of the occupation spectrum to a universal curve is possible in the infrared and deep-infrared momentum region, up to $L_{\mathrm{v}}^{\mathrm{f}}k \lesssim 10$. If the spatial scaling region in the occupation spectrum continues beyond that momentum scale is not unambiguously clear from our data in Fig. VIII.9. The fits of the generalised Cauchy distribution in the upper panel of Fig. VIII.9 indicate a v dependence of ζ (see lower panel for corresponding values of ζ) in the scaling form. On the other hand, the scaling collapse rather indicates that there is one universal curve up to the dissipation scale $k_{\mathrm{d}} = 1/\sqrt{2mn_{\mathrm{f}}g_{\mathrm{d}}} \simeq \xi/3$. This question can be clarified by extending the inertial range between driving scale $1/\lambda$ (see Eq. (VII.4)) and k_{d} on a larger simulation grid.

Nevertheless, we find that the occupation spectrum in the vortex-containing non-equilibrium steady state follows the universal scaling form Eq. (VIII.14). The universality here can be made apparent when rescaling the occupation spectrum with the average defect distance $L_{\mathrm{v}}^{\mathrm{f}}$. In an infrared momentum region below the dissipation scale k_{d}, the v-dependence is solely determined by the vortex scale L_{v}. In the same way, the time dependence of the infrared part of the occupation spectra in Fig. VII.3 is encoded entirely in the time dependence of the vortex scale $L_{\mathrm{v}}(t)$, as we have discussed in Sect. VII.4. Together with the steep power law in the scaling form (see Fig. VIII.9), ζ between $\zeta = 6$ and $\zeta = 5.4$, we find therefore numerical evidence that the vortex-containing non-equilibrium steady state is equivalent to the anomalous non-thermal fixed point, which determines the universal evolution in the isolated Bose gas (see Sect. VII.2).

In addition, it has been shown in [220] that the occupation spectrum in the infrared momentum region can be derived solely from the vortex positions, considering single realisations and using the topological solution for the Gross–Pitaevskii vortex. This means that, in contrast to Sect. VIII.1, the universal aspects of the steady state here originate in vortex-generated, incompressible hydrodynamic fluxes. It remains to be clarified and quantified how the statistics of the driving force influences the vortex configuration in the non-equilibrium steady state.

VIII.4 Summary

In this chapter, we demonstrated in Sect. VIII.1 that the driven-dissipative Bose gas hosts non-equilibrium steady states with universal scaling laws even in the absence of vortices. We presented evidence that that the universal properties of the vortex-less non-equilibrium steady state are determined by an underlying fixed point structure of an effective Kardar-Parisi-Zhang equation. Provided that the stochastic forcing of the Bose gas does not introduce density fluctuations on too small scales, the power spectrum of the effective driving force attains a power-law scaling exponent $\gamma = 1.4$. It is universal in the sense that it is independent from the power-spectrum which drives the Bose gas, characterised by a scaling exponent v. The corresponding scaling law in correlation spectra of several order parameter fields, on the other hand, was found to consistently reflect a linear dependence between the scaling exponents, $\zeta = \gamma + v$. This suggests that there is actually a fixed line instead of a point from the underlying effective Kardar–Parisi–Zhang equation responsible for the non-equilibrium steady state. Similar fixed point structures in renormalisation group flows have been found from a non-perturbative renormalisation group treatment [218], although the range of applicability does not extend to our value for γ.

Finally, we have demonstrated that stochastic driving stabilises vortex configurations tremendously, turning them into non-equilibrium steady states. The corresponding hydrodynamic flow fields contain highly coherent structures. The occupation spectrum in the vortex-containing non-equilibrium steady state was found to follow a driving-independent scaling form, when computed in units of the average defect distance. Thus, the defect ensemble provides the only relevant scale for the steady state. The defect ensemble itself in the steady state was found to be controllable by the driving. The scaling law in the scaling form of the steady state is characterised by a exponent $\zeta = 5.7 \pm 0.3$, exceeding the defect scaling exponent. This provides evidence that the vortex-containing non-equilibrium steady state in the driven-dissipative Bose gas is deeply connected to the anomalous non-thermal fixed point in the isolated Bose gas.

IX Conclusion

In this work, we have studied dynamical critical behaviour in a two-component Bose gas in one spatial dimension and a one-component Bose gas in two-spatial dimensions. As a way to set off dynamics far from equilibrium we utilised sudden changes, quenches, in couplings. For the pseudo spin-$1/2$ gas, which we studied completely isolated from environment, the critical behaviour was provoked, since the quench parameter there was a tuning parameter connected to an equilibrium phase transition. In the case of the single-component gas, the quench consisted of a sudden coupling to a thermal environment or a stochastic driving force, violating the thermal fluctuation dissipation relation. In either case, we obtained dynamical critical behaviour in form of a critically slow approach to non-equilibrium stationary states, without referencing a known equilibrium critical point.

A common guiding principle throughout our investigations was the application, or the test for, non-equilibrium scaling hypotheses. This means, as a direct extension of the concept of universality in equilibrium [17], that distribution functions at quasi-stationary states are assumed to be homogeneous in a scale s which rescales *all* dimensionful dependencies of the distribution, including time or non-equilibrium driving forces, with universal exponents. The key feature of this concept is, that it allows measuring critical exponents or, testing for criticality in the first place, by testing distribution functions for a scaling collapse, instead of fitting power-laws. This is especially helpful for experiments, where accessible time and length scales do not always allow determining power-laws directly. A first step into the direction of experimentally measure scaling out of equilibrium was taken in [73], which we also highlighted in chapter IV.

In chapters V and VI we applied the scaling hypothesis to the quench dynamics of the spinor Bose gas in one spatial dimension. In chapter V we found that the scaling hypothesis partially fails when tuning the system parametrically close to the critical point. This is not surprising, as it would likewise for a thermally equilibrated system in one spatial dimension. However, we found numerical evidence that rescaling in the post-quench time direction is restored when a shifted (renormalised) excitation gap is used as scale. In this context, we also advised a way to determine numerically the full quasi-particle dispersion spectrum, which led us to the conclusion that also speed of sound and dynamical critical exponent begin to renormalise for quenches close to criticality. An application of renormalisation group ideas along the lines of [183, 207, 208] likely will lead to an analytic understanding. However, we highlight that our method to compute the dispersion from two-time correlation functions is amenable for implementation in quench experiments similar to [73], if densities can be measured non-destructively (see for example [209]).

The failure of the full scaling hypothesis does actually not contradict universality in one dimensional systems, as there exists the notion of universal crossovers. In this case, distribution functions are described in terms of non-homogeneous universal function, where

still only ratios of dimensionful quantities enter. We applied this idea to the quench dynamics in the spinor gas in chapter VI, in light of the structural similarities between the spinor gas and the Ising chain in a transverse field, for which crossover functions are analytically known [89]. We find that, already in the early post-quench time evolution of the spinor gas, correlations in the spinor gas follow the thermal Ising crossover function when quenching to the critical point. The rescaling in time direction is important for this observation, as this Ising-like behaviour becomes only apparent when comparing times in units of the gap oscillation frequency (in practice, when analysing maximal correlations). We furthermore demonstrated in this context that an effective temperature for this early post-quench behaviour can be derived, which characterises the crossover function in ratio to the excitation gap long before a prethermalised stationary state is reached. Thereby, the effective temperature can be derived *a priori* from a generalised Gibbs ensemble describing Gaussian fluctuating modes in the spinor gas. Together with the decay of oscillations in the spin correlations, we interpret this effectively thermal crossover behaviour at early times as a precursor of an actual prethermalisation plateau [35] in the post-quench dynamics of the spinor gas.

Furthermore, we provided evidence that the quench in the spinor Bose gas triggers a critical dynamic evolution in occupation distributions characterising the individual components (instead of the pseudo-spin). We find that these distributions evolve self-similar in time and that the time-dependence can be collapsed to a universal function without reference to the post-quench distance to the critical point. In [47] this kind of behaviour has been put forward as a criterion for the presence of a non-thermal fixed point in the time evolution. In the light of these findings, we attribute the critical scaling in single-component occupation distributions of the spinor gas to a non-thermal fixed point which is connected to an effectively relativistic local energy transport.

In chapter VII, we investigated critical dynamical behaviour in the one-component Bose gas in two spatial dimension, where we set off dynamics by locally 'stirring' (*i. e.* placing vortices by hand) the gas. Using regular lattices of vortices (as they emerge for example when rotating the gas cloud as a whole [232]) as initial state, we discovered a new non-thermal fixed point in the Bose gas, which comes with an anomalously slow self-similar time evolution of occupation spectra. We also demonstrated that the critical self-similar evolution is not destroyed by a thermal environment and that, instead, the dynamical critical exponent of the kinetic ordering process is changed to its smaller non-anomalous value, such that the ordering process evolves much faster in time but still following a power law. We clarified the connection between phase ordering kinetics [54, 99] and the fixed point structure [47, 59] in the Bose gas. This allowed us to map the anomalous critical exponent, defining our newly discovered anomalous fixed point, to an anomalously high dynamical critical exponent $z = 5$ of the ordering process. Based on our results and in the light of findings for vortex glass phases in superconductors [100–104], we put forward that the anomalous fixed point in the Bose gas signals a glass-like phase of the vortex distribution.

In chapter VIII, we probed the structure of true non-equilibrium steady states in the Bose gas by driving the gas externally. As a result from the non-equilibrium driving, we obtained that non-equilibrium steady states with universal properties in the occupation distribution emerge, where we identified a vortex-less and vortex-containing class of

steady states. As for the time evolution, also in this case the scaling hypothesis, which needs here to include scales from the driving, allowed us to characterise the universal features. We demonstrated that scaling properties of distribution functions in the vortex-less steady state can be understood in terms of the Kardar–Parisi–Zhang universality class [105–108]. In particular, we provided numerical evidence that the vortex-less steady state is connected to a fixed line in the Kardar–Parisi–Zhang equation, to which the vortex-less Bose gas effectively maps [48, 109, 110]. For the second, vortex-containing class of non-equilibrium steady states in the Bose gas, we demonstrated that scaling properties of distribution functions can fully be understood in terms of the vortex ensemble. Stationary occupation numbers for different realisation of the driving can be rescaled to a universal function, using scales of the vortex distribution, specifically the mean defect distance. From this we found a scaling collapse to be possible. With the form of the emerging universal function and the vortex ensemble in the steady state itself, we find strong numerical evidence that the vortex-containing steady state is in one-to-one correspondence with the anomalous non-thermal fixed point appearing in the isolated time evolution. This case would then constitute the first numerical demonstration of driving a system directly into the non-thermal fixed point (as true stationary state) which acts as partial attractor for the isolated dynamic evolution. The question if every non-thermal fixed point has a non-equilibrium steady state as counterpart remains, however, open.

Every setup we studied and presented results on in this work, remarkably, realises more than one concept of critical dynamics simultaneously or within the same context, prethermalisation and a generalised Gibbs ensemble together with non-thermal fixed points, non-thermal fixed points together with phase ordering kinetics, or together with non-equilibrium stationary states from external driving. At the same time, all techniques we employed to probe critical dynamics, in particular the ways how set off dynamics and the observables to measure the response, are well realisable in experiments for ultracold quantum gases. With this in mind, we believe that our results contribute to the understanding of universality classes far from equilibrium. Simultaneously, our work provides a good starting point, for theory and experiment alike, to methodically deepen the understanding of non-equilibrium universality in the Bose gas.

A Representations of the Two-Component Bose Gas

Here, we summarise a number of useful representations of the two-component Bose gas, which have not explicitly been introduced in the main text. We derive the actions for them, based on the model for the two-component Bose gas in the language of fundamental fields Eq. (II.1). We also give more details on the derivation of the phase–density representation Eq. (II.4) of the model Eq. (II.1).

A.1 Dressed Field Basis

The action in phase–density representation Eq. (II.4) reveals a complex coupling structure between the two phase–density sectors of the full system, already on the level of the microscopic action. It is even more troublesome that this coupling structure can not be studied on the level of the Bogoliubov approximation, since symmetric and anti-symmetric Bogoliubov excitations completely decouple from each other. Hence, a field theoretic treatment is needed in which a perturbation expansion of the relevant coupling terms can be performed to the up to the first non-trivial order. It turns out that the phase–density representation is particularly unsuited for this purpose and, thus, we turn back to the description in terms of Bose fields.

It is helpful, also for this case, to transform the degrees of freedom to the symmetric–anti-symmetric basis in a first step, $\psi_\pm = (\psi_1 \pm \psi_2)/\sqrt{2}$. As a result, the linear coupling between the two fields in this so-called dressed–state basis vanishes in favour of additional mass terms, yielding

$$\begin{aligned}\mathcal{S} = \int \mathrm{d}t\mathrm{d}y \, \Big\{ & \frac{\mathrm{i}}{2}\left[\psi_+^\dagger \partial_t \psi_+ + \psi_-^\dagger \partial_t \psi_- - \text{h.c.}\right] \\ & \psi_+^\dagger \left[\frac{1}{2m}\partial_y^2 + J + \mu\right]\psi_+ + \psi_-^\dagger \left[\frac{1}{2m}\partial_y^2 - J + \mu\right]\psi_- \\ & - \frac{g_+}{4}\left(|\psi_+|^2 + |\psi_-|^2\right)^2 \\ & - \frac{g_-}{4}\left[2|\psi_+|^2|\psi_-|^2 + \psi_-^\dagger\psi_-^\dagger\psi_+\psi_+ + \psi_+^\dagger\psi_+^\dagger\psi_-\psi_-\right]\Big\} \,. \end{aligned} \tag{A.1}$$

A.2 Hydrodynamic Representations

Starting from the polar representation of the fields, $\phi_j = \sqrt{\rho_j}\mathrm{e}^{\mathrm{i}\varphi_j}$, and $\partial\phi_j = \mathrm{e}^{\mathrm{i}\varphi_j}\partial\sqrt{\rho_j} + \mathrm{i}\phi_j\partial\varphi_j$ the action of the Gross–Pitaevskii model, see Eq. (II.1), can be brought to the form

(with dimensionless quantities)

$$\mathrm{S} = \iint \mathrm{d}^D x \mathrm{d}t \Bigg[-\rho_j \partial_t \varphi_j - \frac{1}{2}(\nabla\sqrt{\rho_j}\nabla\sqrt{\rho_j} + \rho_j |\nabla\varphi_j|^2) - \frac{g}{2}(\rho_j\rho_j)^2 + g(1-\alpha)\rho_1\rho_2 \Bigg], \tag{A.2}$$

in the classical limit. The variation with respect to the phases, $\frac{\delta S}{\delta \varphi_j} = 0$, yields the continuity equations. The variation with respect to the densities, $\frac{\delta S}{\delta \rho_j} = 0$, yields the remaining two classical equations of motion. Taking the gradient of these and using $\frac{1}{2}\nabla(\mathbf{v})^2 = \mathbf{v}\cdot\nabla\mathbf{v} + \mathbf{v}\times\nabla\times\mathbf{v}$ one arrives at the Euler equations for the velocities, $\mathbf{v}_j = \nabla\varphi_j$,

$$\partial_t \mathbf{v}_1 + \mathbf{v}_1\cdot\nabla\mathbf{v}_1 = -\nabla\left[-\frac{\nabla^2\sqrt{\rho_1}}{2\sqrt{\rho_1}} + g(\rho_1 + \alpha\rho_2)\right], \tag{A.3a}$$

$$\partial_t \mathbf{v}_2 + \mathbf{v}_2\cdot\nabla\mathbf{v}_2 = -\nabla\left[-\frac{\nabla^2\sqrt{\rho_2}}{2\sqrt{\rho_2}} + g(\rho_2 + \alpha\rho_1)\right]. \tag{A.3b}$$

Note that for this a perfectly irrotational flow (no vortices), $\nabla\times\mathbf{v}$, has to be assumed.
In order to transform the classical action Eq. (A.2) into the spin–fluid representation we use $\varphi_1 = \frac{1}{2}(\Theta_T + \theta_r)$ and $\varphi_2 = \frac{1}{2}(\Theta_T - \theta_r)$. Note that in addition from the definition of the spin densities, see Eq. (II.2), the identity $\left[1-(S^z)^2\right]\partial\theta_r = S^x\partial S^y - \partial S^x S^y$ can be computed. With this the dynamic (time derivative) part of Eq. (A.2) assumes the form

$$\begin{aligned} -\rho_1\partial_t\varphi_1 - \rho_2\partial_t\varphi_2 &= -\frac{1}{2}\left[(\rho_1+\rho_2)\partial_t\Theta_T + (\rho_1-\rho_2)\partial_t\theta_r\right] \\ &= -\frac{1}{2}\rho_T\left[\partial_t\Theta_T + S^z\partial_t\theta_r\right] \\ &= -\frac{1}{2}\rho_T\left[\partial_t\Theta_T + \frac{S^z}{[1-(S^z)^2]}(S^x\partial_t S^y - \partial_t S^x S^y)\right]. \end{aligned} \tag{A.4}$$

The transformation of the static part of Eq. (A.2) is elaborated in Ref. [121]. Eventually, the full classical action in spin–fluid representation is given by

$$\begin{aligned} \mathrm{S} = \iint \mathrm{d}^D x \mathrm{d}t \Bigg\{ &-\frac{\rho_T}{2}\left[\partial_t\Theta_T + \frac{S^z}{[1-(S^z)^2]}(S^x\partial_t S^y - \partial_t S^x S^y)\right] \\ &-\frac{1}{2}|\nabla\sqrt{\rho_T}|^2 - \frac{\rho_T}{8}\nabla S^a\nabla S^a - \frac{1}{2}\rho_T|\mathbf{v}_{\mathrm{eff}}|^2 \\ &-\frac{g\rho_T^2}{2} + \frac{g\rho_T^2}{4}(1-\alpha)\left[1-(S^z)^2\right]\Bigg\}. \end{aligned} \tag{A.5}$$

The local constraint $(S^x)^2 + (S^y)^2 + (S^z)^2 \equiv 1$ can be implemented by projecting the normalised spin vector onto the complex plane, defining $u = \frac{S^x - \mathrm{i}S^y}{1-S^z}$. With the identities

$|u|^2 = \frac{1+S^z}{1-S^z} \Leftrightarrow S^z = \frac{|u|^2-1}{|u|^2+1}$ and $\partial u = \mathrm{e}^{\mathrm{i}\theta_r}\partial|u| - \mathrm{i}u\partial\theta_r$ the action Eq. (A.5) can be obtained in the stereographically projected form

$$\begin{aligned} \mathrm{S} = \iint \mathrm{d}^D x \mathrm{d}t \Bigg\{ & -\frac{\rho_T}{2}\left[\partial_t \Theta_T + \frac{\mathrm{i}}{2}\frac{(1-|u|^4)(u^*\partial_t u - \partial_t u^* u)}{|u|^2(1+|u|^2)^2}\right] \\ & -\frac{1}{2}|\nabla\sqrt{\rho_T}|^2 - \frac{\rho_T}{2}\frac{\nabla u^* \nabla u}{(1+|u|^2)^2} - \frac{1}{2}\rho_T |\mathbf{v}_{\mathrm{eff}}|^2 \\ & -\frac{g\rho_T^2}{2}\left[1 + \frac{(1-\alpha)|u|^2}{(1+|u|^2)^2}\right]\Bigg\}. \end{aligned} \tag{A.6}$$

B Numerics

A major part of the results of this work have been obtained by means of numerical simulation. The employed semi-classical simulation techniques have been introduced in the main text. Here, we give additional practical information, in particular on the employed unit systems (referred to as 'natural units' in the main text) and on the algorithms with which we solve the coupled and driven Gross–Pitaevskii equations.

B.1 Units and Dimensions

For the discussion of scaling behaviour in the context of critical phenomena it is convenient to measure observables and their dependencies on time, space, coupling constants, *etc.* in units of the critical coupling. This approach allows, for example, to determine the engineering dimensions of observables, which determines their trivial scaling behaviour due to their physical dimension, right away. One only needs to count the powers of the critical coupling needed to express the operator in 'critical' units. As we will make frequently use of that critical unit system in the following chapters, we discuss it for the spin sector in this section. For the sake of clarity we restore powers of $\hbar$ in all expressions in this section. In Sect. II.1.2 we have deduced an expression of the critical linear coupling in terms of properties of the Bose gas. This defines a characteristic energy scale given by $\hbar J_c$. In practice, we insert an additional factor of 2 for convenience, such that energies will be measured in units of $2\hbar n_+ \left|g_{\uparrow\downarrow} - g\right|$. The mean single-component density n_+ is to be seen as d-dimensional density as the physical dimensions of the coupling constants change accordingly. In one spatial dimension, for example, one finds $g_{ij}^{1d} = 2\hbar^2 a_{ij}^{3d}/(m a_\perp^2)$ [233] if the experimental system is effectively one dimensional with a transverse extent of $a_\perp$ and $3d$ scattering lengths a_{ij}^{3d} for the hyperfine states. In two spatial dimensions, an effective $2d$ scattering length can be computed if the system is tightly confined in the third direction, $a_{ij}^{2d} = 4a_\perp(\pi/B)^{1/2}\exp\{-\sqrt{\pi}a_\perp/a_{ij}^{3d}\}$ [234], where $B \simeq 0.915$. It maps to the $2d$ coupling constants via $g_{ij}^{2d} = -(4\pi\hbar^2/m)[\log\{\mu m (a_{ij}^{2d})^2/4\}]^{-1}$.

Form the critical energy unit the rest of the unit system derives naturally using powers of $\hbar$ and m. Most prominently, we measure time in units of $(2J_c)^{-1}$, momenta in units of $\sqrt{4mJ_c}/\hbar$, and lengths in units of $\hbar/\sqrt{4mJ_c}$. In the latter two expressions contain another convenient factor of 2 such that the kinetic energy in critical units is simply the momentum in critical units squared. Note that the unit of length is the analogue of the condensate healing length on the spin sector. Thus, a similar helpful unit system for the symmetric sector, despite not being related to a critical point, is obtained by replacing g_- with g_+ in all expressions above. A comprehensive overview is given in Table B.1. Subsequently, numerical and analytic results will be discussed in terms of critical units, if physical dimensions are not made explicit. In particular, observables and their dependen-

Table B.1: Table of physical dimensions and their respective unit in terms of the 'critical' unit system. For observables from the spin sector g_- is to be inserted in the expressions and a unit system in terms of the critical coupling $J_c = n_+ g_-$ is obtained therewith. If units are not made explicit in plots or for analytic expressions in the remainder of this work we refer to the critical unit system. When presenting results from the symmetric sector, a unit system with g_+ inserted in the expressions below will be convenient, in isolated cases. In that cases we will state the units nevertheless explicitly.

energy	time	momentum	length	speed
$2\hbar n_+ \lvert g_\pm \rvert$	$(2n_+ \lvert g_\pm \rvert)^{-1}$	$\sqrt{4mn_+ \lvert g_\pm \rvert}/\hbar$	$\hbar/\sqrt{4mn_+ \lvert g_\pm \rvert}$	$\hbar\sqrt{n_+ g_\pm / m}$

cies in plots are shown in those units if not stated otherwise. In this way, if a comparison to a specific experiment is desired, one simply needs to calculate the expressions in Table B.1 in terms of the coupling constants of the experiment and multiply the numeric values of the observable in question with the respective unit.

B.2 Algorithms

The coupled Gross–Pitaevskii equations, Eq. (II.42), can be efficiently numerically integrated with the Spectral-Split-Step method. Since the algorithm is based on spatial Fourier transformations instead of discrete derivatives it provides numerical stability and exact conservation of particle number and energy. Let $H_{ij} = T_{ij} + V_{ij}$ with $T = \delta_{ij}\frac{\nabla^2}{2}$ and $V_{11} = g(|\phi_1(\mathbf{x})|^2 + \alpha|\phi_2(\mathbf{x})|^2)$, $V_{22} = g(|\phi_2(\mathbf{x})|^2 + \alpha|\phi_1(\mathbf{x})|^2)$, $V_{12} = V_{21} = 0$. Then one integration step in time by Δt can be performed via

$$\begin{aligned}\phi_i(\mathbf{x}, t+\Delta t) &= \mathrm{e}^{-\mathrm{i}H_{ij}\Delta t}\phi_j(\mathbf{x},t)\\ &= \mathrm{e}^{-\mathrm{i}(T_{ij}+V_{ij})\Delta t}\phi_j(\mathbf{x},t)\\ &= \mathrm{e}^{-\mathrm{i}T_{ik}\frac{\Delta t}{2}}\mathrm{e}^{-\mathrm{i}T_{kl}\Delta t}\mathrm{e}^{-\mathrm{i}T_{kj}\frac{\Delta t}{2}}\phi_j(\mathbf{x},t) + O(\Delta t^3)\,,\end{aligned} \tag{B.1}$$

where the Baker–Campbell-Hausdorff formula is used for the last equality. Since the operator V is diagonal in real space and the operator T is diagonal in Fourier space the operator exponentials can be evaluated and the operators can be applied to the field vector by simple multiplication in the respective spaces. For this the field vector has to be Fourier transformed successively, which can be numerically done very efficiently with the `Fast-Fourier-Transform` algorithm. We implement the algorithm in C++, using the `fftw3` library [235] for Fourier transformations and the `Eigen` library [236] for high-performance linear algebra. We parallelise the numerical code for multicore architectures with `OpenMP` [237]. We implement the described numerical procedure on a graphics processing unit using NVIDIA's `CUDA` toolkit and libraries, which allows for a highly parallelised implementation [238].

The code which is employed in this thesis was developed by us, apart from the cited

Table B.2: One standard set of parameters for the simulation of quench dynamics on the paramagnetic side in one spatial dimension. In particular, this set has been used for the comparison between simulation and experiment.

L	N	a	α	g	h
2^{14}	$1 \cdot 10^6$	1	1.23	0.00025	0.2

Table B.3: One standard set of parameters for the simulation of quench dynamics on the paramagnetic side in one spatial dimension. As compared to Table B.2, the resolved modes concentrate on the momentum region up to the critical momentum. We use it to obtain properties of the excitation spectrum and scaling exponents from self-similar time evolution, as this set reduces noise from high-energy free-particle modes

L	N	a	α	g	h
2^{14}	$8 \cdot 10^6$	1	1.23	0.002048	0.003

third-party libraries. It is originally based on the code developed in the course of [59] but largely extends its applicability, in particular to driven-dissipative Gross–Pitaevskii equations and coupled multi-component Gross–Pitaevskii equations. The code has not been published but can be obtained upon personal communication and negotiation with the author of this work.

B.3 Simulation Parameters

In this section we summarise the parameter sets we have used for the presented simulation data. Specifically, we give the number of grid points or Fourier modes L, the number of particles in one component N ($N_\uparrow = N_\downarrow = N$), the lattice spacing a, and the non-linear couplings g ($g_\uparrow = g_\downarrow = g$) and $g_{\uparrow\downarrow} = \alpha g$. Other parameters such as the linear coupling or the sample size are to be retrieved from the figure captions. We point out, that we use lattice momenta of the form $k = 2/a \sin(\pi i/L)$, where $i \in [0, L-1]$, such that the ultra-violet cut-off is $k_{\mathrm{UV}} = 2/a$.

For the simulations of the two-component Bose in one spatial dimension we employ two sets of parameters (referring to the model Eq. (II.1), a is the spatial lattice constant and h the temporal). The first Table B.2 resolves a comparatively large part of momentum modes beyond the critical momentum which ensures that the system is large enough not to be influenced by finite size effects. The second set Table B.3 concentrates the resolution of modes to the momentum region up to the critical momentum. We use it to obtain properties of the excitation spectrum and scaling exponents from self-similar time evolution, as this set reduces noise from high-energy free-particle modes. For both parameter sets we average observables over $\mathcal{N} = 8192$ realisations of Truncated Wigner noise, see Sect. II.5.1.

Table B.4: Standard set of parameters for the simulation of the one component Bose gas in two spatial dimensions. The dissipation and driving parameters are explained in the respective chapters in the main text.

$L \times L$	N	a	μ	g	h
1024×1024	$3.2 \cdot 10^9$	1	ng	$3 \cdot 10^{-5}$	0.2

Finally, for all simulations of the one-component Bose gas in two spatial dimensions, we use the set of parameters Table B.4 for the non-dissipative part of the Gross–Pitaevskii equation (referring to Eq. (VII.2)). The dissipation and driving parameters are explained in the respective chapters in the main text. Here, averaging processes differ between the different driving settings (thermal, non-thermal, placed vortex configurations) and are explained in the respective sections of the main text.

References

[1] J. P. Boyd, *Chebyshev and Fourier Spectral Methods*. Dover Publications, 2nd ed., 2001.

[2] J. M. Deutsch, "Quantum statistical mechanics in a closed system," *Phys. Rev.* **A43** (1991) 2046–2049.

[3] M. Srednicki, "Chaos and quantum thermalization," *Phys. Rev.* **E50** (1994) 888–901, cond-mat/9403051.

[4] M. Rigol, V. Dunjko, and M. Olshanii, "Thermalization and its mechanism for generic isolated quantum systems," *Nature* **452** (2008) 854–858, arXiv:0708.1324 [cond-mat.stat-mech].

[5] T. Kinoshita, T. Wenger, and D. S. Weiss, "A quantum Newton's cradle," *Nature* **440** (2006) 900.

[6] J.-S. Caux and J. Mossel, "Remarks on the notion of quantum integrability," *J. Stat. Mech. Theor. Exp.* **2011** (2011) P02023.

[7] V. E. Korepin, N. M. Bogoliubov, and A. G. Izergin, *Quantum Inverse Scattering Method and Correlation Functions*. CUP, Cambridge, UK, 1997.

[8] G. Mussardo, *Statistical Field Theory: An Introduction to Exactly Solved Models in Statistical Physics: An Introduction to Exactly Solved Models in Statistical Physics*. Oxford Graduate TextsOUP, Oxford, 2009.

[9] E. H. Lieb and W. Liniger, "Exact analysis of an interacting Bose gas. I. The general solution and the ground state," *Phys. Rev.* **130** (1963) 1605.

[10] E. H. Lieb, "Exact analysis of an interacting Bose gas. II. The excitation spectrum," *Phys. Rev.* **130** (1963) 1616.

[11] M. Rigol, V. Dunjko, V. Yurovsky, and M. Olshanii, "Relaxation in a Completely Integrable Many-Body Quantum System: An Ab Initio Study of the Dynamics of the Highly Excited States of 1D Lattice Hard-Core Bosons," *Phys. Rev. Lett.* **98** (2007) 050405, arXiv:cond-mat/0604476 [cond-mat.other].

[12] E. T. Jaynes, "Information Theory and Statistical Mechanics," *Phys. Rev.* **106** (1957) 620–630.

[13] E. T. Jaynes, "Information Theory and Statistical Mechanics. II," *Phys. Rev.* **108** (1957) 171–190.

[14] A. C. Cassidy, C. W. Clark, and M. Rigol, "Generalized Thermalization in an Integrable Lattice System," *Physical Review Letters* **106** (2011) 140405, arXiv:1008.4794 [cond-mat.stat-mech].

[15] A. Polkovnikov, K. Sengupta, A. Silva, and M. Vengalattore, "Colloquium: Nonequilibrium dynamics of closed interacting quantum systems," *Rev. Mod. Phys.* **83** (2011) 863, 1007.5331 [cond-mat.stat-mech].

[16] E. J., F. M., and G. C., "Quantum many-body systems out of equilibrium," *Nat Phys* **11** (2015) 124–130, arXiv:1408.5148 [quant-ph].

[17] L. P. Kadanoff, "Scaling and universality in statistical physics," *Physica A* **163** (1990) 1–14.

[18] L. P. Kadanoff, "Scaling laws for Ising models near T_c," *Physics* **2** (1966) 263–272.

[19] K. G. Wilson, "Renormalization group and critical phenomena. II. Phase-space cell analysis of critical behavior," *Phys. Rev.* **B4** (1971) 3184.

[20] K. G. Wilson, "The renormalization group: Critical phenomena and the Kondo problem," *Rev. Mod. Phys.* **47** (1975) 773.

[21] S. L. Veatch, O. Soubias, S. L. Keller, and K. Gawrisch, "Critical fluctuations in domain-forming lipid mixtures," *Proceedings of the National Academy of Sciences* **104** (2007) 17650–17655.

[22] G. Hinshaw, D. Larson, E. Komatsu, D. N. Spergel, C. L. Bennett, J. Dunkley, M. R. Nolta, M. Halpern, R. S. Hill, N. Odegard, L. Page, K. M. Smith, J. L. Weiland, B. Gold, N. Jarosik, A. Kogut, M. Limon, S. S. Meyer, G. S. Tucker, E. Wollack, and E. L. Wright, "Nine-year Wilkinson Microwave Anisotropy Probe (WMAP) Observations: Cosmological Parameter Results," *Astrophys. J. Suppl.* **208** (2013) 19, arXiv:1212.5226 [astro-ph.CO].

[23] **Planck Collaboration** Collaboration, P. Ade *et al.*, "Planck 2013 results. XVI. Cosmological parameters," *Ast. & Ast.* **571** (2014) A16, arXiv:1303.5076 [astro-ph.CO].

[24] P. Coleman and A. J. Schofield, "Quantum criticality," *Nature* **433** (2005) 226–229, arXiv:cond-mat/0503002 [cond-mat.str-el].

[25] T. Donner, S. Ritter, T. Bourdel, A. Öttl, M. Köhl, and T. Esslinger, "Critical Behavior of a Trapped Interacting Bose Gas," *Science* **315** (2007) 1556, arXiv:0704.1439 [cond-mat.stat-mech].

[26] X. Zhang, C.-L. Hung, S.-K. Tung, and C. Chin, "Observation of quantum criticality with ultracold atoms in optical lattices," *Science* **335** (2012) 1070–1072.

[27] S. Braun, M. Friesdorf, S. S. Hodgman, M. Schreiber, J. P. Ronzheimer, A. Riera, M. del Rey, I. Bloch, J. Eisert, and U. Schneider, "Emergence of coherence and the

dynamics of quantum phase transitions," *Proceedings of the National Academy of Sciences* **112** (2015) 3641–3646.

[28] N. Navon, A. L. Gaunt, R. P. Smith, and Z. Hadzibabic, "Critical dynamics of spontaneous symmetry breaking in a homogeneous Bose gas," *Science* **347** (2015) 167–170, arXiv:1410.8487 [cond-mat.quant-gas].

[29] R. Landig, F. Brennecke, R. Mottl, T. Donner, and T. Esslinger, "Measuring the dynamic structure factor of a quantum gas undergoing a structural phase transition," *Nature Communications* **6** (2015) 7046, arXiv:1503.05565 [cond-mat.quant-gas].

[30] P. C. Hohenberg and B. I. Halperin, "Theory of Dynamic Critical Phenomena," *Rev. Mod. Phys.* **49** (1977) 435–479.

[31] A. Lamacraft, "Quantum Quenches in a Spinor Condensate," *Phys. Rev. Lett.* **98** (2007) 160404, arXiv:cond-mat/0611017 [cond-mat.stat-mech].

[32] D. Rossini, A. Silva, G. Mussardo, and G. E. Santoro, "Effective Thermal Dynamics Following a Quantum Quench in a Spin Chain," *Phys. Rev. Lett.* **102** (2009) 127204, arXiv:0810.5508 [cond-mat.stat-mech].

[33] E. G. Dalla Torre, E. Demler, and A. Polkovnikov, "Universal Rephasing Dynamics after a Quantum Quench via Sudden Coupling of Two Initially Independent Condensates," *Phys. Rev. Lett.* **110** (2013) 090404, arXiv:0810.5508 [cond-mat.stat-mech].

[34] G. Aarts, G. F. Bonini, and C. Wetterich, "Exact and Truncated Dynamics in Nonequilibrium Field Theory," *Phys. Rev.* **D63** (2000) 025012, arXiv:hep-ph/0007357 [hep-ph].

[35] J. Berges, S. Borsanyi, and C. Wetterich, "Prethermalization," *Phys. Rev. Lett.* **93** (2004) 142002, arXiv:hep-ph/0403234 [hep-ph].

[36] M. Moeckel and S. Kehrein, "Interaction Quench in the Hubbard Model," *Phys. Rev. Lett.* **100** (2008) 175702, arXiv:0802.3202 [cond-mat.str-el].

[37] M. Moeckel and S. Kehrein, "Real-time evolution for weak interaction quenches in quantum systems," *Annals of Physics* **324** (2009) 2146–2178, arXiv:0903.1561 [cond-mat.str-el].

[38] M. Moeckel and S. Kehrein, "Crossover from adiabatic to sudden interaction quenches in the Hubbard model: prethermalization and non-equilibrium dynamics," *New J. Phys* **12** (2010) 055016, arXiv:0911.0875 [cond-mat.quant-gas].

[39] A. Rosch, D. Rasch, B. Binz, and M. Vojta, "Metastable Superfluidity of Repulsive Fermionic Atoms in Optical Lattices," *Phys. Rev. Lett.* **101** (2008) 265301, arXiv:0809.0505 [cond-mat.other].

[40] M. Kollar, F. A. Wolf, and M. Eckstein, "Generalized Gibbs ensemble prediction of prethermalization plateaus and their relation to nonthermal steady states in integrable systems," *Phys. Rev.* **B84** (2011) 054304, arXiv:1102.2117 [cond-mat.str-el].

[41] J. Marino and A. Silva, "Relaxation, prethermalization, and diffusion in a noisy quantum ising chain," *Phys. Rev.* **B86** (2012) 060408, arXiv:1203.2108 [cond-mat.stat-mech].

[42] M. van den Worm, B. C. Sawyer, J. J. Bollinger, and M. Kastner, "Relaxation timescales and decay of correlations in a long-range interacting quantum simulator," *New J. Phys.* **15** (2013) 083007.

[43] M. Gring, M. Kuhnert, T. Langen, T. Kitagawa, B. Rauer, M. Schreitl, I. Mazets, D. A. Smith, E. Demler, and J. Schmiedmayer, "Relaxation and Prethermalization in an Isolated Quantum System," *Science* **337** (2012) 1318, arXiv:1112.0013 [cond-mat.quant-gas].

[44] J. Berges, A. Rothkopf, and J. Schmidt, "Non-thermal fixed points: Effective weak-coupling for strongly correlated systems far from equilibrium," *Phys. Rev. Lett.* **101** (2008) 041603, arXiv:0803.0131 [hep-ph].

[45] J. Berges and G. Hoffmeister, "Nonthermal fixed points and the functional renormalization group," *Nucl. Phys.* **B813** (2009) 383, arXiv:0809.5208 [hep-th].

[46] C. Scheppach, J. Berges, and T. Gasenzer, "Matter-wave turbulence: Beyond kinetic scaling," *Phys. Rev.* **A81** (2010) 033611, arXiv:0912.4183 [cond-mat.quant-gas].

[47] Orioli, A. Pineiro and Boguslavski, K. and Berges, J., "Universal self-similar dynamics of relativistic and nonrelativistic field theories near nonthermal fixed points," *Phys. Rev.* **D92** (2015) 025041, arXiv:1503.02498 [hep-ph].

[48] S. Mathey, T. Gasenzer, and J. M. Pawlowski, "Anomalous scaling at nonthermal fixed points of Burgers' and Gross-Pitaevskii turbulence," *Phys. Rev.* **A92** (2015) 023635, arXiv:1405.7652 [cond-mat.quant-gas].

[49] T. Gasenzer and J. M. Pawlowski, "Towards far-from-equilibrium quantum field dynamics: A functional renormalisation-group approach," *Phys. Lett.* **B670** (2008) 135, arXiv:0710.4627 [cond-mat.other].

[50] V. Zakharov, V. L'vov, and G. Falkovich, *Kolmogorov Spectra of Turbulence I: Wave Turbulence*. Springer, 1992.

[51] U. Frisch, *Turbulence: The Legacy of A. N. Kolmogorov*. CUP, Cambridge, UK, 1995.

[52] M. Tsubota, "Quantum turbulence," *J. Phys. Soc. Jpn.* **77** (2008) 111006, arXiv:0806.2737 [cond-mat.other].

[53] W. F. Vinen, "An introduction to quantum turbulence," *J. Low Temp. Phys.* **145** (2006) 7.

[54] A. J. Bray, "Theory of phase-ordering kinetics," *Adv. Phys.* **43** (1994) 357, arXiv:cond-mat/9501089 [cond-mat].

[55] B. Nowak, J. Schole, D. Sexty, and T. Gasenzer, "Nonthermal fixed points, vortex statistics, and superfluid turbulence in an ultracold Bose gas," *Phys. Rev.* **A85** (2012) 043627, arXiv:1111.6127 [cond-mat.quant-gas].

[56] B. Nowak, D. Sexty, and T. Gasenzer, "Superfluid Turbulence: Nonthermal Fixed Point in an Ultracold Bose Gas," *Phys. Rev.* **B84** (2011) 020506(R), arXiv:1012.4437 [cond-mat.quant-gas].

[57] B. Nowak, J. Schole, and T. Gasenzer, "Universal dynamics on the way to thermalisation," *New J. Phys.* **16** (2014) 093052, arXiv:1206.3181 [cond-mat.quant-gas].

[58] M. Schmidt, S. Erne, B. Nowak, D. Sexty, and T. Gasenzer, "Nonthermal fixed points and solitons in a one-dimensional Bose gas," *New J. Phys.* **14** (2012) 075005, arXiv:1203.3651 [cond-mat.quant-gas].

[59] J. Schole, B. Nowak, and T. Gasenzer, "Critical dynamics of a two-dimensional superfluid near a non-thermal fixed point," *Phys. Rev.* **A86** (2012) 013624, arXiv:1204.2487 [cond-mat.quant-gas].

[60] M. Karl, B. Nowak, and T. Gasenzer, "Universal scaling at nonthermal fixed points of a two-component Bose gas," *Phys. Rev.* **A88** (2013) 063615, arXiv:1307.7368 [cond-mat.quant-gas].

[61] T. Gasenzer, B. Nowak, and D. Sexty, "Charge separation in reheating after cosmological inflation," *Phys. Lett.* **B710** (2012) 500, arXiv:1108.0541 [hep-ph].

[62] J. Berges, K. Boguslavski, S. Schlichting, and R. Venugopalan, "Universal attractor in a highly occupied non-Abelian plasma," *Phys. Rev.* **D89** (2014) 114007, arXiv:1311.3005 [hep-ph].

[63] T. Gasenzer, L. McLerran, J. M. Pawlowski, and D. Sexty, "Gauge turbulence, topological defect dynamics, and condensation in Higgs models," *Nucl. Phys.* **A930** (2014) 163, arXiv:1307.5301 [hep-ph].

[64] B. Nowak, S. Erne, M. Karl, J. Schole, D. Sexty, and T. Gasenzer, "Non-thermal fixed points: universality, topology, & turbulence in Bose gases," *ArXiv e-prints* (2013) 1, arXiv:1302.1448 [cond-mat.quant-gas].

[65] C. Ewerz, T. Gasenzer, M. Karl, and A. Samberg, "Non-Thermal Fixed Point in a Holographic Superfluid," *JHEP* **05** (2015) 070, arXiv:1410.3472 [hep-th].

[66] S. S. Gubser, "Breaking an Abelian gauge symmetry near a black hole horizon," *Phys. Rev.* **D78** (2008) 065034, arXiv:0801.2977 [hep-th].

[67] S. A. Hartnoll, C. P. Herzog, and G. T. Horowitz, "Building a Holographic Superconductor," *Phys. Rev. Lett.* **101** (2008) 031601, arXiv:0803.3295 [hep-th].

[68] C. P. Herzog, P. K. Kovtun, and D. T. Son, "Holographic model of superfluidity," *Phys. Rev.* **D79** (2009) 066002, arXiv:0809.4870 [hep-th].

[69] J. Berges, K. Boguslavski, S. Schlichting, and R. Venugopalan, "Universality far from equilibrium: From superfluid Bose gases to heavy-ion collisions," *Phys. Rev. Lett.* **114** (2015) 061601, arXiv:1408.1670 [hep-ph].

[70] S. Trotzky, Y.-A. Chen, A. Flesch, I. P. McCulloch, U. Schollwöck, J. Eisert, and I. Bloch, "Probing the relaxation towards equilibrium in an isolated strongly correlated one-dimensional Bose gas," *Nature Phys.* **8** (2012) 325–330, arXiv:1101.2659 [cond-mat.quant-gas].

[71] R. Geiger, T. Langen, I. E. Mazets, and J. Schmiedmayer, "Local relaxation and light-cone-like propagation of correlations in a trapped one-dimensional Bose gas," *New J. Phys.* **16** (2014) 053034.

[72] T. Langen, S. Erne, R. Geiger, B. Rauer, T. Schweigler, M. Kuhnert, W. Rohringer, I. E. Mazets, T. Gasenzer, and J. Schmiedmayer, "Experimental observation of a generalized Gibbs ensemble," *Science* **348** (2015) 207–211, arXiv:1411.7185 [cond-mat.quant-gas].

[73] E. Nicklas, M. Karl, M. Höfer, A. Johnson, W. Muessel, H. Strobel, J. Tomkovič, T. Gasenzer, and M. K. Oberthaler, "Observation of scaling in the dynamics of a strongly quenched quantum gas," *Phys. Rev. Lett.* **115** (2015) 245301, arXiv:1509.02173 [cond-mat.quant-gas].

[74] L. E. Sadler, J. M. Higbie, S. R. Leslie, M. Vengalattore, and D. M. Stamper-Kurn, "Spontaneous symmetry breaking in a quenched ferromagnetic spinor Bose-Einstein condensate," *Nature* **443** (2006) 312, arXiv:cond-mat/0605351 [cond-mat.stat-mech].

[75] J. Kronjäger, C. Becker, P. Soltan-Panahi, K. Bongs, and K. Sengstock, "Spontaneous Pattern Formation in an Antiferromagnetic Quantum Gas," *Phys. Rev. Lett.* **105** (2010) 090402, arXiv:0904.2339 [cond-mat.quant-gas].

[76] M. Cheneau, P. Barmettler, D. Poletti, M. Endres, P. Schauß T. Fukuhara, C. Gross, I. Bloch, C. Kollath, and S. Kuhr, "Light-cone-like spreading of correlations in a quantum many-body system," *Nature* **481** (2012) 484–487, arXiv:1111.0776 [cond-mat.quant-gas].

[77] G. Lamporesi, S. Donadello, S. Serafini, F. Dalfovo, and G. Ferrari, "Spontaneous creation of Kibble-Zurek solitons in a Bose-Einstein condensate," *Nat. Phys.* **9** (2013) 656, arXiv:1306.4523 [cond-mat.quant-gas].

[78] L. Corman, L. Chomaz, T. Bienaimé, R. Desbuquois, C. Weitenberg, S. Nascimbène, J. Dalibard, and J. Beugnon, "Quench-Induced Supercurrents in an Annular Bose Gas," *Phys. Rev. Lett.* **113** (2014) 135302, arXiv:1406.4073 [cond-mat.quant-gas].

[79] L. Chomaz, L. Corman, T. Bienaimé, R. Desbuquois, C. Weitenberg, S. Nascimbène, J. Beugnon, and J. Dalibard, "Emergence of coherence via transverse condensation in a uniform quasi-two-dimensional Bose gas," *Nat. Comm.* **6** (2015) 6162, arXiv:1411.3577 [cond-mat.quant-gas].

[80] J. P. Ronzheimer, M. Schreiber, S. Braun, S. S. Hodgman, S. Langer, I. P. McCulloch, F. Heidrich-Meisner, I. Bloch, and U. Schneider, "Expansion dynamics of interacting bosons in homogeneous lattices in one and two dimensions," *Phys. Rev. Lett.* **110** (2013) 205301, arXiv:1301.5329 [cond-mat.quant-gas].

[81] Tim Langen and Remi Geiger and Jörg Schmiedmayer, "Ultracold Atoms Out of Equilibrium," *Annual Review of Condensed Matter Physics* **6** (2015) 201–217, arXiv:1408.6377 [cond-mat.quant-gas].

[82] J. Berges and T. Gasenzer, "Quantum versus classical statistical dynamics of an ultracold Bose gas," *Phys. Rev.* **A76** (2007) 033604, arXiv:cond-mat/0703163 [cond-mat.other].

[83] P. B. Blakie, A. S. Bradley, M. J. Davis, R. J. Ballagh, and C. W. Gardiner, "Dynamics and statistical mechanics of ultra-cold Bose gases using c-field techniques," *Adv. Phys.* **57** (2008) 363, arXiv:0809.1487 [cond-mat.stat-mech].

[84] A. Polkovnikov, "Phase space representation of quantum dynamics," *Ann. Phys.* **325** (2010) 1790, arXiv:0905.3384 [cond-mat.stat-mech].

[85] E. D. Siggia and A. E. Ruckenstein, "Bose condensation in spin-polarized atomic hydrogen," *Phys. Rev. Lett.* **44** (1980) 1423.

[86] E. Timmermans, "Phase separation of Bose-Einstein condensates," *Phys. Rev. Lett.* **81** (1998) 5718, arXiv:cond-mat/9709301 [cond-mat].

[87] M. Karl, B. Nowak, and T. Gasenzer, "Tuning universality far from equilibrium," *Sci. Rep.* **3** (2013) 2394, arXiv:1302.1122 [cond-mat.quant-gas].

[88] P. Pfeuty, "The one-dimensional Ising model with a transverse field," *Ann. Phys.* **57** (1970) 79–90.

[89] S. Sachdev, "Universal, finite-temperature, crossover functions of the quantum transition in the Ising chain in a transverse field," *Nucl. Phys.* **B464** (1996) 576–595, arXiv:cond-mat/9509147 [cond-mat].

[90] P. Calabrese, F. H. L. Essler, and M. Fagotti, "Quantum Quench in the Transverse-Field Ising Chain," *Physical Review Letters* **106** (2011) 227203, arXiv:1104.0154 [cond-mat.str-el].

[91] P. Calabrese, F. H. L. Essler, and M. Fagotti, "Quantum quench in the transverse field Ising chain: I. Time evolution of order parameter correlators," *J. Stat. Mech. Theor. Exp.* **7** (2012) 16, arXiv:1204.3911 [cond-mat.quant-gas].

[92] P. Calabrese, F. H. L. Essler, and M. Fagotti, "Quantum quenches in the transverse field Ising chain: II. Stationary state properties," *J. Stat. Mech.* **2012** (2012) P07022, arXiv:1205.2211 [cond-mat.stat-mech].

[93] P. Calabrese and J. Cardy, "Quantum quenches in extended systems," *J. Stat. Mech.* **0706** (2007) P06008, arXiv:0704.1880 [cond-mat.stat-mech].

[94] F. H. L. Essler, S. Evangelisti, and M. Fagotti, "Dynamical Correlations After a Quantum Quench," *Phys. Rev. Lett.* **109** (2012) 247206, arXiv:1208.1961 [cond-mat.stat-mech].

[95] M. Fagotti and F. H. L. Essler, "Reduced density matrix after a quantum quench," *Phys. Rev.* **B87** (2013) 245107, arXiv:1302.6944 [cond-mat.stat-mech].

[96] J. Kasprzak, M. Richard, S. Kundermann, A. Baas, P. Jeambrun, J. M. J. Keeling, F. M. Marchetti, M. H. Szymaska, R. Andrel, J. L. Straehli, V. Savona, P. B. Littlewood, B. Deveaud, and L. S. Dang, "Bose-Einstein condensation of exciton polaritons," *Nature* **443** (2006) 409.

[97] K. Lagoudakis, M. Wouters, M. Richard, A. Baas, I. Carusotto, R. André, L. Dang, and B. Deveaud-Plédran, "Quantized vortices in an exciton–polariton condensate," *Nature Phys.* **4** (2008) 706, arXiv:0801.1916 [cond-mat.other].

[98] A. Amo, S. Pigeon, D. Sanvitto, V. G. Sala, R. Hivet, I. Carusotto, F. Pisanello, G. Leménager, R. Houdré, E. Giacobino, C. Ciuti, and A. Bramati, "Polariton Superfluids Reveal Quantum Hydrodynamic Solitons," *Science* **332** (2011) 1167, arXiv:1101.2530 [cond-mat.quant-gas].

[99] K. Damle, S. Majumdar, and S. Sachdev, "Phase ordering kinetics of the Bose gas," *Phys. Rev.* **A54** (1996) 5037, arXiv:cond-mat/9511058 [cond-mat].

[100] R. H. Koch, V. Foglietti, W. J. Gallagher, G. Koren, A. Gupta, and M. P. A. Fisher, "Experimental evidence for vortex-glass superconductivity in Y-Ba-Cu-O," *Phys. Rev. Lett.* **63** (1989) 1511–1514.

[101] P. L. Gammel, L. F. Schneemeyer, and D. J. Bishop, "SQUID picovoltometry of $YBa_2Cu_3O_7$ single crystals: Evidence for a finite-temperature phase transition in the high-field vortex state," *Phys. Rev. Lett.* **66** (1991) 953–956.

[102] K. H. Lee and D. Stroud, "I-V characteristics of a model vortex glass: A numerical study," *Phys. Rev.* **B44** (1991) 9780–9783.

[103] D. S. Fisher, M. P. A. Fisher, and D. A. Huse, "Thermal fluctuations, quenched disorder, phase transitions, and transport in type-II superconductors," *Phys. Rev.* **B43** (1991) 130–159.

[104] A. T. Dorsey, M. Huang, and M. P. A. Fisher, "Dynamics of the normal to vortex-glass transition: Mean-field theory and fluctuations," *Phys. Rev.* **B45** (1992) 523–526.

[105] M. Kardar, G. Parisi, and Y. Zhang, "Dynamic scaling of growing interfaces," *Phys. Rev. Lett.* **56** (1986) 889–892.

[106] E. Medina, T. Hwa, M. Kardar, and Y.-C. Zhang, "Burgers equation with correlated noise: Renormalization-group analysis and applications to directed polymers and interface growth," *Phys. Rev.* **A39** (1989) 3053–3075.

[107] L. Canet, H. Chaté, B. Delamotte, and N. Wschebor, "Nonperturbative renormalization group for the Kardar-Parisi-Zhang equation," *Phys. Rev. Lett.* **104** (2010) 150601, arXiv:0905.1025 [cond-mat.stat-mech].

[108] L. Canet, H. Chaté, B. Delamotte, and N. Wschebor, "Nonperturbative renormalization group for the Kardar-Parisi-Zhang equation: General framework and first applications," *Phys. Rev.* **E84** (2011) 061128, arXiv:1107.2289 [cond-mat.stat-mech].

[109] L. M. Sieberer, S. D. Huber, E. Altman, and S. Diehl, "Dynamical Critical Phenomena in Driven-Dissipative Systems," *Phys. Rev. Lett.* **110** (2013) 195301, arXiv:1301.5854 [cond-mat.quant-gas].

[110] L. M. Sieberer, S. D. Huber, E. Altman, and S. Diehl, "Nonequilibrium functional renormalization for driven-dissipative bose-einstein condensation," *Phys. Rev.* **B89** (2014) 134310, arXiv:1309.7027 [cond-mat.quant-gas].

[111] H. Takeuchi, S. Ishino, and M. Tsubota, "Binary quantum turbulence arising from countersuperflow instability in two-component Bose-Einstein condensates," *Phys. Rev. Lett.* **105** (2010) 205301, arXiv:1008.4664 [cond-mat.quant-gas].

[112] S. Ishino, M. Tsubota, and H. Takeuchi, "Countersuperflow instability in miscible two-component Bose-Einstein condensates," *Phys. Rev.* **A83** (2011) 063602, arXiv:1106.0884 [cond-mat.quant-gas].

[113] J. Sabbatini, W. H. Zurek, and M. J. Davis, "Phase separation and pattern formation in a binary Bose-Einstein condensate," *Phys. Rev. Lett.* **107** (2011) 230402, arXiv:1106.5843 [cond-mat.quant-gas].

[114] H. Takeuchi, K. Kasamatsu, M. Nitta, and M. Tsubota, "Vortex Formations from Domain Wall Annihilations in Two-component Bose-Einstein Condensates," *J. Low. Temp. Phys.* **162** (2011) 243, arXiv:1205.2328 [cond-mat.quant-gas].

[115] M. Nitta, K. Kasamatsu, M. Tsubota, and H. Takeuchi, "Creating vortons and three-dimensional skyrmions from domain wall annihilation with stretched vortices in Bose-Einstein condensates," *Phys. Rev.* **A85** (2012) 053639, arXiv:1203.4896 [cond-mat.quant-gas].

[116] F. Zhan, J. Sabbatini, M. J. Davis, and I. P. McCulloch, "Miscible-immiscible quantum phase transition in coupled two-component Bose-Einstein condensates in one-dimensional optical lattices," *Phys. Rev.* **A90** (2014) 023630, arXiv:1403.4823 [cond-mat.quant-gas].

[117] M. Karl, "The emergence of topological defects and their role in non-equilibrium dynamics and turbulence in an ultracold two-component bose gas," master's thesis, Universität Heidelberg, 2012.

[118] E. Nicklas, H. Strobel, T. Zibold, C. Gross, B. A. Malomed, P. G. Kevrekidis, and M. K. Oberthaler, "Rabi flopping induces spatial demixing dynamics," *Phys. Rev. Lett.* **107** (2011) 193001, arXiv:1109.5601 [cond-mat.quant-gas].

[119] J. Sabbatini, W. H. Zurek, and M. J. Davis, "Causality and defect formation in the dynamics of an engineered quantum phase transition in a coupled binary Bose–Einstein condensate," *New J. Phys.* **14** (2012) 095030, arXiv:1208.5295 [cond-mat.quant-gas].

[120] J. W. Weyssenhoff, "Relativistic dynamics of spin-fluids and spin-particles," *Nature* **157** (1946) 766.

[121] K. Kasamatsu, M. Tsubota, and M. Ueda, "Spin textures in rotating two-component Bose-Einstein condensates," *Phys. Rev.* **A71** (2005) 043611, arXiv:cond-mat/0411544 [cond-mat].

[122] U. Schollwöck, J. Richter, D. Farnell, and R. Bishop, eds., *Quantum Magnetism*. No. 645 in Lecture Notes in Physics. Springer, Berlin, 2004.

[123] K. Kasamatsu and M. Tsubota, "Modulation instability and solitary-wave formation in two-component Bose-Einstein condensates," *Phys. Rev.* **A74** (2006) 013617, arXiv:cond-mat/0603838 [cond-mat.other].

[124] A. M. J. Schakel, *Boulevard of Broken Symmetries – Effective Field Theories of Condensed Matter*. World Scientific, 2008.

[125] A. Altland and B. Simons, *Condensed Matter Field Theory*. Cambridge University Press, second ed., 2010.

[126] K. Kasamatsu, H. Takeuchi, M. Tsubota, and M. Nitta, "Wall-vortex composite solitons in two-component Bose-Einstein condensates," *Phys. Rev.* **A88** (2013) 013620, arXiv:1303.7052 [cond-mat.quant-gas].

[127] J. Zinn-Justin, *Quantum Field Theory and Critical Phenomena*. International series of monographs on physics. Clarendon Press, 2004.

[128] S. Sachdev, *Quantum Phase Transitions*. CUP, New York, 2000.

[129] A. A. Nersesyan, A. Luther, and F. V. Kusmartsev, "Scaling properties of the two-chain model," *Phys. Lett.* **A176** (1993) 363, arXiv:cond-mat/9303041 [cond-mat].

[130] M. Peskin and D. Schroeder, *An Introduction to Quantum Field Theory*. Advanced book classics. Addison-Wesley Publishing Company, 1995.

[131] T. W. B. Kibble, "Topology of cosmic domains and strings," *J. Phys. A: Math. Gen.* **9** (1976) 1387.

[132] W. H. Zurek, "Cosmological experiments in superfluid helium?," *Nature* **317** (1985) 505.

[133] D. Nelson, *Defects and geometry in condensed matter physics*. CUP, Cambridge, UK, 2002.

[134] E. B. Bogomolnyi, "The stability of classical solutions," *Sov. J. Nucl. Phys.* **24** (1976) 449. [Yad. Fiz. 24, 861 (1976)].

[135] M. K. Prasad and C. M. Sommerfield, "Exact Classical Solution for the 't Hooft Monopole and the Julia-Zee Dyon," *Phys. Rev. Lett.* **35** (1975) 760–762.

[136] Y. Isozumi, M. Nitta, K. Ohashi, and N. Sakai, "All exact solutions of a $1/4$ Bogomol'nyi-Prasad-Sommerfield equation," *Phys. Rev.* **D71** (2005) 065018, arXiv:hep-th/0405129 [hep-th].

[137] K. Kasamatsu, H. Takeuchi, M. Nitta, and M. Tsubota, "Analogues of D-branes in Bose-Einstein condensates," *JHEP* **11** (2010) 068, arXiv:1002.4265 [cond-mat.quant-gas].

[138] D. Kivotides, J. C. Vassilicos, D. C. Samuels, and C. F. Barenghi, "Kelvin Waves Cascade in Superfluid Turbulence," *Phys. Rev. Lett.* **86** (2001) 3080.

[139] W. F. Vinen, M. Tsubota, and A. Mitani, "Kelvin-Wave Cascade on a Vortex in Superfluid ^{4}He at a Very Low Temperature," *Phys. Rev. Lett.* **91** 135301, arXiv:cond-mat/0306191 [cond-mat].

[140] J. A. Espichán Carrillo, A. Maia, Jr., and V. M. Mostepanenko, "Jacobi Elliptic Solutions of $\lambda\phi^4$ Theory in a Finite Domain," *Int. J. Mod. Phys.* **A15** (2000) 2645, arXiv:hep-th/9905151 [hep-th].

[141] M. Lakshmanan and A. Saxena, "Dynamic and static excitations of a classical discrete anisotropic Heisenberg ferromagnetic spin chain," *Physica* **D237** (2008) 885–897, arXiv:0712.2503 [nlin.SI].

[142] T. Schweigler, V. Kasper, S. Erne, B. Rauer, T. Langen, T. Gasenzer, J. Berges, and J. Schmiedmayer, "On solving the quantum many-body problem," *ArXiv e-prints* (2015) 1, arXiv:1505.03126 [cond-mat.quant-gas].

[143] C. Pethick and H. Smith, *Bose-Einstein condensation in dilute gases*. CUP, Cambridge, UK, 2006.

[144] O. Penrose and L. Onsager, "Bose-Einstein condensation and liquid helium," *Phys. Rev.* **104** (1956) 576.

[145] A. Schakel, "Entangled vortices: Onsager's geometrical picture of superfluid phase transitions," *J. Low. Temp. Phys.* **129** no. 5, (2002) 323.

[146] X. Wen, *Quantum Field Theory of Many-Body Systems:From the Origin of Sound to an Origin of Light and Electrons.* Oxford Graduate Texts. OUP Oxford, 2004.

[147] R. Rajaraman, *Solitons and Instantons.* North Holland, 1987.

[148] J. Berges and J. Serreau, "Parametric resonance in quantum field theory," *Phys. Rev. Lett.* **91** (2003) 111601, arXiv:hep-ph/0208070 [hep-ph].

[149] J. Berges, D. Gelfand, and J. Pruschke, "Quantum theory of fermion preheating," *Phys. Rev. Lett.* **107** (2011) 061301, arXiv:1012.4632 [hep-ph].

[150] J. Berges, J. Pruschke, and A. Rothkopf, "Instability-induced fermion production in quantum field theory," *Phys. Rev.* **D80** (2009) 023522, arXiv:0904.3073 [hep-ph].

[151] P. Tommasini, E. J. V. de Passos, A. F. R. de Toledo Piza, M. S. Hussein, and E. Timmermans, "Bogoliubov theory for mutually coherent condensates," *Phys. Rev.* **A67** (2003) 023606.

[152] W. Zhang, D. L. Zhou, M.-S. Chang, M. S. Chapman, and L. You, "Dynamical Instability and Domain Formation in a Spin-1 Bose-Einstein Condensate," *Phys. Rev. Lett.* **95** (2005) 180403, arXiv:cond-mat/0509549 [cond-mat.other].

[153] H.-J. Miesner and D. M. Stamper-Kurn and J. Stenger and S. Inouye and A. P. Chikkatur and W. Ketterle, "Observation of Metastable States in Spinor Bose-Einstein Condensates," *Phys. Rev. Lett.* **82** (1999) 2228, arXiv:cond-mat/9811161 [cond-mat].

[154] H. Saito and M. Ueda, "Spontaneous magnetization and structure formation in a spin-1 ferromagnetic Bose-Einstein condensate," *Phys. Rev.* **A72** (2005) 023610, arXiv:cond-mat/0504398 [cond-mat.other].

[155] K. W. Schwarz, "Turbulence in superfluid helium: Steady homogeneous counterflow," *Phys. Rev.* **B18** (1978) 245.

[156] K. Fujimoto and M. Tsubota, "Counterflow instability and turbulence in a spin-1 spinor Bose-Einstein condensate," *Phys. Rev.* **A85** (2012) 033642, arXiv:1112.2443 [cond-mat.quant-gas].

[157] K. Fujimoto and M. Tsubota, "Spin turbulence in a trapped spin-1 spinor Bose-Einstein condensate," *Phys. Rev.* **A85** (2012) 053641, arXiv:1204.0619 [cond-mat.quant-gas].

[158] C. Hamner, J. J. Chang, P. Engels, and M. A. Hoefer, "Generation of Dark-Bright Soliton Trains in Superfluid-Superfluid Counterflow," *Phys. Rev. Lett.* **106** (2011) 065302, arXiv:1005.2610 [cond-mat.quant-gas].

[159] C. Lee, "Universality and Anomalous Mean-Field Breakdown of Symmetry-Breaking Transitions in a Coupled Two-Component Bose-Einstein Condensate," *Phys. Rev. Lett.* **102** (2009) 070401, arXiv:0806.0423 [cond-mat.mes-hall].

[160] S. P. Cockburn, D. Gallucci, and N. P. Proukakis, "Quantitative study of quasi-one-dimensional Bose gas experiments via the stochastic Gross–Pitaevskii equation," *Phys. Rev.* **A84** (2011) 023613, arXiv:1103.2740 [cond-mat.quant-gas].

[161] D. Gallucci, S. P. Cockburn, and N. P. Proukakis, "Phase coherence in quasicondensate experiments: An ab initio analysis via the stochastic Gross-Pitaevskii equation," *Phys. Rev.* **A86** (2012) 013627, arXiv:1205.6075 [cond-mat.quant-gas].

[162] S. P. Cockburn and N. P. Proukakis, "*Ab initio* methods for finite-temperature two-dimensional Bose gases," *Phys. Rev.* **A86** (2012) 033610, arXiv:1206.5787 [cond-mat.quant-gas].

[163] D. S. Hall, M. R. Matthews, J. R. Ensher, C. E. Wieman, and E. A. Cornell, "Dynamics of component separation in a binary mixture of Bose-Einstein condensates," *Phys. Rev. Lett.* **81** (1998) 1539, arXiv:cond-mat/9804138 [cond-mat].

[164] J. Guzman, G.-B. Jo, A. N. Wenz, K. W. Murch, C. K. Thomas, and D. M. Stamper-Kurn, "Long-time-scale dynamics of spin textures in a degenerate $F = 1$ ^{87}Rb spinor Bose gas," *Phys. Rev.* **A84** (2011) 063625, arXiv:1107.2672 [cond-mat.quant-gas].

[165] C. Nore, M. Abid, and M. Brachet, "Decaying Kolmogorov turbulence in a model of superflow," *Phys. Fl.* **9** (1997) 2644.

[166] C. Nore, M. Abid, and M. Brachet, "Kolmogorov turbulence in low-temperature superflows," *Phys. Rev. Lett.* **78** (1997) 3896.

[167] G. Porod, "Die Röntgenkleinwinkelstreuung von dichtgepackten kolloiden Systemen," *Kolloid-Zeitschrift* **124** 83–114.

[168] G. Porod, "Die Röntgenkleinwinkelstreuung von dichtgepackten kolloiden Systemen," *Kolloid-Zeitschrift* **125** 51–57.

[169] T. Lee and Y. Pang, "Nontopological solitons," *Physics Reports* **221** (1992) 251–350.

[170] A. Rajantie, "Formation of topological defects in gauge field theories," *Int. J. Mod. Phys.* **A17** (2002) 1, arXiv:hep-ph/0108159 [hep-ph].

[171] C. Castelnovo, R. Moessner, and S. Sondhi, "Magnetic monopoles in spin ice," *Nature* **451** (2008) 42, arXiv:0710.5515 [cond-mat.str-el].

[172] J. Ruostekoski and J. R. Anglin, "Creating vortex rings and three-dimensional skyrmions in Bose-Einstein condensates," *Phys. Rev. Lett.* **86** (2001) 3934, arXiv:cond-mat/0103310 [cond-mat.stat-mech].

[173] I. Dierking, *Textures of liquid crystals*. Wiley-VCH, 2003.

[174] J. Stenger, S. Inouye, D. Stamper-Kurn, H. Miesner, A. Chikkatur, and W. Ketterle, "Spin domains in ground-state Bose-Einstein condensates," *Nature* **396** (1998) 345, arXiv:cond-mat/9901072 [cond-mat.stat-mech].

[175] M. Vengalattore, S. R. Leslie, J. Guzman, and D. M. Stamper-Kurn, "Spontaneously Modulated Spin Textures in a Dipolar Spinor Bose-Einstein Condensate," *Phys. Rev. Lett.* **100** (2008) 170403, arXiv:0712.4182 [quant-ph].

[176] M. Ueda, "Bose Gases with Nonzero Spin," *Ann. Rev. Cond. Mat. Phys.* **3** (2012) 263.

[177] L. P. Pitaevskii and S. Stringari, *Bose-Einstein Condensation*. Clarendon Press, Oxford, 2003.

[178] S. M. Barnett and P. M. Radmore, *Methods in Theoretical Quantum Optics*. CPO, Oxford, 1997.

[179] B. Wouters, J. De Nardis, M. Brockmann, D. Fioretto, M. Rigol, and J.-S. Caux, "Quenching the Anisotropic Heisenberg Chain: Exact Solution and Generalized Gibbs Ensemble Predictions," *Phys. Rev. Lett.* **113** (2014) 117202, arXiv:1405.0172 [cond-mat.str-el].

[180] M. Fagotti, M. Collura, F. H. L. Essler, and P. Calabrese, "Relaxation after quantum quenches in the spin-1/2 Heisenberg XXZ chain," *Phys. Rev.* **B89** (2014) 125101, arXiv:1311.5216 [cond-mat.stat-mech].

[181] J.-S. Caux and F. H. L. Essler, "Time Evolution of Local Observables After Quenching to an Integrable Model," *Phys. Rev. Lett.* **110** (2013) 257203, arXiv:1301.3806 [cond-mat.stat-mech].

[182] E. Ilievski, J. De Nardis, B. Wouters, J.-S. Caux, F. H. L. Essler, and T. Prosen, "Complete Generalized Gibbs Ensembles in an Interacting Theory," *Phys. Rev. Lett.* **115** (2015) 157201, arXiv:1507.02993 [quant-ph].

[183] A. Maraga, A. Chiocchetta, A. Mitra, and A. Gambassi, "Aging and coarsening in isolated quantum systems after a quench: Exact results for the quantum $O(N)$ model with $N \to \infty$," *Phys. Rev.* **E92** (2015) 042151, arXiv:1506.04528 [cond-mat.stat-mech].

[184] M. H. Anderson, J. R. Ensher, M. R. Matthews, C. E. Wieman, and E. A. Cornell, "Observation of Bose-Einstein condensation in a dilute atomic vapor," *Science* **269** (1995) 198.

[185] K. B. Davis, M.-O. Mewes, M. R. Andrews, N. J. van Druten, D. S. Durfee, D. M. Kurn, and W. Ketterle, "Bose-Einstein condensation in a gas of sodium atoms," *Phys. Rev. Lett.* **75** (1995) 3969.

[186] C. K. Law, H. Pu, and N. P. Bigelow, "Quantum Spins Mixing in Spinor Bose-Einstein Condensates," *Phys. Rev. Lett.* **81** (1998) 5257, arXiv:cond-mat/9807258 [cond-mat.soft].

[187] H. Pu, C. K. Law, S. Raghavan, J. H. Eberly, and N. P. Bigelow, "Spin-mixing dynamics of a spinor Bose-Einstein condensate," *Phys. Rev.* **A60** (1999) 1463.

[188] T.-L. Ho and S. K. Yip, "Fragmented and Single Condensate Ground States of Spin-1 Bose Gas," *Phys. Rev. Lett.* **84** (2000) 4031, arXiv:cond-mat/9905339 [cond-mat].

[189] M.-S. Chang, C. D. Hamley, M. D. Barrett, J. A. Sauer, K. M. Fortier, W. Zhang, L. You, and M. S. Chapman, "Observation of Spinor Dynamics in Optically Trapped ^{87}Rb Bose-Einstein Condensates," *Phys. Rev. Lett.* **92** (2004) 140403, arXiv:cond-mat/0309164 [cond-mat.soft].

[190] Y. Kawaguchi, H. Saito, K. Kudo, and M. Ueda, "Spontaneous magnetic ordering in a ferromagnetic spinor dipolar Bose-Einstein condensate," *Phys. Rev.* **A82** (2010) 043627, arXiv:0909.0565 [cond-mat.quant-gas].

[191] S. De, D. L. Campbell, R. M. Price, A. Putra, B. M. Anderson, and I. B. Spielman, "Quenched binary Bose-Einstein condensates: Spin-domain formation and coarsening," *Phys. Rev.* **A89** (2014) 033631, arXiv:1211.3127 [cond-mat.quant-gas].

[192] S. Raghavan, A. Smerzi, S. Fantoni, and S. R. Shenoy, "Coherent oscillations between two weakly coupled Bose-Einstein condensates: Josephson effects, π oscillations, and macroscopic quantum self-trapping," *Phys. Rev.* **A59** (1999) 620, arXiv:cond-mat.soft [cond-mat/9706220].

[193] S. Raghavan, H. Pu, P. Meystre, and N. P. Bigelow, "Generation of arbitrary Dicke states in spinor Bose-Einstein condensates," *Opt. Commun.* **188** (2001) 149, arXiv:cond-mat/0010140 [cond-mat.soft].

[194] Ö. E. Müstecaplioğlu, M. Zhang, and L. You, "Spin squeezing and entanglement in spinor condensates," *Phys. Rev.* **A66** (2002) 033611, arXiv:quant-ph/0203015 [quant-ph].

[195] M. Erhard, H. Schmaljohann, J. Kronjäger, K. Bongs, and K. Sengstock, "Measurement of a mixed-spin-channel Feshbach resonance in ^{87}Rb," *Phys. Rev.* **A69** (2004) 032705, arXiv:cond-mat/0309318 [cond-mat.other].

[196] D. H. Santamore and E. Timmermans, "Spin critical opalescence in zero-temperature Bose-Einstein condensates," *Eur. Phys. Lett.* **97** (2012) 36009, arXiv:1202.3365 [cond-mat.stat-mech].

[197] H. Strobel, W. Muessel, D. Linnemann, T. Zibold, D. B. Hume, L. Pezzè, A. Smerzi, and M. K. Oberthaler, "Fisher information and entanglement of non-Gaussian spin states," *Science* **345** (2014) 424–427, arXiv:1507.03782 [quant-ph].

[198] W. Muessel, H. Strobel, D. Linnemann, T. Zibold, B. Juliá-Díaz, and M. K. Oberthaler, "Twist-and-turn spin squeezing in Bose-Einstein condensates," *Phys. Rev.* **A92** (2015) 023603, arXiv:1507.02930 [quant-ph].

[199] E. Zohar, J. I. Cirac, and B. Reznik, "A cold-atom quantum simulator for SU(2) Yang-Mills lattice gauge theory," *Phys. Rev. Lett.* **110** (2013) 125304, arXiv:1211.2241 [quant-ph].

[200] D. Banerjee, M.Boegli, M. Dalmonte, E. Rico, P. Stebler, U.-J. Wiese, and P. Zoller, "Atomic Quantum Simulation of U(N) and SU(N) Non-Abelian Lattice Gauge Theories," *Phys. Rev. Lett.* **110** (2013) 125303, arXiv:1211.2242 [cond-mat.quant-gas].

[201] E. Zohar, J. I. Cirac, and B. Reznik, "Quantum simulations of gauge theories with ultracold atoms: Local gauge invariance from angular-momentum conservation," *Phys. Rev.* **A88** (2013) 023617, arXiv:1303.5040 [quant-ph].

[202] T. Zibold, E. Nicklas, C. Gross, and M. K. Oberthaler, "Classical Bifurcation at the Transition from Rabi to Josephson Dynamics," *Phys. Rev. Lett.* **105** (2010) 204101, arXiv:1008.3057 [cond-mat.quant-gas].

[203] A. Widera, O. Mandel, M. Greiner, S. Kreim, T. W. Hänsch, and I. Bloch, "Entanglement Interferometry for Precision Measurement of Atomic Scattering Properties," *Phys. Rev. Lett.* **92** (2004) 160406, arXiv:cond-mat/0310719 [cond-mat.soft].

[204] E. Timmermans, "Phase Separation of Bose-Einstein Condensates," *Phys. Rev. Lett.* **81** (1998) 5718–5721, arXiv:cond-mat/9709301 [cond-mat].

[205] S. Sachdev, "Quantum Criticality: Competing Ground States in Low Dimensions," *Science* **288** (2000) 475, arXiv:cond-mat/0009456 [cond-mat.str-el].

[206] J. Berges, "Introduction to nonequilibrium quantum field theory," *AIP Conf. Proc.* **739** (2005) 3, hep-ph/0409233.

[207] A. Maraga, P. Smacchia, and A. Silva, "Dynamics following a linear ramps in the $O(N)$ model: dynamical transition and statistics of excitations," *ArXiv e-prints* (2016) 1, arXiv:1602.01763 [cond-mat.stat-mech].

[208] A. Chiocchetta, M. Tavora, A. Gambassi, and A. Mitra, "Short-time universal scaling in an isolated quantum system after a quench," *Phys. Rev.* **B91** (2015) 220302, arXiv:1411.7939 [cond-mat.quant-gas].

[209] J. M. Higbie, L. E. Sadler, S. Inouye, A. P. Chikkatur, S. R. Leslie, K. L. Moore, V. Savalli, and D. M. Stamper-Kurn, "Direct Nondestructive Imaging of

Magnetization in a Spin-1 Bose-Einstein Gas," *Phys. Rev. Lett.* **95** (2005) 050401, arXiv:cond-mat/0502517 [cond-mat.other].

[210] A. Mitra, "Time Evolution and Dynamical Phase Transitions at a Critical Time in a System of One-Dimensional Bosons after a Quantum Quench," *Phys. Rev. Lett.* **109** (2012) 260601, arXiv:1207.3777 [cond-mat.str-el].

[211] M. Tavora and A. Mitra, "Quench dynamics of one-dimensional bosons in a commensurate periodic potential: A quantum kinetic equation approach," *Phys. Rev.* **B88** (2013) 115144, arXiv:1306.6121 [cond-mat.stat-mech].

[212] H. Cakir, "Dynamics of the Transverse Field Ising Chain after a Sudden Quench," master's thesis, Universität Heidelberg, 2015.

[213] E. Lieb, T. Schultz, and D. Mattis, "Two soluble models of an antiferromagnetic chain," *Annals of Physics* **16** (1961) 407–466.

[214] B. Bertini, F. H. L. Essler, S. Groha, and N. J. Robinson, "Prethermalization and Thermalization in Models with Weak Integrability Breaking," *Phys. Rev. Lett.* **115** (2015) 180601.

[215] S. Weinberg, *The Quantum Theory of Fields, Vol. II.* CUP, Cambridge, UK, 1996.

[216] G. Dagvadorj, J. M. Fellows, S. Matyjaskiewicz, F. M. Marchetti, I. Carusotto, and M. H. Szymanska, "Non-equilibrium Berezinskii-Kosterlitz-Thouless Transition in a Driven Open Quantum System," *Phys. Rev.* **X5** (2015) 041028, arXiv:1412.7361 [cond-mat.quant-gas].

[217] E. Altman, L. M. Sieberer, L. Chen, S. Diehl, and J. Toner, "Two-dimensional superfluidity of exciton-polaritons requires strong anisotropy," *Phys. Rev.* **X5** (2015) 011017, arXiv:1311.0876 [cond-mat.stat-mech].

[218] S. Mathey, T. Gasenzer, and J. M. Pawlowski, "Anomalous scaling at nonthermal fixed points of Burgers' and Gross-Pitaevskii turbulence," *Phys. Rev.* **A92** (2015) 023635.

[219] A. P. Orioli, "Turbulence and self-similarity in strongly correlated scalar field theories," master's thesis, Universität Heidelberg, 2014.

[220] F. Brock, "Universal scaling in driven ultracold bose gases far from equilibrium," master's thesis, Universität Heidelberg, 2015.

[221] A. Adams, P. M. Chesler, and H. Liu, "Holographic turbulence," *Phys. Rev. Lett.* **112** (2014) 151602, arXiv:1307.7267 [hep-th].

[222] T. Müller, "Universelles Skalenverhalten im Spektrum $n(k)$ ultrakalter Bosegase in zwei Dimensionen," master's thesis, Universität Heidelberg, 2014.

[223] V. Berezinskii, "Destruction of long-range order in one-dimensional and two-dimensional systems having a continuous symmetry group I. Classical systems," *JETP* **32** (1971) 493.

[224] J. Kosterlitz and D. Thouless, "Ordering, metastability and phase transitions in two-dimensional systems," *J. Phys. C: Sol. St. Phys.* **6** (1973) 1181.

[225] A. J. Bray and A. D. Rutenberg, "Growth laws for phase ordering," *Phys. Rev.* **E49** (1994) 27(R), arXiv:cond-mat/9303011 [cond-mat].

[226] A. J. Bray and S. Puri, "Asymptotic structure factor and power-law tails for phase ordering in systems with continuous symmetry," *Phys. Rev. Lett.* **67** (1991) 2670–2673.

[227] A. J. Bray and K. Humayun, "Universal amplitudes of power-law tails in the asymptotic structure factor of systems with topological defects," *Phys. Rev.* **47** (1993) 9(R).

[228] A. J. Bray, "Topological defects, correlation functions, and power-law tails in phase-ordering kinetics," *Phys. Rev.* **E47** (1993) 228–235.

[229] A. J. Bray, "Exact renormalization-group results for domain-growth scaling in spinodal decomposition," *Phys. Rev. Lett.* **62** (1989) 2841–2844.

[230] A. J. Bray, "Renormalization-group approach to domain-growth scaling," *Phys. Rev.* **B41** (1990) 6724–6732.

[231] J. L. Cardy, "Random initial conditions and nonlinear relaxation," *Journal of Physics A: Mathematical and General* **25** (1992) 2765.

[232] J. R. Abo-Shaeer, C. Raman, J. M. Vogels, and W. Ketterle, "Observation of Vortex Lattices in Bose-Einstein Condensates," *Science* **292** (2001) 476.

[233] M. Olshanii, "Atomic Scattering in the Presence of an External Confinement and a Gas of Impenetrable Bosons," *Phys. Rev. Lett.* **81** (1998) 938, arXiv:cond-mat/9804130 [cond-mat].

[234] D. S. Petrov, M. Holzmann, and G. V. Shlyapnikov, "Bose-Einstein Condensation in Quasi-2D Trapped Gases," *Phys. Rev. Lett.* **84** (2000) 2551, arXiv:cond-mat/9909344 [cond-mat.stat-mech].

[235] M. Frigo and S. G. Johnson, "The design and implementation of FFTW3," in *Proceedings of the IEEE*, pp. 216–231. 2005.

[236] G. Guennebaud, B. Jacob, *et al.*, "Eigen v3." http://eigen.tuxfamily.org, 2010.

[237] L. Dagum and R. Menon, "OpenMP: an industry standard API for shared-memory programming," *Computational Science Engineering, IEEE* **5** (1998) 46.

[238] J. Nickolls, I. Buck, M. Garland, and K. Skadron, "Scalable Parallel Programming with CUDA," *Queue* **6** (2008) 40–53.